

Structural and Electrochemical Studies of Positive Electrode Materials
in the Li-Mn-Ni-O System for Lithium-ion Batteries

by

Aaron William Rowe

Submitted in partial fulfillment of the requirements
for the degree of Doctor of Philosophy

at

Dalhousie University

Halifax, Nova Scotia

May 2014

© Copyright by Aaron William Rowe, 2014

Dedication

To my parents, Hubert and Lorraine Rowe.

I never could have done it without you.

Table of Contents

List of Tables	vii
List of Figures	viii
Abstract	xiii
List of Abbreviations and Symbols Used	xiv
Acknowledgements.....	xvi
Chapter 1 Introduction	1
1.1 Lithium-ion Batteries	1
1.2 Positive Electrode Materials.....	5
1.3 Li-Mn-Ni-O Materials	7
1.3.1 Crystal Structures	7
1.3.2 Ternary Diagrams	15
1.3.3 Electrochemical Characteristics	17
1.4 Li-Mn-Ni-O Pseudo-ternary Phase Diagrams	22
1.4.1 General Features of Ternary Phase Diagrams.....	22
1.4.2 Phase Diagrams from Combinatorial Studies	24
1.4.3 Positive Electrode Materials Region	31
1.5 Scope and Structure of Thesis.....	33
Chapter 2 Synthesis, Characterization, and Analysis Techniques.....	35
2.1 Synthesis.....	35
2.1.1 Starting Reagents.....	36
2.1.2 Hydroxide Precursors	36

2.1.3	Li-Mn-Ni-O Materials	38
2.2	Materials Characterization	40
2.2.1	Elemental Analysis.....	40
2.2.2	Powder X-ray Diffraction and Structural Refinement	40
2.2.3	Scanning Electron Microscopy	44
2.2.4	BET Surface Area Analysis	44
2.3	Electrochemical Characterization.....	45
2.3.1	Electrode Preparation	45
2.3.2	Coin Cells.....	46
2.3.3	Electrochemical Measurements	47
2.3.4	Ultra High Precision Coulometry.....	48
Chapter 3	Pseudo-ternary Phase Diagrams of the Positive Electrode Materials Region of the Li-Mn-Ni-O System for Bulk Samples.....	49
3.1	Experimental.....	51
3.2	Li-Mn-Ni-O Compositions for Phase Mapping.....	51
3.3	XRD Analysis of Samples Synthesized at 900°C	54
3.3.1	The 1:1 Composition Series.....	56
3.3.2	The 3:5 Composition Series.....	60
3.3.3	The 1:3 Composition Series.....	63
3.3.4	The 1:5 Composition Series.....	67
3.3.5	Summary of XRD Analysis of Samples at 900°C.....	71
3.4	XRD Analysis of Samples Synthesized at 800°C in Air.....	71
3.4.1	Quenched Samples	72
3.4.2	Slow Cooled Samples.....	75

3.4.3	Summary of XRD Analysis of Samples at 800°C.....	77
3.5	Analysis of Unique 900°C Quenched Compositions	78
3.5.1	Cubic to Layered Phase Transition.....	78
3.5.2	Location of Sample K in Multi-phase Regions.....	80
3.5.3	The Spinel End-member	83
3.5.4	Single-phase Layered Boundary “Bump” Region.....	87
3.6	Lattice Constant Comparisons Between Samples	88
3.7	Contour Plots of the Single-phase Layered Region	92
3.8	Li-Mn-Ni-O Pseudo-ternary Phase Diagrams at 900°C and 800°C in Air	94
3.9	Concluding Remarks on Phase Diagrams	97
Chapter 4	Electrochemical Characterization of Li-deficient Single-phase Layered Li-Mn-Ni-O Compositions.....	101
4.1	Experimental.....	102
4.2	Materials Characterization.....	103
4.3	The Effect of Upper Potential Limit on the Cycling Behaviour of the Li- deficient Bump Materials	111
4.4	Differential Capacity Analysis of Bump Materials.....	118
4.5	Extended Cycling Analysis	122
4.6	Discussion of Electrochemical Analysis.....	128
4.7	Summary of Electrochemical Characterization of Li-deficient Materials.	129
Chapter 5	Anomalous Capacity Growth in Slow Cooled Single-phase and Multi- phase Li-Mn-Ni-O Compositions.....	131
5.1	Experimental.....	132
5.2	Materials Characterization.....	133

5.3	First Cycle Analysis and Observed Capacity Increase.....	138
5.4	Extended Cycling Electrochemical Characterization	142
5.5	Summary of Capacity Growth Materials	151
Chapter 6 Ultra High Precision Coulometry Measurements of Li-rich and Li-deficient Single-phase Layered Li-Mn-Ni-O Materials		
6.1	Experimental.....	156
6.2	Materials Characterization.....	157
6.3	Voltage Curves	159
6.4	The Effect of Potential Limit on Electrolyte Oxidation and Phase Conversion	163
6.5	Coulombic Efficiency and Charge Endpoint Capacity Slippage Analysis	167
6.6	Discussion of the Inherent Cycling Stability of $\text{Li}[\text{Li}_{0.16}\text{Ni}_{0.12}\text{Mn}_{0.65}\square_{0.07}]\text{O}_2$	169
6.7	Summary of UHPC Analysis.....	170
Chapter 7 Conclusions and Future Work.....		
7.1	Conclusions.....	172
7.2	Future Work.....	175
Appendix.....		
	References	187

List of Tables

Table 1.1. Average potential, reversible capacity, crystallographic density, and volumetric energy density of various positive electrode materials.	7
Table 3.1. Sample label, composition series (Ni:Mn ratio), metal mole fractions, and phase diagram coordinates in (Li, Mn) notation for samples A through AC in Figure 3.1.	53
Table 3.2. Lattice parameters of various copper plate quenched compositions at 900°C in air. The lattice parameters of sample K from liquid nitrogen quenching (LNQ) are also shown.	89
Table 3.3. Lattice parameters of various slow cooled compositions at 900°C in air.	91
Table 4.1. Elemental composition, layered notation, metal vacancy estimate, hexagonal lattice constants, and BET surface area results of samples B ₁ to B ₅	104
Table 5.1. Elemental compositions and lattice parameters of component phases of samples G ₁ to G ₅	134
Table 5.2. Cycling data from cycles 1 to 150 of samples G ₁ to G ₅ . Note that the specific capacity and capacity percent increase of sample G ₅ is based 110 cycles only	140
Table 6.1. Elemental composition, standard layered notation, and hexagonal lattice constants of samples L ₁ , L ₂ , and L ₃	158

List of Figures

Figure 1.1. The basic components of a Li-ion cell.	4
Figure 1.2. Lithium metal oxides showing the (a) hexagonal layered (e.g., LiCoO_2) and (b) cubic spinel (e.g., LiMn_2O_4) crystal structures.....	9
Figure 1.3. The crystal structures of monoclinic $\text{Li}[\text{Li}_{1/3}\text{Mn}_{2/3}]\text{O}_2$ (Li_2MnO_3) and hexagonal $\text{Li}[\text{Ni}_{1/2}\text{Mn}_{1/2}]\text{O}_2$ end-members combined to form the Li-rich oxide layered solid solution series $\text{Li}[\text{Ni}_x\text{Li}_{(1/3-2x/3)}\text{Mn}_{(2/3-x)}]\text{O}_2$	10
Figure 1.4. A comparison of the positions of the layered and monoclinic unit cells in a Li-rich layered structure.....	12
Figure 1.5. (a) An illustration of stacking faults between hexagonal layers in monoclinic Li_2MnO_3 and (b) XRD patterns of Li_2MnO_3 with increasing amounts of stacking faults.	14
Figure 1.6. (a) A simple ternary diagram showing compositions with one component (at vertices), two components (on lines), and three components (in triangle) and (b) The general pseudo-ternary diagram of the Li-Mn-Ni-O system, highlighting the locations of positive electrode materials which are commonly studied or commercially available.	16
Figure 1.7. Potential versus specific capacity plots of cycles 1 (a-f) and 2 (g-l) of the positive electrode materials highlighted in Figure 1.6(b).	19
Figure 1.8. The Li-Mn-Ni-O pseudo-ternary phase diagrams at 800°C in O_2 for combinatorial samples that were (a) quenched and (b) slow cooled.....	25
Figure 1.9. XRD patterns of the four end-members of the two three-phase regions for quenched samples prepared at 800°C in O_2	26
Figure 1.10. XRD patterns of the four end-members of the three-phase regions in the 42° to 46° scattering angle range obtained by quenching (left panel) and regular cooling (right panel) combinatorial samples prepared at 800°C in O_2	28

Figure 1.11. The positive electrode materials region of the Li-Mn-Ni-O pseudo-ternary phase diagrams at 800°C in O ₂ for combinatorial samples that were (a) quenched and (b) slow cooled.	32
Figure 2.1 An image (a) and a schematic (b) of the continuously-stirred tank reactor used to synthesize the hydroxide precursors.	37
Figure 2.2. Solid state synthesis steps of the Li-Mn-Ni-O samples.	39
Figure 2.3. A simple illustration of Bragg X-ray diffraction.	41
Figure 2.4. A schematic showing the components of a standard 2325 coin cell.	47
Figure 3.1 Pseudo-ternary phase diagrams of the Li-Mn-Ni-O system at 900°C in air for samples that were (a) quenched and (b) slow cooled.	52
Figure 3.2. XRD patterns of samples in the 1:1 Ni:Mn series that were quenched (solid red) and slow cooled (dashed blue).	57
Figure 3.3. XRD patterns of samples in the 3:5 Ni:Mn series that were quenched (solid red) and slow cooled (dashed blue).	61
Figure 3.4. XRD patterns of samples in the 1:3 Ni:Mn series that were quenched (solid red) and slow cooled (dashed blue).	64
Figure 3.5. (a) Total XRD pattern fits from 10° to 90° and component phase fits from 43° to 45° of samples P, R, T, and V, all quenched at 900°C, and (b) Magnified component phase fits of sample R from 43° to 45°.	66
Figure 3.6. XRD patterns of samples in the 1:5 Ni:Mn series that were quenched (solid red) and slow cooled (dashed blue).	68
Figure 3.7. XRD patterns of samples at 800°C in air that were quenched (solid red) and slow cooled (dashed blue) within the following series: (a) 1:1, (b) 3:5, (c) 1:3, and (d) 1:5.	74
Figure 3.8. Lattice parameters of single-phase layered fits of samples A to H (left to right) in the quenched 1:1 series versus the Li metal mole fraction of each	

sample. The cubic to hexagonal transition at $\sqrt{24} c/a$ is indicated by the dashed line in the top panel.....	79
Figure 3.9. Component phase fits of the XRD patterns for sample K in the 3:5 series that were (a) quenched in liquid nitrogen, (b) quenched between copper plates, and (c) slow cooled to room temperature.....	82
Figure 3.10. XRD pattern and cubic Rietveld refinement of the 900°C quenched sample W in the 1:5 series on the single-phase spinel boundary of the phase diagram.	84
Figure 3.11. XRD pattern and monoclinic Rietveld refinement of sample AA in the 1:5 series at the top of the “bump” in the single-phase layered region boundary of the phase diagram at 900°C quenched.....	88
Figure 3.12. Lattice parameter contour plots of the single-phase layered region of the Li-Mn-Ni-O phase diagram at 900°C in air (quenched).	93
Figure 3.13. Pseudo-ternary phase diagrams of the Li-Mn-Ni-O system in air at (a) 900°C quenched, (b) 900°C slow cooled, (c) 800°C quenched, and (d) 800°C slow cooled.	95
Figure 4.1. Pseudo-ternary phase diagram of the Li-Mn-Ni-O system at 900°C in air (quenched) highlighting the “bump” in the layered boundary.	102
Figure 4.2. XRD patterns of samples B ₁ through B ₅ located within the bump in the single-phase layered boundary of the quenched phase diagram at 900°C in air.....	105
Figure 4.3. XRD patterns and monoclinic Rietveld refinements of (a) sample B ₁ and (b) sample B ₂ near the top of the “bump” in the single-phase layered region boundary of the quenched phase diagram at 900°C in air.....	107
Figure 4.4. SEM images of samples B ₁ to B ₅	110
Figure 4.5. Potential versus specific capacity plots of cycles 1, 2, and 35 of sample B ₁	112

Figure 4.6. Potential versus specific capacity plots of cycles 1, 2, and 35 of sample B ₂	114
Figure 4.7. Potential versus specific capacity plots of cycles 1, 2, and 35 of sample B ₃	114
Figure 4.8. Potential versus specific capacity plots of cycles 1, 2, and 35 of sample B ₄	115
Figure 4.9. Potential versus specific capacity plots of cycles 1, 2, and 35 of sample B ₅	115
Figure 4.10. IRC, discharge capacity, and average discharge potential of different cycles for half-cells of samples B ₁ to B ₅	117
Figure 4.11. Differential capacity plots of cycles 1 (red), 2 (green), and 35 (blue) of samples B ₁ to B ₅	119
Figure 4.12. Specific capacity versus cycle number of samples B ₁ to B ₅ initially cycled from 2.5 V to (a) 4.4 V, (b) 4.6 V, then 4.8 V, and finally from 2.0 V to 4.8 V, and (c) 4.8 V, then from 2.0 V to 4.8 V.	124
Figure 4.13. Potential versus specific capacity plots (left panel) and differential capacity plots (right panel) of cycle 100 for samples B ₁ to B ₅ cycled initially from 2.5 V to 4.8 V, then from 2.0 V to 4.8 V.	126
Figure 4.14. Specific capacity versus cycle number of samples B ₃ and B ₄ at each upper potential limit.	127
Figure 5.1. The pseudo-ternary phase diagram of the Li-Mn-Ni-O system at 900°C slow cooled highlighting the capacity “growth” compositions in the 1:5 composition series.	132
Figure 5.2. XRD patterns of samples G ₁ to G ₅	135
Figure 5.3. SEM images of secondary particles of samples G ₁ to G ₅	137
Figure 5.4. Potential versus specific capacity plots of the first cycle of half-cells for each growth composition from 2.5 V to 4.9 V at 5 mA g ⁻¹ and 30°C.	139

Figure 5.5. Specific discharge capacity versus cycle number for half-cells of compositions G_1 to G_5 cycled between 2.5 V to 4.9 V at 30 °C.....	141
Figure 5.6. Differential specific capacity versus potential plots for half-cells of each growth composition from cycles 1 to 50 in 10 cycle increments.	143
Figure 5.7. Specific capacity versus potential plots for half-cells of each growth composition after 5, 50, 100 and 150 cycles (110 cycles for sample G_5). All cycles were from 2.5 V to 4.9 V at 20 mA g^{-1} and 30°C.....	145
Figure 5.8. Differential specific capacity versus potential plots for half-cells of each growth composition from cycles 50 to 150 (110 for sample G_5) in 25 cycle increments.	148
Figure 5.9. Differential specific capacity versus potential for half-cells of compositions G_1 to G_5	150
Figure 5.10. Specific discharge capacity versus cycle number for half-cells of compositions G_1 to G_5 cycled from 3.0 V to 4.9 V initially, then from 2.0 V to 4.9 V (see arrows).	151
Figure 6.1. The pseudo-ternary phase diagram of the Li-Mn-Ni-O system at 900°C in air quenched showing layered samples L_1 , L_2 , and L_3 at (Li, Mn) coordinates of (0.55, 0.22), (0.56, 0.28), and (0.60, 0.34), respectively.	155
Figure 6.2. XRD patterns of samples L_1 , L_2 , and L_3	159
Figure 6.3. Potential versus specific capacity plots for half-cells of samples L_1 , L_2 , and L_3 from 2.5 V to 4.6 V collected using the UHPC.	160
Figure 6.4. Potential versus specific capacity plots of sample L_3 from 2.5 V to 4.6 V and 2.5 V to 4.8 V collected using the UHPC.	164
Figure 6.5. Differential capacity plots of sample L_3 from 2.5 V to 4.6 V and 2.5 V to 4.8 V collected using the UHPC.....	166
Figure 6.6. Coulombic efficiency, specific discharge capacity, and normalized charge endpoint versus cycle number. The left column compares samples L_1 , L_2 , and L_3 , while the right column compares sample L_3 with $Li[Ni_{1/3}Mn_{1/3}Co_{1/3}]O_2$	168

Abstract

Emerging energy storage applications are driving the demand for Li-ion battery positive electrode materials with higher energy densities and lower costs. The recent production of complete pseudo-ternary phase diagrams of the Li-Mn-Ni-O system generated using combinatorial methods has provided a greater understanding of the impact of initial composition, synthesis temperature, and cooling rate on the phases that form in the final materials.

This thesis focuses on the synthesis and characterization of gram-scale positive electrode materials in the Li-Mn-Ni-O system. Structural analysis of these samples has resulted in the production of partial pseudo-ternary phase diagrams focusing on the positive electrode materials region of the Li-Mn-Ni-O system at 800°C and 900°C in air for both quenched and slow cooled compositions. These bulk-scale diagrams support the observations of the combinatorial diagrams, and show similar layered and cubic structures contained within several single- and multi-phase regions. The phases that form at each composition are shown to be dependent on both the reaction temperature and cooling rate used during synthesis.

The electrochemical characterization of two composition series near Li_2MnO_3 , one quenched and one slow cooled, is presented. The quenched compositions exhibited reversible cycling at 4.4 V, voltage plateaus and small increases in capacity above 4.6 V, and large first cycle irreversible capacity losses at 4.8 V. In the slow cooled series, all but one composition exhibited initial capacities below 100 mAh g^{-1} which began to continually increase with cycling, with several compositions exhibiting capacity increases of 300% over 150 cycles at 4.9 V. In both series, analysis of the voltage and differential capacity plots indicated that significant structure rearrangements are taking place in these materials during extended cycling, the possible origins of which are discussed.

Finally, high precision coulometry studies of one Li-deficient and two Li-rich single-phase layered compositions are discussed. These materials exhibit minimal oxidation of simple carbonate-based electrolyte when cycled to high potential, with the Li-deficient composition producing less electrolyte oxidation at 4.6 V vs. Li/Li⁺ than commercial $\text{Li}[\text{Ni}_{1/3}\text{Mn}_{1/3}\text{Co}_{1/3}]\text{O}_2$ at 4.2 V. The inherent inertness of this composition may make it suitable for use as a thin protective layer in a core-shell particle.

List of Abbreviations and Symbols Used

AM	active material
BET	Brunauer-Emmett-Teller
ccp	cubic-close packed
CE	coulombic efficiency
CGMs	capacity growth materials
CPQ	copper plate quenched
CSTR	continuously stirred tank reactor
DEC	diethyl carbonate
DMC	dimethyl carbonate
EC	ethylene carbonate
EMC	ethyl methyl carbonate
EVs	electric vehicles
HV	high voltage
JCPDS	Joint Committee on Powder Diffraction Standards
ICP-OES	inductively coupled plasma optical emission spectroscopy
IRC	irreversible capacity loss
LNQ	liquid nitrogen quenched
LRO	lithium rich oxide(s)
LV	low voltage
NMP	1-Methyl-2-pyrrolidinone
OCV	open circuit voltage
PVdF	poly(vinylidene) fluoride
R_B	Bragg factor

SC	slow cooled
SEI	solid electrolyte interphase
SEM	scanning electron microscopy
TGA	thermal gravimetric analysis
TM	transition metal
UHPC	ultra high precision charger
XANES	X-ray absorption near edge structure
XRD	X-ray diffraction
a_{cubic}	cubic lattice parameter
a_{hex}	hexagonal lattice parameter
c_{hex}	hexagonal lattice parameter
2θ	scattering angle
λ	X-ray wavelength
c	speed of light
e	electron charge
F_{hkl}	geometric structure factor
f_o, f_n	atomic scattering factor
I_e	electron intensity
I_i	diffraction pattern intensity
I_o	incident X-ray intensity
m_e	electron mass
χ^2	goodness of fit, chi-squared
σ	uncertainty
w_i	statistical weight

Acknowledgements

I would like to thank Dr. Jeff Dahn for his supervision, guidance, and financial support over the course of this degree. I would also like to thank several past members of the Dahn lab for their contributions to the research presented in this thesis: Dr. Eric McCalla, with whom I collaborated extensively on the phase diagram project and from whom I learned so much; Chris White, who synthesized many samples and coin cells in the early stages of the project; and finally Luke Hacquebard, who synthesized and scanned most of the samples that led to the bulk-scale phase diagrams found in this thesis.

On the technical side, I'd like to thank David Stevens, Robbie Sanderson, Nupur Sinha, and Chris Burns for their assistance, advice, and good humour when things went sideways, as well as Simon Trussler, Andy George, Dan Chevalier, and Kevin Borgel for their help with many things. For help with administrative tasks, thank you to Barbara Gauvin, Anne Murphy, Heather Anne Jennex, Alicia Kirk, and especially Giselle Andrews, who always put a smile on my face when I needed it most.

To Patrick Bonnick, Laura Downie, Lee Moshurchak, Adil Kassam, Arnd & Rita Garsuch, Trevor Byrne, Jock Smith, Jennifer Romero, Ramesh Shunmugasundaram, Andrew Todd, Pierre Ferguson, and many other Dahn lab members with whom I have worked and laughed over the years, a warm thanks to all of you. It's meant a great deal to me to have spent time with such quality folks.

And finally, to my family, friends, and Heidi, your support and encouragement throughout the entire process have been equal parts motivational and humbling, and can be found on every page of this thesis.

Chapter 1

Introduction

1.1 Lithium-ion Batteries

Electrochemical energy storage and conversion technologies are important for developing sustainable and environmentally friendly alternatives to traditional energy sources such as fossil fuels. Owing to high energy densities and long cycle lives, lithium-ion (Li-ion) batteries have become the most ubiquitous form of portable energy storage currently in use, primarily by powering consumer electronics such as smartphones, tablets, and laptops. The performance demands of emerging applications, namely electric vehicles (EVs), require further advances in Li-ion battery materials in order to increase energy density, improve safety, and lower cost.

In general, the term “battery” actually refers to two or more electrochemical “cells” connected either in series or parallel. When discharging a Li-ion cell, the anode, or negative electrode, is oxidized during the electrochemical reaction, providing electrons to an external load via a current collector to do electrical work. Conversely, the cathode, or positive electrode, is reduced during the electrochemical reaction, accepting the electrons from the external load via a current collector to complete the electrical circuit. As such, the negative and positive electrodes are “active materials” which function as both redox-active masses and charge-transfer media during cell operation. The electrolyte contains positive charge carriers, usually cations from dissolved salts,

which flow either to the negative or positive electrode in order to balance the withdrawal and/or accumulation of electrons. Without the electrolyte, the electrical circuit would not be complete, and no electrons would flow. Placed between the two electrodes is a separator, which is both ionically conductive to allow transfer of positive charge carriers between negative and positive electrodes, and electronically insulating to prevent short-circuiting during operation. The extent of Faradaic charge storage is referred to as capacity, measured in units of either Ampere hours (Ah) or Coulombs (C). Over the voltage range of operation (typically 2.5 V to 4.3 V), Li-ion batteries maintain a relatively constant potential when discharged, making them suitable for applications which require a consistent delivery of high energy. Current generation commercial Li-ion batteries can produce specific energy densities up to 240 Wh kg⁻¹, volumetric energy densities up to 640 Wh L⁻¹, cycle lives in excess of 1000 cycles, and cell operating voltages in the range of 2.5 V to nearly 5.0 V [1].

Figure 1.1 shows the components and configuration of a simple Li-ion cell, consisting of negative and positive electrode active materials, a separator, an electrolyte containing conductive salts, and current collectors for both electrodes. Current generation Li-ion batteries typically use graphitic carbon (C₆) as the negative electrode and layered metal oxides of the general form LiMO₂ (where M is one or more transition metals) as the positive electrodes, such as LiCoO₂, as shown. The key characteristic of these particular species is their classification as lithium intercalation materials. Intercalation is the process whereby a species can be inserted between the layers, sheets, slabs or molecular groups in a host material without significantly altering the host's structure [2]. When used in Li-ion batteries, these materials act as the hosts for Li which is intercalated (inserted) and de-intercalated (extracted) during cycling.

The electrolyte used in Li-ion batteries is composed of two components: a non-aqueous solvent which must be stable at high potentials, and a Li-salt, the solution of which must provide high ionic conductivity [1]. Solvents must be able to solvate lithium salts at high concentration and be unable to dissolve electrode materials, all while remaining stable during cycling. Examples of electrolytes used in Li-ion batteries include solutions of LiPF_6 dissolved in carbonates such as ethylene carbonate (EC), diethyl carbonate (DEC), dimethyl carbonate (DMC), and ethyl methyl carbonate (EMC), as well as mixtures of these solvents. Relative to the cell chemistry, the solvent formulation is chosen to maximize ionic conductivity, temperature range, and overall performance of the cell when compared to a single solvent. Modern Li-ion electrolytes generally use 1.0 M LiPF_6 dissolved in a mixture of EC, EMC, and/or DMC, which provides a balance between conductivity, diminished capacity fade, and low temperature operation [1, 3].

Most important is the stability of the electrolyte at the potential of the negative electrode, which nears 0 V vs. Li/Li^+ , and that of the positive electrode, which normally exceeds 4.0 V vs. Li/Li^+ . Non-aqueous solvents such as EC are unstable with negative electrodes near 0 V, reacting with the electro-active material to produce a passivation film on the electrode known as the solid electrolyte interphase (SEI) [4]. The formation of the SEI incorporates lithium, resulting in an irreversible loss of capacity. However, the SEI maintains good ionic conductivity and contact with the electrolyte while at the same time stabilizing the electrode by physically separating it from further reaction with the bulk solvent [1].

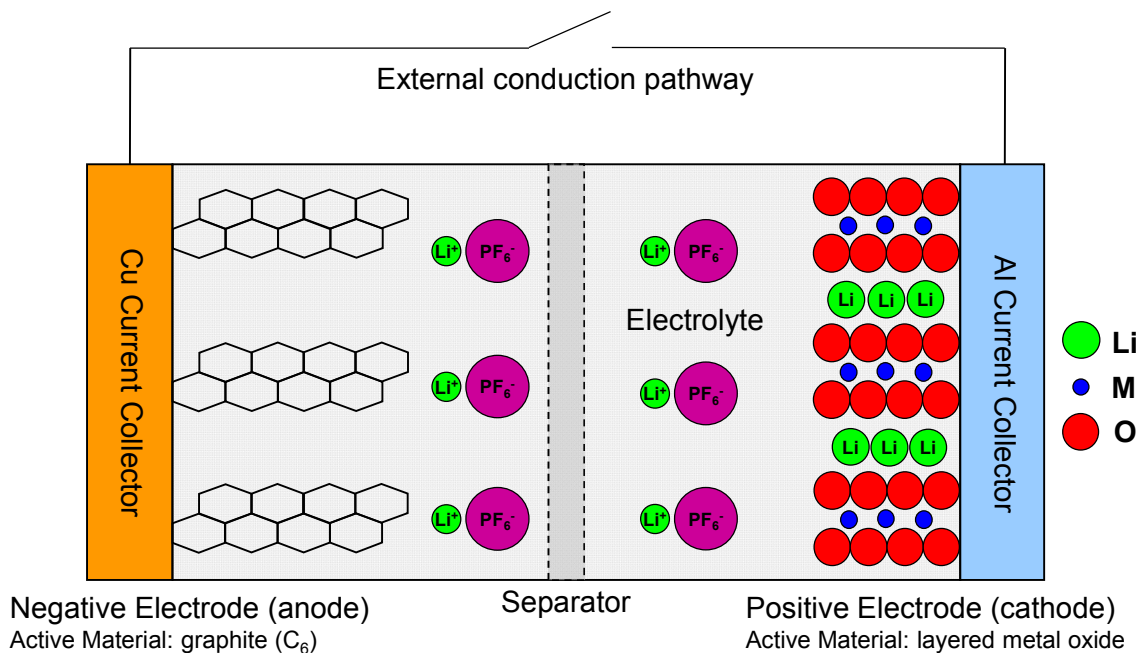


Figure 1.1. The basic components of a Li-ion cell.

A separator that is electrically insulating must be used between the positive and negative electrodes. Separators must exhibit properties such as submicron pore size, good wettability, compatibility with various electrolytes and electrode materials, and resistance to puncturing and/or shrinking. They are typically made of microporous polyolefins, such as polyethylene and polypropylene, which are fabricated into thin sheets with thicknesses ranging from 10 to 30 microns [5].

While the research of each component discussed above is essential for producing Li-ion batteries with improved performance, this thesis will focus specifically on the synthesis and characterization of new positive electrode materials in an effort to both improve their energy densities and lower their overall cost.

1.2 Positive Electrode Materials

Li-ion positive electrodes have undergone significant development since their inception in the early 1970s. In terms of capacity, the target characteristic of these materials is the reversible insertion/extraction of Li in a 1:1 ratio with the transition metal (TM) atom(s). Layered dichalcogenides, namely TiS_2 , were the most promising of these materials in this respect, as they are able to reversibly extract all Li (e.g., from $x = 0$ to $x = 1$ in Li_xTiS_2) resulting in high capacities [3]. This contrasts with some layered metal oxides such as LiCoO_2 , which can undergo phase changes before complete Li extraction, denying the full theoretical capacity of the material as per the above criteria [1]. However, the high capacity of the dichalcogenides was contrasted with low voltage, low energy density, and high cost, thereby limiting their practical use. At present, high capacity layered metal oxides such as $\text{Li}[\text{Ni}_{0.80}\text{Co}_{0.15}\text{Al}_{0.05}]\text{O}_2$ and $\text{Li}[\text{Ni}_{1/3}\text{Mn}_{1/3}\text{Co}_{1/3}]\text{O}_2$, and high power spinel metal oxides such as LiMn_2O_4 and $\text{LiNi}_{1/2}\text{Mn}_{3/2}\text{O}_4$ have become the positive electrode materials of choice from both a research and commercialization perspective [1, 3].

Table 1.1 shows the electrochemical and crystallographic properties of several layered, spinel, and olivine positive electrode materials. In order to meet the performance demands of emerging technologies, positive electrode materials must have high operating voltages (> 4.0 V vs. Li/Li^+), high specific capacities (in mAh g^{-1}), and most importantly, maximized volumetric energy densities (in Wh cm^{-3}) [6]. The most common positive electrode material used commercially, layered LiCoO_2 , exhibits several of these desired properties, yet is relatively unsafe and expensive compared to other compositions, such as $\text{Li}[\text{Ni}_{1/3}\text{Mn}_{1/3}\text{Co}_{1/3}]\text{O}_2$ [1]. However, the inclusion of Co in these materials increases their cost and toxicity, both of which are important factors that impact industrial production from raw materials [6]. Therefore, Co-free materials which maxim-

ize volumetric energy density are of considerable interest for future positive electrode materials. For example, layered $\text{Li}[\text{Ni}_{1/2}\text{Mn}_{1/2}]\text{O}_2$ exhibits a specific capacity and energy density comparable to LiCoO_2 , while lithium-rich oxides (LRO) such as $\text{Li}[\text{Li}_{1/9}\text{Ni}_{1/3}\text{Mn}_{5/9}]\text{O}_2$ (which have “excess” Li in the transition metal layer by comparison) have even higher specific capacities (240 - 260 mAh g^{-1}) and energy densities near 4.0 Wh cm^{-3}) [1]. However, these materials have limited rate capabilities, resulting in reduced power densities in comparison to materials such as LiFePO_4 which, while offering good safety and low cost, has a low volumetric energy density [7]. By contrast, the spinel materials have relatively high rate capabilities and consistent operating voltages, but are limited in terms of their achievable capacity. Thus, depending on the performance requirements of a specific application, compromises in the choice of positive electrode material must be made at present, while further research is required in the search for an “all-in-one” material that performs as required. The properties in Table 1.1 indicate that several compositions in the Li-Mn-Ni-O system meet the requirements of high specific capacity and theoretical volumetric energy density, while also eliminating the use of cobalt.

At present, the EV market is the driving force for Li-ion battery positive electrode material research and development, requiring battery chemistries with high energy densities, long cycle lives, and minimized production costs. Therefore, in line with these requirements, this thesis will focus exclusively on positive electrode materials in the Li-Mn-Ni-O system. Section 1.3 will discuss the crystal structures and electrochemical characteristics of several compositions in the Li-Mn-Ni-O system.

Table 1.1. Average potential, reversible capacity, crystallographic density, and volumetric energy density of various positive electrode materials.

Material	Structure	Average Potential / V vs. Li/Li ⁺	Reversible Specific Capacity / mAh g ⁻¹	Crystallographic Density / g cm ⁻³	Volumetric Energy Density / Wh cm ⁻³
LiCoO ₂	Layered	3.90	155	5.09	3.07
Li[Ni _{1/3} Mn _{1/3} Co _{1/3}]O ₂	Layered	3.80	160	4.77	2.90
Li[Ni _{1/2} Mn _{1/2}]O ₂	Layered	3.75	150	4.98	2.80
Li[Li _{1/9} Ni _{1/3} Mn _{5/9}]O ₂	Layered (LRO)	3.70	240	4.43	3.99
LiMn ₂ O ₄	Spinel	4.05	120	4.29	2.08
LiNi _{1/2} Mn _{3/2} O ₄	Spinel	4.60	130	4.43	2.65
LiFePO ₄	Olivine	3.45	160	3.60	1.99

1.3 Li-Mn-Ni-O Materials

1.3.1 Crystal Structures

Figure 1.2 shows the crystalline structures of a hexagonal layered and cubic spinel structure. Layered transition metal oxide materials are of the general form Li[M]O₂, where M is one or more first-row transition metals. The stoichiometry of M sums to 1, resulting in a total metal-to-oxygen ratio of 1:1. These oxides adopt the α -NaFeO₂ crystal structure, which is described by the R-3m crystallographic space group. Within

the unit cell, Li is located at octahedral 3a interstitial sites, transition metals are located at octahedral 3b interstitial sites (typically denoted by square brackets), and oxygen is located at 6c sites. This results in the Li and transition metal ions forming separate layers (dubbed the Li layer and TM layer) in which the atoms generate 2-D hexagonal arrangements. The O^{2-} ions form a 3-D cubic-close packed (ccp) lattice bonded with the metals in the transition metal layer, forming continual “sheets” of MO_6 octahedra (shown as shaded polyhedra in Figure 1.2). Overall, this results in an O-M-O-Li-O- layered sequence throughout the structure along the c-axis [6]. Li diffusion within the structure is therefore 2-D, as Li can only move within the confines of the Li *layer*. Commonly studied examples of this material are $LiCoO_2$ and $Li[Ni_{1/2}Mn_{1/2}]O_2$.

By contrast, cubic spinel transition metal oxides are of the general form LiM_2O_4 , where again M equals one or more first-row transition metals, primarily Mn and Ni. The stoichiometry of M sums to 2, resulting in a total metal-to-oxygen ratio of 3:4. These oxides adopt the $MgAl_2O_4$ crystal structure, which is described by the cubic Fd-3m crystallographic space group. Within the unit cell, Li is located at tetrahedral 8a sites, transition metals are located at 16d octahedral sites (often denoted by square brackets), and oxygen is located at 32e sites. The spinel structure is very similar to the hexagonal layered structure, as the O^{2-} ions also form a 3-D ccp lattice, and also bond with the transition metals to form MO_6 octahedra. Unique to the spinel structure, however, is the resultant M_2O_4 framework, which results in Li occupying interstitial sites in “tunnels” within a three-dimensional network. Accordingly, Li diffusion within the spinel structure is 3-D, as Li can move within the tunnels in any direction during charge and discharge. Commonly studied examples of this material are $LiMn_2O_4$ and $LiNi_{1/2}Mn_{3/2}O_4$.

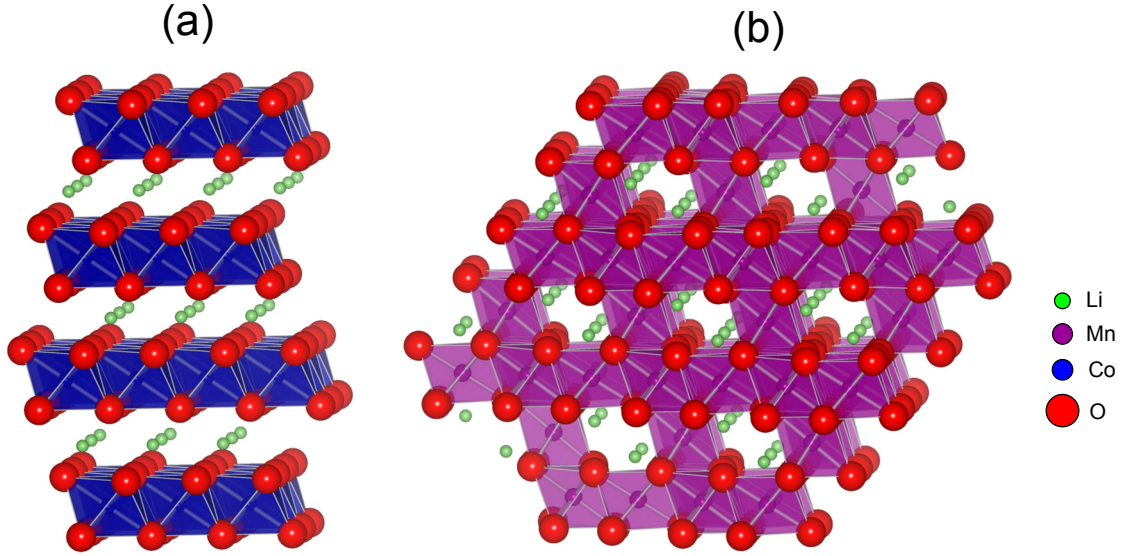


Figure 1.2. Lithium metal oxides showing the (a) hexagonal layered (e.g., LiCoO_2) and (b) cubic spinel (e.g., LiMn_2O_4) crystal structures. The MO_6 octahedra are shown to illustrate the similarities between the two structures.

The lithium-rich layered transition metal oxides are a special class of layered materials of the general form $\text{Li}[\text{Li}_x\text{M}_{1-x}]\text{O}_2$, where M is again one or more transition metals, often Ni, Mn, and/or Co. In this case, an excess of Li (relative to the Li-to-oxygen ratio of 1:2 in LiMO_2) occupies octahedral sites in the *transition* metal layer, where the sum of Li and M on the layer equals one, again exhibiting a total metal-to-oxygen ratio of 1:1. The most commonly studied range of LROs is the series $\text{Li}[\text{Ni}_x\text{Li}_{(1/3-2x/3)}\text{Mn}_{(2/3-x/3)}]\text{O}_2$ for $0 < x < \frac{1}{2}$ [8].

From a structural viewpoint, this series is primarily a solid solution between hexagonal $\text{Li}[\text{Ni}_{0.5}\text{Mn}_{0.5}]\text{O}_2$ and monoclinic Li_2MnO_3 [9, 10]. Figure 1.3(a) shows the structural compatibility of these two materials along the hexagonal c-axis. Both have ccp oxygen arrays, hexagonal Li and TM layers, MO_6 octahedra, and alternating layers of Li and MO_2 in the $-\text{O}-\text{M}-\text{O}-\text{Li}-\text{O}-$ layered sequence. The TM layer of $\text{Li}[\text{Ni}_{1/2}\text{Mn}_{1/2}]\text{O}_2$

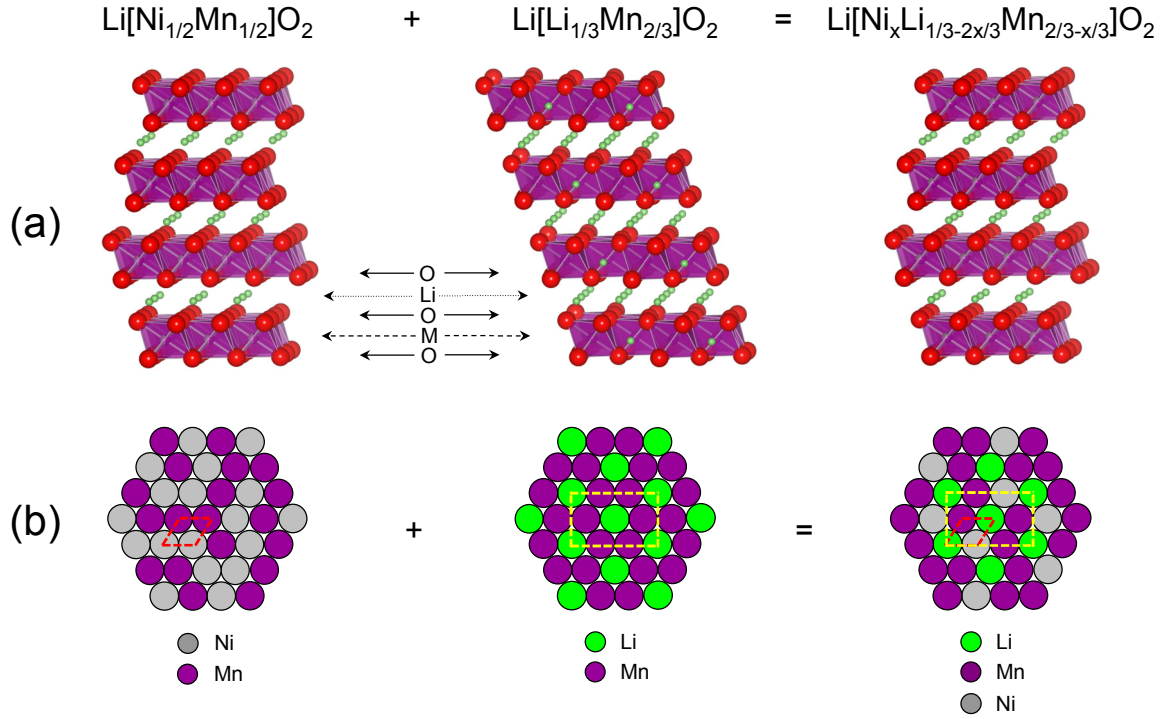


Figure 1.3. Top panel (a): The crystal structures of monoclinic $\text{Li}[\text{Li}_{1/3}\text{Mn}_{2/3}]\text{O}_2$ (Li_2MnO_3) and hexagonal $\text{Li}[\text{Ni}_{1/2}\text{Mn}_{1/2}]\text{O}_2$ end-members combined to form the Li-rich oxide layered solid solution series $\text{Li}[\text{Ni}_x\text{Li}_{1/3-2x/3}\text{Mn}_{2/3-x/3}]\text{O}_2$. Bottom panel: (b) the hexagonal arrangement of atoms on the transition metal layer of each material in (a). The hexagonal unit cell is indicated by the dashed red lines, while the monoclinic unit cell is indicated by the dashed yellow lines.

contains random cation mixing of Ni and Mn, while the TM layer of Li_2MnO_3 contains an ordered arrangement of $1/3$ Li and $2/3$ Mn ions. This allows Li_2MnO_3 to be expressed in layered notation as $\text{Li}[\text{Li}_{1/3}\text{Mn}_{2/3}]\text{O}_2$. The differences between these two layered structures can be seen in the TM layer illustrations in Figure 1.3(b), which show the unit cells of $\text{Li}[\text{Ni}_{1/2}\text{Mn}_{1/2}]\text{O}_2$ (dashed red) and Li_2MnO_3 (dashed yellow). As shown, the Mn ions lie on a different lattice than those of the randomly distributed cations in $\text{Li}[\text{Ni}_{1/2}\text{Mn}_{1/2}]\text{O}_2$, producing a superstructure which is larger than the hexagonal lattice in each direction by an amount of $\sqrt{3}$. This ordered arrangement of atoms in Li_2MnO_3 is often referred to as a $\sqrt{3} \times \sqrt{3}$ superstructure and/or superlattice, a convention which

will be referenced frequently when discussing Li_2MnO_3 and Li_2MnO_3 -related materials throughout this thesis. Within a LRO solid solution material, the Li and Mn order in this superstructure, while Ni occupies random sites, generating a layered material that can be described by either hexagonal or monoclinic symmetry, as shown by the TM layer of $\text{Li}[\text{Ni}_x\text{Li}_{(1/3-2x/3)}\text{Mn}_{(2/3-x/3)}]\text{O}_2$ in Figure 1.3(b). The LROs in the Li-Mn-Ni-O system will be referred to frequently throughout the structural and electrochemical analysis presented in this thesis.

Li_2MnO_3 has a monoclinic unit cell, which is best described by the cubic $C2/m$ space group. However, it can also be relatively well described by a hexagonal unit cell, which is related to the monoclinic cell. Figure 1.4(a) shows the hexagonal unit cell in the TM layer, while Figure 1.4(b) shows the monoclinic unit cell in the “TM layer” of Li_2MnO_3 . Superimposing the hexagonal unit cell over the monoclinic unit cell (in dashed red) and comparing the lattice vectors of each shows how the a and c lattice parameters of the two structures are related: a_{mon} is equal to $\sqrt{3}a_{hex}$, while b_{mon} is equal to $3a_{hex}$. Figure 1.4(c) shows how the unit cells compare along the layered c -axis. As shown, the monoclinic cell is 3 times smaller than the hexagonal unit cell in the direction of the layered c -axis. This indicates that Li_2MnO_3 contains a stacked sequence of hexagonal layers such that it can be interpreted as layered $\text{Li}[\text{Li}_{1/3}\text{Mn}_{2/3}]\text{O}_2$.

Figure 1.4(c) displays an ideal, undistorted Li_2MnO_3 crystal structure with long range order, which can be only obtained after high temperature annealing for extended periods [11]. This structure contains cubic close packed (ABCABC) hexagonal $[\text{Li}_{1/3}\text{Mn}_{2/3}]$ layers along the c -axis direction without any fault in the stacking sequence. However, Li_2MnO_3 usually contains various degrees of stacking faults depending on reaction temperature [12, 13].

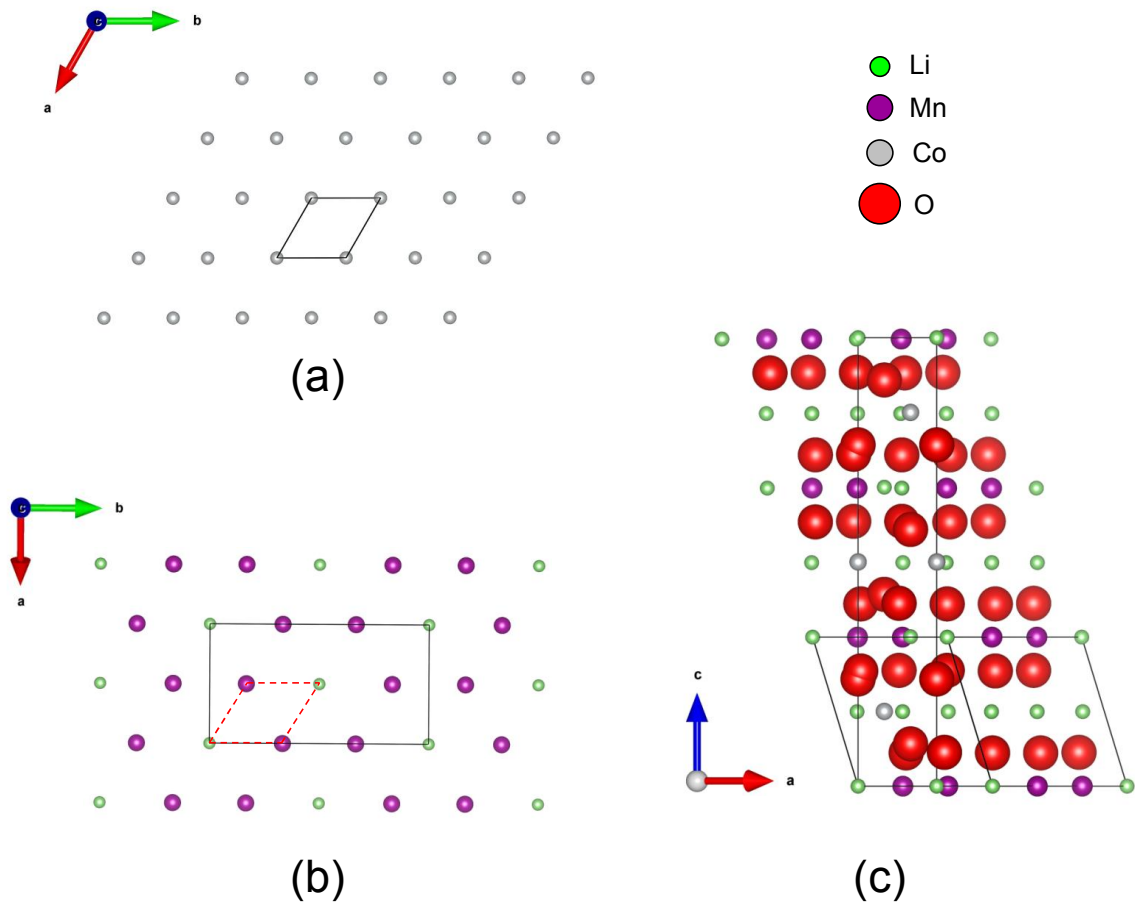


Figure 1.4. (a) The layered transition metal layer projected along the c -axis indicating the hexagonal unit cell. (b) The monoclinic transition metal layer projected along the c -axis showing the ordering of Li and Mn; the monoclinic unit cell is shown in black, while the hexagonal unit cell is indicated in dashed red. (c) A comparison of the positions of the layered and monoclinic unit cells in a Li-rich layered structure projected along the layered b -axis, with Li at the origin.

Figure 1.5(a) illustrates different types of ABC stacking of the hexagonal $[\text{Li}_{1/3}\text{Mn}_{2/3}]$ layers in the c -axis direction. A single layer, A_1 , can be stacked with a second layer in either the B or C interstitial ccp site. In this example, the Mn atoms (grey circles) occupy the B sites, resulting in A_1B_1 stacking. A third layer, C, can now be stacked in one of two interstitial sites to give either $A_1B_1C_1$ or $A_1B_1C_2$ stacking. The

$A_1B_1C_1$ stacking is the “ideal” stacking shown in Figure 1.4(c), with the red lines representing mirror planes of the $C2/m$ space group. The $A_1B_1C_2$ stacking is an example of a stacking fault, in which the third $[Li_{1/3}Mn_{2/3}]$ layer occupies the C_2 site resulting in the creation of a “fault” that produces a three-fold screw axis (red triangles) relative to the ideal non-faulted stacking of $A_1B_1C_1$. Within a hexagonal unit cell (which contains three TM layers), this stacking sequence can be followed by other stacking fault sequences, resulting in combinations such as $A_1B_1C_2A_2B_3C_1$ [11], and so on throughout the crystal structure.

The presence and propagation of these stacking faults has a significant impact on the X-ray diffraction (XRD) pattern of Li_2MnO_3 . Figure 1.5(b) shows the XRD patterns of Li_2MnO_3 as a function of the degree of stacking faults present in the lattice. The effect of stacking faults is primarily seen in the peaks between scattering angles of 20.0° and 35.0° , which are due to the 2-D ordering of Li and Mn in the metal layer (i.e., the Li-Mn superstructure). When there are no stacking faults (top pattern), the stacked $[Li_{1/3}Mn_{2/3}]$ layers exhibit long-range, 3-D ordering within the crystal structure, resulting in very sharp ordering peaks. As the number of stacking faults increases, the amount of 3-D ordering decreases, and the superlattice peaks become increasingly broad and less intense. Once the structure contains 50% stacking faults (bottom pattern), the ordering peaks coalesce into a single, extremely broad peak starting at about 20.0° . Thus, the degree of stacking faults has a very significant effect on the resultant XRD patterns of Li_2MnO_3 and LROs, which both contain ordering of Li and Mn on the TM layer.

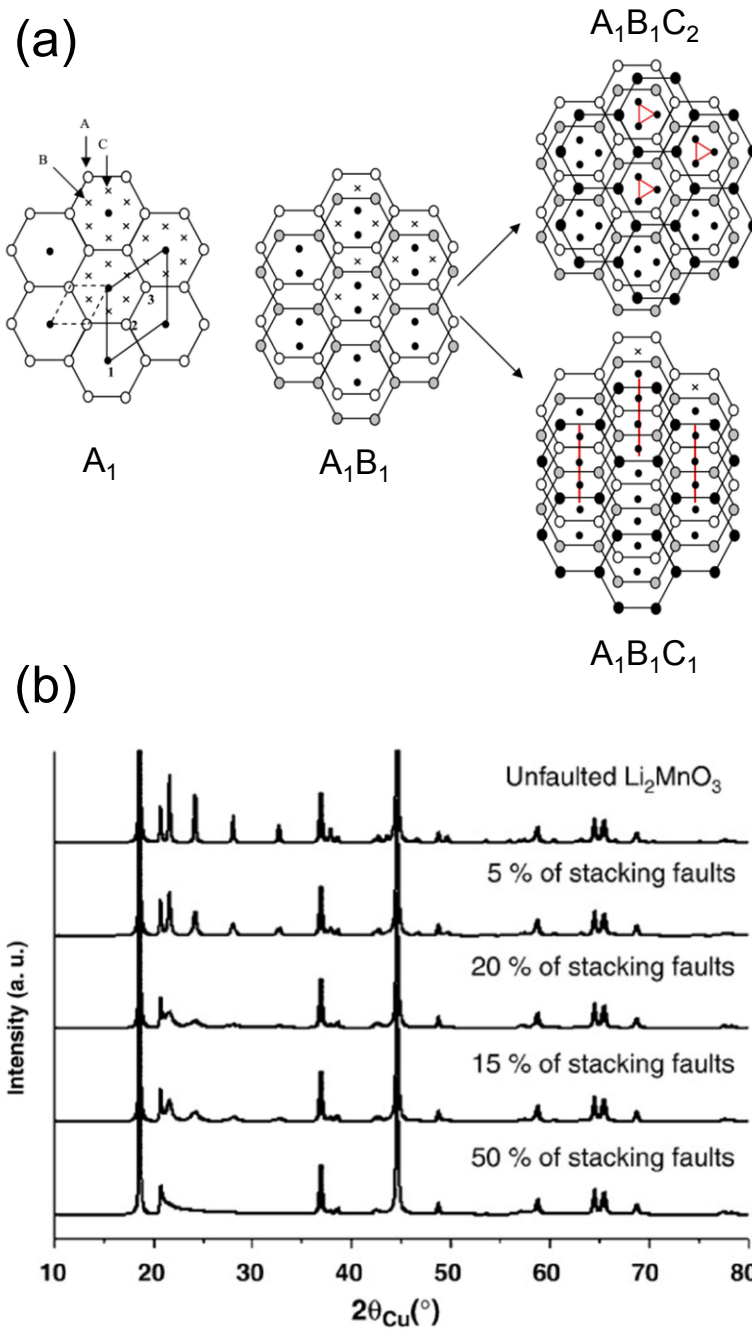


Figure 1.5. (a) An illustration of stacking faults between hexagonal layers in monoclinic Li_2MnO_3 , adapted from Reference [11] with the permission of Elsevier. The black circles are Li, the white and grey circles are Mn, and the crosses indicate the location of close-packing B and C interstitial sites on the hexagonal layer. (b) XRD patterns of Li_2MnO_3 with increasing amounts of stacking faults, from Reference [13] with the permission of Elsevier.

Overall, the examination of the crystal structures of LROs and Li_2MnO_3 provide useful information for the identification of phases in single- and multi-phase Li-Mn-Ni-O compositions. In particular, looking at Li_2MnO_3 in layered notation as $\text{Li}[\text{Li}_{1/3}\text{Mn}_{2/3}]\text{O}_2$ allows the $\text{Li}[\text{Ni}_x\text{Li}_{(1/3-2x/3)}\text{Mn}_{(2/3-x/3)}]\text{O}_2$ series to be thought of as a solid solution in which Ni substitutes for Li and Mn on the transition metal layer. As the Ni content increases, the Ni ions order randomly on the TM layer, as shown in Figure 1.3(c). This increases the probability of stacking faults within the nominal Li_2MnO_3 monoclinic structure, resulting in less 3-D ordering as observed by broader, less sharp superstructure peaks in the range of 20.0° to 35.0° . This observation has been confirmed for the LRO solid solution series $\text{Li}[\text{Ni}_x\text{Li}_{(1/3-2x/3)}\text{Mn}_{(2/3-x/3)}]\text{O}_2$ from $x = 0$ to $x = \frac{1}{2}$ [14]. Therefore, the width and intensity of the superstructure peaks provide a way to distinguish between 2-D ordering, which is more prevalent in LROs, and 3-D ordering, which is found in Li_2MnO_3 and other layered compositions with monoclinic character, within the Li-Mn-Ni-O system [15].

1.3.2 Ternary Diagrams

Although the Li-Mn-Ni-O system is a four-component quaternary system, it can be described using a three-component Li-Mn-Ni ternary diagram in which the oxygen content is dictated by the reaction equilibrium conditions [16]. A general ternary diagram is shown in Figure 1.6(a), and will be used to explain the fundamentals of ternary diagrams in general. The axes are labelled as x, y, and z, where for any given composition, $x + y + z = 1$. The compositions at the vertices have a single component (x, y, or z), those on the axes have two components (xy, yz, zx), and those within the triangle have three components (xyz). The amount of each component in a given com-

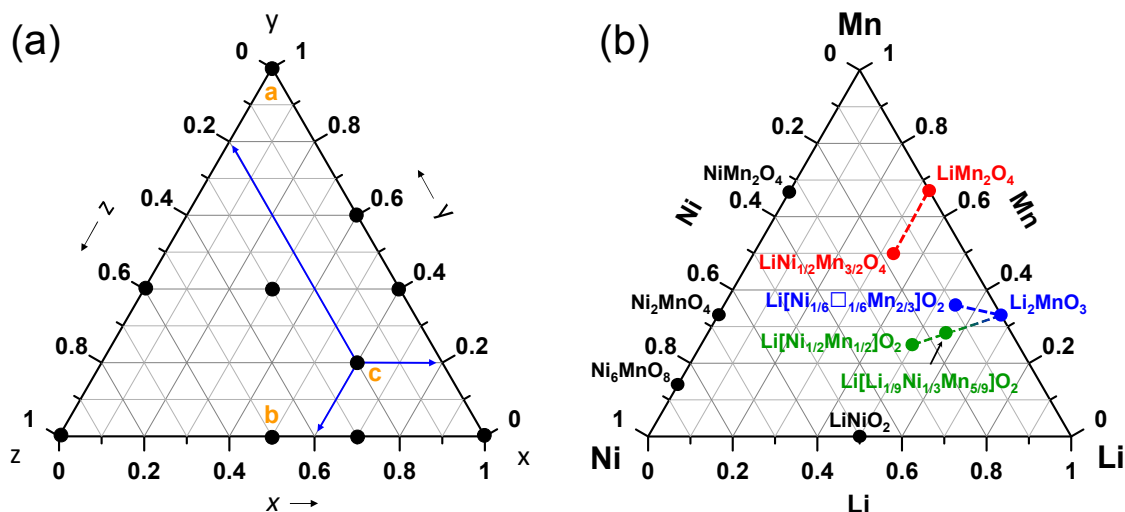


Figure 1.6. (a) A simple ternary diagram showing compositions with one component (at vertices), two components (on lines), and three components (in triangle). For all compositions in the diagram, $x + y + z = 1$. The blue arrows indicate how to read the axes for a three-component composition. (b) The general pseudo-ternary diagram of the Li-Mn-Ni-O system, highlighting the locations of positive electrode materials which are commonly studied or commercially available. The dashed lines represent nominal solid solutions between end-members.

position is indicated by the fractions of x , y , and z as (x, y, z) coordinates. For example, point a is located at $(0, 1, 0)$, point b at $(0.5, 0.0, 0.5)$, and point c at $(0.6, 0.2, 0.2)$. To simplify the nomenclature, the compositions can also be written in two-component coordinate notation as (x, y) where $z = 1 - x - y$.

As discussed above, the Li-Mn-Ni-O system is a quaternary system, which forms a pyramid with Li, Mn, Ni, and O at the vertices. This requires the use of 3-D graphing software to plot and visualize the whole system. By comparison, placing only the Li, Mn, and Ni metal mole fractions on the x , y , and z axes of a ternary diagram as shown in Figure 1.6(b) provides a simple and convenient way of plotting and comparing compositions within the Li-Mn-Ni-O system in two dimensions. When displayed in this

format, the overall system is in fact “pseudo-ternary”, in that the oxygen content is not plotted on the diagram directly, but rather reported as part of the total empirical formula of each solid phase in any given composition. The location of each composition in the pseudo-ternary diagram can therefore be written in metal mole fraction two-component notation as (Li, Mn) where $Ni = 1 - Li - Mn$. This notation will be used throughout the thesis to describe all compositions studied in the Li-Mn-Ni-O system as they appear on each pseudo-ternary diagram.

1.3.3 Electrochemical Characteristics

Figure 1.6(b) shows the pseudo-ternary diagram of the Li-Mn-Ni-O system labelled with various commonly studied compositions. The compositions and formulae of various Li-ion battery positive electrode materials of interest are colour-coded according to their parent crystal structure: spinel is shown in red, hexagonal layered in green, and monoclinic layered in blue. Each material has a distinct set of electrochemical properties, several of which are described in Table 1.1. To maintain charge balance within the host structure of the positive electrode materials while cycling, the removal of Li generally results in transition metal ion oxidation, with subsequent re-insertion resulting in transition metal ion reduction. Ideally, the same amount of Li would be removed and inserted from the host material during charge and discharge, but in practice this does not always occur, resulting in an irreversible capacity (IRC) loss. This can be seen as the difference between the charge and discharge capacities of a cycle in the voltage curves. Each composition also has an inherent hysteresis in its voltage profile which can vary during cycling due to polarization. This section will describe the redox

reactions and overall electrochemical behaviour exhibited by each material during cycling in order to outline the strengths and weaknesses of each composition.

Figure 1.7 shows the potential versus specific capacity plots (also called voltage curves or profiles) of the highlighted compositions in Figure 1.6(b). Starting with the spinel materials, LiMn_2O_4 extracts Li^+ reversibly via a $\text{Mn}^{3+/4+}$ redox couple, resulting in a flat voltage profile at 4 V during charge and discharge with little polarization. However, this material suffers from capacity fade mainly due to Mn dissolution [6]. Cycling this composition to higher potentials, as shown for cycle 2, results in higher capacities, but increases polarization and IRC. Substituting Ni for Mn in LiMn_2O_4 results in the solid solution series $\text{LiNi}_x\text{Mn}_{2-x}\text{O}_4$, indicated by the dashed red line in Figure 1.6(b), which terminates at $x = 1/2$ or $\text{LiNi}_{1/2}\text{Mn}_{3/2}\text{O}_4$. The voltage curve of this composition exhibits a small sloped region near 4 V due to $\text{Mn}^{3+/4+}$ redox, followed by a flat voltage curve at approximately 4.7 V due to $\text{Ni}^{2+/3+}$ and $\text{Ni}^{3+/4+}$ redox couples, resulting in a total capacity of 140 mAh g^{-1} up to 5.0 V. While this material cycles reversibly as shown in cycle 2, its higher operating voltage results in significant electrolyte oxidation with continued cycling [17, 18]. Due to the differences in their average voltages, LiMn_2O_4 and $\text{LiNi}_{1/2}\text{Mn}_{3/2}\text{O}_4$ are often referred to as low voltage (LV) and high voltage (HV) spinel, respectively.

Layered Li-Mn-Ni-O materials typically have higher reversible capacities and lower rate capabilities than the spinels. As shown, the layered $\text{Li}[\text{Ni}_{1/2}\text{Mn}_{1/2}]\text{O}_2$ and Li-rich layered $\text{Li}[\text{Li}_{1/9}\text{Ni}_{1/3}\text{Mn}_{5/9}]\text{O}_2$ compositions both exhibit continually sloping voltage curves during charge from 3.8 V to about 4.45 V. This is referred to as the “normal” deintercalation region, and corresponds to transition metal ion oxidation associated with $\text{Ni}^{2+/3+}$ oxidization to Ni^{4+} as Li^+ is extracted from the layered lattice.

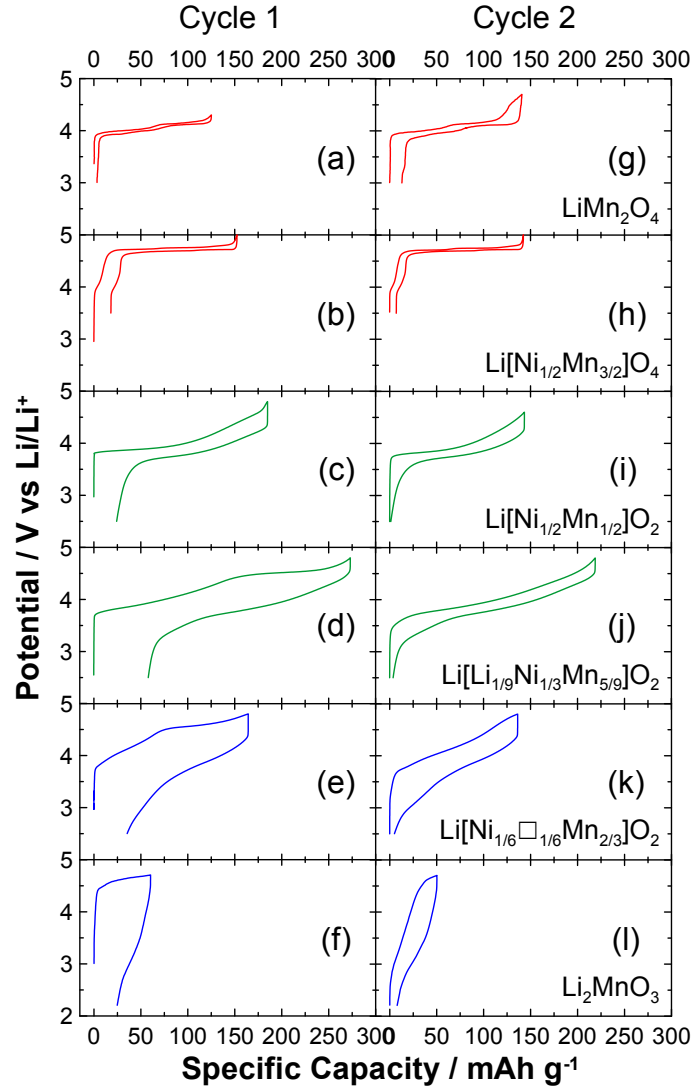


Figure 1.7. Potential versus specific capacity plots of cycles 1 (a-f) and 2 (g-l) of the positive electrode materials highlighted in Figure 1.6(b). Spinel materials are shown in red, layered materials in green, and monoclinic in blue. During cycle 1, all compositions were cycled from open circuit to upper potential limits of (a) 4.3 V, (b) 5.0 V, (c)-(e) 4.8 V, and (f) 4.7 V. During cycle 2, the potential ranges were (g) 3.0 V to 4.7 V, (h) 3.0 V to 5.0 V, (i)-(k) 2.5 V to 4.8 V, and (l) 2.25 V to 4.7 V.

$\text{Li}[\text{Ni}_{1/2}\text{Mn}_{1/2}]\text{O}_2$ has a small IRC in cycle 1, and cycles reversibly up to 150 mAh g^{-1} with moderate polarization as shown in cycle 2.

In contrast, the voltage curve of $\text{Li}[\text{Li}_{1/9}\text{Ni}_{1/3}\text{Mn}_{5/9}]\text{O}_2$ remains relatively constant above 4.45 V until the upper cutoff potential is reached. This behaviour is typical of LRO materials (shown in Figure 1.6(b) as the dashed green line), and corresponds to irreversible loss of $\text{O}_{2(\text{g})}$ from the electrode material particle surface with the simultaneous reversible oxidation of O^{2-} in the particle bulk as the excess Li^+ in the TM layer is extracted from the lattice [19, 20]. This region is often referred to as a high voltage (HV) plateau, oxygen loss plateau, and/or oxygen release plateau, and accounts for the large initial capacity of the LRO materials during charge [21, 22]. While traversing the plateau is necessary to access the material’s capacity during charge, not all of the deintercalated Li^+ can be reinserted on discharge due to TM migration and structural densification within the host material [22, 23]. This results in an IRC of up to 30% of the initial charge capacity on discharge, and an increase in voltage curve hysteresis, as shown in Figure 1.7(d). During subsequent cycling, the composition cycles with a high reversible capacity of 225 mAh g^{-1} due to both reversible TM and anionic O^{2-} redox without further oxygen release [20]. While initially containing Mn in the 4+ oxidation state only, a small sloped region near 3.25 V is associated with $\text{Mn}^{3+/4+}$ reduction during discharge [24].

The voltage curves of Li_2MnO_3 ($\text{Li}[\text{Li}_{1/3}\text{Mn}_{2/3}]\text{O}_2$) and $\text{Li}[\text{Ni}_{1/6}\square_{1/6}\text{Mn}_{2/3}]\text{O}_2$ are shown in blue at the bottom of Figure 1.7. These compositions form the end-members of the vacancy-containing solid solution series $\text{Li}[\text{Li}_{(1/3-x)}\text{Ni}_{x/2}\square_{x/2}\text{Mn}_{2/3}]\text{O}_2$ (shown in Figure 1.6(b) as the dashed blue line), in which a Ni^{2+} ion and a vacancy can replace two Li^+ ions in $\text{Li}[\text{Li}_{1/3}\text{Mn}_{2/3}]\text{O}_2$ [15]. While Li_2MnO_3 has a high theoretical capacity of 459 mAh g^{-1} , it exhibits very low practical capacities and poor cycling behaviour due to the presence of electrochemically inactive Mn^{4+} [25]. Complete replacement of Li on the TM layer with Ni and vacancies as in $\text{Li}[\text{Ni}_{1/6}\square_{1/6}\text{Mn}_{2/3}]\text{O}_2$ produces voltage curves

with normal TM redox and a small high voltage plateau during charge, as shown. During discharge, normal intercalation is again observed, resulting in a large IRC and significant polarization. In addition, the voltage curve hysteresis suggests that not all the Li removed during charge reinserts into the same layered crystal structure during discharge, introducing the possibility of phase transformations occurring while cycling as in other Mn-rich layered materials [26]. During the second cycle, the material exhibits reversible cycling with little IRC, as well as the $\text{Mn}^{4+/3+}$ redox at 3.25 V on discharge as observed in the LRO. $\text{Li}[\text{Ni}_{1/6}\square_{1/6}\text{Mn}_{2/3}]\text{O}_2$ has also been shown to have a monoclinic crystal structure similar to $\text{Li}[\text{Li}_{1/3}\text{Mn}_{2/3}]\text{O}_2$, as both compositions have 2/3 Mn in the TM layer [15]. Given such similarities in composition and structure, this vacancy-containing layered material represents an electrochemically active analog of the mostly inactive Li_2MnO_3 , introducing the possibility that other such vacancy-containing materials exhibit promising electrochemical behaviour. The search for such materials will be discussed in greater detail in Section 1.4.3.

Overall, it has been demonstrated that different Li-Mn-Ni-O compositions and crystal structures yield positive electrode materials with different strengths and weaknesses. The spinel materials operate at voltages near or above 4 V at high rates, but have limited capacities. The layered materials have intermediate average voltages from 3.5 V to 3.75 V during discharge with capacities that can exceed 240 mAh g^{-1} (for the LROs), but have limited rate capabilities. Finally, the monoclinic $\text{Li}[\text{Ni}_{1/6}\square_{1/6}\text{Mn}_{2/3}]\text{O}_2$ has capacities similar to $\text{LiNi}_{1/2}\text{Mn}_{3/2}\text{O}_4$ and $\text{Li}[\text{Ni}_{1/2}\text{Mn}_{1/2}]\text{O}_2$, but exhibits significant voltage curve hysteresis. While similar to Li_2MnO_3 , this material represents a significant leap in electrochemical capability by comparison while minimizing total Ni content compared to most Li-Mn-Ni-O materials. This highlights such materials as having the potential to be less toxic, cost-effective positive electrode materials.

1.4 Li-Mn-Ni-O Pseudo-ternary Phase Diagrams

1.4.1 General Features of Ternary Phase Diagrams

The Li-Mn-Ni-O pseudo-ternary system can be expressed as a Gibbs ternary phase diagram (also called a Gibbs triangle or phase stability diagram) which shows the various single-phase, two-phase, and three-phase regions that form at equilibrium. Such phase diagrams follow the Gibbs phase rule:

$$F = C - P + n \quad (1.1)$$

where F equals the degrees of freedom (or independent variables) required to specify the number of phases in equilibrium, C equals the number of chemical components (elements) in the system, P equals the number of phases present in a specific region of the diagram, and n represents extra variables required to define the system, such as temperature and pressure. The entire Li-Mn-Ni-O system is considered to be in equilibrium with $O_{2(g)}$ once the final crystalline phases form at constant temperature and $O_{2(g)}$ partial pressure (0.21 atm). Overall, this results in each composition within the Li-Mn-Ni-O system having values of $C = 4$ (representing Li, Mn, Ni, and O) and $n = 0$ (since temperature and pressure are fixed), simplifying the phase rule to $F = C - P$.

Single-phase compositions have $C = 4$ and $P = 2$ (representing the selected solid phase and $O_{2(g)}$ in equilibrium) producing $F = 2$. This value corresponds to the choice of two of the three mole fractions in the pseudo-ternary phase diagram when specifying the sample location, such that the final mole fraction is fixed by $X_{Li} + X_{Mn} + X_{Ni} = 1$. In a ternary phase diagram, two-phase compositions are found in linear co-existence regions called tie-lines which link or “tie” together two individual solid phases, often dubbed as tie-line “end-members”. As such, all two-phase compositions within the Li-Mn-Ni-O pseudo-ternary system have $C = 4$ and $P = 3$. This yields $F = 1$,

which represents the location of the composition on a tie-line that itself fixes the quantity of both phases according to the lever rule [27]. Finally, three-phase compositions are found in co-existence regions bounded by three separate tie-lines in the shape of a triangle, often referred to as a three-phase triangle. Compositions in such three-phase co-existence regions have $C = 4$ and $P = 4$ producing $F = 0$. In this case, all possible variables are fixed by the three-phase region under equilibrium, resulting in zero degrees of freedom.

The principles of Gibbs ternary phase diagrams were essential in several recent in-depth publications by McCalla et al. focusing on the structural characterization of the entire Li-Mn-Ni-O system using over 300 milligram-scale samples analyzed by XRD [16, 28, 29]. Several new single-phase cubic and layered compositions were discovered and found to form the end-members of numerous two- and three-phase co-existence regions which were previously unknown to the positive electrode materials research community. This work was conducted by Dr. Eric McCalla as part of his doctoral research, and has resulted in the production of complete Gibbs phase diagrams of the Li-Mn-Ni-O system at 800°C in an $O_{2(g)}$ atmosphere [30]. Several bulk samples were also synthesized in $O_{2(g)}$ to confirm the findings of the combinatorial studies. These studies also outline the dependence of phase formation on composition, synthesis temperature, and cooling rate for materials in the Li-Mn-Ni-O system. Overall, this work provides detailed yet practical phase diagrams for researchers, and represents a major contribution to Li-ion battery positive electrode materials research. As such, these diagrams will be discussed in the following section, as they form the basis for the structural studies of Li-Mn-Ni-O bulk samples prepared in air as presented in Chapter 3 of this thesis.

1.4.2 Phase Diagrams from Combinatorial Studies

Figure 1.8 shows the Li-Mn-Ni-O pseudo-ternary phase diagrams at 800°C in O_{2(g)} for both quenched and slow cooled samples [28]. Quenching was achieved by removing the samples at 800°C and placing them on a steel plate at room temperature, while slow cooling was achieved by simply turning off the furnace and letting the samples cool to room temperature naturally (also referred to as “natural” or “regular” cooling throughout this thesis). To simplify the presentation of the diagrams, single-phase region boundaries are shown as solid red lines, tie-lines between single-phase boundaries as dashed green lines, tie-lines that bound three-phase triangles as dashed red lines, and individual single-phase compositions as black points. Each single-phase region is labelled according to the parent crystal structure of that region. Finally, the dotted blue line represents a continuous phase transition boundary separating cubic rocksalt and hexagonal layered structures. All of these features were found to exist in both phase diagrams, albeit to different extents and often describing different phase regions, which will be discussed below.

A good starting point for explaining the complexity of these diagrams is with the four single-phase end-members of the quenched samples, labelled as M, N, R, and S in Figure 1.8, the XRD patterns of which are shown in Figure 1.9. The M and N compositions were best fit with the R-3m space group (the Miller indices of which are shown on the pattern of M), indicating that both materials have layered structures. The M composition was found to be a Mn-rich layered phase containing significant 3-D ordering while exhibiting an average discharge capacity of 237 mAh g⁻¹. By contrast, the N composition was characterized as a Ni-rich layered phase containing a large amount of Li and TM layer disorder in which the Li layer was found to have nearly 30% Ni site occupancy. This was found to hamper the removal of Li from the Li layer while cy-

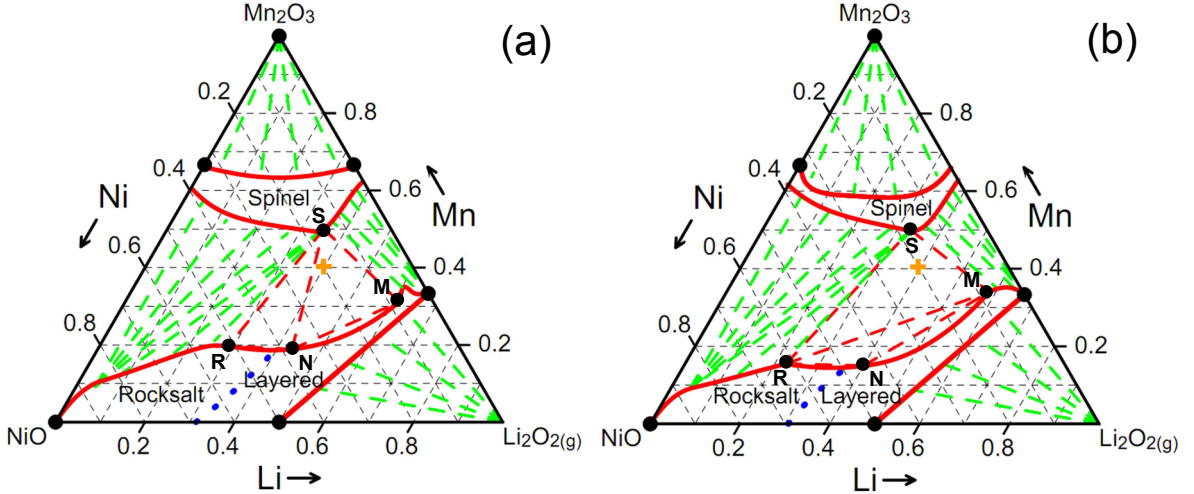


Figure 1.8. The Li-Mn-Ni-O pseudo-ternary phase diagrams at 800°C in O₂ for combinatorial samples that were (a) quenched and (b) slow cooled, as described in and adapted from Reference [28]. The solid red lines are single-phase region boundaries, the dashed red lines are two-phase tie-lines, and the dashed blue line represents the cubic to layered transition boundary. The ordered rocksalt (R), spinel (S), N-layered (N), and M-layered (M) end-member compositions are shown in black.

cling, yielding a low average discharge capacity of about 50 mAh g⁻¹. Overall, the Mn-rich and Ni-rich contents of these two compositions resulted in the choice of labelling as M (or M-layered) and N (or N-layered), which will be used frequently throughout this thesis.

The R composition was found to be a cubic rocksalt phase containing three intense peaks that match the XRD pattern of Li_xNi_{1-x}O (for x < 0.31) as well as several weaker peaks that match the XRD pattern of Ni₆MnO₈. Careful structural refinement indicated that the sample contained 4b sites of the cubic Fm3m space group occupied by Li and 10% vacancies [16]. This results in the ordering of Mn on the 4a sites producing a 2a x 2a x 2a cubic lattice with the simultaneous ordering of Li on the occupied 4b sites to form another 2a x 2a x 2a cubic lattice. The combination of this order-

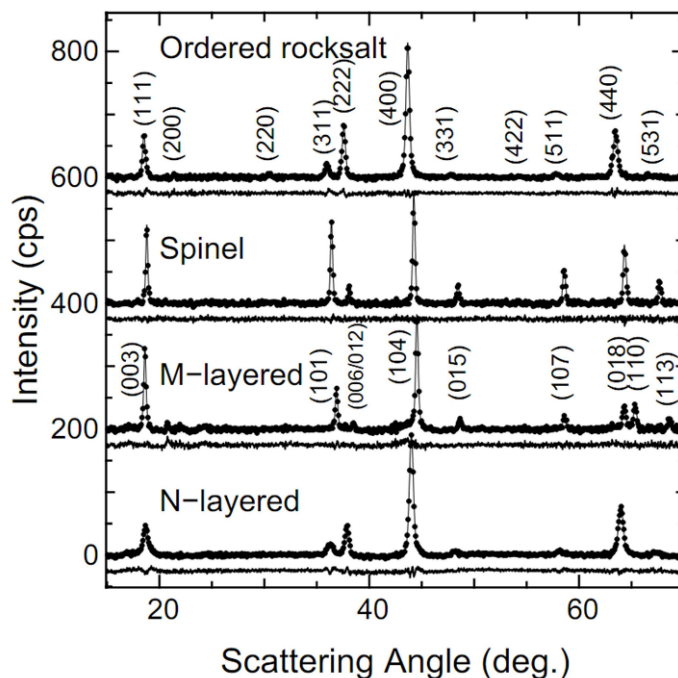


Figure 1.9. XRD patterns of the four end-members of the two three-phase regions for quenched samples prepared at 800 in O_2 . The peak indices correspond to JCPDS #80-4619 for the ordered rocksalt, and JCPDS # 52-0457 for the M- and N-layered phases. The spinel shares the same indices as the rocksalt except for the (200), (331), and (422) peaks. While the two layered phases have the same indices, the N-layered (018) and (110) peaks exhibit significant overlap. This figure is reprinted from Reference [28] with permission from the American Chemical Society.

ing within the cubic lattice produces an “ordered rocksalt” phase that is virtually electrochemically inactive when cycled [29]. Comparison of the lattice constant of this phase with those reported in literature further identified this phase as the “contaminant” rocksalt often found when synthesizing spinel materials such as $LiNi_{1/2}Mn_{3/2}O_4$ [31]. Thus, the ordered rocksalt phase is labelled as R (or R-phase) in the phase diagram, and its peaks are indicated by Fm3m Miller indices in Figure 1.9. Finally, the S composition was found to be the cubic spinel structure $LiNi_{1/2}Mn_{3/2}O_4$, and is best described by the Fd-3m space group, as discussed in Section 1.3.1.

Confirmation of the presence of one or more of the four phases above in a given composition was most readily determined by the position and intensity of the peaks from each phase in the range of scattering angles between approximately 42° to 46° 2θ . Figure 1.10 shows the positions of the cubic (400) peaks of the R- and S-phases and the hexagonal (104) peaks of the M- and N-phases in this narrow range. The peaks appear in the order of R, N, S, and M from lower to higher angle at positions of approximately 43.5° , 44.0° , 44.2° , and 44.5° , respectively for both the quenched and slow cooled samples. The differentiation between these peaks allowed for the qualitative identification of the phases found in each sample. This in turn allows for custom fitting of the XRD pattern of each sample using in-house software to extract the lattice parameters of each phase.

In short, the development of each pseudo-ternary phase diagram involved the following general procedure. Samples encompassing the entire Li-Mn-Ni-O system were synthesized using combinatorial methods and either quenched or slow cooled. Elemental analysis was used to determine the metal mole fractions of Li, Mn, and Ni in each composition, allowing for their placement on the ternary diagram. Qualitative XRD analysis provided the identification of the phase or phases present in each sample, which allowed for those phases to be fit using custom software to extract their lattice constants. Samples containing phases with the same (or very similar) lattice parameters were concluded to contain both phases, as every individual phase had a unique lattice constant governed by the total metal content and cooling rate used. Thus, comparison of the lattice constants between the phase(s) in single- and multi-phase samples established the locations of the end-members, tie-lines, and three-phase triangles within the phase diagram according to their solid crystalline structure(s). Single-phase boundaries were determined by observing the changes in peak positions

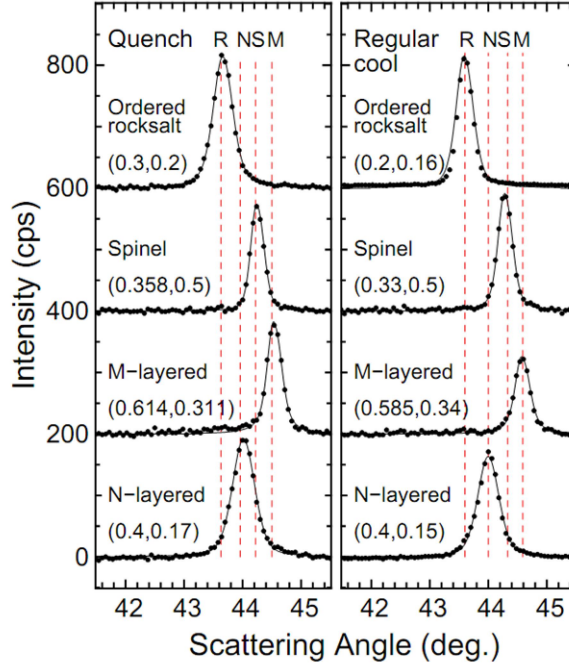


Figure 1.10. XRD patterns of the four end-members of the three-phase regions in the 42° to 46° scattering angle range obtained by quenching (left panel) and regular cooling (right panel) combinatorial samples prepared at 800°C in O_2 . This figure is reprinted from Reference [28] with permission from the American Chemical Society.

and lattice parameters between single-phase samples with the same crystal structure until the samples became multi-phase, at which point a co-existence region was identified and the boundary adjusted according to existing tie-line and end-member locations. The specific details of the development of the Li-Mn-Ni-O pseudo-ternary phase diagrams from combinatorial samples can be found in References [16] and [30].

The phase diagrams in Figure 1.8 clearly show the impact of the cooling method on the phases that form. Quenching effectively “locks in” the crystal structures that form under equilibrium conditions at elevated temperature. The higher temperature (relative to the gradually decreasing temperature when slow cooled) results in greater system entropy which favours more disorder in the system and therefore fewer total

crystalline phases overall. As shown, this results in larger single-phase regions (which have a lower total degree of order due to containing only a single phase), and smaller multi-phase regions (which have a higher total degree of order due to containing two or more crystalline phases). The opposite is true for slow cooling, where less entropy favours more ordering in the system, resulting in a higher quantity of crystalline phases overall. As seen in the slow cooled phase diagram, this resulted in smaller single-phase regions and larger multi-phase regions.

Among the single-phase regions, quenching effectively results in upper single-phase rocksalt, layered, and spinel boundaries which are at “higher” positions on the diagram (relative to the position of the Li axis, which is at the “bottom” of the phase diagram). Thus, both boundaries are viewed as moving “up” when quenching. By contrast, slow cooling results in the upper single-phase rocksalt, layered, and spinel boundaries being at “lower” positions on the diagram, moving “down” relative to the position of the Li axis. The cooling rate was found to have little impact on the lower single-phase layered and spinel boundaries positions respectively, which were found to be at approximately the same locations whether quenching or slow cooling.

The movement of the single-phase boundaries also resulted in the M, N, and R end-members being located at different compositions when quenched and slow cooled. The difference in composition of each quenched and slow cooled end-member is shown by the (Li, Mn) coordinates reported in Figure 1.10. In particular, the lower Li metal mole fractions of the M, R, and S slow cooled compositions relative to those of the quenched samples reflect the movement of single-phase rocksalt, layered, and spinel boundaries according to the cooling rate used.

The largest difference between the two phase diagrams is the type of co-existence regions which form in the positive electrode materials region at each cooling rate.

When quenching, two-phase tie-lines exist between N-R, N-S, N-M, R-S, and M-S. These tie-lines form the sides of two three-phase co-existence regions of N-R-S and M-N-S in the shapes of triangles. Crescent-shaped two-phase regions are also observed between the N-R tie-line and the rocksalt boundary, and between the N-M tie-line and the layered boundary. When slow cooled, the co-existence regions described above are different than those of the quenched samples. As shown, tie-lines between M-R, M-S, and R-S bound a large three-phase triangle containing M-R-S, while tie-lines between M-R, N-R, and M-N bound a second M-N-R triangle. The two crescent-shaped, two-phase co-existence regions from the quenched diagram are also observed in the slow cooled diagram, but are slightly larger than their quenched counterparts, owing to the lower positions of N and R on the single-phase boundary. In both diagrams, two-phase co-existence regions are located between the boundaries of the rocksalt and spinel phases, and between those of the spinel and layered phases, as denoted by dashed green lines.

Overall, the phase diagrams show numerous single-phase and co-existence regions which contain many compositions suitable for use as positive electrode materials. As discussed above, the N and R phases are poor positive electrode materials that can be viewed as unwanted phases if the goal of a particular composition is to maximize capacity. The compositions marked by orange crosses on the phase diagrams in Figure 1.8 illustrate how changing the cooling method impacts the final phases that form at the same composition. Thus, the choice of starting composition, and especially the cooling rate, must be carefully selected in order to achieve the desired electrochemical performance of a particular material in the Li-Mn-Ni-O system.

1.4.3 Positive Electrode Materials Region

Figure 1.11 highlights the positive electrode materials regions of each phase diagram. The various single- and multi-phase regions in each diagram are labelled for clarity. The phase diagrams have helped to explain several previously unsolved findings of materials in this region within the literature, the summaries of which are found in Reference [30]. Two examples illustrating how these diagrams have helped resolve such confusion will be briefly summarized here.

The first example is the case of the Li-rich oxide series $\text{Li}[\text{Ni}_x\text{Li}_{(1/3-2x/3)}\text{Mn}_{(2/3-x/3)}]\text{O}_2$, where two different descriptions of the complex structural characteristics of the series have been established. One view contends that the LRO series' compositions contain nano-domains of layered $\text{Li}[\text{Li}_{1/3}\text{Mn}_{2/3}]\text{O}_2$ within a matrix of layered $\text{Li}[\text{Ni}_{1/2}\text{Mn}_{1/2}]\text{O}_2$ [32–34]. Others believe that the LRO series exists as a homogeneous solid solution between Li_2MnO_3 and $\text{Li}[\text{Ni}_{1/2}\text{Mn}_{1/2}]\text{O}_2$ with no discernable phase differentiation on the nano-scale [9, 10]. The phase diagram studies of McCalla et al. have shown that, when quenched, the compositions in the LRO series remain single phase, and that the nominal composition series is actually contained within the single-phase layered region. When slow cooled, however, compositions in the series near the $\text{Li}[\text{Ni}_{1/2}\text{Mn}_{1/2}]\text{O}_2$ end-member phase separate into two-phase layered-layered composites, as indicated by the N-M tie-line and the crescent-shaped region between it and the single-phase boundary.

The second example is the case of integrated layered-spinel composites in the composition series $x\text{Li}[\text{Ni}_{0.5}\text{Mn}_{1.5}]\text{O}_4 \bullet (1-x)\text{Li}[\text{Li}_{0.2}\text{Ni}_{0.2}\text{Mn}_{0.6}]\text{O}_2$ [35, 36], which were synthesized in an effort to combine the rate capability of the spinel with the high capacity and energy density of the LRO. While several compositions in this series exhibited capacities of 225 mAh g^{-1} up to rates of C/3, the phase diagram studies indicate that these materials cannot form layered-spinel composites at the compositions reported, all

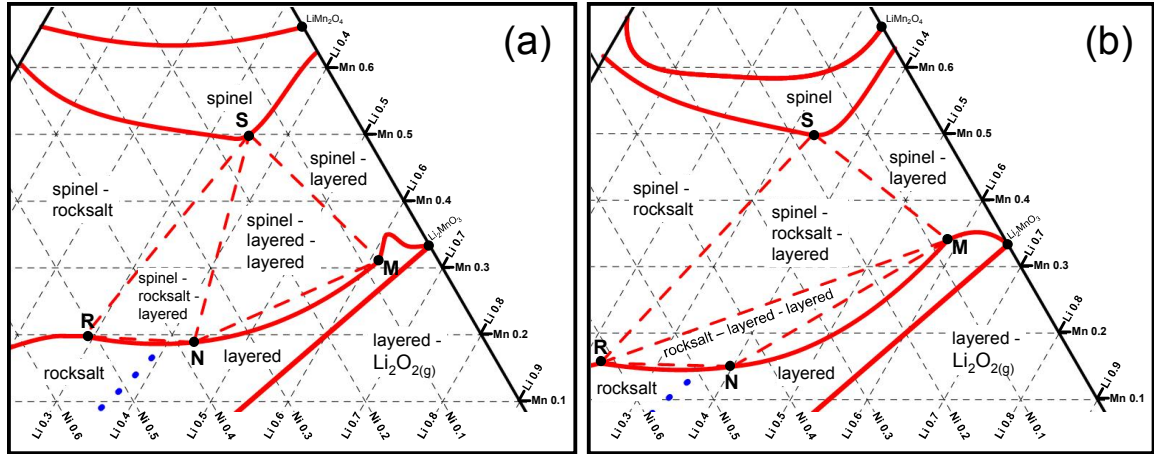


Figure 1.11. The positive electrode materials region of the Li-Mn-Ni-O pseudoternary phase diagrams at 800°C in O₂ for combinatorial samples that were (a) quenched and (b) slow cooled. Single- and multi-phase regions are labelled according to their constituent crystalline phase(s).

of which have fixed Ni:Mn ratios of 1:3. Instead, two-phase layered-spinel materials can only be found in the region between the spinel and layered boundaries, bounded on the left side by the M-S tie-line and on the right side by the Mn-axis. Therefore, other structural factors must contribute to the high capacity and rate capability of such materials.

The discovery of the extended single-phase layered region above the LRO composition series presents opportunities for the structural and electrochemical characterization of new Li-Mn-Ni-O materials. The expansion of the lithium-rich oxide solid-solution beyond its nominal composition as a line into a single-phase layered region presents many research opportunities, for example. In particular, however, is the discovery of the “bump” in the single-phase layered boundary, found between Li₂MnO₃ and the M-layered phase. Studies by McCalla et al. determined that compositions in this bump region contain metal site vacancies, allowing for Mn to fill up to 2/3 of the TM layer and thereby order on two $\sqrt{3}a_{hex} \times \sqrt{3}a_{hex}$ lattices [15]. While it has been

shown that Li_2MnO_3 exhibits low practical capacities and poor cycling behaviour, both $\text{Li}[\text{Ni}_{1/6}\square_{1/6}\text{Mn}_{2/3}]\text{O}_2$ (which is near the top of the bump) and the M-layered phase (which is near the base of the bump) have been shown to exhibit reversible capacities of 150 mAh g^{-1} and 240 mAh g^{-1} , respectively. This introduces the possibility that the compositions in the bump region, which are effectively Ni-substituted, Mn-rich LRO analogues of Li_2MnO_3 , may also have interesting and promising electrochemical properties.

Since Mn is relatively cheap, plentiful, and non-toxic compared to Ni, the potential for the discovery of materials with large capacities and minimal Ni content is both economically and environmentally desirable. However, the phase diagrams were prepared using milligram scale samples in a 100% $\text{O}_{2(\text{g})}$ atmosphere, the scale and reaction conditions of which are not amenable to industrial synthesis or scale-up. As such, bulk samples prepared on the gram scale at both 800°C and 900°C in air will be used to generate partial quenched and slow cooled Li-Mn-Ni-O phase diagrams in the positive electrode materials region. The combinatorial phase diagrams at 800°C will therefore be used to help direct the development of the phase diagrams for the bulk samples to be discussed in this thesis, providing a starting point for establishing the locations of end-members, single-phase boundaries, and multi-phase regions.

1.5 Scope and Structure of Thesis

This thesis will focus on the structural and electrochemical analysis of numerous quenched and slow cooled compositions in the positive electrode materials region of the Li-Mn-Ni-O phase diagram for bulk-scale samples prepared in air. Chapter 2 will detail the experimental and analytical techniques used to synthesize and characterize

the samples presented. Chapter 3 will use the methodology developed in the combinatorial study to map the phase space of the positive electrode materials region for bulk-scale samples prepared at 800°C and 900°C in air.

Chapter 4 will present the structural and electrochemical characterization of quenched compositions within the single-phase layered bump region of the phase diagram cycled to different upper potential limits. Several of these compositions were found to exhibit specific capacities and cycling behaviour that make them desirable for high energy density positive electrode material applications. Chapter 5 will focus on the structural and electrochemical characterization of the single- and multi-phase slow cooled counterparts of the single-phase quenched compositions in the bump region. Many of these materials were found to exhibit anomalous increases in capacity with extended cycling, the magnitude and possible origins of which will be discussed.

Chapter 6 contains a high precision coulometry study of two Li-rich layered compositions and one Li-deficient layered composition all located within the single-phase layered region. It will be shown that the Li-deficient material, located in the middle of the bump region, exhibited minimal reaction with the electrolyte at high potential resulting in stable cycling behaviour, thus making it suitable for use as a thin protective “shell” in a core-shell particle configuration. Finally, Chapter 7 summarizes the studies presented in this thesis, and outlines future research opportunities within the Li-Mn-Ni-O system focusing on positive electrode material development.

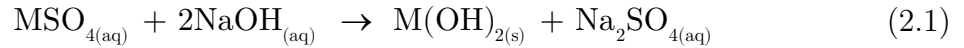
Chapter 2

Synthesis, Characterization, and Analysis Techniques

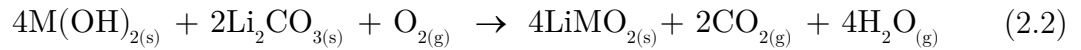
This chapter contains a summary of the experimental methods used for the synthesis, characterization, and analysis of the Li-Mn-Ni-O samples discussed in this thesis. In addition, Chapters 3, 4, 5, and 6 will begin with an “Experimental” section detailing any experimental parameters specific to the samples and results discussed therein.

2.1 Synthesis

Wet-chemical, co-precipitation reactions [37] between aqueous metal sulfate salt and basic solutions were used to generate metal hydroxide precursors according to the general reaction:



where M is Ni and/or Mn. The hydroxide precursors were then lithiated using Li_2CO_3 at high temperature in air to produce the final Li-Mn-Ni-O samples according to the general solid-state reaction:



2.1.1 Starting Reagents

The metal salts used to produce the hydroxide precursors were $\text{NiSO}_4 \cdot 6\text{H}_2\text{O}_{(s)}$ (98%, Fluka Analytical) and $\text{MnSO}_4 \cdot 4\text{H}_2\text{O}_{(s)}$ (99.5%, Fluka Analytical). The bases used for co-precipitation and particle growth were $\text{NaOH}_{(s)}$ (98+%, Sigma-Aldrich) and $\text{NH}_4\text{OH}_{(aq)}$ (28.0-30.0%, Sigma-Aldrich). Deionized water that was deaerated by boiling for 10 to 15 minutes was used to make aqueous solutions of the above-mentioned reagents.

2.1.2 Hydroxide Precursors

A continuous-stirred tank reactor (CSTR), shown in Figure 2.1(a), was used to generate the hydroxide precursors. The CSTR setup consisted of digital peristaltic pumps (Masterflex L/S 07524), a 2.0 L jacketed glass reaction vessel, a pH meter (In-Lab 424, Mettler-Toledo), and digital controllers (Biostat M) for monitoring and adjusting pH, temperature, and stirring rate. The pumps were calibrated using 5.0 mL volumes of reagent solution, while the pH meter and electrode were calibrated at 60.0°C using buffer solutions with pH values of 7.0 (Fisher Scientific) and 11.1 (Fixanal, Riedel-de Haen). A schematic showing the important features and general operation of the CSTR is shown in Figure 2.1(b). A typical co-precipitation reaction using the CSTR to produce the hydroxide precursors is described below.

It has been shown that hydroxide precursor particle size impacts both the particle size and electrochemical performance of layered transition metal oxides [38, 39], with smaller sizes yielding larger total capacities. At low rate and room temperature, the HV plateau capacities of the Li-rich oxides $\text{Li}[\text{Li}_{1/9}\text{Ni}_{1/3}\text{Mn}_{5/9}]\text{O}_2$ and $\text{Li}[\text{Li}_{1/5}\text{Mn}_{1/5}\text{Mn}_{3/5}]\text{O}_2$ have also been shown to increase as the average particle size decreases due to shorter Li diffusion pathways [40, 41]. As such, the co-precipitation re-

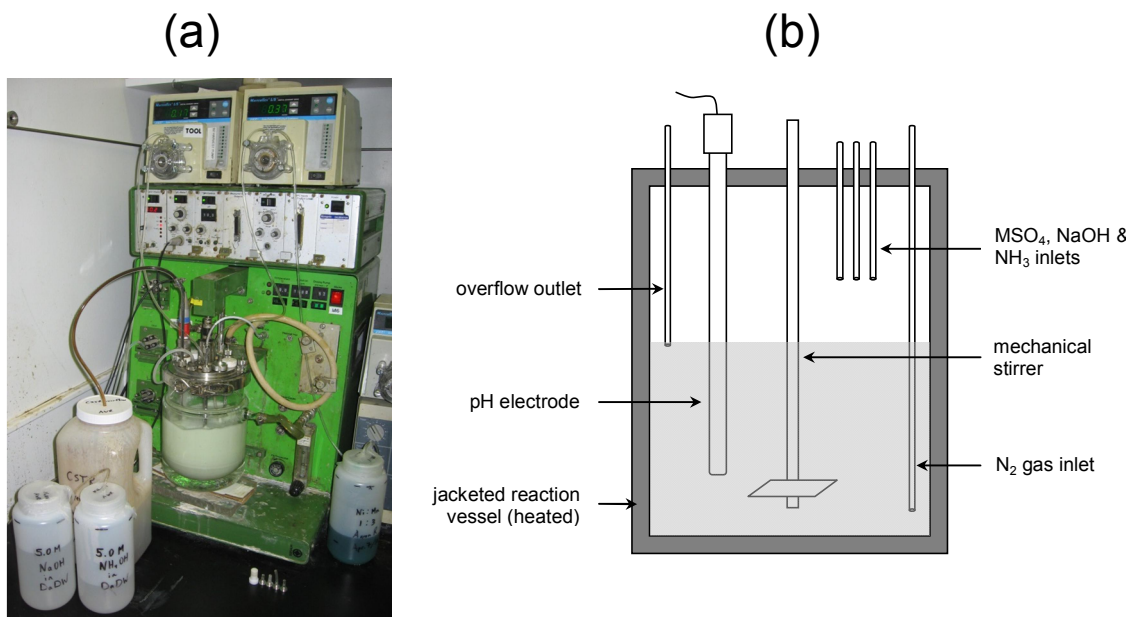


Figure 2.1 An image (a) and a schematic (b) of the continuously-stirred tank reactor used to synthesize the hydroxide precursors.

action conditions described below were selected to produce hydroxide precursor particles that were approximately 5 μm in diameter as outlined in Reference [41].

Aqueous solutions of mixed nickel and manganese sulfate in deaerated deionized water were prepared with Ni:Mn mole ratios of 1:1, 3:5, 1:3, and 1:5. The total metal ion concentration of each solution was 2.0 M. A 5.0 M $\text{NaOH}_{(\text{aq})}$ solution was used as the source of base for co-precipitation, while a 5.0 M $\text{NH}_4\text{OH}_{(\text{aq})}$ solution was used for metal ion coordination with ammonia to facilitate gradual particle growth during the reaction [42]. For each precursor reaction, the mixed metal sulfate and NH_4OH solutions were added at fixed rates of 0.37 mL min^{-1} and 0.17 mL min^{-1} , respectively over a total reaction time of either 10 or 20 hours. The pH of each reaction was maintained at a constant value of either 10.3 or 11.1 via the automatic addition of the NaOH solution as required. Nitrogen gas was bubbled into the reactor at a rate of $1.0 \text{ cm}^3 \text{ min}^{-1}$ to deaerate the solution and to create an inert reaction atmosphere, preventing the

oxidation of Mn^{2+} to Mn^{3+} and allowing the reaction solution, $\text{NH}_{3(\text{g})}$, and $\text{N}_{2(\text{g})}$ to be ejected via an overflow pipe to maintain a constant volume of 1.0 L in the tank. The reaction temperature was maintained at 60.0 °C as monitored by a temperature probe, and the solution was stirred at a rate of 1000 RPM using a mechanical agitator.

Once the reactions were complete, the hydroxide precursors were rinsed with 4.0 L of deaerated deionized water under suction filtration, and then dried at 120°C in a forced-air convection oven for a minimum of 12 hours. Each dried precursor was recovered, ground in a mortar and pestle, and stored in a scintillation vial prior to further use. The total yield of each hydroxide precursor reaction was approximately 40 g.

2.1.3 Li-Mn-Ni-O Materials

A solid-state reaction between the hydroxide precursor and Li_2CO_3 in air was used to produce the final Li-Mn-Ni-O powders. Figure 2.2 shows the various steps involved in the metal oxide powder synthesis, which is described below. Each of the four composition series (1:1, 3:5, 1:3, and 1:5) were designed to contain Li-Mn-Ni-O compositions with nominal Li metal mole fractions increased in regular increments. Each series initially ranged from compositions with $X_{\text{Li}}=0.333$ to compositions with X_{Li} values equal to those of the series $x\text{LiNiO}_2 \cdot (1-x)\text{Li}_2\text{MnO}_3$, with $x=0.5$ for the 1:1 series, $x=3/8$ for the 3:5 series, $x=1/4$ for the 1:3 series, and $x=1/6$ for the 1:5 series. To achieve this, stoichiometrically measured amounts of precursor powder and Li_2CO_3 (99+%, FMC) were mixed by mechanical grinding in a mortar and pestle until a homogenous visual consistency was achieved. The powder mixtures were put into alumina boats and sintered in a benchtop muffle furnace (Ney Vulcan 3-550 or Barnstead-

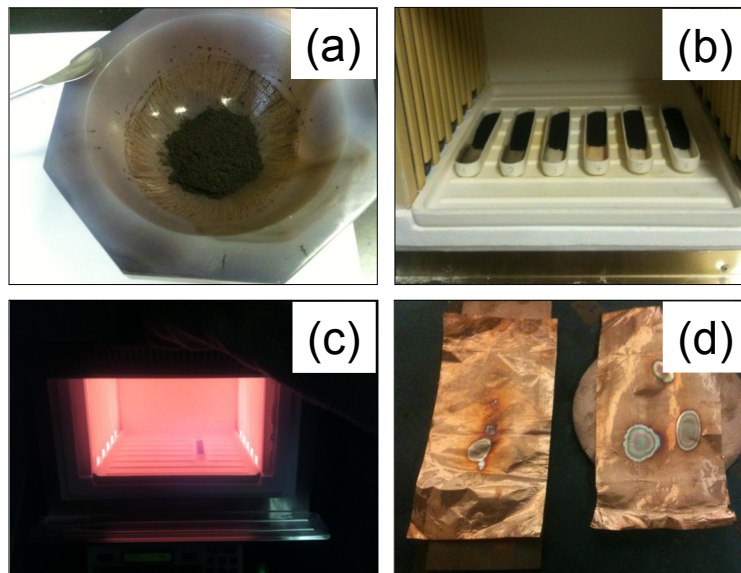


Figure 2.2. Solid state synthesis of the Li-Mn-Ni-O samples showing the (a) precursor mixed with Li_2CO_3 , (b) powder mixture in alumina boats placed in the high temperature furnace, (c) sample at 900°C prior to removal from the furnace, and (d) copper sheets used to hold the sample while quenching between two copper blocks.

Thermolyne 1400) at 800°C , 900°C or 950°C in air for 10 or 12 hours, depending on the system under study. An initial heating rate of $10^\circ\text{C min}^{-1}$ was used for all samples.

The samples were cooled using either one of two quenching methods or one slower method. For quenched samples, the powders were removed from the furnace at high temperature as shown in Figure 2.2(c) and either cooled to room temperature between two copper foil sheets compressed between two thicker copper plates, or quenched by dumping the powder into a liquid nitrogen bath. For slow cooled samples, the furnace was simply turned off, allowing the powders to come to room temperature via natural convection (equaling about 5°C min^{-1} on average). The final Li-Mn-Ni-O products were mechanically ground and passed through a 75 micron sieve prior to characterization.

2.2 Materials Characterization

The following sections outline the characterization techniques, instrumentation, and analysis techniques used to characterize the Li-Mn-Ni-O materials in terms of their elemental compositions, crystalline structures, particle morphologies, and physical properties. The specific techniques and details of sample characterization in Chapters 3 through 6 will be discussed in each chapter's "Experimental" section.

2.2.1 Elemental Analysis

The Li, Mn, and Ni content of the oxide powders was obtained using inductively coupled plasma optical emission spectroscopy (ICP-OES) [43] performed at the Minerals Engineering Centre at Dalhousie University. Approximately 10 mg of each sample was dissolved in reagent grade HCl:HNO₃ (aqua regia) solution which was then diluted to 50 mL prior to measurement. For each sample, elemental compositions were reported as mass fractions of Li, Mn, and Ni relative to the total sample mass in units of mg kg⁻¹, with a 5% relative error for each mass fraction.

2.2.2 Powder X-ray Diffraction and Structural Refinement

X-ray diffraction is a characterization technique used to analyze the arrangement and periodicity of atoms in crystalline materials. It is based on the principle of Bragg diffraction, which is illustrated in Figure 2.3. When a crystal is bombarded by electromagnetic radiation, the atoms in the material scatter the incident rays. Since X-ray wavelengths are of the same order of magnitude as the distance between atomic planes in a crystal, scattering results in both constructive and destructive interference of the

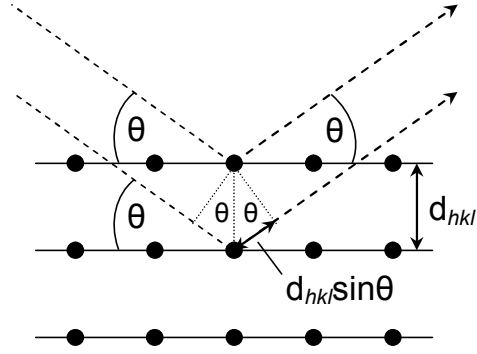


Figure 2.3. A simple illustration of Bragg X-ray diffraction.

X-rays [44]. Constructive interference is observed when the following condition, called the Bragg Law, is satisfied:

$$n\lambda = 2d_{hkl} \sin \theta \quad (2.3)$$

where n is an integer, λ is the x-ray wavelength, d_{hkl} is the interplanar spacing specified by the Miller indices hkl and θ is the angle between the incident ray and the hkl atomic planes. When the angle of the incident X-rays satisfies the Bragg diffraction condition, the reflected waves are in phase. Constructive interference yields large diffracted beam intensities which can be measured as a function of the scattering angle, 2θ . Thus, monitoring the angles at which monochromatic X-rays are diffracted from a crystal surface provides the distance between lattice planes, d_{hkl} . The lattice plane spacing can then be used to calculate the lattice constants of the crystal structure.

X-rays scattered by a single electron at a distance R have an intensity I_e that can be described by the Thomson equation:

$$I_e = I_o \frac{e^4}{m_e^2 c^4 R^2} \left(\frac{1 + \cos^2(2\theta)}{2} \right) \quad (2.4)$$

where I_o is the incident X-ray intensity, e is the electron charge, m_e is the electron mass, c is the speed of light, and θ is one-half of the scattering angle. The atomic scattering factor, f_o , is proportional to the number of electrons in an atom or ion, and

describes the total scattering arising from these electrons. Its value is dependent on both X-ray wavelength and diffraction angle, and is also specific to each element.

To determine the intensity of scattered X-rays at different Bragg angles, the positions of the atoms within the crystalline unit cell must be considered. The geometric structure factor, F_{hkl} , describes the contribution of each atom to Bragg reflections at Miller indices (hkl) as

$$F_{hkl} = \sum_n f_n e^{2\pi i(hx_n + ky_n + lz_n)} \quad (2.5)$$

where f_n is the atomic scattering factor, and x_n , y_n , and z_n are the fractional atomic coordinates of the n^{th} atom in the unit cell. The sum in equation 2.3 runs over all the atoms in the unit cell. The intensity of scattered X-rays from each Bragg reflection is proportional to F_{hkl}^2 .

Powder XRD was used to structurally characterize the samples described in this thesis. Prior to analysis, each powder was tightly packed into a stainless steel flat-plate sample holder. The surface of the compacted powder was flattened and smoothed until it was flush with the sample holder surface. All samples prepared at 800°C were measured on a JD2000 diffractometer, while all samples prepared at 900°C were measured on a Siemens D5000 diffractometer. Both instruments were equipped with a Cu target X-ray tube and a diffracted beam monochromator. The scans were typically performed from 10.0° to 90.0° with a step size of 0.05° and a dwell time of 5 seconds per step.

Two different programs were used to refine lattice parameters from the XRD patterns. To extract hexagonal and/or cubic lattice parameters from samples containing single and multiple phases, a modified LeBail refinement routine developed by Dr. Eric McCalla was used [30]. The software was written in the programming language Yorick

[45], and uses the Levenberg-Marquardt algorithm of the *curfit* subroutine to perform a non-linear, least-squares fit [46]:

$$\chi^2 = \sum \left(\frac{1}{\sigma_i^2} [y_i - \mathcal{Y}(x_i)]^2 \right) \quad (2.6)$$

where χ^2 is the goodness of fit parameter, σ_i^2 are the uncertainties in the data points y_i (where $\sigma_i = \sqrt{y_i}$), and $y(x_i)$ is a non-linear fitting function. The fitting process calculates the optimal values of adjustable fitting parameters a_j contained within $y(x_i)$ by minimizing the value of the partial derivative of χ^2 with respect to each of the fitting parameters simultaneously [46]:

$$\frac{\partial}{\partial a_j} \chi^2 = 0 \quad (2.7)$$

The uncertainty of each parameter a_j is determined by the following equation [46]:

$$\sigma_{a_j}^2 = \sum \left[\sigma_i^2 \left(\frac{\partial a_j}{\partial y_i} \right)^2 \right] \quad (2.8)$$

where $\sigma_{a_j}^2$ is the uncertainty of a_j , σ_i is the standard deviation of each data point y_i , and the partial derivative represents the effect that y_i has on the determination of a_j in the fitting function $y(x_i)$. The adjustable parameters which can be released for refinement using the in-house software are the peak positions (in 2θ), peak intensities, and peak widths (full width at half maximum).

When more detailed structural information was required, Rietveld profile refinement was performed on select single-phase samples. The Rietveld method [47] also involves minimizing the sum of the weighted least-squares residual, R , between an experimental and a calculated diffraction pattern:

$$R = \sum_i w_i [I_i(\text{obs}) - I_i(\text{calc})]^2 \quad (2.9)$$

where i designates the i -th data point, w_i is the statistical weight, $I_i(\text{obs})$ is the observed diffraction pattern, and $I_i(\text{calc})$ is the calculated diffraction pattern. In addition to the adjustable parameters described above for the modified LeBail fitting routine, the Rietveld method allows for the release of additional parameters for fitting, including peak shape variables, atom positions, and site occupancies. For all refinements, the total site occupancies of each of Li, Mn, and Ni were constrained according to their values as determined by ICP-OES. The oxygen content was fixed at 2 for layered structures and 4 for spinel structures unless otherwise stated. The fitting software Rietica [48] was used to perform the Rietveld refinements presented in this thesis.

2.2.3 Scanning Electron Microscopy

Scanning Electron Microscopy (SEM) was used to study the particle size and morphology of the compositions discussed in Chapters 4 and 5. The SEM images shown in Chapter 4 were obtained with a Phenom G2 Pro benchtop scanning electron microscope. The SEM images shown in Chapter 5 were obtained with a Hitachi S4700 field-emission scanning electron microscope using an electron beam energy and current of 15 KeV and 5 μA , respectively.

2.2.4 BET Surface Area Analysis

Surface area analysis is important for determining if the exposed area of a Li-Mn-Ni-O sample impacts its electrochemical performance. Brunauer-Emmett-Teller (BET) surface area measurements of the Li-Mn-Ni-O powders were performed using a Micromeritics Flowsorb II 2300 surface area analyzer. The resultant surface areas were

normalized by the mass of sample analyzed and are reported as specific surface areas in units of $\text{m}^2 \text{g}^{-1}$.

2.3 Electrochemical Characterization

The electrochemical results presented in this thesis were collected using half-cells in which the Li-Mn-Ni-O positive electrode were cycled against a Li metal negative electrode. The following sections outline the details of electrode preparation, coin cell assembly, electrochemical charger equipment, and testing protocols.

2.3.1 Electrode Preparation

In order to make Li-Mn-Ni-O positive electrodes, slurries were prepared to coat the material onto a conductive backing. Each slurry was composed of the 86 wt% Li-Mn-Ni-O as the active material (AM), 7 wt% Super-S carbon black powder (MMM Carbon) as the conductive agent, and 7 wt% poly(vinylidene fluoride) (PVdF) resin (Grade 301F, Arkema, Inc.) as the binder. 1-Methyl-2-pyrrolidinone (NMP) anhydrous, (99.5%, Sigma-Aldrich, Inc.) was used as the solvent medium. The slurry was mixed in a planetary mixer (Kurabo Mazeurestar KK-50S) for 15 to 20 minutes until a homogeneous consistency was achieved. Coatings were prepared by spreading the slurry mixture on an Al foil current collector with a 0.006" notch bar spreader. The freshly coated electrodes were dried overnight at 120° . The final electrodes had mass fractions of 0.86 AM, 0.07 carbon black, and 0.07 PVdF. The coated electrodes were compressed by passing them through a roller-mill (DPM Solutions) at 200 PSI of tank

pressure (approximately 2000 atm of direct pressure at the electrode surface) prior to further use.

2.3.2 Coin Cells

Electrodes 1.0 cm² in diameter were punched out of the dried coatings using a spring-loaded die, and then weighed on an analytical balance (Sartorius CPA225D), with an average mass of 10 mg. These punched electrodes were used as the positive electrodes in 2325 coin cells. The coin cell components and order of assembly are depicted in Figure 2.4. The negative electrode was Li foil (>99.8%, Chemetalle Foote Corp.), and the separator (2 per cell) was Celgard 2320 (Celgard, LLC). For the electrolyte, LiPF₆ (99.9%, BASF) was used in a 1.0 M solution containing ethylene carbonate (EC, 99.96%, BASF) and diethyl carbonate (DEC, 99.96%, BASF) combined in a 1:2 v/v ratio. All casings, springs, and spacers were made of stainless steel. All coin cells were assembled in an argon glove box (H₂O < 5 ppm, O₂ < 5 ppm), and doubly-sealed using a pressure driven coin cell crimper. Once the coin cells were assembled and sealed, thin strips of stainless steel were spot-welded to the top and bottom casings of each cell as electrical leads.

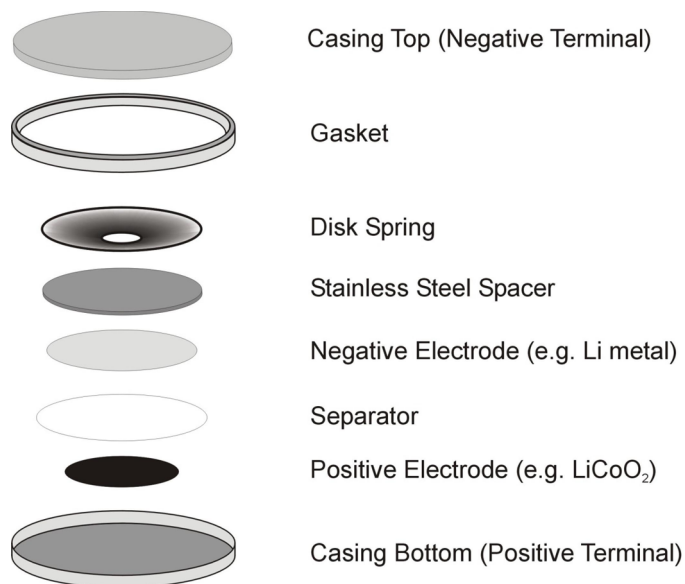


Figure 2.4. A schematic showing the components of a standard 2325 coin cell.

2.3.3 Electrochemical Measurements

The majority of the electrochemical results presented in this thesis were collected using a Moli Charger System (Moli Energy) via galvanostatic charge/discharge measurements. In general, the half-cells were cycled from lower potential limits of 2.0 V, 2.5 V, and 3.0 V to upper potential limits of 4.4 V, 4.6 V, 4.8 V, and 4.9 V (all vs. Li/Li⁺). The currents used, normalized to the mass of active material in each half-cell as specific currents reported in units of mA g⁻¹, were typically 5 mA g⁻¹, 10 mA g⁻¹, or 20 mA g⁻¹. These specific currents correspond to C-rates of C/50, C/25, and C/12.5, respectively for a material exhibiting a capacity of 250 mAh g⁻¹, and are relatively low compared to C-rates typically used for positive electrode materials such as LiCoO₂ and LiMn₂O₄. However, since the Li-Mn-Ni-O materials reported in this thesis are all previously undiscovered compositions, lower charging rates were required in order to

observe any and all redox processes occurring during charge and discharge. The “Experimental” sections in Chapters 4 through 6 will detail the specific cycling protocols of the electrochemical tests discussed therein.

2.3.4 Ultra High Precision Coulometry

The ultra high precision charger (UHPC) system [49] developed at Dalhousie University yields accurate current, coulombic efficiency (CE) and charge endpoint capacity slippage measurements of both Li-ion full cells and half-cells [50]. These measurements provide information about parasitic reactions which occur between the active electrode material and the electrolyte during cycling. UHPC is therefore a useful tool for measuring and comparing the cycling stability of different positive electrode materials in half-cells. Chapter 6 contains UHPC cycling results for three single-phase layered Li-Mn-Ni-O compositions, and compares them in terms of their coulombic efficiencies, specific capacities, and charge endpoint capacities. In order to limit corrosion at higher potentials, Al-coated casings and spacers were used on the positive electrode side of each half-cell [51].

Chapter 3

Pseudo-ternary Phase Diagrams of the Positive Electrode Materials Region of the Li-Mn-Ni-O System for Bulk Samples

As discussed in the introduction, recent studies by McCalla et al. have resulted in the production of detailed pseudo-ternary phase diagrams of the Li-Mn-Ni-O system at 800°C in a 100% O_{2(g)} atmosphere [16, 28]. The use of oxygen was required in order to suppress significant Li loss from the milligram scale combinatorial samples in lower oxygen partial pressures during heating [30]. To confirm that the phase diagrams produced were valid for gram-scale samples (i.e., bulk samples), selected materials were also made at 800°C in a pure O_{2(g)} atmosphere made for comparison with combinatorial samples. These bulk samples supported the findings of the combinatorial phase diagram study, mostly in the single-phase layered region. However, bulk samples made on the industrial scale for commercial use are typically made at higher temperatures to limit the heating time needed to produce appropriate crystallite sizes and in air due to practical considerations. It was decided that the production of the phase diagrams based on bulk-scale samples synthesized at 900°C in air was essential, both to confirm the findings of the combinatorial-based phase diagram study and to provide academic and industrial researchers with a greater overall understanding of the Li-Mn-Ni-O sys-

tem. The goals were to learn how initial compositions, synthesis conditions, and cooling methods impact the phases which form in the final material.

Indeed, it would have been much more difficult to establish these phase diagrams with the accuracy that they display without having the phase diagrams at 800°C in O₂ shown in Figure 1.8 and Figure 1.11 as a general guide for which phases to look for in different locations within the positive electrode materials region. In particular, the discovery of the ordered rocksalt, the differentiation between the N- and M-layered phases, and the use of in-house software to extract lattice constants of the four end-members were all crucial for the development of these phase diagrams, without which the complex data presented herein would have been extremely difficult to put into the broader concept of general phase diagram development. In this regard, the author gratefully acknowledges Dr. Eric McCalla for his contributions to this work. The exceptional scope and overall contribution of his PhD research to the Li-ion battery research community in the form of the Li-Mn-Ni-O phase diagrams at 800°C in O₂ was instrumental in the development of the bulk sample Li-Mn-Ni-O phase diagrams produced in this study.

In order to limit confusion when viewing individual samples on the diagram, the nomenclature used to differentiate between sample labels (as letters) and the four end-members requires clarification. The end-member compositions R, S, N, and M (shown in black on the phase diagrams) will be referred to either by their letter only or with a qualifying term, e.g., N-phase, N end-member, or N-layered. In addition, when referring to two-phase tie-lines and three-phase regions, the nomenclature used (e.g., M-R-S triangle) will refer exclusively to the R, S, N, and M end-member compositions. By contrast, the individual sample compositions (shown in blue on the phase diagrams to

be presented) will always be prefaced with the term “sample” or “composition” when referenced, e.g., sample N, compositions M and N, samples M through O, and so on.

3.1 Experimental

The samples used to produce the phase diagrams discussed in this chapter were prepared according to the synthesis conditions described in Section 2.1 and analyzed according to the techniques described in Sections 2.2.1 and 2.2.2. All samples underwent ICP-OES and XRD analysis. For XRD analysis, the samples were each scanned from 10.0° to 90.0° with a step size of 0.05° and a dwell time of 3 seconds per step, followed by a narrow range scan from 42.0° to 46.0° with a step size of 0.02° and a dwell time of 30 seconds per step. This lower step size scan was required in order to differentiate between the various end-members that formed in multi-phase samples due to significant overlapping of the (104) peaks of the two hexagonal layered phases and the (111) peaks of the cubic spinel and rocksalt phases. The majority of the samples discussed in this chapter were synthesized and scanned by undergraduate co-op student Luke Hacquebard.

3.2 Li-Mn-Ni-O Compositions for Phase Mapping

Figure 3.1 shows the quenched and slow cooled phase diagrams labelled with the individual compositions used to map them. Each composition is labelled by letter from A through AC, and appears on the diagram at its (Li, Mn) coordinates as determined by elemental analysis. The various single-phase and multi-phase regions elucidated from the structural analysis of the labelled samples are intentionally being shown prior

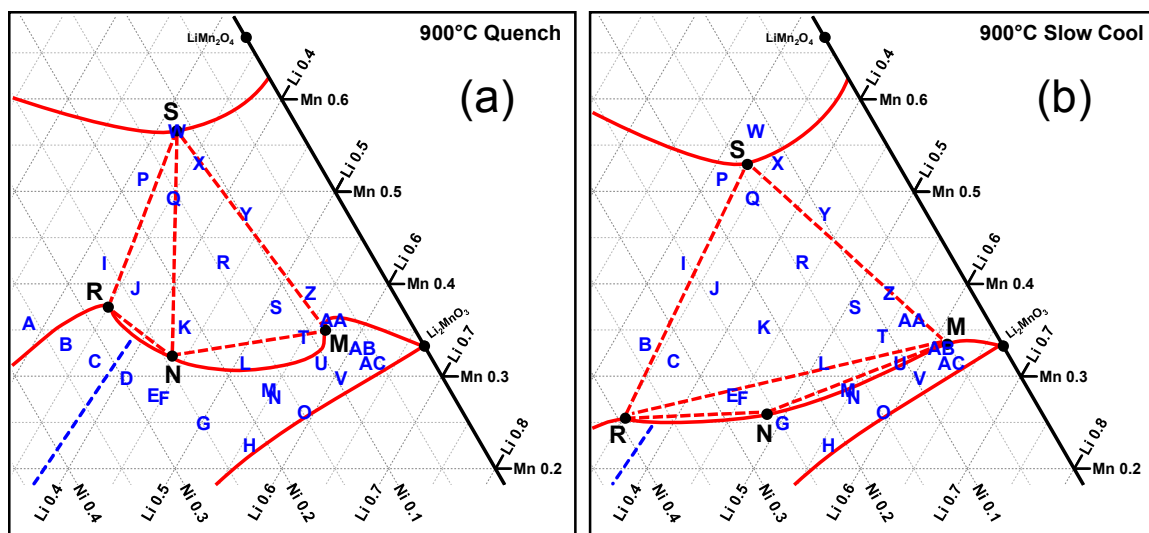


Figure 3.1 Pseudo-ternary phase diagrams of the Li-Mn-Ni-O system at 900°C in air for samples that were (a) quenched and (b) slow cooled. Sample compositions used to elucidate the phase diagrams are labelled in blue as points A to AC, and will be referred to by their letter label throughout the thesis. The coordinates of each sample in (Li, Mn) notation are shown in Table 3.1.

to their establishment in the upcoming sections in order to provide context when viewing the XRD patterns of each sample in Figure 3.2 to Figure 3.7.

Table 3.1 shows the sample label, Ni:Mn composition series, metal mole fraction, and (Li, Mn) coordinates as determined by ICP-OES of each sample. As shown, the samples were prepared as four separate composition series, each with a fixed Ni:Mn ratio as determined by the hydroxide precursor. For example, the 1:1 series was produced by starting with a $\text{Ni}_{0.5}\text{Mn}_{0.5}(\text{OH})_2$ precursor, then adding stoichiometrically determined amounts of Li_2CO_3 in a series of solid-state reactions to produce individual samples forming a Li-Mn-Ni-O composition series with a Ni:Mn ratio of 1:1. Therefore, within each composition series, the Li content increases when moving down the diagram toward the Li corner of the ternary diagram, e.g., from sample A to sample H in

Table 3.1. Sample label, composition series (Ni:Mn ratio), metal mole fractions, and phase diagram coordinates in (Li, Mn) notation for samples A through AC in Figure 3.1.

Sample	Ni:Mn Series	Metal Mole Fraction			(Li, Mn) notation*
		Li	Mn	Ni	
A	1:1	0.284	0.357	0.359	(0.28, 0.36)
B	1:1	0.330	0.335	0.335	(0.33, 0.34)
C	1:1	0.367	0.317	0.316	(0.37, 0.32)
D	1:1	0.406	0.298	0.296	(0.41, 0.30)
E	1:1	0.441	0.280	0.279	(0.44, 0.28)
F	1:1	0.450	0.276	0.274	(0.45, 0.28)
G	1:1	0.502	0.250	0.248	(0.50, 0.25)
H	1:1	0.557	0.226	0.217	(0.56, 0.23)
I	3:5	0.323	0.423	0.254	(0.32, 0.42)
J	3:5	0.363	0.393	0.244	(0.36, 0.39)
K	3:5	0.431	0.354	0.215	(0.43, 0.35)
L	3:5	0.508	0.314	0.178	(0.51, 0.31)
M	3:5	0.549	0.279	0.172	(0.55, 0.28)
N	3:5	0.551	0.279	0.170	(0.55, 0.28)
O	3:5	0.591	0.261	0.148	(0.59, 0.26)
P	1:3	0.314	0.513	0.173	(0.31, 0.51)
Q	1:3	0.352	0.493	0.155	(0.35, 0.49)
R	1:3	0.433	0.424	0.143	(0.43, 0.42)
S	1:3	0.507	0.375	0.118	(0.51, 0.38)
T	1:3	0.549	0.343	0.108	(0.55, 0.34)
U	1:3	0.580	0.315	0.105	(0.58, 0.32)
V	1:3	0.606	0.299	0.095	(0.61, 0.30)
W	1:5	0.319	0.566	0.115	(0.32, 0.57)
X	1:5	0.357	0.531	0.112	(0.36, 0.53)
Y	1:5	0.429	0.475	0.096	(0.43, 0.48)
Z	1:5	0.524	0.394	0.082	(0.52, 0.39)
AA	1:5	0.568	0.359	0.073	(0.57, 0.36)
AB	1:5	0.612	0.323	0.065	(0.61, 0.32)
AC	1:5	0.618	0.321	0.061	(0.62, 0.32)

* where Ni = 1 - Li - Mn

the 1:1 series. This can also be seen in the increasing Li metal mole fraction within each series shown in Table 3.1.

3.3 XRD Analysis of Samples Synthesized at 900°C

The general location of the four end-members, single-phase boundaries, two-phase tie-lines, and three-phase regions can be ascertained when viewing the XRD patterns in order from the first to the last sample of each of the four composition series at each reaction temperature and cooling rate. With the exception of the single-phase layered compositions, the peaks of quenched samples (solid red) typically appear at lower 2θ values than their slow cooled counterparts (dashed blue). Viewing the individual diffraction peaks in the most important 2θ ranges enables the identification of the individual phases present in each composition, as well as the establishment of the various features of the phase diagrams as per the steps outlined for phase diagram development in Section 1.4.2. Therefore, each sample will be presented in a sequence of five scattering angle ranges arranged in panels, rather than showing the entire XRD pattern, to allow for easier presentation of data and discussion of results. Each range/panel will be referred to by number or order (e.g., panel 1 or the first panel). A description of the data typically found in each of the five 2θ ranges, namely the diffraction peaks associated with each hexagonal and/or cubic phase (identified by Miller indices), and the role of such peaks in the phase identification process, is provided below.

The five scattering angle ranges discussed are from 18.0° to 19.5°, 20.0° to 30.0°, 35.0° to 39.0°, 43.0° to 45.0°, and 63.0° to 66.0°. For each XRD plot stack, the pattern at the very top is that of a cubic phase (rocksalt and/or spinel), while the pattern at

the very bottom is that of a hexagonal phase (layered). As such, the peaks of the quenched cubic and hexagonal crystal structures in the very top and very bottom patterns are labelled with Miller indices of the cubic space group Fd-3m and hexagonal space group R-3m, respectively. These labels are shown on each XRD stack for reference, are equally applicable to the slow cooled samples, and aid in comparing the different phases present in each composition.

Each of the five scattering angle ranges provides important information for phase identification. In the 18.0° to 19.5° range, the hexagonal (003) and cubic (111) peaks, typically the most intense for layered and spinel phases, help differentiate between these two crystal structures. The same is true in the 35.0° to 39.0° range for the cubic (311) and (222) peaks, and hexagonal (101), (006), and (012) peaks. The 20.0° to 30.0° range typically contains peaks from two phases. The cubic peak (200) of the ordered rocksalt phase can sometimes be observed, but is often very low in intensity and indistinguishable from the background [30]. By comparison, the more intense monoclinic peaks at (020), (110), (111), and (021) can often be observed, and are associated with TM layer ordering due to the presence of either Li-rich and/or Li-deficient layered materials. The Li-rich materials have superstructure peaks due to 2-D ordering, while the Li-deficient materials have superstructure peaks due to 3-D ordering as found in Li_2MnO_3 . As discussed in Section 1.3.3, the presence of metal site vacancies in Li-deficient materials results in two-thirds of the TM layers containing Mn (as in $\text{Li}[\text{Li}_{1/3}\text{Mn}_{2/3}]\text{O}_2$) which orders on two of the three $\sqrt{3}a$ by $\sqrt{3}a$ lattices [15].

The 43.0° to 45.0° range is very important for differentiating between the four possible phases and/or end-members present in a sample; for this reason, it was scanned with a smaller step size and larger count time as discussed in Section 3.1. The cubic ordered rocksalt and spinel phases both have a (400) peak, while the N- and M-layered

hexagonal phases both have a (104) peak. For quenched samples at 900°C, the R, N, S, and M end-member peaks appear at 43.5°, 43.75°-44.0°, 43.75°-44.0°, and 44.5°, respectively. For slow cooled samples at 900°C, the R, N, S, and M end-member peaks appear at 43.75°, 44.1°, 44.2°, and 44.6°, respectively. The most difficult peaks to resolve are those of the S and N phases of the quenched samples, which experience significant overlap between 43.75° and 44.0°. Careful manual inspection of these peaks was required when differentiating between the two, but conclusive qualitative separation was not always possible. As such, the 63.0° to 66.0° range becomes very important when identifying these structures, as the cubic spinel phase has a single (440) peak, while the hexagonal layered phase has two peaks, (018) and (110).

3.3.1 The 1:1 Composition Series

Figure 3.2 shows the XRD patterns of samples in the 1:1 composition series. The quenched samples will be discussed first. While sample A appears to be predominantly rocksalt, the broadened “tails” seen in the (400) and (440) peaks are due to a small amount of spinel phase. Moving down the composition series from sample A to C, panel 1 shows a gradual decrease in the intensity of the rocksalt (111) peak until a transition into a layered (003) peak takes place in sample D. Panel 3 also shows a decrease in intensity of the cubic (311) and (222) peaks until a switch to hexagonal (101), (006), and (012) peaks occurs. Panel 4 shows a definitive transition from the cubic (400) peak into the layered (104) peak from sample D onward. Finally, panel 5 shows a definitive change from the (440) peak in sample A into overlapping layered peaks in sample D, which finally separate into two peaks, (018) and (110), in sample H. These results indicate that a cubic to layered transition occurs over the range of

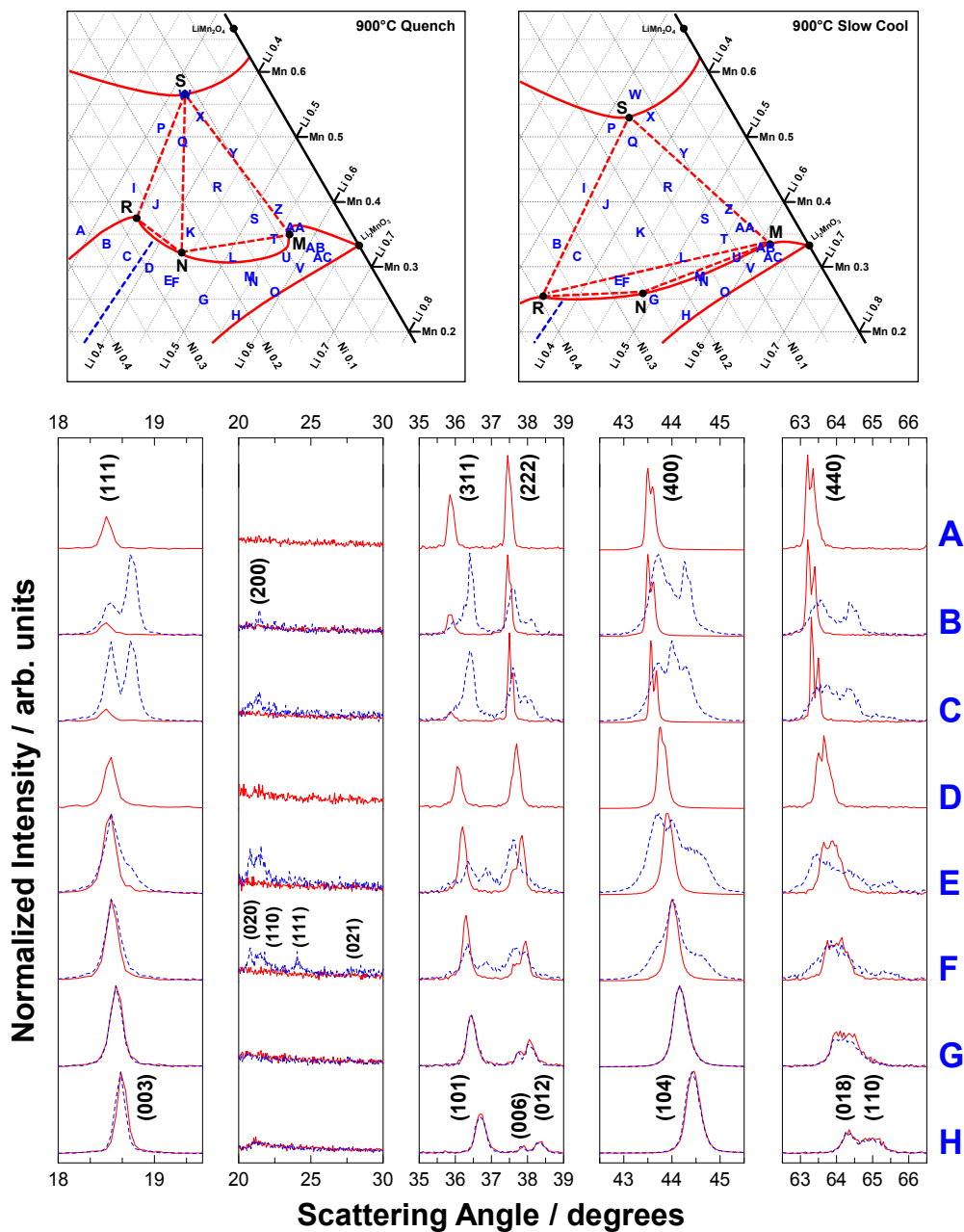


Figure 3.2. XRD patterns of samples in the 1:1 Ni:Mn series that were quenched (solid red) and slow cooled (dashed blue). The labelled phase diagrams are shown for reference.

the 1:1 series. This distinct phase conversion was also observed in the combinatorial phase diagrams at 800°C in O₂ [28], and is confirmed here for the bulk-scale quenched samples at 900°C. The layered peaks continue to shift to higher scattering angles from

sample D to H, indicating a decrease in the size of the hexagonal unit cell as the Li content increases. Panel 2 shows very weak superstructure peaks in sample H, confirming that this composition has some short range 2-D ordering on the TM layer. Overall, these results indicate that the quenched 1:1 composition series starts in a two-phase rocksalt-spinel region, moves into a single-phase rocksalt region, and finally transitions into a single-phase layered region. The phase diagram in Figure 3.1 reflects this, with a single-phase rocksalt boundary drawn between samples A and B, and a cubic to layered transition boundary drawn between samples C and D.

In contrast to the quenched samples, the slow cooled 1:1 composition series is quite different. In sample B, panels 1 through 5 show two sets of cubic peaks due to the presence of both a rocksalt phase and a spinel phase. This indicates that the sample is in a rocksalt-spinel co-existence region. In sample C, a clear change in phase composition is observed in panel 4, as the sample contains peaks due to rocksalt, spinel, and the M-layered phase. Ordering peaks from the M-layered phase are seen in panel 2, as is the M-layered (104) peak in panel 3. Moving down the series, sample E represents the first encounter with a composition that contains four phases, of which there are several throughout the slow cooled phase diagram. This occurred because the slow cooled samples in this region of the phase diagram never reached equilibrium during the cooling step, resulting in the appearance of all four possible phases due to the sample's location between two three-phase coexistence regions [30]. However, the phases present and their peaks do match the end-members found throughout the phase diagram, so the sample is included in the phase diagram analysis while acknowledging the difficulty of its precise placement due to often trace amounts of a fourth phase, typically N-layered. By comparison, sample F contains peaks due to rocksalt, N-layered, and M-layered, as seen in panel 4. This indicates that the sample is in a three-

phase region containing the R, N, and M end-members. Moving down the composition series, samples G and H are both single-phase layered materials. Overall, these results indicate that the slow cooled 1:1 composition series starts in a two-phase rocksalt-spinel region, as did the quenched series, but that it quickly moves into a three-phase region containing R, S, and M phases, then moves into another three-phase region containing R, N, and M phases, before finally returning to a single-phase layered region.

The effect of cooling method on the phase composition of each sample in the 1:1 series is dramatic. Samples which are single-phase when quenched, namely C, E, and F, become multi-phase when slow cooled. This provides the basis for establishing that the single-phase boundary moves depending on the type of cooling used. When the samples are quenched, they are effectively at equilibrium and maintain a large amount of cation disorder due to higher entropy, preferring to form materials with fewer ordered crystalline structures. This results in large single-phase regions and therefore an upper single-phase cubic/layered boundary which is “higher” on the diagram (relative to the position of the Li axis, which is at the “bottom” of the phase diagram). When slow cooling is used, the single-phase regions shrink in size so as to increase order and minimize entropy, forming numerous crystalline phases (such as rocksalt and N-layered in this region of the diagram) in two separate three-phase regions. This results in the upper single-phase cubic/layered boundary being “lower” on the diagram, again relative to the position of the Li axis. The approximate position of the lower single-phase layered boundary in the 1:1 composition series presented here is set by the location of sample H, the composition closest to the Li corner of the ternary diagram within this series. A simple description of this phenomenon is that the single-phase boundary shifts “up” when quenching and shifts “down” when slow cooling. The concept of boundary movement as established here will be referred to in the analysis of the three

remaining Ni:Mn compositions, as will the concepts of two- and three-phase co-existence regions. The problems associated with the R and N-layered phases in terms of electrochemical capability will be discussed in the summary of this chapter.

3.3.2 The 3:5 Composition Series

Figure 3.3 shows the XRD patterns of samples in the 3:5 composition series. Again, the quenched samples will be discussed first. Sample I is a two-phase rocksalt-spinel composite, showing intense rocksalt peaks with broadened tails in panels 4 and 5, again due to a small amount of a spinel phase. Sample J is similar, but its peaks in panels 4 and 5, and panel 1 in particular, begin to broaden more than those of sample I. The decreasing intensity and broadening of the (111) peak in particular indicates the presence of what is most likely the N-layered phase. The difference between these samples indicates that they are in separate phase regions. They also have the same approximate cubic peak positions as samples B and C, with the exception of their broadened shapes. While further study is necessary to determine the exact position of the rocksalt end-member, its position is approximated here to be near samples A, B, I, and J, as reflected in its placement on the phase diagram. Sample K is mostly composed of the N-layered phase, but contains small amounts of R and S, and just a fraction of a Mn-rich layered phase (discerned from its extremely broad peak from 44.0° to 45.75°). This sample, which is unique among the Li-Mn-Ni-O samples studied in this chapter, is important for determining both where and how the quenched and slow cooled phase diagrams differ, and will be discussed in greater detail in Section 3.5. Sample L has a broad (003) peak in panel 1, intense 3-D ordering peaks in panel 2, overlapping layered peaks in panel 3, and two separate peaks in panel 4. In addition,

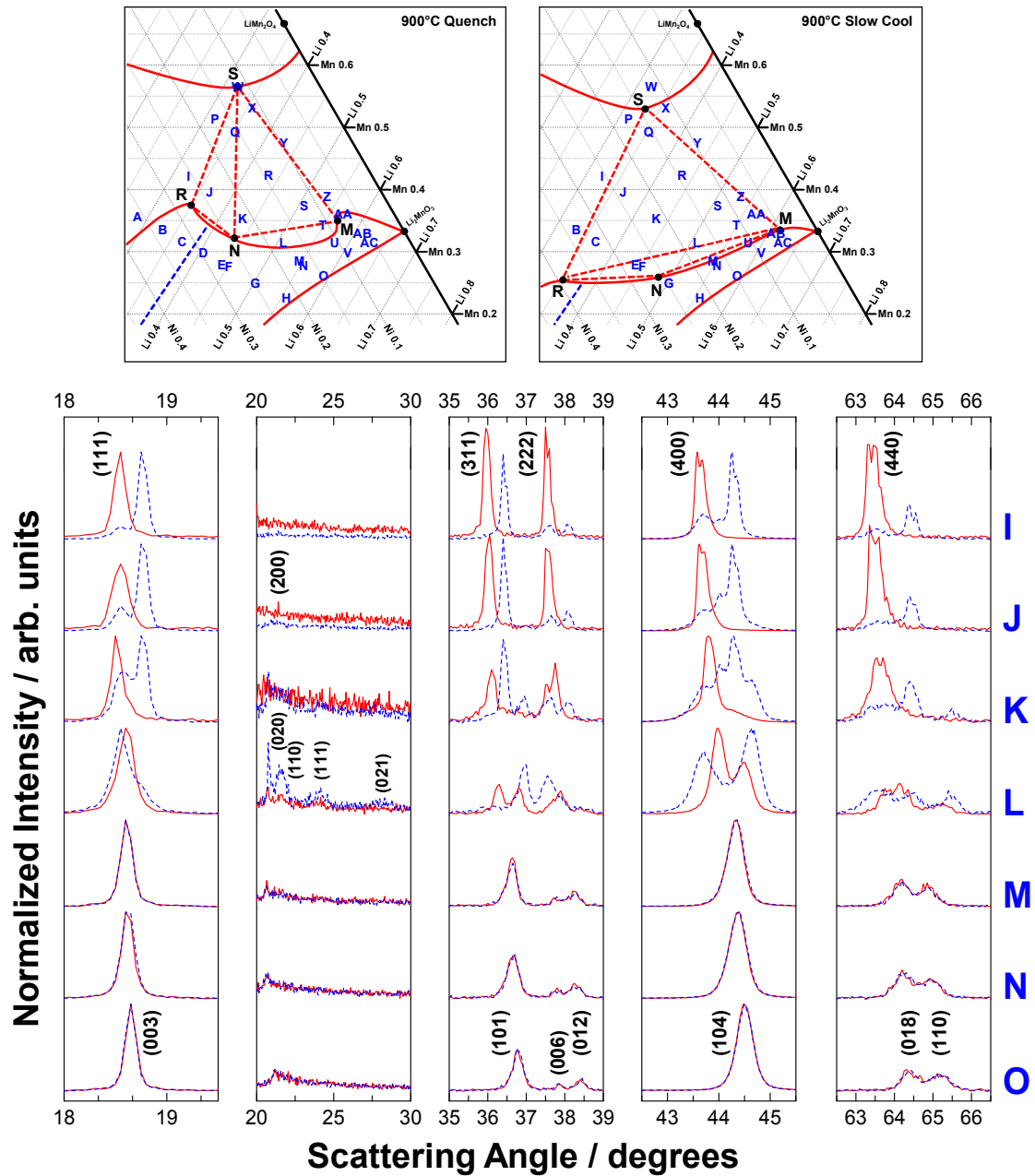


Figure 3.3. XRD patterns of samples in the 3:5 Ni:Mn series that were quenched (solid red) and slow cooled (dashed blue). The labelled phase diagrams are shown for reference.

the position of the first (104) peak in panel 4 does not match any of the four end-members, while the position of the second (104) peak is close to 44.5° . These results indicate that this material is a unique two-phase layered-layered composition. A region

containing such layered-layered composites has been identified in the phase diagrams at 800°C in O₂, and is confirmed here for the quenched 900°C samples.

Moving down from sample L, samples M, N, and O are all single-phase layered according to their peak positions in panels 1 to 5. These three samples contain short-range ordering in the TM layer, as indicated by the broad and weak 2-D ordering peaks in panel 2. Overall, the results suggest that the quenched 3:5 composition series covers five separate phase regions. The series starts in a two-phase rocksalt-spinel region, moves through one three-phase co-existence region of N-R-S phases, then through a second three-phase coexistence region of M-N-S phases, followed by a two-phase layered-layered region before ending in a single-phase layered region. Combined with the information from the quenched 1:1 series, this allows for the establishment of the approximate location of the R and N phases, as well as the tie-line that joins them. In addition, sample L establishes the existence of a two-phase layered-layered region containing layered samples which have different layered lattice constants than the N and M phases. It will be shown in Section 3.8 that this region is crescent-shaped, bounded by the N-M tie-line and the upper boundary of the single-phase region.

The slow cooled 3:5 composition series is similar to the quenched series at the beginning and end, but varies considerably in the middle. Sample I is again two-phase rocksalt-spinel, with the spinel peaks being of higher intensity. Sample J contains peaks from the R, N, S, and M phases, as seen in panel 4. Sample K contains four phases as it did when quenched, as both samples did not reach equilibrium when cooling by either method. However, the presence of sharp ordering peaks in panel 2 suggests that the dominant layered phase is M, not N. For sample L, panels 1 and 4 indicate that it is a two phase rocksalt-layered composite, with the sharp and intense or-

dering peaks in panel 2 confirming the layered phase as M. This indicates that this composition sits on or near the R-M tie-line. Moving down the series, the compositions M, N, and O are all once again single-phase layered as they were with the quenched samples.

Again, the effect of cooling method on the phase composition in the 3:5 series is dramatic. Sample I and samples M through O in both the quenched and slow cooled series are in two-phase rocksalt-spinel and single-phase layered regions, respectively. For samples J to L, the quenched series moves from a three-phase N-R-S region to a three-phase M-N-S region, then into a two-phase layered-layered region. This region may contain some of the M-layered phase, but the identity of the second layered phase is unknown. The upper single-phase layered boundary begins near sample M, while the lower single-phase boundary ends near sample O, as shown. By contrast, samples J and K of the slow cooled series are both four-phase, indicating that they are located in the M-R-S coexistence region, while sample L establishes the approximate location of the R-M tie-line. While the single-phase layered boundary moves somewhat downward when comparing quenched and slow cooled samples, the difference between the coexistence regions that form is the most significant finding in this region. Sample K is of particular importance, as it is located near the N-phase in the M-N-S region of the quenched diagram, and near the centre of the M-R-S region of the slow cooled diagram.

3.3.3 The 1:3 Composition Series

Figure 3.4 shows the XRD patterns of samples in the 1:3 composition series. The quenched series will be discussed first. Sample P is predominantly single-phase spinel,

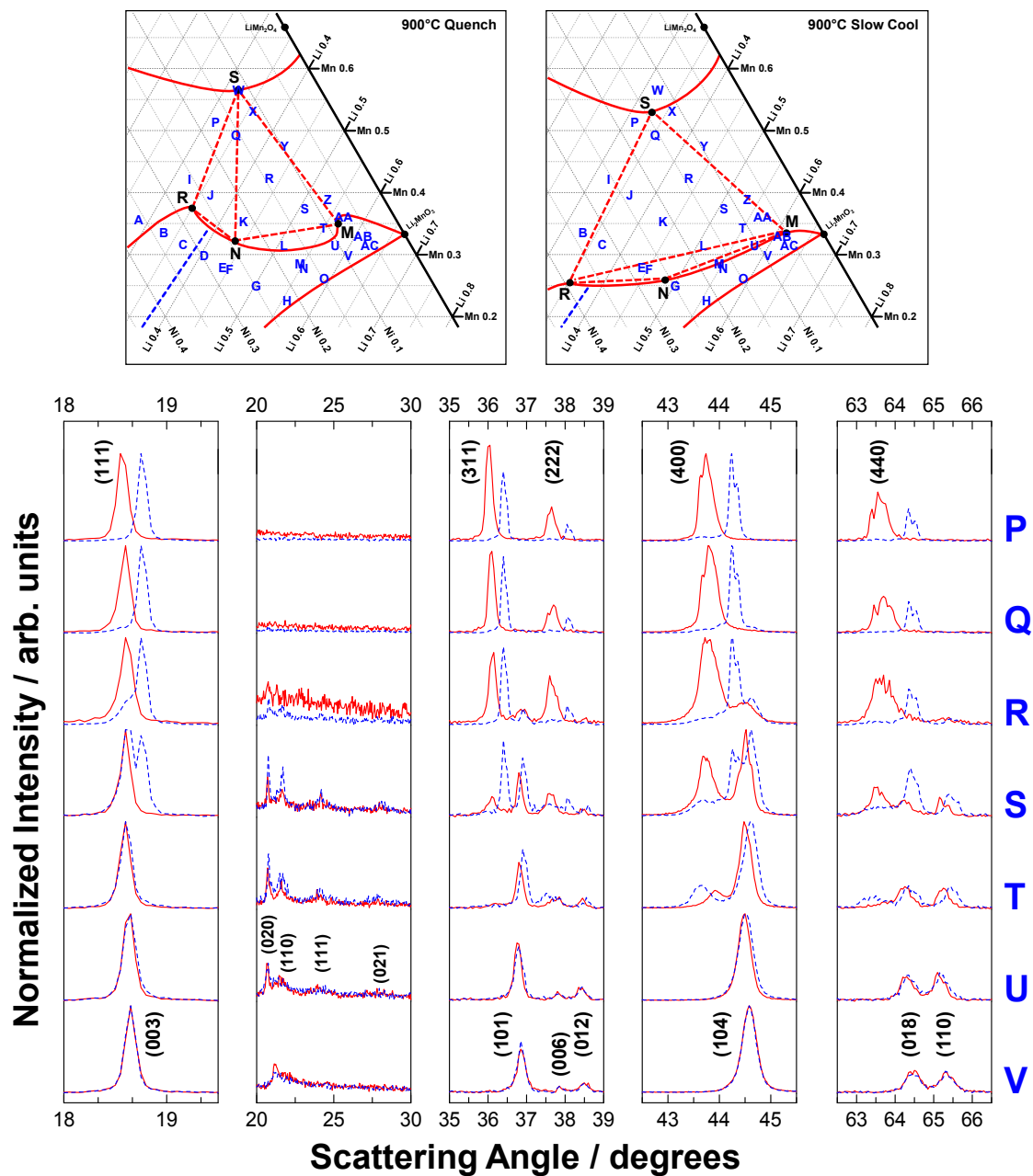


Figure 3.4. XRD patterns of samples in the 1:3 Ni:Mn series that were quenched (solid red) and slow cooled (dashed blue). The labelled phase diagrams are shown for reference.

showing cubic peaks in all five ranges, but contains some rocksalt seen in the shoulder of the peak in panel 4. In sample Q, the spinel is again the main phase, but the slight broadening at the beginning of the (111) peak and the tail ends of the (400) and (440)

peaks suggest that a small amount of rocksalt and layered phases are present. The broadening of the tail end of the (440) occurs at the same position as the overlapping (018)/(110) peak of sample K, which is very close to the N-layered phase. Thus, sample Q is located close to the S-N tie-line just inside in the N-R-S region. Sample R and sample S are squarely in the M-N-S coexistence region, showing broadened, overlapping peaks of N-phase and S-phase, in combination with a separate M-layered peak at 44.5° . The M-layered phase increases in intensity from sample R to sample S, as shown by the increasing intensity and sharp superstructure peaks in panel 2 and increasing intensity of the (104) peak in panel 4. Sample T shows two peaks in panel 4: one at approximately 43.9° , corresponding to a composition likely located near the N-phase on the single-phase layered boundary, and the other at 44.5° , corresponding to the M phase. The presence of the M-phase is further supported by strong ordering peaks in panel 2. This establishes that sample T is near or on the N-M tie-line. Samples U and V are both single-phase layered compositions, and help establish the upper and lower limits of the single-phase layered boundary in this region of the phase diagram.

Figure 3.5(a) shows total pattern and component phase fits of samples P, R, T, and V from the 1:3 composition series. The XRD patterns are well fitted by the component phases of each composition, as highlighted by the fits of each phase shown in the 43° to 45° range. The fit of the most complex sample in the series, sample R, is highlighted in Figure 3.5(b) to demonstrate the versatility of the fitting routine given multiple phases to fit which exhibit significant peak overlap.

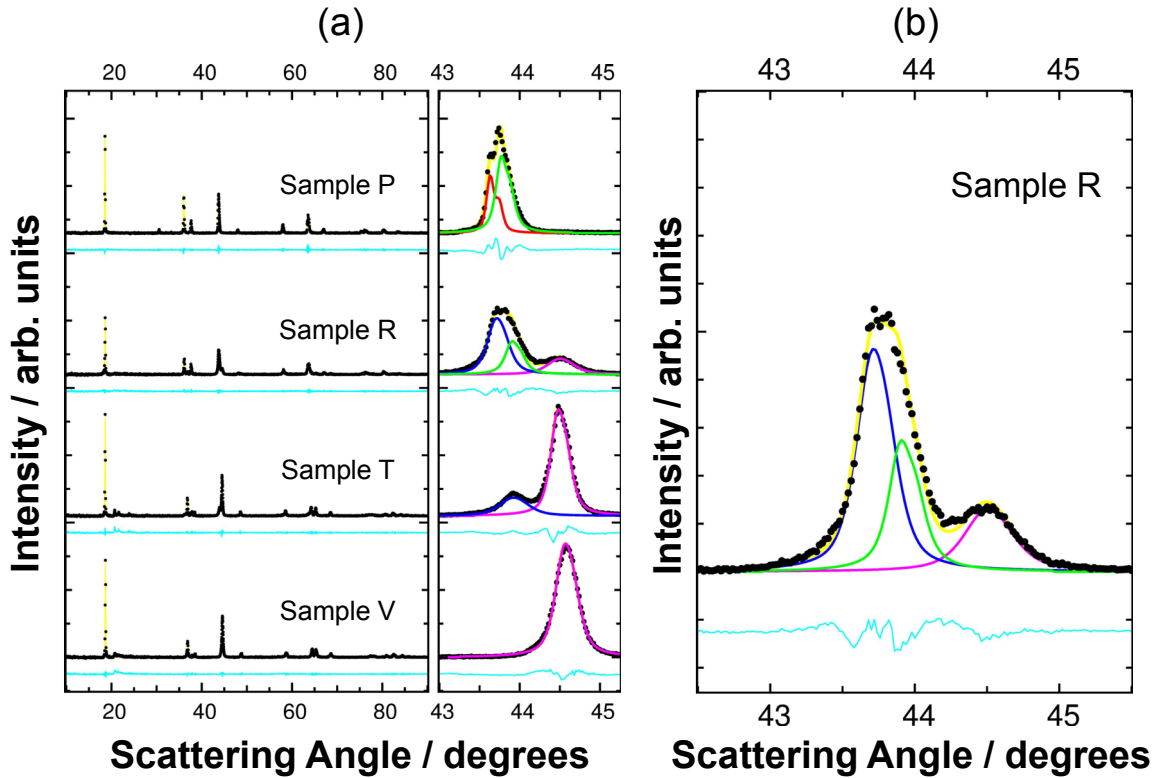


Figure 3.5. (a) Total XRD pattern fits from 10° to 90° and component phase fits from 43° to 45° of samples P, R, T, and V, all quenched at 900°C . (b) Magnified component phase fits of sample R from 43° to 45° . The individual phase fits are shown in red (ordered rocksalt), blue (N-layered), green (spinel), and purple (M-layered). Total fits are shown in yellow, and difference plots are shown in aqua.

The slow cooled 1:3 composition series begins in the two-phase rocksalt-spinel region at sample P, with the spinel phase dominating; a trace amount of the rocksalt phase is shown by the broad, flat peak at 43.75° in panel 4. Samples Q through S all contain four phases in variable amounts. Sample Q is barely inside the three-phase M-R-S region, with the S-phase being dominant, while sample R and sample S show marked increases in the intensities of the superstructure ordering peaks and the (104) peaks of the M-layered phase, indicating that they are increasingly closer to the M

end-member. In sample T, two clearly separated peaks are again seen, as was the case for sample L, indicating that it is also a two-phase rocksalt-layered composite which lies on or near the R-M tie-line. Finally, samples U and V are both single-phase layered compositions which help establish the upper and lower locations of the single-phase boundary in this region.

The effect of cooling method on the phase composition is again significant. Sample P is in a two-phase rocksalt-spinel region, while samples U and V are in single-phase layered regions in both quenched and slow cooled samples. The N-S and M-N tie-lines in the quenched series are partially established by samples Q and T, respectively, while their slow cooled counterparts are in the M-R-S coexistence region. Finally, the quenched sample R and sample S are in the M-N-S three-phase region, while their slow cooled counterparts are in the M-R-S three-phase region. Overall, the effect of cooling rate in this composition series is observed in the difference between the quenched M-N-S region and the slow cooled M-R-S region. The upper boundary of the single-phase layered region barely moves downward when slow cooling, indicating that the boundary is relatively fixed in place in this region regardless of cooling rate.

3.3.4 The 1:5 Composition Series

Figure 3.6 shows the XRD patterns of samples in the 1:5 composition series. The quenched samples will again be discussed first. Sample W is a single-phase spinel material, containing individual cubic peaks in panels 1 through 5. Samples X through Z contain both a spinel and layered phase, and show a clear transition from spinel to layered when moving down the series via the decrease in intensity of the spinel peaks and increase in intensity of the layered peaks, namely the (003) and (104) peaks. The

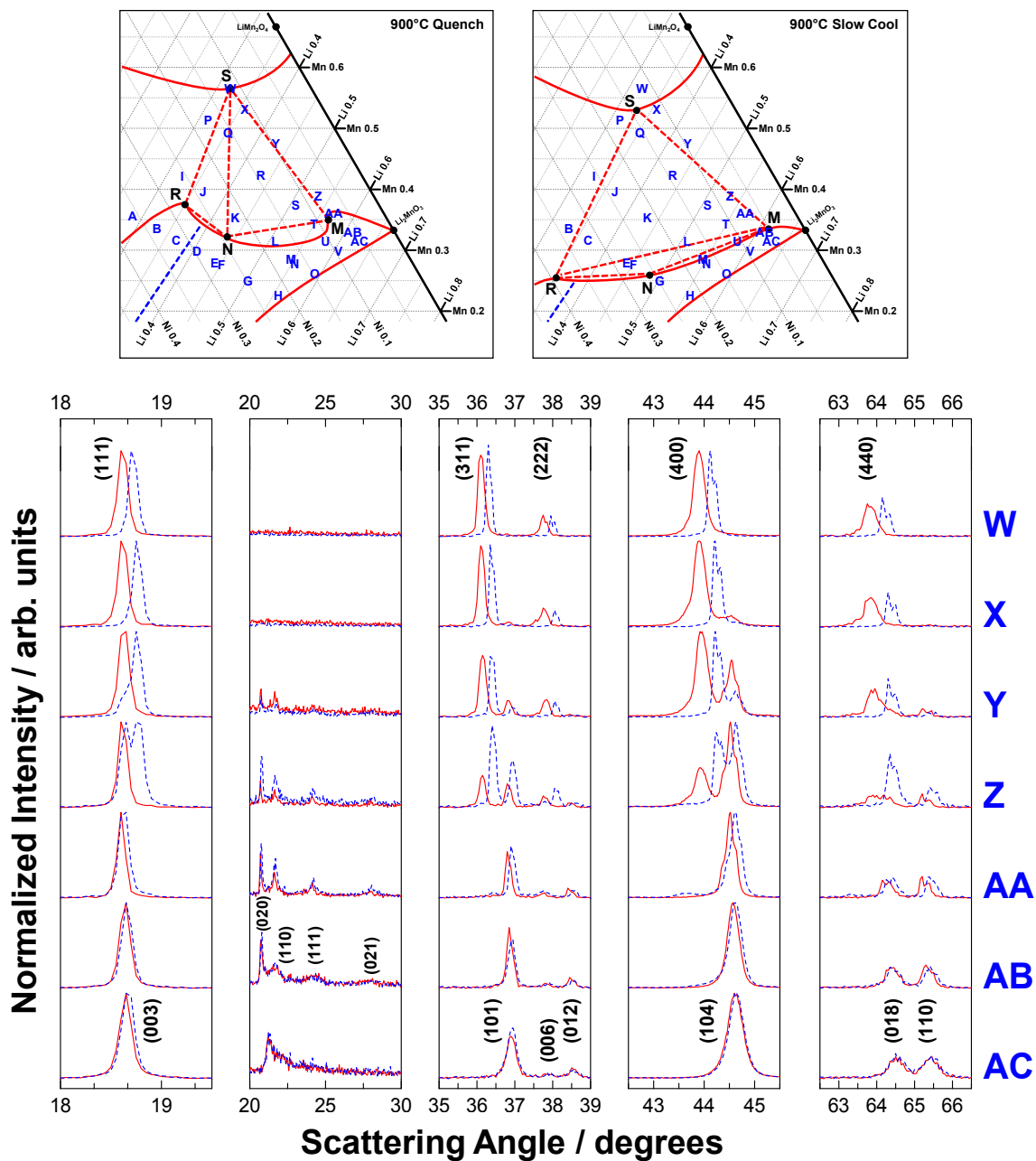


Figure 3.6. XRD patterns of samples in the 1:5 Ni:Mn series that were quenched (solid red) and slow cooled (dashed blue). The labelled phase diagrams are shown for reference.

superstructure ordering peaks also increase in sharpness and intensity towards sample Z. Therefore, samples X, Y, and Z are all approximately located on the R-M tie-line.

Sample AA represents the movement into a single-phase region, as the diffraction pattern exhibits peaks corresponding to a single hexagonal phase in panels 1, 3, 4, and 5. However, the (104) layered peak is observed to be distorted relative to the symmetric (104) peaks typically seen in other layered materials. In addition, very sharp and intense ordering peaks are observed in panel 2, indicating a very well-defined superstructure on the TM layer. These two features highlight sample AA as a unique composition within the Li-Mn-Ni-O phase diagram, as it marks the top of the single-phase layered boundary, the approximate location of the M-layered phase, and the beginning of a region of structurally distinct materials.

As discussed in Section 1.3.3, recent theoretical and experimental studies have indicated that materials in this region contain monoclinic distortions in the hexagonal lattice due to metal site vacancies on the TM layer [15]. When present in sufficient quantities, the vacancies allow Mn to order on two $\sqrt{3}a$ by $\sqrt{3}a$ lattices, as discussed at the beginning of Section 3.3, producing materials that are essentially vacancy containing, Ni-rich analogues of the monoclinic phase Li_2MnO_3 . The replacement of two Li^+ ions by a Ni^{2+} ion and a vacancy in $\text{Li}[\text{Li}_{1/3}\text{Mn}_{2/3}]\text{O}_2$ produces the solid solution series $\text{Li}[\text{Li}_{(1/3)-x}\text{Ni}_{x/2}\square_{x/2}\text{Mn}_{2/3}]\text{O}_2$ for $0 < x < 1/3$. Compositions in this solid solution series are defined as being “Li-deficient”, as they contain less Li relative to their stoichiometric counterparts with the same Ni:Mn ratio in the Li-rich oxide solid solutions series $\text{Li}[\text{Ni}_x\text{Li}_{(1/3-2x/3)}\text{Mn}_{(2/3-x/3)}]\text{O}_2$ for $0 < x < 1/2$. Overall, due to their monoclinic features and their proximity to Li_2MnO_3 on the phase diagram, materials on and partly inside the single-phase boundary of this region, collectively coined as the “bump” region due to the shape of the boundary itself, can be fit as single-phase monoclinic structures with reasonable accuracy. A more in-depth structural analysis of sample AA is presented in Section 3.5.4. Additionally, Chapter 4 focuses on the thorough structural and

electrochemical evaluation of five compositions in or near this unique “bump” region of the phase diagram (as discussed in Section 1.4.3), with one of the materials from this analysis becoming the primary focus of the UHPC study presented in Chapter 6. Moving from sample AA to AB indicates that the size of the bump region is relatively small, as sample AB contains no monoclinic distortion of the (104) peak as well as broader, less intense ordering peaks. Finally, sample AC is a single-phase layered material with 2-D short-range ordering peaks more characteristic of Li-rich materials than of the sharp 3-D ordering peaks in the Li-deficient compositions. This sample also represents the lower limit of the single-phase layered boundary in this region of the phase diagram within the range of samples studied.

The slow cooled 1:5 composition series begins distinctly in a single-phase spinel region, as shown by the cubic peaks in the XRD pattern of sample W. Sample X is primarily composed of the S end-member, but shows the emergence of a layered phase as indicated by the small peak at 44.6° in panel 4. The peaks from this phase increase in intensity when moving from sample X to AA, with a simultaneous decrease in the intensity of the spinel peaks. These features help establish the approximate locations of the S end-member, the M end-member, and the R-M tie-line that joins them. The superstructure and (104) peaks of samples Z and AA indicate that these compositions are also monoclinically distorted due to the presence of metal site vacancies and 3-D ordering within the lattice, though less so than their quenched counterparts. Samples AB and AC indicate a return to a single-phase layered region, as indicated by broader ordering peaks and undistorted hexagonal (104) peaks. Sample AB helps mark the upper limit of the single-phase layered boundary, while sample AC helps mark the lower limit of the boundary in this region of the slow cooled phase diagram within the range of samples studied.

3.3.5 Summary of XRD Analysis of Samples at 900°C

The combined XRD analysis of each composition series resulted in a detailed phase-mapping of the Li-Mn-Ni-O diagram within the range of the samples studied. The consolidation of this analysis into a phase diagram is achieved via a piece-by-piece estimation of the positions of the four end-member phases, the tie-lines that join them, the two- and three-phase regions that form between the tie-lines, and the relative shape and location of the single-phase cubic and layered boundaries for both the quenched and slow cooled samples. This analysis is presented in Section 3.6 in conjunction with lattice constant analysis from XRD refinement, and will show how the final phase diagrams are constructed for bulk samples at 900°C.

3.4 XRD Analysis of Samples Synthesized at 800°C in Air

Bulk samples were also prepared at 800°C in air in order to provide an understanding of how a lower synthesis temperature impacts the resultant phases in the Li-Mn-Ni-O materials of the positive electrode region relative to the samples at 900°C in air. These samples were also used to confirm that the results of the phase diagrams produced for milligram-scale combinatorial samples at 800°C in O₂ were applicable to bulk-scale samples synthesized under more practical synthetic conditions, such as those of gram-scale samples in air. By comparison, the peaks of the four end-member compositions in the 800°C in air appear at almost the same scattering angle values as the combinatorial samples at 800°C in O₂. For the quenched samples, the approximate peak positions of the R, N, S, and M end-members are 43.75°, 44.0°, 44.2°, and 44.55°, respectively, while those of the slow cooled end-members are 43.75°, 44.0°, 44.35°, and

44.6°, respectively. Again, these peak positions help identify which phases form in the samples at each of the two different cooling rates.

Fewer samples were used to establish the 800°C phase diagrams, equal to about two-thirds the number of samples used to generate the 900°C phase diagrams. As such, the analysis and placement of end-members, tie-lines, coexistence regions, and boundaries in these phase diagrams required more estimation than those of the 900°C samples. As will be shown, the 800°C sample patterns generally contain broader XRD peaks than their 900°C equivalents due to the smaller crystallites which form at the lower reaction temperature. This also results in significant overlap of many of the individual diffraction peaks found in each of the five 2θ ranges, making their deconvolution quite difficult. In order to simplify the presentation of the XRD analysis of the 800°C samples, only data from the most important 2θ range, 43.0° to 45.0°, will be presented and discussed here. However, the same overall methodology used to analyze the 900°C samples was also applied to the 800°C sample analysis, again with the caveat that the lower number of samples resulted in more estimation being used when elucidating the specific features of each phase region in the phase diagrams. Figure 3.7 shows the XRD peaks from 43.0° to 45.0° of each sample within the four compositions series studied. Each sample letter corresponds to the same sample label and (Li, Mn) coordinates shown in Table 3.1.

3.4.1 Quenched Samples

Starting with the quenched 1:1 series in the first panel of Figure 3.7, sample B contains two cubic phases, a rocksalt and a spinel, as determined by their peak positions. This indicates that this composition is in a two-phase region. It also provides evidence

that the single-phase cubic boundary is lower at 800°C than at 900°C, as sample B at 900° is single-phase rocksalt. Sample C is a three-phase composition containing primarily R but with low amounts of N and S, indicating it is in the N-R-S coexistence region. Samples E through G are all single-phase layered materials, and help mark the upper and lower limits of the layered boundary within the range of samples studied in this series.

In the 3:5 composition series, sample I begins with separate cubic peaks of equal height, while sample J has a less intense spinel peak compared to the rocksalt peak. These results indicate that both samples are very close to the R-S tie-line, with sample I likely closer to the S end-member and sample J closer to the R end-member. Sample K contains a broad asymmetric peak composed mainly of the N phase at approximately 43.9° to 44.0°, with the broadening at the tail end most likely due to the M and S phases. This indicates that sample K is in the three-phase M-N-S region. Sample L displays two peaks at 44.0° and 44.5°, respectively, indicating that it is a two-phase layered-layered composite located on or near the N-M tie-line. Finally, sample M contains a very broad peak ranging from 43.75° to 45.0° that resembles the (104) peak of a layered structure, thus marking it as being in the single-phase layered region.

The 1:3 composition series starts with sample P, which shows a small rocksalt peak and a large spinel peak, indicating that it is located closer to the S phase and that it is on or near the R-S tie-line. Moving to sample Q, a large spinel peak is observed with two weaker broadening peaks on either end of the peak, indicating the presence of small amounts of N and M. This suggests that the composition is located just inside the three-phase M-N-S region. This trend continues in sample S, where the M-layered clearly emerges at 44.5° and increases in intensity at the expense of the N-layered peak

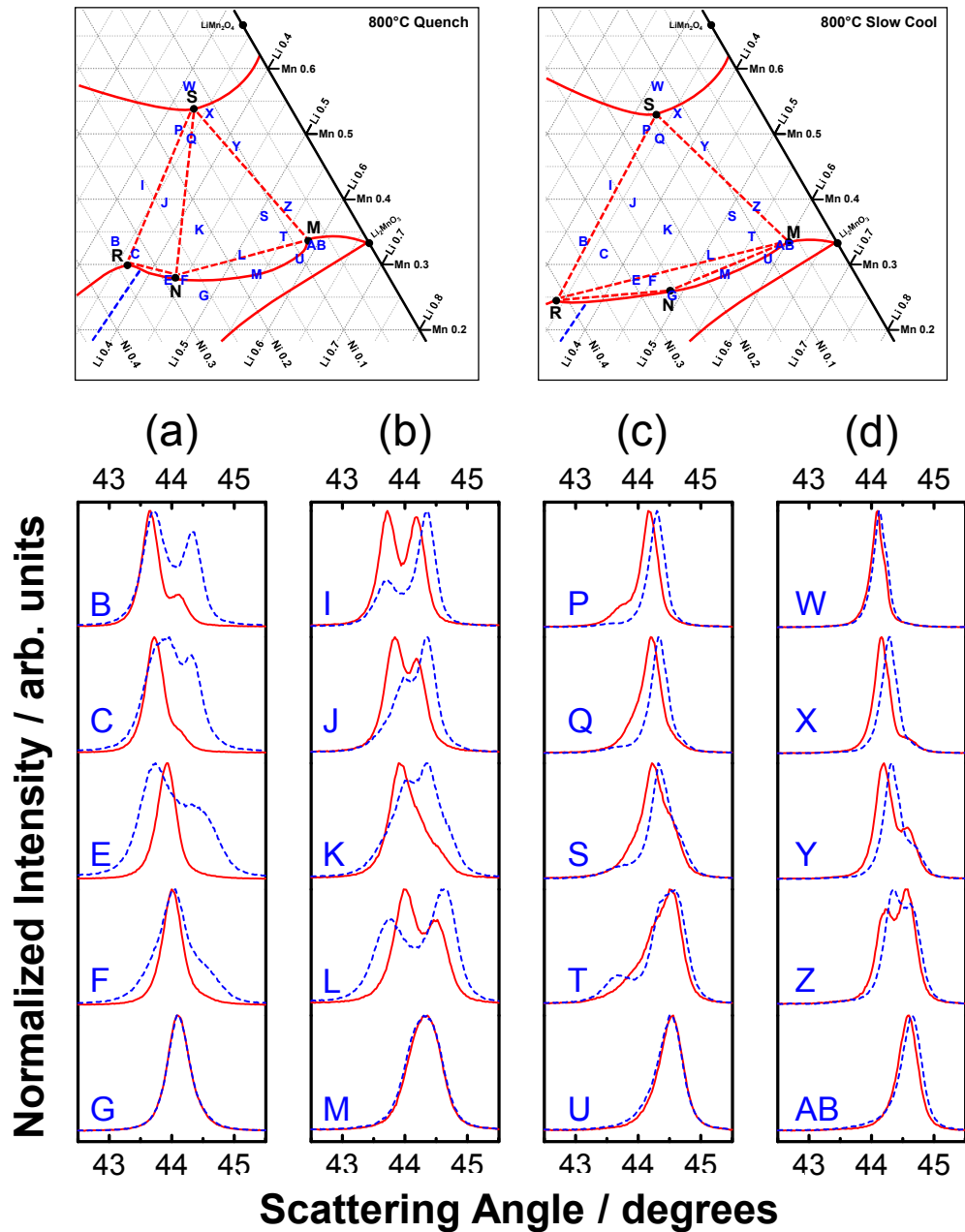


Figure 3.7. XRD patterns of samples at 800°C in air that were quenched (solid red) and slow cooled (dashed blue) within the following series: (a) 1:1, (b) 3:5, (c) 1:3, and (d) 1:5. The labelled phase diagrams are shown for reference.

at 44.0°. By sample T, the M-layered peak is dominant, and is broadened by the diminishing peaks of the N and S phases. Finally, sample U is single-phase layered.

Sample W of the 1:5 composition series is a single-phase spinel material, and is very close to the S end-member and spinel boundary. In samples X through Z, the spinel peaks continually decrease in intensity with a simultaneous increase in intensity of the M-layered phase (104) peak. This indicates that these materials are on or just to the right of the S-M tie-line. Finally, sample AB is a single-phase layered composition. Overall, moving from sample B to W across the top XRD patterns, the intensity of the rocksalt peaks decreased while those of the spinel phase increase, eventually becoming 100% spinel at sample W. This indicates that these four samples are all approximately on or near the R-S tie-line in regular increments. Moving across samples C through X indicates a transition from N-R-S to M-N-S and finally into the spinel-layered co-existence region near the S-M tie-line. Samples S and T confirm the extension of the M-N-S region towards the ends of the 1:3 and 1:5 series, while the 1:5 series helps identify the approximate locations of the S and M end-members, as well as the tie-line joining them.

3.4.2 Slow Cooled Samples

The slow cooled phase diagram at 800°C is again different than that of the quenched diagram. The 1:1 series begins with almost equal parts R- and S-phases in sample B, indicating it is on or near the R-S tie-line. Sample C shows multiple peaks with significant overlap over the entire four-peak range from 43.75° to almost 44.6°, indicating the presence of three to four phases. As was the case with the 900°C slow cooled diagram in Figure 3.1, this composition is identified as not having reached equilibrium during cooling. As such, it is best described by including it in the three-phase M-R-S region. Samples E and F both fall within the M-N-R three-phase region, with

sample E being closer to the R-M tie-line due to its more intense R and M peaks, and sample F much closer to the N end-member due to the high intensity of the (104) peak at 44.0°. Finally, sample G is once again a layered structure in the single-phase region.

The slow cooled 3:5 composition series begins at sample I, which is again a two-phase rocksalt-spinel composite. There is more spinel than rocksalt, indicating that the sample is closer to the S end-member. Samples J and K both show multiple overlapping peaks in the 43.75° to 44.6° range, again indicating the presence of the four end-member phases. The spinel phase in sample J is the most intense peak, while both the N-layered and spinel phase peaks in sample K are strong. This reflects the location of each composition within the M-R-S coexistence region, as sample J is closer to S and the R-S tie-line, while sample K is near the middle of the region, resulting in more N-layered due to non-equilibrium conditions. Moving down the series to sample L shows the rocksalt and M-layered phases in co-existence, indicating that this composition is on or near the R-M tie-line. Sample M is a single-phase layered composition with a broad (104) peak. The peak shape suggests that the composition is on or very close to the single-phase boundary, and that its proximity to the previously discussed layered-layered composite region accounts for the relatively broad peak.

The 1:3 composition series is similar to the 3:5 series in that it begins in a two-phase rocksalt-spinel region, this time being almost entirely spinel with only a small, broad rocksalt peak. The same observation is made for sample Q. This indicates that the S end-member is very close to these compositions, which are on or near the end of the R-S tie-line. Sample S shows peaks of the R-, S-, and M-phases, placing it squarely in the three-phase region. Sample T contains a stronger rocksalt peak and overlapping S and M peaks, marking it as being close to the R-M tie-line in the corner of the M-R-

S coexistence region. The series ends with sample U, which is once again a single-phase layered material.

Finally, sample W begins the slow cooled 1:5 composition series entirely within the single-phase spinel region, and helps to determine the approximate location of the S end-member. Samples X through Z show a trend of decreasing spinel peaks with a simultaneous increase in the M-layered peak. It should be noted that each spinel peak is at a slightly different diffraction angle, indicating that these materials do not directly lie on the S-M tie-line, but rather in a series of individual spinel-layered tie-lines which move in parallel relative to the S-M tie-line [30]. Finally, sample AB returns to the single-phase layered region, providing the approximate location of the M-layered phase.

3.4.3 Summary of XRD Analysis of Samples at 800°C

As is the case for the 900°C samples, the cooling method used for the 800°C samples had a major impact on the resultant phases that form. The conversion from two three-phase regions when quenching to one larger M-R-S region and a smaller M-N-R region when slow cooling was again observed. The downward movement of the single-phase boundary when slow cooling was most pronounced in the 1:1 series, namely at sample B, which is single-phase rocksalt when quenched and two-phase rocksalt-spinel when slow cooled. Overall, the trends in the phase diagrams at 800°C were generally the same as those of the 900°C diagrams, with comparatively smaller single-phase cubic/layered regions for the respective cooling rates. The final assembly of the phase diagrams at 800°C will be discussed in Section 3.8.

3.5 Analysis of Unique 900°C Quenched Compositions

Analysis of the 900°C sample XRD plots has led to the confirmation of several unique features and compositions also found within the combinatorial phase diagrams which are important for accurately mapping the Li-Mn-Ni-O phase space. Chief among these are the cubic to layered transition in the single-phase region of the 1:1 series, the quenching of sample K in the 3:5 series, the unexpectedly large lattice constant of the single-phase spinel near sample W in the 1:5 series, and the monoclinically distorted “bump” in the single-phase layered boundary at sample AA of the 1:5 series. Each of these will be characterized and discussed in the following sections.

3.5.1 Cubic to Layered Phase Transition

Figure 3.8 shows the lattice parameters of the quenched 1:1 composition series for all samples fit as single-phase hexagonal layered phases plotted as a function of their Li metal mole fraction. Even though samples A to C have previously been established as being composed of only cubic structures, fitting them as hexagonal layered phases and comparing their lattice constants to those of the remaining layered materials in the series clearly illustrates the cubic to layered conversion and establishes the transition boundary in the phase diagrams. Therefore, the a and c lattice parameters of these samples, as well as the c/a ratio, are all plotted as a function of their Li metal mole fractions. As the amount of Li increases from samples A to C, a and c decrease proportionally to one another, which is reflected in a constant c/a ratio for all three samples. The value of c/a for these three samples is equal to $24^{1/2}$, which is the ratio exhibited by cubic structures that are fit as hexagonal structures [52]. This value is indicated by the dashed line in the top panel of Figure 3.8, and confirms that samples

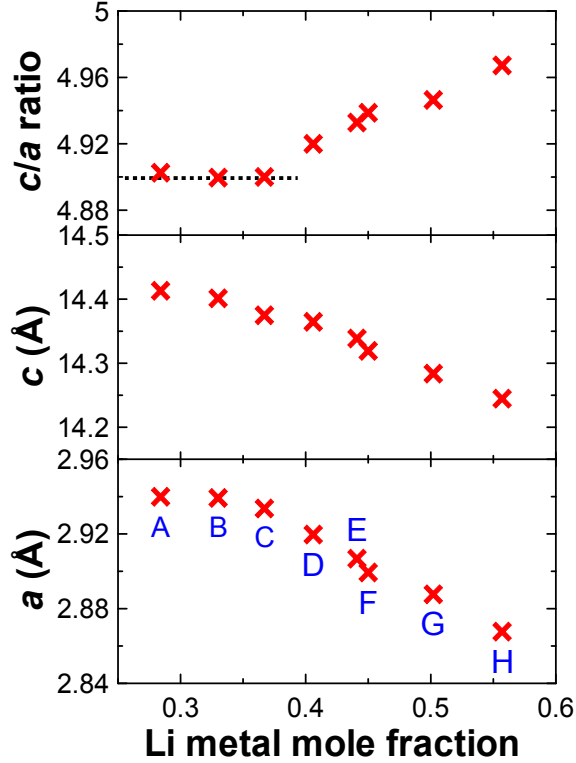


Figure 3.8. Lattice parameters of single-phase layered fits of samples A to H (left to right) in the quenched 1:1 series versus the Li metal mole fraction of each sample. The cubic to hexagonal transition at $\sqrt{24} c/a$ is indicated by the dashed line in the top panel.

A to C are indeed cubic structures. This result is further supported by the same observation in the phase diagrams at 800°C in O₂, in which three separate series with constant Mn contents and incrementally increasing Li contents exhibited the same cubic to layered transformation [16]. Starting at sample D, the c/a ratio begins to increase in a linear fashion throughout the remaining samples in the composition series, indicating that these samples are all indeed single-phase layered materials.

Thus, the cubic to layered transition is established as occurring between samples C and D, and is drawn as the dashed blue line between them in the phase diagram at 900°C in air in Figure 3.1, terminating on the single-phase boundary itself at the top and at LiNiO₂ on the Li-Ni line at the bottom of the diagram. While this transition is

only observable for the quenched samples at 900°C due to the range of examples explored in this thesis, it has been confirmed as existing for slow cooled samples at 800°C in O₂, and is therefore included on all phase diagrams shown in this thesis, at the same location at which it has been found for the quenched samples. Thus it is acknowledged that the placement of this transitional boundary on the remaining phase diagrams serves only as a reasonable approximation subject to further investigation.

3.5.2 Location of Sample K in Multi-phase Regions

Within the range of the bulk samples studied, sample K is the closest composition to representing a “switch-point” between the two-phase diagrams. Rhines et al. discusses the existence of a ternary four-phase equilibrium region that often exists between two three-phase regions during the cooling phase of solid samples [53]. A sample within this region would be able to “switch” back and forth between the two-phase diagrams when heated and cooled at the appropriate rate. This concept can be applied to the four end-members and the three-phase regions which they bound in the Li-Mn-Ni-O system under the cooling conditions studied. The existence of such a point was demonstrated for bulk samples prepared in O₂ at 800°C [28]. The switch-point was demonstrated to exhibit reversible switching from the quenched three-phase region M-N-S to the slow cooled M-R-S triangle after being reheated and slowly cooled. It is therefore possible that a similar ternary four-phase equilibrium exists during slow cooling of the bulk compositions at 900°C in air. The impact of cooling rate on the phases that form at sample K indicate that this is indeed the case.

Figure 3.9 shows the component phase fits of the XRD patterns in the 43.0° to 45.0° range at composition K for samples that were liquid nitrogen quenched (LNQ),

copper plate quenched (CPQ), and slow cooled (SC). The crystalline phase(s) “locked in” within the LNQ sample indicate the phase(s) that form at equilibrium relative to the solid-state reaction conditions of 900°C and 20% O₂ partial pressure (atmospheric pressure in air). As observed by the intense (104) peak, N-layered is the dominant phase. Once the comparatively slower copper plate quenching was employed, however, the material became four-phase, exhibiting peaks from all four end-members, with the N-layered phase remaining the most intense, flanked by R-phase on the left and a broad overlapping peaks of layered and spinel phases on the right. These last two phases do not correspond to the S and M end-members (see Table 3.2 in Section 3.6). It is therefore believed that the sample is only stable at 900°C, and that even the small amount of time required to remove it from the oven and transfer it to the N_{2(l)} bath (approximately 5-10 seconds) is sufficient time for the sample to move out of equilibrium and begin converting rapidly. This has been shown to be especially true of the rocksalt phase, as was determined in the aforementioned bulk sample study at 800°C [30]. This phase forms more rapidly than the quenching process can match, preventing the true equilibrium structure at room temperature from being “locked in”.

Such instability is believed to be due to non-equilibrium conditions within the sample, which appears to be predominantly N-layered in LNQ, but which rapidly begins converting to the three remaining phases for CPQ. Moving to the slow cooled sample K, the material never reaches equilibrium, as seen clearly in the four distinct peaks of R, N, S and M. From left to right, it can be interpreted that as the cooling rate is lowered, the R, S, and M phases develop at the expense of the N phase, the (104) peak of which gradually decreases in intensity. The strong spinel peak in the slow cooled sample indicates that the sample is located in the three-phase M-R-S re-

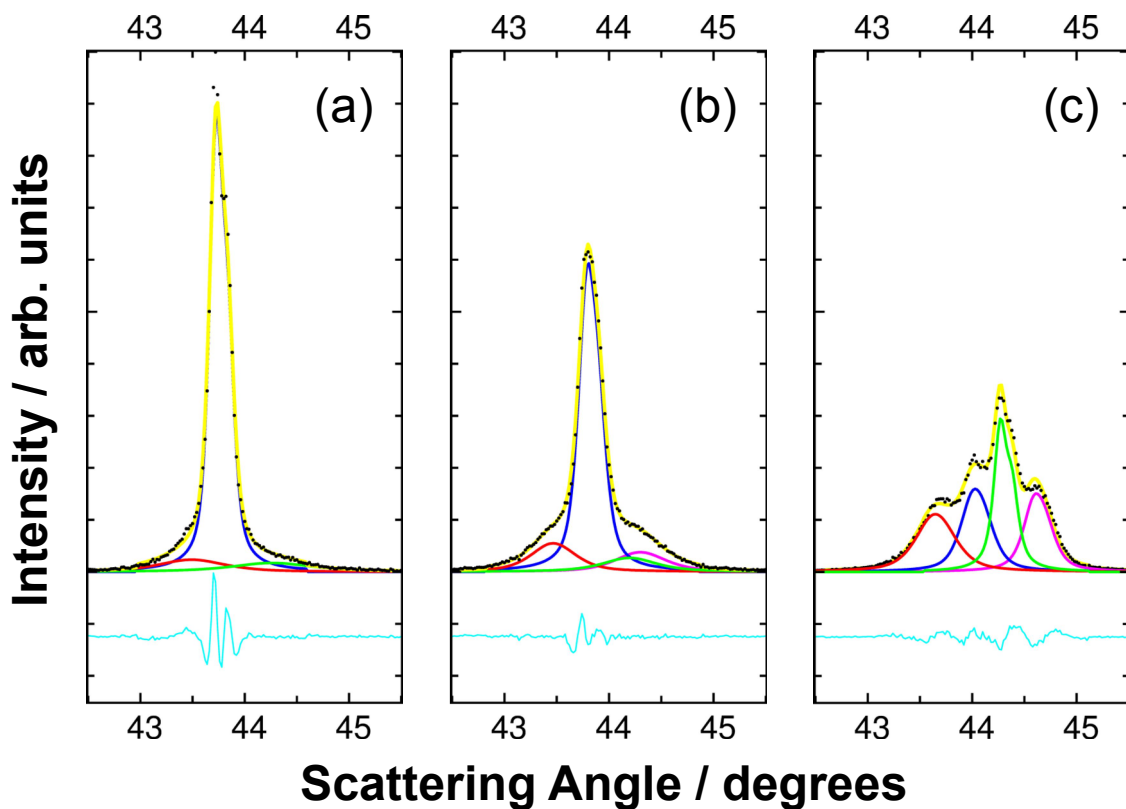


Figure 3.9. Component phase fits of the XRD patterns for sample K in the 3:5 series that were (a) quenched in liquid nitrogen, (b) quenched between copper plates, and (c) slow cooled to room temperature. The individual fits are ordered rocksalt (red), N-layered (blue), spinel (green), and M-layered (purple). The total fit is shown in yellow. The intensity and difference plot scales are the same for each fit.

gion, although the relatively large amount of N-phase highlights the inability of the sample to achieve room temperature equilibrium.

The lattice parameters of the LNQ and CPQ samples for each of the phases fit in Figure 3.9 are shown in Table 3.2, while those of the slow cooled sample are shown in Table 3.3, both in Section 3.6. These lattice parameters are useful for linking together the various end-members into the two- and three-phase co-existence regions, which is

why they are shown with lattice parameter fits from numerous other important compositions. This fine-tuning of the phase diagrams is presented in Section 3.6.

3.5.3 The Spinel End-member

The location of the (400) peak of the spinel end-member between 43.75° and 44.0° is lower than the typical value of about 44.1° to 44.2° [28]. This curious observation introduces the possibility that the spinel phase is oxygen deficient, owing to the quenching process preventing the spinel from incorporating the stoichiometric amount of oxygen required to yield the expected LiM_2O_4 empirical formula with a 3:4 metal:oxygen ratio for materials on the lower boundary of the single-phase spinel region. Oxygen deficient spinels have been reported in the literature when synthesized at higher temperatures, namely $\text{Li}_{1+x}\text{Mn}_{1-y}\text{O}_{4-z}$ [54, 55]. In the high voltage spinel $\text{Li}[\text{Ni}_{0.5}\text{Mn}_{1.5}]\text{O}_4$, higher reaction temperatures (approaching 900°C) and faster cooling rates (namely quenching) have both been shown to give rise to oxygen deficiencies forming in the spinel lattice. It has been observed that HV spinel samples quenched from high temperature ($>750^\circ\text{C}$) in air exhibit an expanded unit cell due to the presence of oxygen vacancies [55]. These oxygen deficiencies in the structure are accommodated by the formation of Mn^{3+} to maintain charge balance. Zhong et al. used thermal gravimetric analysis (TGA) analysis to show that $\text{Li}[\text{Ni}_{0.5}\text{Mn}_{1.5}]\text{O}_4$ continually loses oxygen above 650°C , with a mass loss of 3.5% at 900°C [56]. In addition, the spinel lattice constants of $\text{Li}[\text{Ni}_{0.5}\text{Mn}_{1.5}]\text{O}_4$ samples quenched from 650°C , 750°C , and 850°C were found to continually increase, resulting in a shift of the (400) peak from 44.3° to 44.1° . This is consistent with the spinel structure forming a larger unit cell due to oxygen loss when quenched from high temperature. These materials were also shown to exhib-

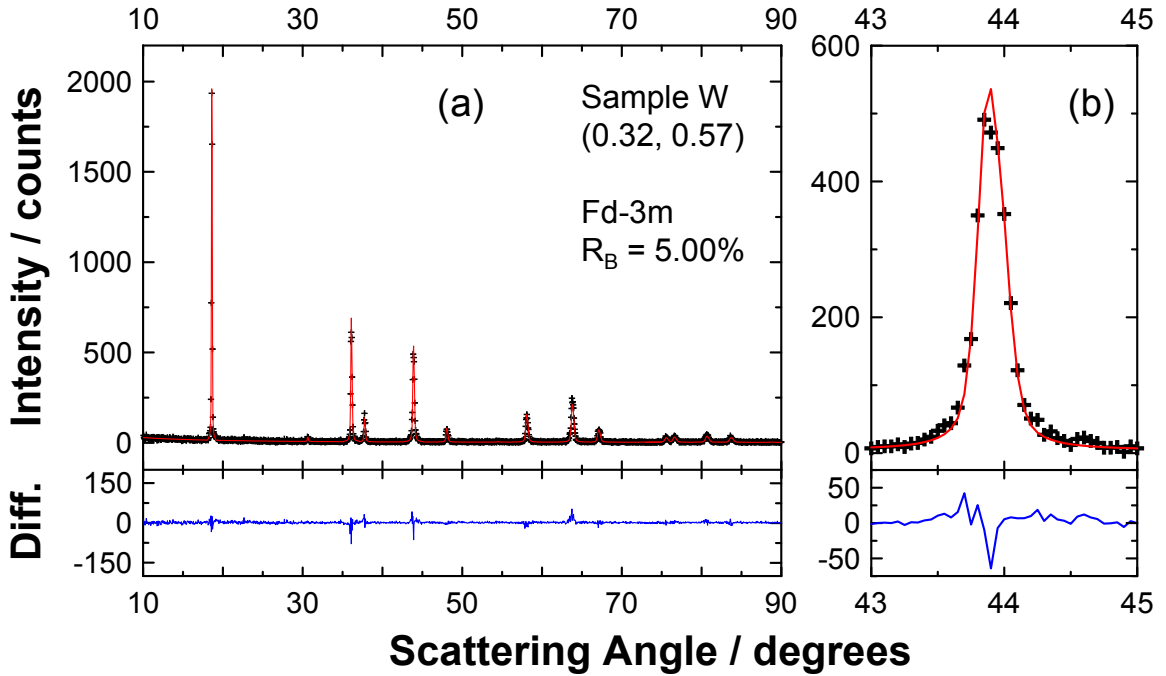


Figure 3.10. XRD pattern and cubic Rietveld refinement of the 900°C quenched sample W in the 1:5 series on the single-phase spinel boundary of the phase diagram.

it a (400) cubic spinel peak shifted to lower angles than the non-oxygen deficient HV spinel, including quenched compositions. As such, Rietveld refinement was performed on sample W to investigate the possibility of the presence of oxygen deficiencies in the lattice.

Figure 3.10 shows the refined XRD pattern of sample W from 10.0° to 90.0° in (a) and an expanded view of the fitted (400) peak in the 43.0° to 45.0° range in (b). The sample was fit as single-phase cubic using the Fd3m space group. A reasonably good fit was obtained for the overall pattern, as shown by the difference plot and the Bragg factor, R_B . The a lattice parameter was determined to be $8.2487 \pm 0.0007 \text{ \AA}$, which as will be shown in Section 3.6, is similar to the lattice parameter of $8.2451 \pm 0.0003 \text{ \AA}$ obtained from the in-house fitting software. The lattice parameter of the standard HV

spinel $\text{Li}[\text{Ni}_{0.5}\text{Mn}_{1.5}]\text{O}_4$ was found to be 8.187 Å when quenching from 800°C in O_2 , while that from slow cooling was 8.179 Å [28], which is part of the spinel solid solution $\text{LiNi}_x\text{Mn}_{2-x}\text{O}_4$. From its hydroxide precursor (with Ni:Mn = 1:5) and at its nominal composition of (0.33, 0.67), sample W is approximately located within this series as $\text{Li}[\text{Ni}_{0.33}\text{Mn}_{1.67}]\text{O}_4$. However, when normalized to an oxygen stoichiometry of 4, ICP-OES analysis gives the composition as $\text{Li}_{0.96}\text{Ni}_{0.34}\text{Mn}_{1.70}\text{O}_4$. While the ratio of metal to oxygen atoms in this composition is that of a standard spinel (3:4), the Li mole fraction implies that vacancies exist on one or more of the three atom sites within the lattice.

McCalla et al. have shown that this solid solution series is contained within a broader single-phase spinel region, which extends both below and to the right of the nominal series composition at 800°C in O_2 for both quenched and slow cooled samples. Furthermore, the spinel compositions in this region are somewhat Li-rich, owing to their closer proximity to the Li corner of the phase diagram (compared to the location of $\text{LiNi}_x\text{Mn}_{2-x}\text{O}_4$). In these materials, the excess Li was believed to occupy Mn 16c sites, and the materials were described as being similar to the series $\text{Li}_{1+x}\text{Mn}_{2-x}\text{O}_4$, albeit with compositions containing Ni. This observation was also found to hold for slow cooled samples at 800°C in air with compositions that were somewhat less Li-rich. This indicates that sample W is likely not Li-deficient in this region of the phase diagram, but rather that oxygen deficiencies likely account for the vacancies within the lattice.

For the Rietveld analysis, the total occupancies for each of Li, Mn, and Ni were fixed according to their ICP-OES values at 0.319, 0.566, and 0.115, respectively. The oxygen occupancy was initially fixed at the stoichiometric value of 1.333, as set by the 3:4 metal:oxygen ratio in LiM_2O_4 . Li and Ni atoms were allowed to occupy both the 8a

and 16d sites, while Mn was fixed at the 16d sites. Once a stable fit was obtained using only the metal atoms, the oxygen occupancy on the 32d site was released for refinement. This resulted in a fit with an R_B value of 5.00%, and resulted in an overall composition of $\text{Li}_{0.319}\text{Mn}_{0.566}\text{Ni}_{0.115}\text{O}_{1.273}$. This suggests that the refinement calculation prefers a structure that contains less than the nominal amount of oxygen (1.333) for the spinel. Normalizing the formula gives $\text{Li}_{1.00}\text{Ni}_{0.36}\text{Mn}_{1.78}\text{O}_{4-z}$, where $z = 0.24$, corresponding to a 1.5% mass loss from the nominal structure, suggesting that sample W is an oxygen-deficient spinel composition.

Overall, the a lattice parameter of sample W from Rietveld is consistent with those obtained for the single- and multi-phase fits of the spinel phase from the in-house fitting software (see Table 3.2), which was also used to generate the phase diagrams at 800°C in O_2 . Thus, the location of the spinel end-member is determined by the combination of ICP-OES analysis, qualitative inspection of the XRD pattern, and lattice constant matching between numerous samples in various single- and multi-phase regions of the phase diagram, as will be shown in Section 3.6. The best approximation for the spinel end-member of the quenched samples is therefore located at the position of sample W, which also establishes the lower limit of the single-phase spinel boundary at 900°C in air. Further study is required to determine whether or not sample W is detrimental to the electrochemical performance of layered-spinel composites as described in Section 1.4.3, and to determine whether or not the S end-member itself is of potential use as a positive electrode material.

3.5.4 Single-phase Layered Boundary “Bump” Region

As discussed above, sample AA at (0.57, 0.36) sits near or at the top of the “bump” feature in the single-phase layered boundary, just to the right of the $\text{Li}[\text{Ni}_{1/6}\square_{1/6}\text{Mn}_{2/3}]\text{O}_2$ composition at (0.55, 0.36). McCalla et al. have determined that this bump, including compositions on the boundary and within part of the layered region, is indicative of monoclinically distorted layered phases containing metal site vacancies, as confirmed by XRD, redox titration, X-ray absorption near-edge structure (XANES), and helium pycnometry studies [15]. The XRD pattern of sample AA contains a monoclinic distortion in the (104) peak, as well as ordering peaks from 20.0° to 30.0° . It is the first sample within the 1:5 composition series to be both single-phase and monoclinically distorted. This potentially indicates that sample AA is likely near or at the top of the bump region. Rietveld analysis was used to determine if the material could be fit as a monoclinic phase in order to confirm its monoclinic character.

Figure 3.11 shows the refined XRD pattern of sample AA from 10.0° to 90.0° in the first plot, and an expanded view of the distorted (104) peak in the 43.0° to 45.0° range in the second plot. The $C2/m$ space group was used to fit the pattern, including the (020), (110), (111), and (021) ordering peaks from 20.0° to 30.0° . The refinement produced a Bragg factor of 4.88%, indicating acceptable agreement between the fit and the data, which is also reflected in the difference plot. The monoclinic lattice constants were determined as $a = 4.9528(6)$ Å, $b = 8.5739(7)$ Å, $c = 5.0491(5)$ Å, and $\beta = 109.294(4)$ Å. The value of β confirms the existence of monoclinic distortions in the crystal structure, as a pure hexagonal lattice exhibits a value of 109.1° when fit as monoclinic. This distinctly marks sample AA as being at or near the top of the bump in the single-phase layered boundary. The electrochemical characterization of several of

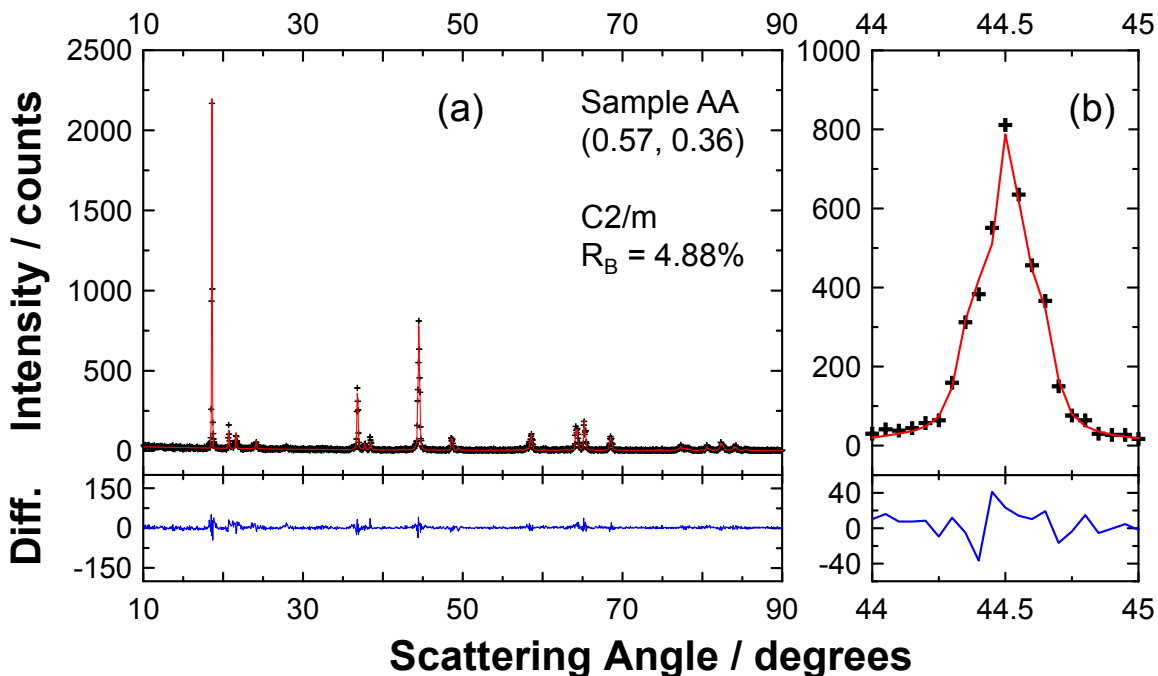


Figure 3.11. XRD pattern and monoclinic Rietveld refinement of sample AA in the 1:5 series at the top of the “bump” in the single-phase layered region boundary of the phase diagram at 900°C quenched. Data points are indicated by crosses, while the fit is shown in red.

these unique monoclinically distorted materials within the bump region is the focus of Chapter 54.

3.6 Lattice Constant Comparisons Between Samples

Using the fitted lattice constants of the phases within each sample and comparing them to the lattice constants of other single- and multi-phase samples represents both a confirmation and fine-tuning of the location of end-members and multiple phase regions established from XRD pattern analysis. Table 3.2 shows fits of numerous quenched samples at 900°C, including those of sample K both quenched in liquid nitrogen and between copper plates. Each column shows the lattice constants of the

Table 3.2. Lattice parameters of various copper plate quenched compositions at 900°C in air. The lattice parameters of sample K from liquid nitrogen quenching (LNQ) are also shown.

Series	Sample	M-layered		N-layered		rocksalt	spinel
		a_{hex} (Å)	c_{hex} (Å)	a_{hex} (Å)	c_{hex} (Å)	a_{cubic} (Å)	a_{cubic} (Å)
1:1	C	-	-	-	-	8.2993(2)	-
	E	-	-	2.9068(2)	14.339(2)	-	-
3:5	I	-	-	-	-	8.3011(6)	8.2797(7)
	K (LNQ)	-	-	2.9190(2)	14.361(2)	8.316(7)	8.179(6)
	K	2.872(2)	14.35(2)	2.9148(3)	14.368(3)	8.325(3)	8.19(1)
	L	2.8592(4)	14.283(5)	2.900(1)	14.324(4)	-	-
1:3	Q	-	-	2.9167(1)	14.352(3)	-	8.2397(2)
	R	2.8585(9)	14.28(1)	2.924(1)	14.356(8)	-	8.240(2)
	T	2.8581(2)	14.293(2)	2.907(1)	14.33(1)	-	-
	U	2.8625(1)	14.270(2)	-	-	-	-
1:5	W	-	-	-	-	-	8.2451(3)
	Y	2.8572(3)	14.278(4)	-	-	-	8.237(1)
	AA	2.8575(1)	14.292(1)	-	-	-	-
	~ M-layered	2.8564(1)	14.282(1)	-	-	-	-

Monoclinic fit lattice parameters:

1:5 AA $a = 4.9528(6)$ Å, $b = 8.5739(7)$ Å, $c = 5.0491(5)$ Å, $\beta = 109.294(6)$

end-member phase(s) fit within a specific sample. Following the lattice constants of a particular phase from top to bottom allows for the comparison of the obtained lattice constants. Starting with the M-layered phase, the hexagonal lattice constants are very similar to each other, with $a_{\text{hex}} \sim 2.8564$ Å and $c_{\text{hex}} \sim 14.282$ Å. This composition is located at approximately (0.56, 0.35), and although monoclinically distorted, is not at the top of the bump region, which was determined to be sample AA, the monoclinic lattice constants of which are shown at the bottom of the table. By comparison, the

M-layered phase fit in the CPQ sample K had much larger lattice constants, which are due to the broad (104) peak occurring at lower angle than does the pure M-layered phase (44.5°). This again highlights that this sample was not in equilibrium when quenched and that the fitted layered phase is likely an unstable intermediate phase that has not yet formed the preferred M-layered phase.

The single-phase ordered rocksalt lattice parameter is similar to the rocksalt parameters from quenched sample K fits, samples B and C fits (both single-phase), and the sample I fit (two-phase rocksalt-spinel), indicating an average value of 8.31 ± 0.01 Å. The a_{cubic} values obtained from Rietveld and in-house fitting software for the S-phase were 8.249 Å and 8.245 Å, respectively. These values are similar to each other and to those of fitted spinel phases in compositions on the N-S tie-line and in the M-N-S co-existence region. This further supports the S end-member in the quenched phase diagram as being oxygen deficient. However, the spinel end-member lattice constants from CPQ and LNQ do not match each other, that of sample W (as discussed in section 3.5.3), or those of any other quenched samples containing spinel. This is likely due to the inability of the multi-phase samples to reach equilibrium at room temperature, as well as the significant overlap of the oxygen-deficient spinel peak with the N and R phases.

Table 3.3 shows the lattice parameters of the fitted slow cooled samples. It is noted that many of the samples were fit with all four phases, reflecting the non-equilibrium conditions of many samples in the M-R-S co-existence region. Starting with the M-layered fits, the lattice constants from sample K are very similar to those of the M-layered fits found in the single- and multi-phase regions except for samples C and E, which are too close to the R end-member to obtain reliable fits for M. However, the remaining samples exhibit similar layered lattice constants, indicating that the

Table 3.3. Lattice parameters of various slow cooled compositions at 900°C in air.

Series	Sample	M-layered		N-layered		rocksalt	spinel
		a_{hex} (Å)	c_{hex} (Å)	a_{hex} (Å)	c_{hex} (Å)	a_{cubic} (Å)	a_{cubic} (Å)
1:1	C	2.864(2)	14.177(5)	2.8982(4)	14.341(5)	8.289(1)	8.173(1)
	E	2.8540(9)	14.23(1)	2.8900(1)	14.331(9)	8.290(2)	8.170(4)
	F	2.8564(8)	14.29(1)	2.8984(4)	14.325(6)	8.282(2)	-
3:5	I	-	-	2.904(1)	14.327(3)	8.2878(8)	8.1750(3)
	K	2.8484(4)	14.259(4)	2.8957(8)	14.327(4)	8.286(1)	8.1700(7)
	L	2.8500(3)	14.265(4)	-	-	8.273(1)	-
1:3	Q	2.8492(8)	14.24(1)	2.903(1)	14.330(5)	8.294(1)	8.1757(2)
	R	2.8491(3)	14.262(3)	2.900(1)	14.340(8)	8.292(1)	8.1753(1)
	T	2.8494(2)	14.275(3)	-	-	8.288(1)	8.169(2)
	U	2.8575(2)	14.262(2)	2.8825(5)	14.316(5)	-	-
1:5	W	-	-	-	-	-	8.2016(2)
	Y	2.8499(2)	14.265(1)	-	-	-	8.1826(2)
	Z	2.8504(1)	14.278(2)	-	-	8.290(2)	8.172(1)

M-layered phase is the same for all samples in the 3-phase M-R-S region. The same is true of the N-layered fits, which show acceptable lattice constant agreement from the multi-phase fits. The only exception is sample T, which is too close to the M-phase corner (see Figure 3.1) to obtain a good fit for N. It should be noted under equilibrium cooling conditions these samples would likely not contain any N-phase, as shown in Figure 3.1. However, the agreement of the lattice parameters of the N-layered “contaminant” does at least indicate that the non-equilibrium conditions are present in numerous slow cooled samples.

Moving to the rocksalt phase, the lattice constant value obtained for sample K is similar to the values obtained for rocksalt in the multi-phase samples, again confirm-

ing its inclusion in the three-phase M-R-S region. It should be noted that the single-phase ordered rocksalt phase was never synthesized directly as it is not found in any of the composition series studied, and that its location on the phase diagram is both an extrapolation of the data presented here and a reflection of its location on the slow cooled phase diagram at 800°C in O₂.

Finally, the spinel lattice constant of sample K, and those of the fitted spinel phase in the multi-phase samples, are also in acceptable agreement with one another. This value is closer to the expected value of Li[Ni_{0.5}Mn_{1.5}]O₄, and indicates that the slow cooling method allowed sufficient time for oxygen to be reincorporated into the spinel structure while cooling. Again, this confirms that spinel forms the final end-member of the M-R-S co-existence region, and while it is never directly synthesized within the composition series studied, indicates that an approximate location between samples that were predominately spinel (P, Q, W, and X) is appropriate.

3.7 Contour Plots of the Single-phase Layered Region

The establishment of the upper and lower single-phase layered region boundary presents the opportunity for mapping the *a* and *c* hexagonal lattice parameters on the phase diagram in the form of contour plots. Such plots are of use to researchers studying materials in this region, allowing for quick identification of sample location based on lattice constant extraction from XRD. The contour plots of the quenched phase diagram are presented in Figure 3.12. These plots were generated by converting the Li and Mn metal mole fractions of 18 single-phase layered samples to Cartesian *x* and *y* values, respectively. Plotting the *a* and *c* constants separately on the Cartesian axes allowed the lattice parameters to be connected by contour lines representing constant

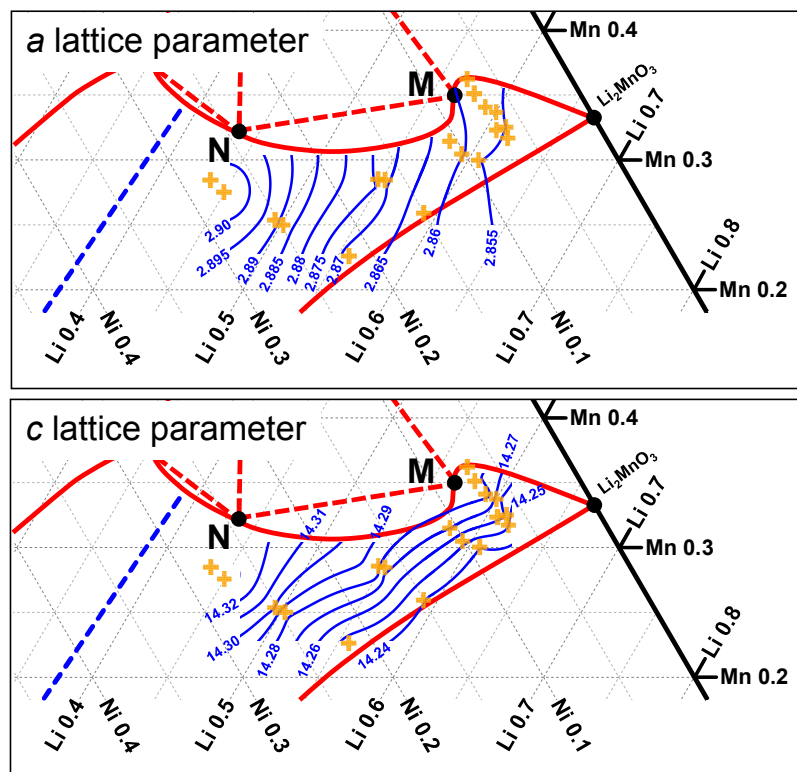


Figure 3.12. Lattice parameter contour plots of the single-phase layered region of the Li-Mn-Ni-O phase diagram at 900°C in air (quenched). The contour plots were generated from the lattice parameters of the samples indicated by the orange crosses.

values throughout the single-phase layered region. The locations of these lines were then added to the single-phase region of the quenched phase diagram.

From left to right, the Li content of the layered materials increases, which is reflected in the a lattice parameter gradually increasing. This indicates that more Li is present in the transition metal layer as the total Li content increases. At the same time, the c lattice parameter continually decreases as the Li content increases from left to right. The original LRO composition series $\text{Li}[\text{Ni}_x\text{Li}_{1/3-2x/3}\text{Mn}_{2/3-x/3}]\text{O}_2$, which was once thought to be a solid solution by itself, has actually been shown to exist within the middle of the layered region from Li_2MnO_3 to $\text{Li}[\text{Ni}_{0.5}\text{Mn}_{0.5}]\text{O}_2$ as discussed in Section 1.4.3 [30]. The contour plots are consistent with the lattice constant values for compo-

sitions along this composition series as determined by Lu et al. [8]. The overlapping diffraction patterns of the quenched and slow cooled samples within the single-phase region indicate that the contour plots are valid for samples cooled at different rates from 900°C.

3.8 Li-Mn-Ni-O Pseudo-ternary Phase Diagrams at 900°C and 800°C in Air

Figure 3.13 shows the pseudo-ternary phase diagrams of the Li-Mn-Ni-O system in the positive electrode materials region. The production of the quenched phase diagram at 900°C will be discussed first. The S end-member location is determined by the single-phase spinel sample W. Since no other single-phase spinel phases were synthesized or observed, this sample is estimated as being on the boundary of the single-phase region. The termination of the boundary on the Mn axis and the sweeping upward direction of its left side are approximated according to that of the phase diagram at 800°C in O₂.

The M-layered end-member is located on the boundary of the vacancy-containing “bump” region in the 1:5 composition series, as determined by its ordering peaks and monoclinically distorted (104) peak. While the exact location of the M-phase on this boundary is difficult to determine, it is approximated here to be slightly below sample AA due to the direction of the N-M tie-line as determined by sample T, shown in Figure 3.1. The overall location of N was chosen to be somewhat intermediary between those of E, F, and K, with the final position just to the bottom-right of K to reflect the presence of spinel in both the LNQ and CPQ samples. The tie-lines were drawn

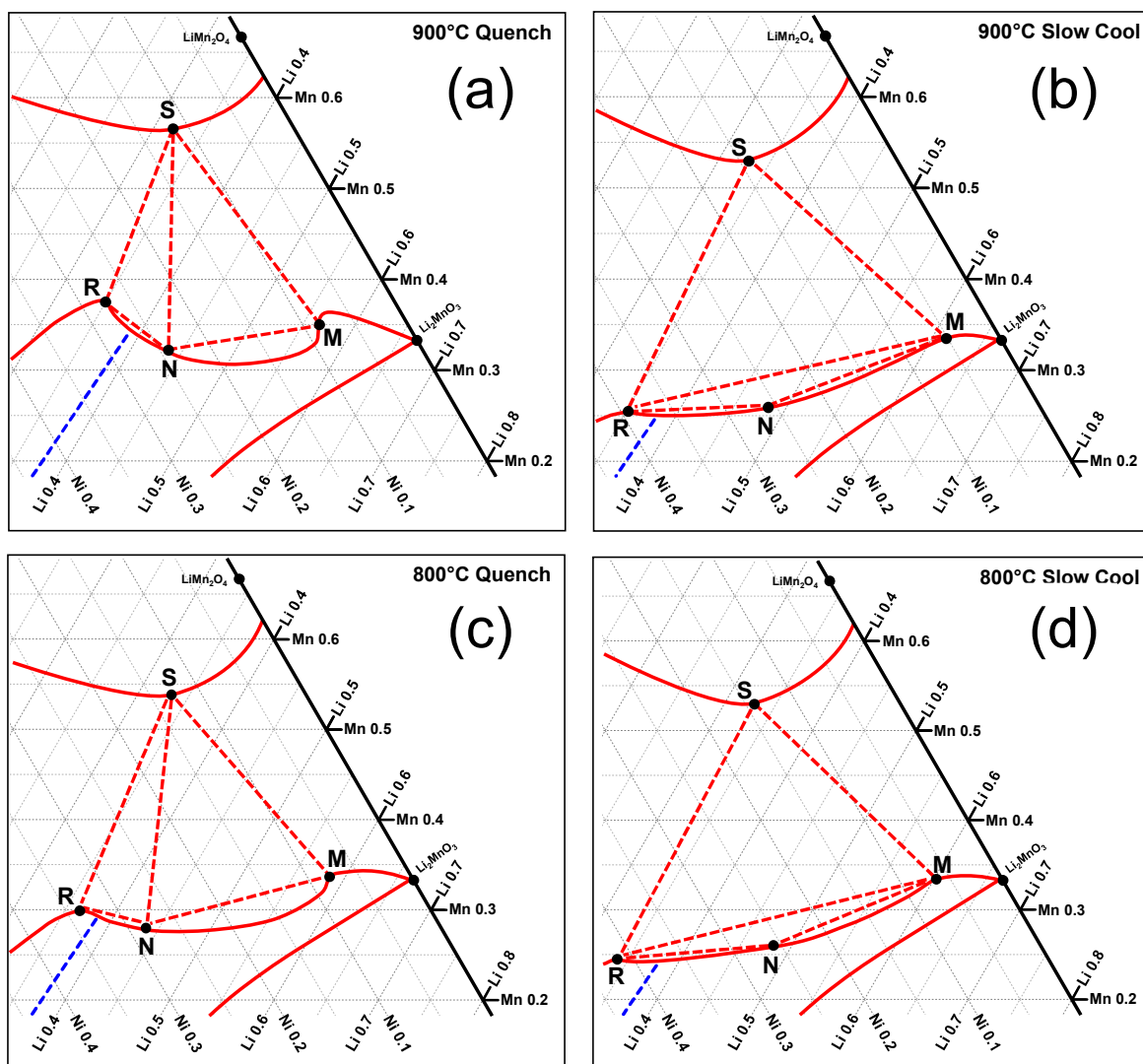


Figure 3.13. Pseudo-ternary phase diagrams of the Li-Mn-Ni-O system in air at (a) 900°C quenched, (b) 900°C slow cooled, (c) 800°C quenched, and (d) 800°C slow cooled.

between each end-member in accordance with the phases observed in XRD. The “bump” is found between the upper layered boundary and its termination at Li_2MnO_3 , reflecting the monoclinic character of the samples contained within it. The lower layered boundary terminates at Li_2MnO_3 and LiNiO_2 , in accordance with the phase diagrams at 800°C in O_2 . The layered-layered composite of sample L indicates that it ex-

ists in the crescent-shaped region between the layered boundary and the N-M tie-line. Finally, the dashed blue line indicates the cubic to layered transition from the single-phase rocksalt to the single-phase layered region. While not thoroughly mapped in this study, the samples in the crescent-shaped region likely contain tie-lines which either fan out from the M composition to different points on the layered boundary, or contain multiple tie-lines in parallel to the N-M tie-line, with each tie-line connecting two unique layered end-members on either side of the boundary.

The slow cooled phase diagram at 900°C was composed in a similar manner. The M phase was determined to be at a lower position than that of the quenched system. This effectively reduces the “height” of the bump in the single-phase boundary, shrinking the region near which monoclinically distorted layered phases form. It is reiterated here that these layered phases still contain metal site vacancies, as seen in the distortions from the XRD pattern analysis in Section 3.3. The location of N is approximated as being similar to that of sample G in Figure 3.1 by XRD analysis. The R-S, S-M, and R-M tie-lines combine to support the establishment of the M-R-S and M-N-R coexistence regions. Unlike the quenched diagram, no samples were found on the N-M tie-line or in the crescent region between it and the layered boundary. However, the observation of both of these features in the phase diagrams at 800°C in O₂ leads to their inclusion here, subject to possible modification based on potential future studies.

The phase diagrams at 800°C were established using the same methodology employed for the 900°C diagram, with more estimation required in the placement of the single-phase end-members and multi-phase coexistence regions. While minor modifications of the locations of the end-members and single-phase boundaries are possible based on future studies, the general locations of these features are considered accurate

as determined by the XRD pattern, lattice constant, and ICP-OES measurements contained herein.

3.9 Concluding Remarks on Phase Diagrams

It must be noted here that several end-members, notably the R phase in the slow cooled diagrams, were not synthesized directly in this study. However, this was not the focus of determining the bulk sample phase diagrams in air. Rather, these diagrams were produced to provide a greater overall understanding of how reaction conditions and cooling rates during synthesis affect the phases that form in the positive electrode materials region of the Li-Mn-Ni-O system under reaction conditions more typically used for bulk-scale commercial sample production as opposed to samples produced combinatorially in milligram-scale quantities.

Several important conclusions can be drawn from general trends observed in the diagrams. In general, the single-phase regions are larger when quenched and smaller when slow cooled. This can be thought of as the materials having higher entropy and therefore being more disordered at equilibrium, resulting in the formation of fewer, more disordered phases when quenched that produce smaller coexistence regions between them. When slow cooled, the decreasing temperature and non-equilibrium conditions begin to favour phase separation in order to minimize entropy, thereby resulting in the formation of larger co-existence regions connected by smaller single-phase regions. When viewing the phase diagram, this phenomenon can be best visualized by the movement of the single-phase layered boundary and the changes in the coexistence regions that result. When quenched, the boundary is higher on the diagram due to the larger single-phase region, and the coexistence regions form two three-phase regions of

N-R-S and M-N-S between it and the spinel boundary. Slow cooling has the effect of shifting the boundary to a lower position on the diagram as the region shrinks in size relative to its quenched counterpart. This results in a significant change in the two three-phase regions, which convert into coexistence triangles of M-R-S and M-N-S. The presence of four phases in the slow cooled system indicates that not all samples reach equilibrium when cooled at intermediate rates, such that formation of a fourth non-equilibrium contaminant phase is present. It bears restating that slow cooling is effectively an intermediate cooling rate relative to quenching (very fast) and extremely slow cooling (less than $1\text{ }^{\circ}\text{C min}^{-1}$), and does not always allow multi-phase samples near the middle of the positive electrode materials region to come to equilibrium, resulting in compositions containing all four end-members in variable amounts relative to their location to the nominal M-N-R and M-R-S coexistence regions.

The movement of the layered boundary must also be considered in terms of Li content. At the end of each composition series (on average, the last two to three samples) and for both reaction temperatures, the quenched and slow cooled layered samples are almost the same materials in terms of phase composition (single-phase layered). This can be seen in the overlap of the solid red and dashed blue lines of the XRD patterns at the very bottom of each XRD plot stack in Figure 3.2 to Figure 3.7, and in the location of the lower single-phase boundary in the phase diagrams. Near the upper portion of the boundary, however, materials that are single-phase when quenched, such as sample F in Figure 3.1, can become multi-phase when slow cooled. This is especially relevant to compositions on or near the layered boundary. Without compensating for Li loss during heating (usually in the form of a 3-5% molar excess of Li during synthesis), and without careful choice of cooling rates, materials that are single- or two-phase layered when quenched can actually become two-phase spinel-layered (sample AA),

three-phase M-N-R (sample F), and/or three-phase M-R-S (sample T) when slow cooled. The electrochemical performance of the R- and N-phases have been shown to be quite poor, impeding Li intercalation and drastically reducing achievable capacity [29]. Thus, researchers wishing to avoid such undesirable phase separation can use the phase diagrams as a guide for determining how much excess Li to use during synthesis, as well as which cooling rate to employ in order to prevent phase separation thereby maintaining single-phase layered compositions with better electrochemical properties.

The locations of the M, N, R, and S end-members and all single-phase boundaries and two phase tie-lines are approximations based on the consolidation of the XRD stacked patterns and lattice constant analysis. While several compositions are very close in terms of elemental composition and crystalline structure, very few of the four end-members phases were synthesized directly. Future work on the phase diagram could include the precise mapping of each of these phases by blanketing the approximate locations reported herein with an array of samples in order to zero in on the precise location. For example, to precisely locate the ordered rocksalt end-member in the slow cooled phase diagram, samples could be prepared from ternary coordinates of (0.33, 0.20) and (0.37, 0.30) with evenly distributed Li and Mn values to form a 3 x 3 composition grid. The Yorick-based fitting routine could then be used to extract the lattice constants of each sample, allowing for the exact location of the desired end-member to be determined. In addition, the precise locations of the single-phase layered boundaries could be determined in a similar manner. This may be of particular importance for researchers looking to make Li-deficient materials (relative to the nominal LRO line) that do not form the electrochemically undesired layered-layered composites within the wedge region, and for researchers looking for novel Li-rich single-phase layered compositions just below and/or along the boundary. Overall, however, the most

important concept arising from the development of the phase diagrams is that the choice of starting composition, reaction temperature, and cooling rate for materials in the Li-Mn-Ni-O all have a significant impact on the final phases that form, and therefore must be chosen both purposefully and carefully.

Overall, it has been thoroughly demonstrated that the phase diagrams as generated from combinatorial samples at 800°C in O₂ are very similar to the phase diagrams produced from bulk samples at 800°C and 900°C in air. The production of these phase diagrams also enabled the identification of several unique regions within the phase diagrams at 900°C which contain compositions with unique and promising electrochemical behaviour. The remainder of this thesis focuses on the material and electrochemical characterization of these materials.

Chapter 4

Electrochemical Characterization of Li-deficient Single-phase Layered Li-Mn-Ni-O Compositions

This chapter contains the structural and electrochemical characterization of a narrow range of samples in the quenched Ni:Mn 1:5 composition series within the “bump” region of the single-phase layered boundary. Figure 4.1 shows the quenched pseudo-ternary phase diagram at 900°C in air, labelled with the various single- and multi-phase regions determined in Chapter 3. The inset highlights the five compositions, B₁ to B₅, which will be discussed throughout this chapter. The (Li, Mn) coordinates of each composition are given in Table 4.1. These samples are effectively the same Li-deficient layered materials discussed in Chapter 1, which were determined by XRD, He pycnometry, redox titration, and near-edge XANES analysis to have measurable quantities of metal site vacancies [15]. In this chapter, it will be shown that several of these materials have good electrochemical properties, namely high specific capacities and low levels of polarization, that make them competitive with the stoichiometric Li-rich solid solution materials (shown for reference as the dashed orange line in Figure 4.1). By comparison, these materials contain less Li and less Ni than most compositions of the LRO solid solution, making them attractive from both a cost and toxicity perspective. One of these compositions in particular, sample B₃, exhibits a very high reversible specific capacity at high potential which is comparable to those of the best Li-Mn-Ni-O LRO materials, albeit at relatively low charging rates.

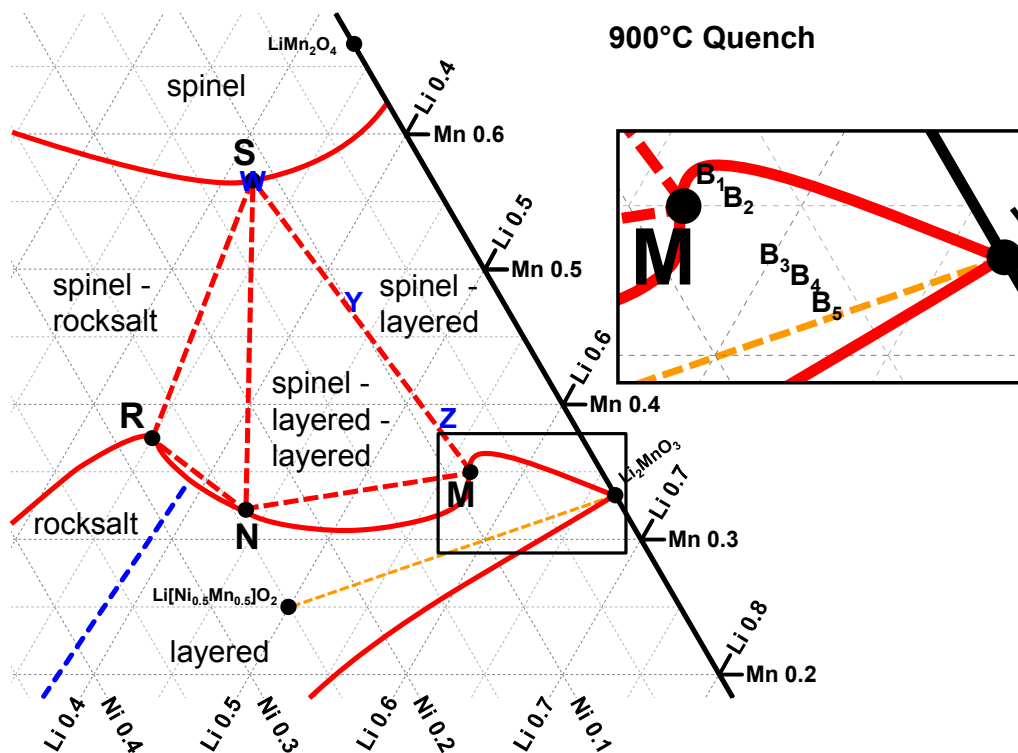


Figure 4.1. Pseudo-ternary phase diagram of the Li-Mn-Ni-O system at 900°C in air (quenched) highlighting the “bump” in the layered boundary. The inset shows the bump region containing samples B₁ to B₅, the (Li, Mn) coordinates of which are shown in Table 4.1. The dashed orange line from Li[Ni_{0.5}Mn_{0.5}]O₂ to Li₂MnO₃ represents the stoichiometric Li-rich solid solution series Li[Ni_xLi_(1/3-2x/3)Mn_(2/3-x/3)]O₂, and is shown for reference. The quenched samples W, Y, and Z from Figure 3.1(a) are shown for comparison with the bump compositions in Figure 4.2.

4.1 Experimental

The materials presented in this chapter were prepared according to the methods described in Section 2.1. For the solid-state synthesis process, two heating steps were used. The materials were first heated at 900°C in air for 10 hours, then quenched between copper plates. Due to the possibility of Li₂CO₃ forming during storage in air while stored for several months prior to testing, all samples (excluding B₂, which was

prepared “fresh”) were re-fired for one additional hour at 900°C in air, and then re-quenched again between copper plates prior to further characterization. XRD measurements of the samples were made using the D5000 diffractometer, while SEM images were collected by Patrick Bonnick using a Phenom G2 Pro benchtop scanning electron microscope.

In terms of electrochemical characterization, half-cells of each composition were cycled from 2.5 V to potential limits of 4.4 V, 4.6 V, and 4.8 V to determine the effect of upper potential limit on cycling behaviour. Once the half-cells were sufficiently cycled for analysis at each potential limit (typically exhibiting a stable trend in cycling behaviour), the limit of each cell was increased to the next highest value. For example, a cell initially cycled to 4.4 V for 100 cycles would be stepped to 4.6 V for several cycles, and then stepped to 4.8 V for several cycles. This voltage-step process provided an evaluation of how the cycling characteristics of each composition changed as the potential was increased. Once each cell exhibited a clear trend in cycling, the lower potential limit was decreased to 2.0 V for several cycles to determine what effect, if any, a lower potential had on observable capacity and voltage curve evolution. All cells were measured on a Moli charging system at a rate of 10 mA g⁻¹ and at 30°C.

4.2 Materials Characterization

The elemental compositions, standard layered notations, vacancy estimates, hexagonal lattice parameters, and BET surface areas of samples B₁ to B₅ are presented in Table 4.1. As shown, normalizing the ICP-OES results of each composition to an oxygen stoichiometry of 2 and assuming average oxidation states of Li¹⁺, Ni²⁺, Mn⁴⁺, and

Table 4.1. Elemental composition, layered notation, metal vacancy estimate, hexagonal lattice constants, and BET surface area results of samples B₁ to B₅.

Sample (Li, Mn)	Layered Notation*	Metal Vac. (%)	Lattice Parameters		BET Surface Area / m ² g ⁻¹
			a _{hex} / Å	c _{hex} / Å	
B ₁ (0.57, 0.36)	Li[Li _{0.06} Ni _{0.13} Mn _{0.67} □ _{0.14}]O ₂	7.0	2.8575(1)	14.292(1)	-
B ₂ (0.58, 0.35)	Li[Li _{0.09} Ni _{0.13} Mn _{0.66} □ _{0.12}]O ₂	5.9	2.8621(1)	14.292(1)	0.91(1)
B ₃ (0.60, 0.34)	Li[Li _{0.16} Ni _{0.12} Mn _{0.65} □ _{0.07}]O ₂	3.6	2.8564(1)	14.261(1)	1.35(1)
B ₄ (0.61, 0.32)	Li[Li _{0.20} Ni _{0.12} Mn _{0.64} □ _{0.04}]O ₂	1.8	2.8537(2)	14.248(2)	0.99(1)
B ₅ (0.62, 0.32)	Li[Li _{0.22} Ni _{0.12} Mn _{0.64} □ _{0.02}]O ₂	1.2	2.8509(2)	14.234(2)	0.88(1)

* normalized to an oxygen stoichiometry of 2; assumes Ni²⁺, Mn⁴⁺

O²⁻ produces layered notations for materials containing varying amounts of metal site vacancies. These vacancies are calculated as a percentage of the total metal fraction of Li, Mn, and Ni of each sample, assuming an average metal site occupation which does not differentiate between the 3a (Li layer) and 3b (TM layer) hexagonal sites. As shown, the samples near the top of the bump region (B₁ and B₂) contain more vacancies than those in the middle (B₃) and those approaching the stoichiometric Li-rich line (B₄ and B₅). The vacancy content of sample B₁ in particular is in excellent agreement with compositions in the vacancy-containing solid solution series Li[Li_(1/3-x)Ni_{x/2}□_{x/2}Mn_{2/3}]O₂, corresponding to the composition x = 0.28 [15]. By comparison, samples B₂ through B₅ are not part of this solid solution (which only contains Ni²⁺), as their Li, Ni, Mn, and vacancy mole fractions are not in agreement with the stoichiometry of the series.

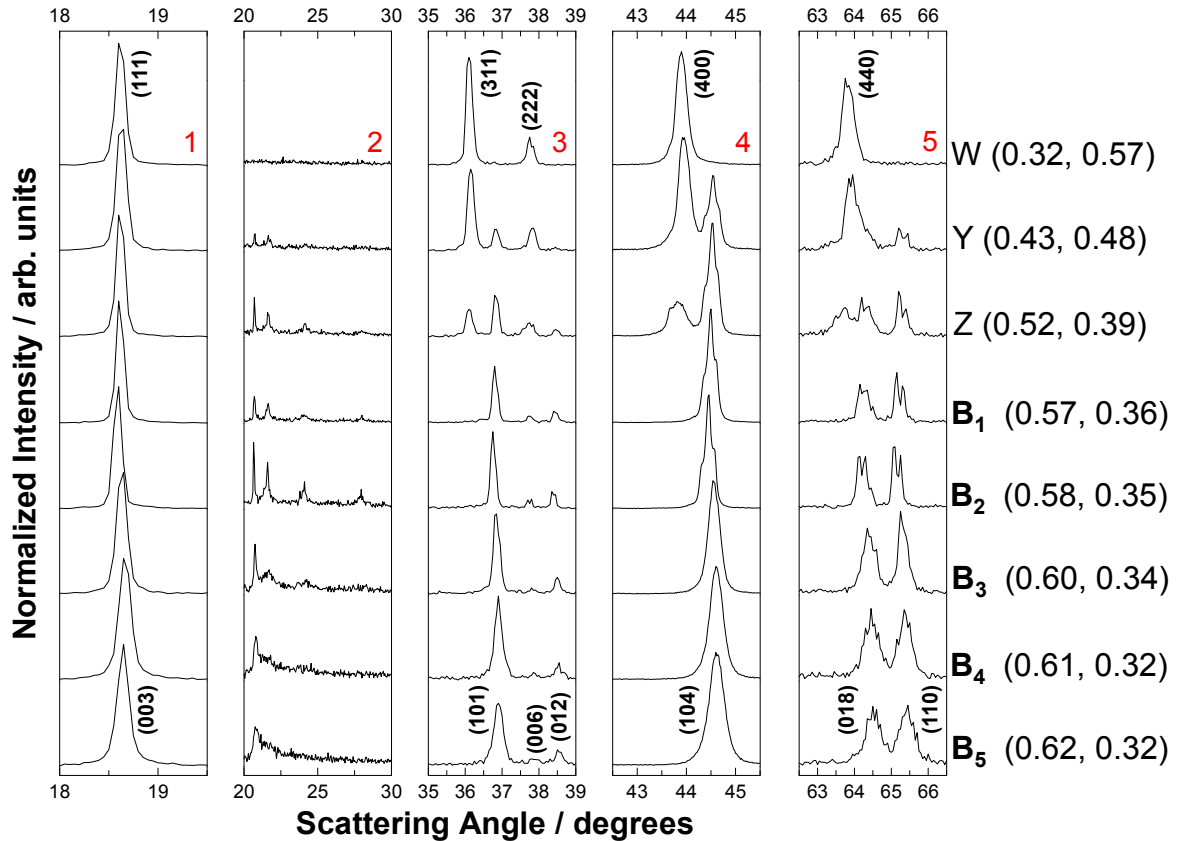


Figure 4.2. XRD patterns of samples B_1 through B_5 located within the bump in the single-phase layered boundary of the quenched phase diagram at 900°C in air. XRD patterns of samples W, Y, and Z from Figure 3.1 and Figure 4.1 are shown to illustrate the transformation from layered to spinel as Li content decreases. Peaks of a single-phase spinel (sample W) and single-phase layered (sample B_5) pattern are labelled with Fd-3m and R-3m Miller indices, respectively. The panel number of each scattering angle range is labelled in red.

Figure 4.2 shows the XRD patterns of samples B_1 to B_5 , in addition to those of samples W, Y, and Z (see Figure 4.1) for comparison. The Miller indices of the single-phase cubic spinel (sample W) and single-phase hexagonal layered oxide (approximately sample B_5) are labelled to clearly show the transition from single-phase spinel (sample W) to two-phase spinel-layered (samples Y and Z) to the top of the bump in the single-phase layered boundary (sample B_1) and finally into the single-phase layered region (approximately sample B_3 downward). The lattice constants of samples B_1 to B_5

fit as single-phase hexagonal layered oxides are shown in Table 4.1. The c lattice constant decreases as the Li content increases, indicating that the layered unit cell is decreasing in size along the c -axis. Each of samples B₁ through B₅ in panel 2 show superstructure ordering peaks from 20.0° to 30.0°. Samples B₁ and B₂ have very sharp peaks in this range, indicating that their crystal structures exhibit a significant amount of 3-D ordering. Starting at sample B₃, the ordering peaks become broader and relatively less intense, indicating a decrease in 3-D ordering within the crystal structure due to increased amounts of stacking faults of the hexagonal layers along the c -axis. The ordering peaks of samples B₄ and B₅ become even broader and less defined, indicating that these materials have 2-D ordering on the TM layer.

These peaks resemble the superstructure peaks due to Li and Mn ordering found in Li-rich structures. Comparison of the layered (104) peaks at approximately 44.5° in panel 4 (shown in Figure 4.2) of each sample also offers insight into their crystal structures. Samples B₁ and B₂ exhibit (104) peaks that exhibit asymmetry due to a monoclinic phase, resulting in 3-D ordering.

By comparison, samples B₃, B₄, and B₅ contain no apparent distortion of the (104) peak, indicating that these materials only have 2-D ordering. The XRD analysis indicates that there is a clear difference between the crystal structures of samples B₁ and B₂ and those of samples B₃ to B₅. In order to confirm this observation, samples B₁ and B₂ were fit as single-phase monoclinic structures using the C2/m space group. Figure 4.3 shows the Rietveld refinements of both samples. The fits yielded R_B values of 7.74% and 5.62% for samples B₁ and B₂, respectively, while the a , b , c , and β lattice parameters of the monoclinic unit cells were approximately the same for both samples, as shown on each plot. When fit as monoclinic, a pure hexagonal lattice has an angle,

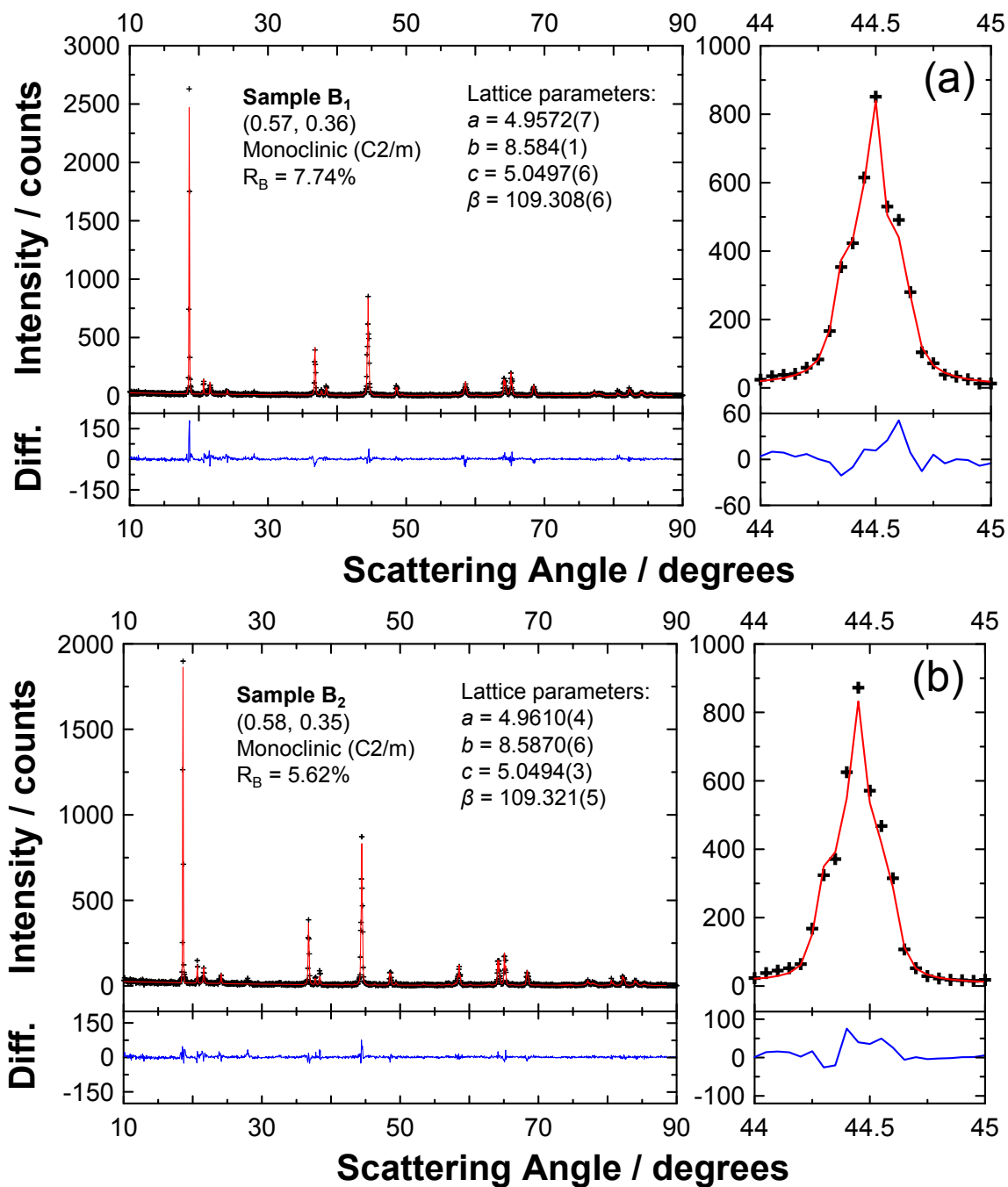


Figure 4.3. XRD patterns and monoclinic Rietveld refinements of (a) sample B₁ and (b) sample B₂ near the top of the “bump” in the single-phase layered region boundary of the quenched phase diagram at 900°C in air. See Figure 4.1 for the positions of B₁ and B₂ in the Li-Mn-Ni-O phase diagram.

β , of 109.1° [11]. The values of $\beta = 109.308(6)^\circ$ for sample B₁ and $\beta = 109.321(5)^\circ$ for sample B₂ therefore confirm that both samples have monoclinic crystal structures.

Figure 4.4 shows SEM images of the bump samples. The increasing Li content from sample B₁ to B₅ is found to have a significant impact on the particle morphologies. The images show a range of secondary particle sizes across all samples, with the average particle size appearing to be approximately the same for each composition. This is due in part to the size of the hydroxide precursor particles being the same for each composition. In terms of overall particle shape, there is a clear difference between those of samples B₁ and B₂, and those of samples B₃ to B₅. Samples B₁ and B₂ exhibit a combination of plate-like particles interspersed with smoother, more ellipsoidal single-crystallites. The plate-like particles exist as larger primary particles and as agglomerations composed of smaller primary particles. The plate-like and ellipsoidal particles appear both separately and as inter-grown agglomerates, with the secondary particles exhibiting little apparent porosity in the SEM images.

By contrast, the particles of samples B₃ to B₅ are composed solely of plate-like primary particles agglomerated into larger, more spherical secondary particles. No qualitative difference in pore size is observed between the secondary particles of the three samples, although in general, they do appear to have more porosity than the particles in samples B₁ and B₂. Overall, there is an obvious difference between the average particle shape of samples B₁ and B₂ and those of samples B₃, B₄, and B₅. This may in part be due to greater crystallization in samples B₁ and B₂ owing to increased transition metal ion diffusion facilitated by the greater number of metal site vacancies in samples near the top of the bump. The higher amount of 3-D ordering in these materials may also be a contributing factor, as the sharp peaks from 20.0° to 30.0° and from 63.0° to 65.0° observed in the XRD patterns indicate greater crystal growth in

these samples compared to the layered materials which only exhibit 2-D ordering. While this may indeed be a contributing factor to their unique particle shapes, relatively sharp ordering peaks are also observed for sample B₃, indicating that further study is required to ascertain the reasons for the differences in particle morphology.

Overall, the combination of ICP-OES, vacancy, XRD, and SEM analysis confirm that the bump region contains materials with distinct structural, physical, and morphological characteristics. It has been established that from samples B₁ to B₅ the metal vacancy content decreases as Li content increases. However, samples B₁ and B₂ exhibit significant 3-D ordering due to Mn ordering on the TM layer which is facilitated by larger vacancies contents; samples B₃ through B₅ contain fewer vacancies and exhibit only 2-D ordering. As such, samples B₁ and B₂ are considered to be significantly distorted hexagonal phases that can be equally considered as single-phase monoclinic materials akin to Li₂MnO₃, as shown by Rietveld refinement. For the purposes of the phase diagrams, these compositions are effectively Ni-rich analogues of Li₂MnO₃, which is close to the bump region. Qualitatively, samples B₁ and B₂ can be viewed as “vacancy-rich” monoclinic materials, while samples B₃, B₄, and B₅ can be viewed as comparatively “vacancy-poor” layered materials.

The materials examined in this chapter have unique structural and physical properties. It will be shown in section 4.5 that each of these compositions exhibits significant electrochemical activity with extended cycling to different upper potential limits. Even without cycling comparisons, the materials near the top of the bump in the layered boundary are distinct from their layered counterparts closer to the middle of the bump region.

Sample B₁
(0.57, 0.36)

Sample B₂
(0.58, 0.35)

Sample B₃
(0.60, 0.34)

Sample B₄
(0.61, 0.32)

Sample B₅
(0.62, 0.32)

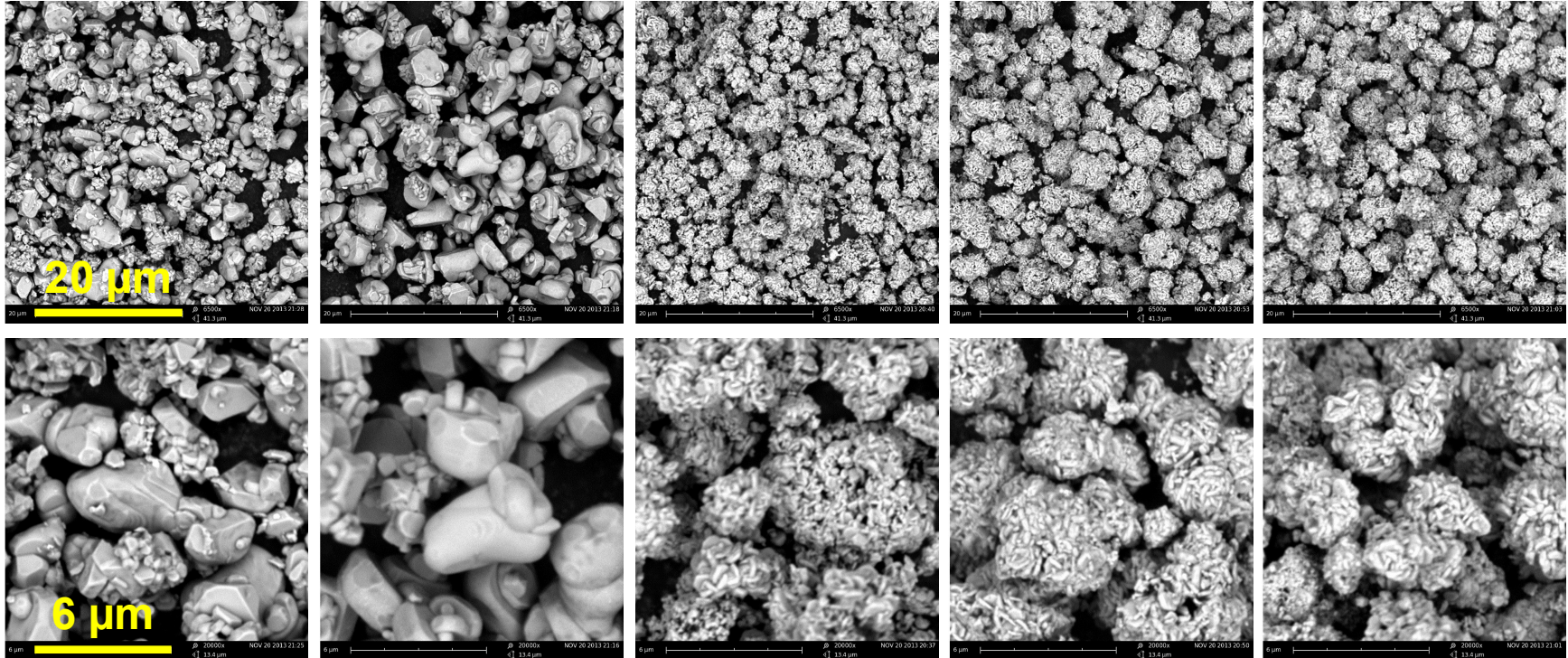


Figure 4.4. SEM images of samples B₁ to B₅. Images in the top row have a 20 micron scale bar, while images in the bottom row have 6 micron scale bar.

4.3 The Effect of Upper Potential Limit on the Cycling Behaviour of the Li-deficient Bump Materials

Half-cells of the bump materials were cycled from 2.5 V to upper potential limits of 4.4 V, 4.6 V, and 4.8 V (vs. Li/Li⁺). Figure 4.5 to Figure 4.9 show the voltage versus capacity plots of each material at each potential limit after cycles 1, 2, and 35. Throughout these plots, unique electrochemical behaviour is seen at every potential limit in terms of reversible capacity, hysteresis, and overall voltage curve shape for each composition. This section will analyze the general features and behaviour seen in the voltage curves of sample B₁, and then summarize the same general observations for samples B₂ to B₅. The effect of potential limit will be discussed by cycle number.

Figure 4.5 shows the voltage curves for sample B₁. In general, when cycled to 4.4 V, the half-cells of each composition only exhibit TM redox through the “normal” sloped region from 3.5 V to 4.4 V. When cycled to 4.6 V and 4.8 V, high voltage plateaus are observed in varying lengths for the first cycle of every composition. During charge in cycle 1, the capacity in the normal deintercalation region is the same up to each limit, as the cells exhibit the same amount of TM redox when cycled below 4.4 V. Accordingly, moving to 4.6 V results in a partial traverse of the HV plateau, while moving to 4.8 V results in a full traverse of the plateau. During discharge, TM redox is again observed from each potential limit until 2.5 V. A small sloped region from 3.25 V to 3.0 V, which increases as the potential limit increases, is also observed, the impact and possible origins of which will be discussed later. In addition, the IRC increases as the potential limit is increased, as does the voltage curve hysteresis.

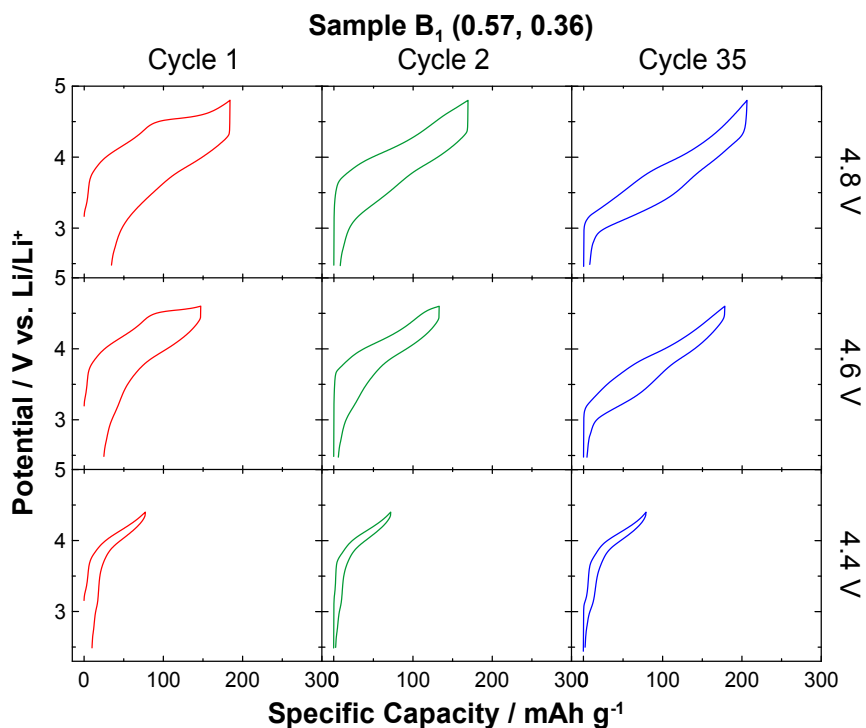


Figure 4.5. Potential versus specific capacity plots of cycles 1, 2, and 35 of sample B₁.

The voltage curves' shapes are different during cycle 2. At 4.4 V, reversible cycling is observed, while at the 4.6 V limit, TM redox is followed by a small amount of oxygen release from the HV plateau above 4.5 V. At the 4.8 V limit, TM redox is observed, with no further plateau during charge. In general, hysteresis and IRC are lowest at 4.4 V and increase as the potential limit is raised. By cycle 35, the voltage curves exhibit different shapes than at cycle 2. At 4.4 V, a small sloped region emerges at about 3.2 V during charge and 3.0 V during discharge. The same regions are observed at 4.6 V with greater capacities, which are larger still up to 4.8 V, both of which are accompanied by decreases in the average charge and discharge voltages. Interestingly, when compared to cycle 2, increases in capacity are observed at the 4.6 V and 4.8 V limits. This may be due to a continual increase in the capacity of the lay-

ered composition with cycling associated with crystal structure rearrangement, and will be discussed later in the thesis.

The capacity versus potential curves of samples B₂ to B₅ are shown from Figure 4.6 to Figure 4.9. The cycling behaviour and changes of the voltage curves described for sample B₁ are generally the same as those of cycles 1, 2, and 35 at the limits of 4.4 V, 4.6 V, and 4.8 V within each bump composition, and will be summarized here. During cycle 1, the charge capacity observed increases as the potential limit is increased from 4.4 V to 4.6 V to 4.8 V due to greater traversal of the HV plateau. This is mirrored by an increase in discharge capacity from each potential to the lower potential limit, accompanied by an increase in IRC and hysteresis. At cycle 2, the shape of the voltage curve at 4.4 V remains the same as in cycle 1, while those of the 4.6 V and 4.8 V limits have approximately the same discharge capacity and less hysteresis than their voltage profiles in cycle 1. At cycle 35, little change is observed at the 4.4 V limit, while the 4.6 V and 4.8 V voltage curves show decreases in polarization and hysteresis while exhibiting capacity increases relative to cycle 2. Overall, the high capacities and lower polarizations of the voltage profiles of sample B₃ indicate it has the best electrochemical characteristics among the Li-deficient bump materials studied. Indeed, at 4.6 V and 4.8 V it exhibits cycling performance similar to several LRO compositions containing more Li and Ni by comparison [8].

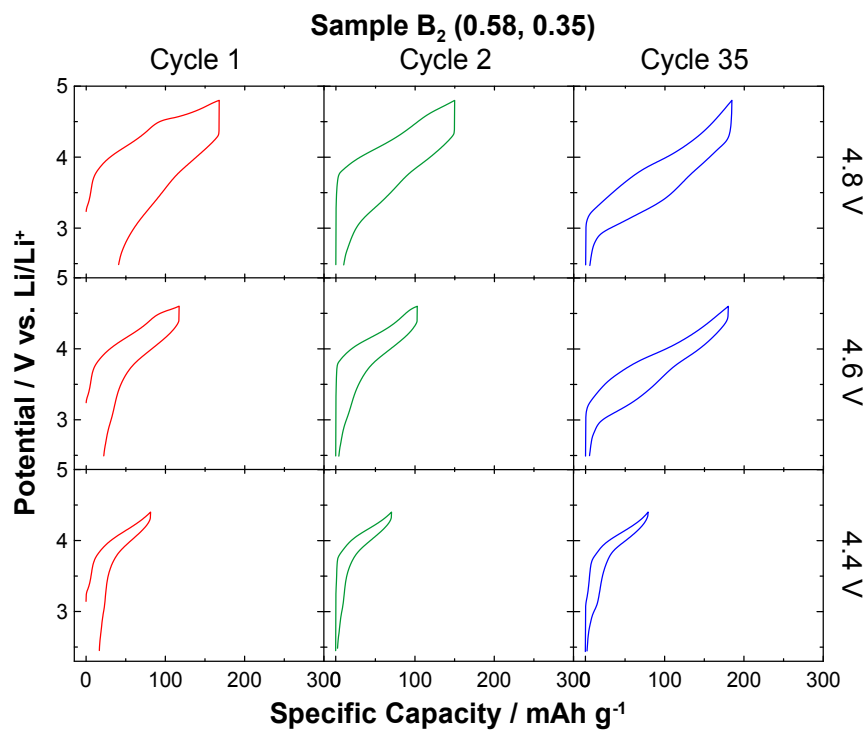


Figure 4.6. Potential versus specific capacity plots of cycles 1, 2, and 35 of sample B₂.

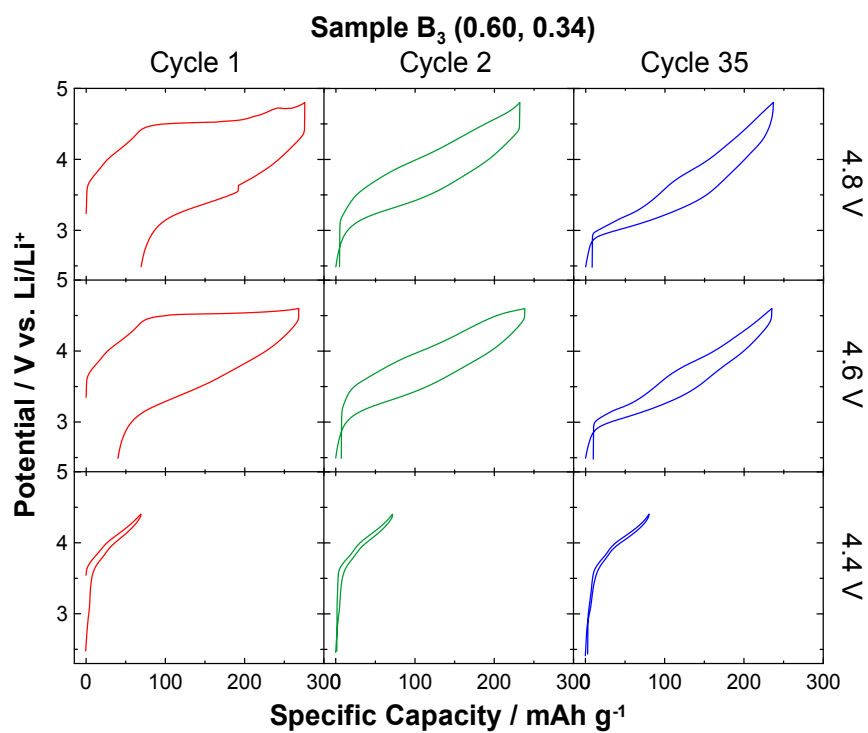


Figure 4.7. Potential versus specific capacity plots of cycles 1, 2, and 35 of sample B₃.

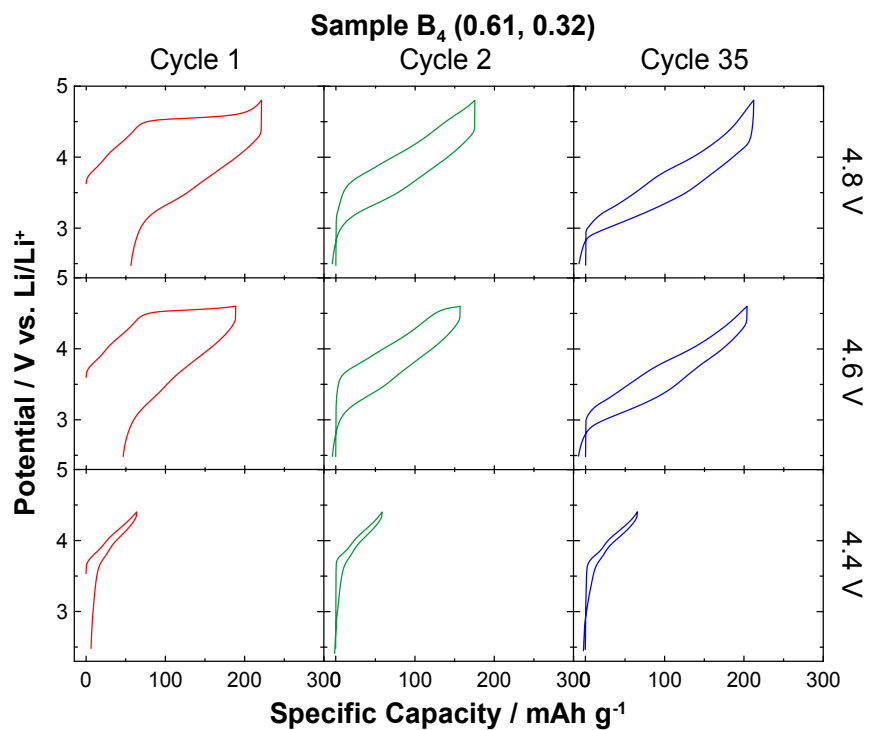


Figure 4.8. Potential versus specific capacity plots of cycles 1, 2, and 35 of sample B₄.

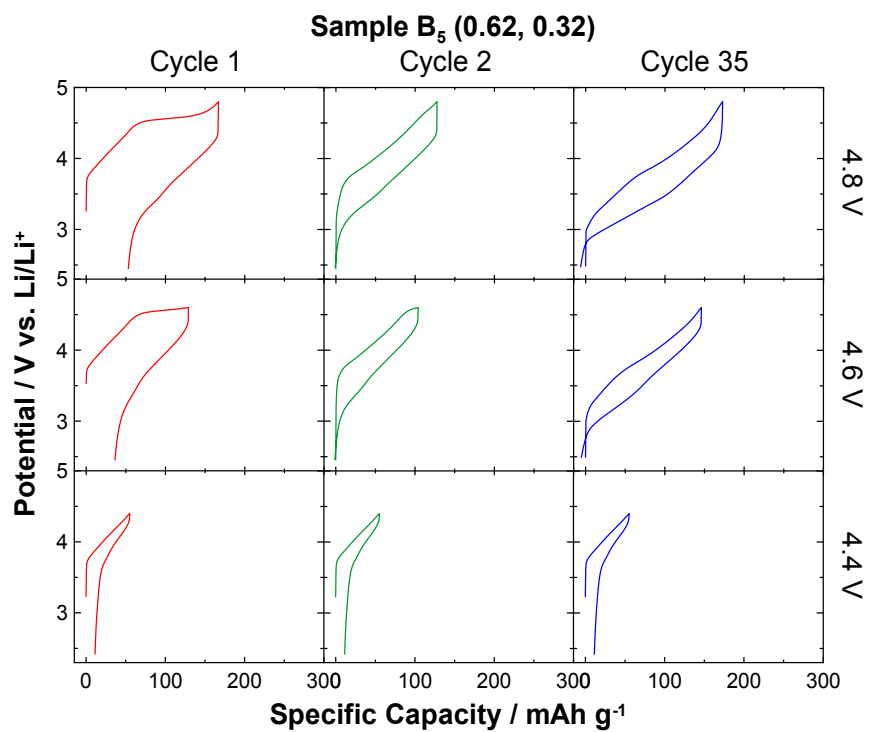


Figure 4.9. Potential versus specific capacity plots of cycles 1, 2, and 35 of sample B₅.

Figure 4.10 summarizes the IRC, discharge capacity, and average discharge voltage of samples B₁ to B₅ as a function of their Li mole fraction. For each bump composition, the IRC continually increases from 4.4 V to 4.8 V. For samples B₁ and B₂, the difference between the IRC value at each potential limit is relatively small. Sample B₃ exhibits a distinct change in behaviour, as the IRC at 4.4 V is almost zero. As the potential limit increases, the IRC increases dramatically due to the HV plateau. Sample B₄ exhibits similar behaviour, with less difference between IRC values, while sample B₅ exhibits even less difference between the IRC at each limit. The IRC at 4.6 V and 4.8 V generally increases as the Li metal mole fraction increases from sample B₁ to B₅, again reflecting the extent of traverse across the HV plateau, as shown in the voltage profiles. However, sample B₄, and B₃ in particular, exhibit extremely low IRC values at 4.4 V, mirroring the minimal amount of polarization observed in their voltage curves, marking these compositions as distinct in terms of their initial cycling.

In general, the discharge capacity of each composition increases as the upper potential limit increases. On average, the discharge capacity of each sample up to 4.4 V ranged from 50 mAh g⁻¹ to 75 mAh g⁻¹ at cycle 2, with 10% to 20% increases in capacity observed at cycle 35. At the 4.6 V limit, all samples at cycle 35, except B₃, exhibited capacity increases between 32% (sample B₄) and 77% (sample B₂) of their values at cycle 2. At cycle 35 of the 4.8 V limit, the discharge capacities increased between 23% and 40% of their values at cycle 2. After 100 cycles from 2.0 V to 4.8 V (where the lower limit of the 4.8 V samples was decreased to 2.0 V as seen in Figure 4.13), discharge capacities between 175 mAh g⁻¹ and 220 mAh g⁻¹ were observed for each composition as shown by the orange crosses in Figure 4.10. Only sample B₃ exhibited similar capacities at the 4.6 V and 4.8 V potentials limit with little to no observable

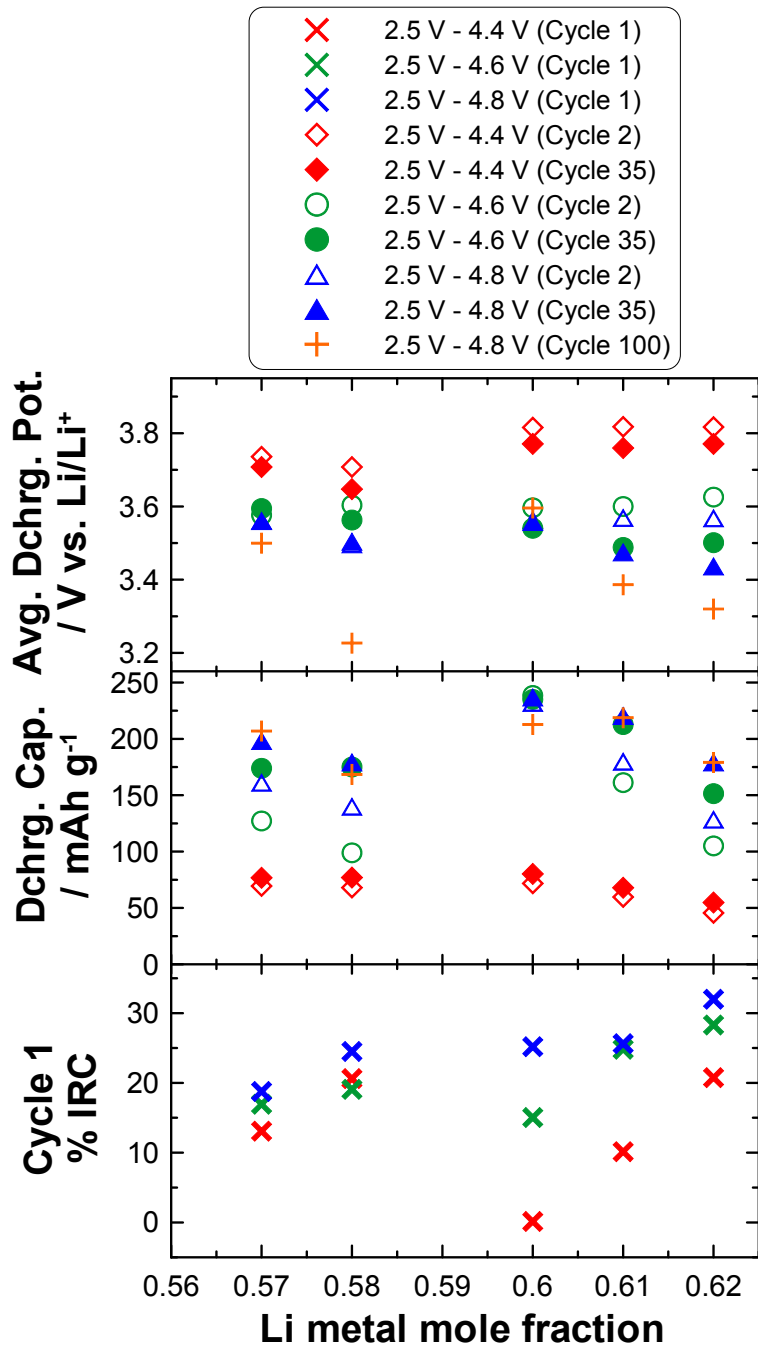


Figure 4.10. IRC, discharge capacity, and average discharge potential of different cycles for half-cells of samples B₁ to B₅. Note that the discharge capacity and average potential of cycle 100 (orange crosses) were calculated from 2.5 V to 4.8 V after each cell's lower potential limit was decreased from 2.5 V to 2.0 V (see Figure 4.12(c)).

increase in capacity between cycles 2 and 35, again indicating a notable difference in behaviour from the other compositions.

The average discharge voltage was found to decrease at the 4.4 V limit within each composition from cycle 2 to 35. At 4.6 V, the average voltage remained unchanged for sample B₁, and decreased incrementally from samples B₂ to B₅. At 4.8 V, the voltage remained unchanged for samples B₁ to B₃, and decreased incrementally in samples B₄ and B₅. Over 100 cycles, the average voltage further decreased in all compositions except sample B₃.

LRO materials have been shown to also exhibit continual decreases in average voltage on discharge with extended cycling, often referred to as “voltage decay” [57, 58]. Such changes in the voltage profiles of LROs and other layered materials such as LiMnO₂ have been attributed to a conversion from the layered phase to a spinel or “spinel-like” phase due to TM migration and subsequent structural rearrangement during cycling [59, 60]. It therefore appears that the Li-deficient layered materials within the bump also experience this phenomenon, in addition to the HV plateau of the LROs. Given the wide range of IRC, capacity, and average potential values exhibited by the bump materials, differential capacity analysis was conducted to study the phase(s) present in each composition responsible for Li removal on charge and reinsertion during discharge.

4.4 Differential Capacity Analysis of Bump Materials

Figure 4.11 shows differential capacity (dQ/dV) versus potential plots of each bump sample from cycle 1 to 35. The plots of sample B₁ will be used to describe

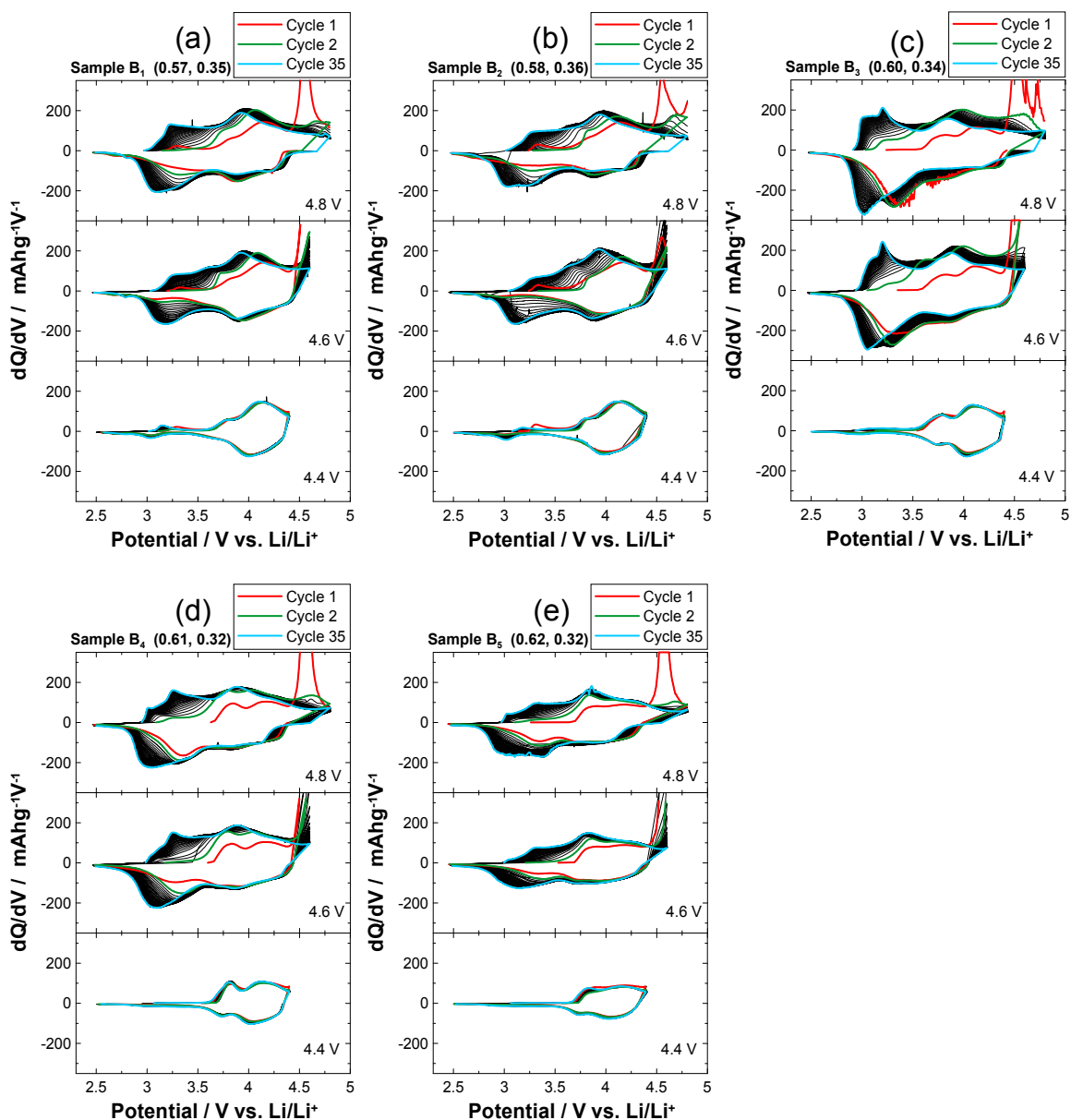


Figure 4.11. Differential capacity plots of cycles 1 (red), 2 (green), and 35 (blue) of samples B_1 to B_5 .

the general observations of dQ/dV for each composition. During the first charge (shown in red), two peaks of the same shape and magnitude in the range of 3.5 V to 4.4 V were observed at each upper potential limit. These peaks correspond to normal TM redox in the layered phase. At 4.6 V, the increase in peak magnitude at 4.45 V

corresponds to the beginning and partial traversal of the HV plateau. At 4.8 V, a large peak at 4.5 V indicates a significant removal of Li associated with an almost complete traverse of the HV plateau. The absence of a mirror peak during discharge indicates the irreversible nature of the oxygen release process at high voltage. During the first discharge, reversible TM cycling is observed from 4.4 V to 2.5 V. While the same result is observed at the 4.6 V limit, an increase in peak magnitude in the 3.25 V to 3.0 V range suggests the beginning of spinel conversion. An even larger increase in this range is observed from 4.8 V.

During cycle 2 (highlighted in green), the peak shape and magnitude from 2.5 V to 4.4 V is virtually the same as that of cycle 1 during charge and discharge at the 4.4 V limit. In comparison, the magnitudes of the two charge capacity peaks between 3.5 V and 4.4 V for the 4.6 V and 4.8 V limits increase noticeably compared to their cycle 1 counterparts. These peaks also shift to slightly lower potentials than those of cycle 1, indicating a change in chemical environment within the layered material associated with oxygen loss and TM migration at high potential [22]. During discharge, TM reduction is again observed to be about the same magnitude as that of cycle 1, while the peaks from 3.25 V to 3.0 V increase in magnitude compared to cycle 1.

Observing the changes in dQ/dV features up to cycle 35 (highlighted in blue) suggests that sample B₁ converts from a single-phase layered material into a multi-phase layered-spinel material at higher potentials. At the 4.6 V limit, a new peak emerges near 3.25 V, the peak at 3.75 V shifts to 3.6 V, and the peak at 4.1 V shifts to 3.9 V during charge. During discharge, the magnitudes and positions of the peaks from 4.6 V to 3.5 V remain largely unchanged from cycle 1, while the peak between 3.25 V and 3.0 V both broadens and increases significantly. Very similar changes in the dQ/dV plot are observed at 4.8 V, although the reduction peak from 3.25 V to 3.0 V appears

to actually be two separate, overlapping peaks at 3.1 V and 3.25 V. Finally, two overlapping peaks emerge at 3.05 V and 3.25 V during charge. These peaks may represent the reversible cycling of the new spinel-like and/or the electrochemically active layered phase, respectively, although their origin is unknown and requires further study.

In general, most of the peak positions, shifts in potential, new peaks, and peak magnitude values/changes observed at each potential limit in the dQ/dV plots of sample B₁ were present in each bump material to different extents. Through 35 cycles at the 4.4 V limit, the capacity due to normal TM redox remains mostly the same during charge and discharge within each composition. However, samples B₁ and B₂ show the emergence of peaks near 3.2 V during charge and 3.05 V during discharge, which are at similar positions as peaks observed at the 4.6 V and 4.8 V limits.

The 3.5 V to 3.0 V voltage range during discharge contains an apparent overlap of several peaks at approximately 3.25 V and 3.1 V at both the 4.6 V and 4.8 V limits. The peak at 3.25 V during discharge has been associated with Mn^{3+/4+} reduction in the layered LROs [40]. Viewed as such, more layered redox is observed in earlier cycles, but as spinel conversion proceeds with cycling, increasing capacity is observed during discharge due to the spinel phase. At the 4.6 V limit, these peaks overlap significantly, as conversion to spinel appears to be slower with cycle number, while at the 4.8 V limit, these peaks are more distinct and continue to separate with cycling.

The 4.4 V limit plots of samples B₁ and B₂ also show a single peak at about 3.3 V during charge not seen in the other materials during the first cycle. This peak provides some insight into the origin of the 3.2 V peak during charge. In their pristine forms, samples B₁ and B₂ are single-phase layered/monoclinic compositions near the top of the bump in the single-phase layered boundary. Given that no spinel is initially present in either composition, as determined by XRD analysis, the 3.3 V dQ/dV peak

observed during the first charge must be associated with redox within the layered/monoclinic phase. After the first discharge, a small peak near 3.05 V is observed from cycle 1 onwards that continues to increase in magnitude with cycling. This indicates that while layered to spinel conversion is greater at high potential, decreasing the lower potential limit does not completely inhibit the phase transformation in these compositions. At the same time, the peak at 3.3 V during charge shifts to 3.2 V after 35 cycles in the same manner as observed at higher potential limits. Thus, the peak at 3.2 V during charge is attributed to Li deintercalation from the layered phase, and its increase in magnitude with cycling is in agreement with the increase in specific capacity observed from 3.0 V to 3.5 V manifesting in a broad, overlapping peak at 3.2 V during charge of the voltage profiles at 4.6 V and 4.8 V of each composition. Therefore, the peak that emerges at 3.05 V during charge and discharge seen at 4.6 V and 4.8 V is most likely associated with reversible cycling of the new spinel phase.

The features of the dQ/dV curves indicate that the bump materials have complex structural environments which change significantly while cycling, resulting in a continual evolution of their electrochemical behaviour. The impact of extended cycling to each upper potential limit is discussed in the following section.

4.5 Extended Cycling Analysis

Figure 4.12 shows the specific discharge capacity of each bump composition over 100 cycles at each upper potential limit. The compositions exhibit similar behaviour at each potential limit. For the 4.4 V limit, minimal capacity increase is observed for each bump composition up to cycle 35 (see Figure 4.10), after which the materials cycle reversibly with constant capacity values up to cycle 100. At 4.6 V, the discharge capaci-

ty of each composition increases slowly over 10 to 20 cycles until reaching a maximum or peak value near cycle 35. At this point, the capacity either began to fade (B_1 to B_4) or increase more gradually with cycling (B_5). By contrast, the capacity increase observed at the 4.8 V limit was faster, taking place over 5 to 10 cycles, after which the capacity either remained constant (B_1 to B_3) or increased more gradually with cycling (B_4 and B_5). After plateauing, the capacities of B_1 to B_3 began to increase again with cycling.

Once the cycling trends of each composition were established at 4.6 V, the upper potential limit was increased to 4.8 V to determine whether more capacity could be accessed. This resulted in the first “jump” in capacity seen in each plot in Figure 4.12(b). While accessing more capacity than at 4.6 V, the increase did not inhibit the capacity fade in any discernable manner. Further increasing the voltage range by decreasing the lower potential limit from 2.5 V to 2.0 V up to cycle 100 resulted in the second “jump” in the capacity of each composition, but also did not limit the rate of capacity fade with cycling. In both cases, the capacity jump observed was due to the material being able to access more of the activated layered phase and/or the newly formed spinel phase within the larger potential window. The lower potential limit from the 4.8 V upper limit was also decreased to 2.0 V once the capacity stabilized after increasing in the first 5 to 10 cycles. This also resulted in access to additional capacity within each composition, as shown by the jumps in Figure 4.12(c). The capacity of each composition continued to increase until a maximum value at which the capacity began to slowly fade, as described above for the 2.5 V to 4.6 V range.

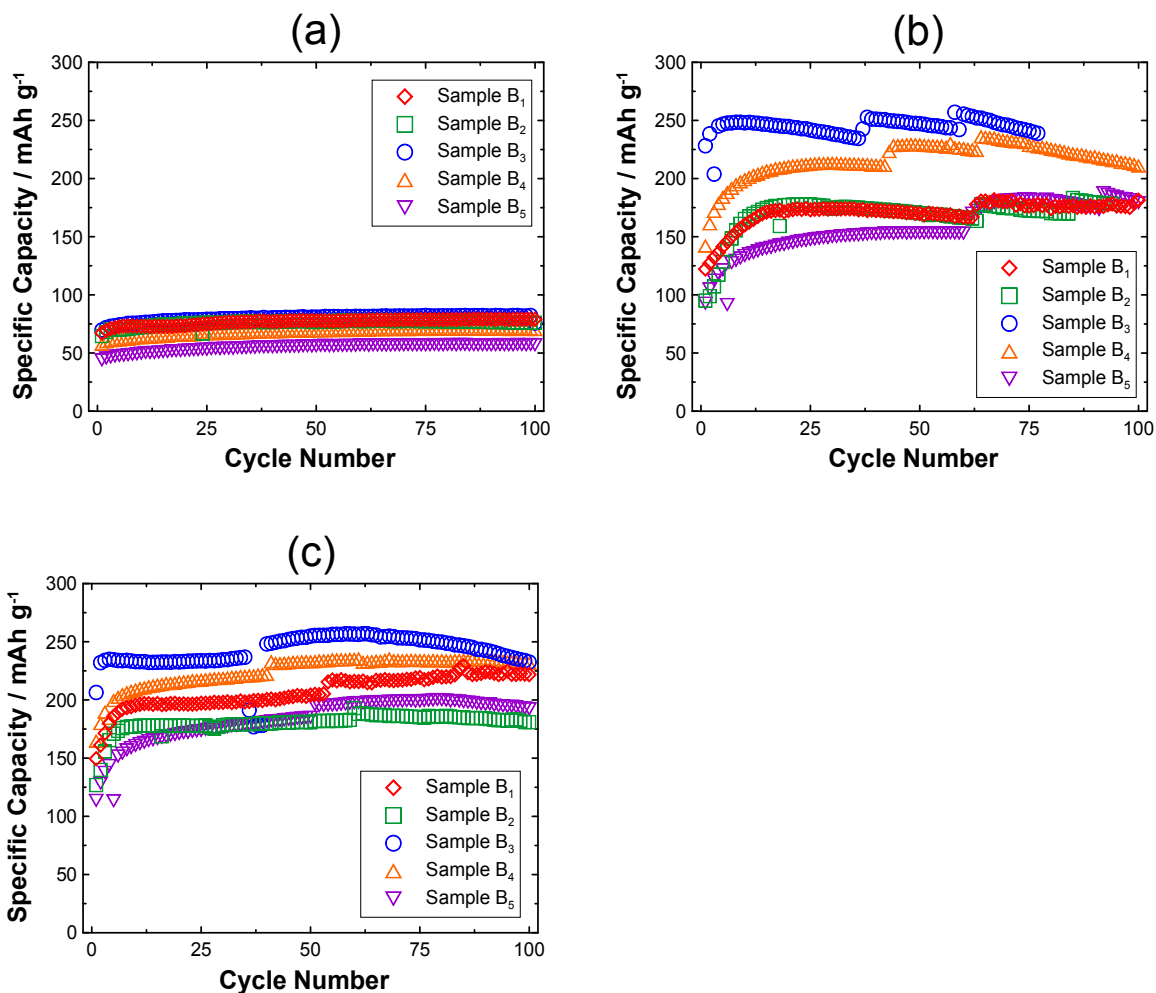


Figure 4.12. Specific capacity versus cycle number of samples B₁ to B₅ initially cycled from 2.5 V to (a) 4.4 V, (b) 4.6 V, then 4.8 V, and finally from 2.0 V to 4.8 V, and (c) 4.8 V, then from 2.0 V to 4.8 V. The steps in potential limits are indicated by the “jumps” in capacity within the data of each sample.

The effect of extended cycling on the degree of layered to spinel conversion in each composition after 100 cycles is shown by the voltage profile and differential capacity plots in Figure 4.13. The discharge capacities of each composition after 100 cycles are all approximately the same as after 35 cycles, as shown by the orange crosses in Figure 4.10. As shown in the voltage profiles, every composition exhibited an elongated plat-

eau from approximately 3.1 V to 2.9 V during discharge. Although not present in the voltage profiles when cycled to 4.8 V after cycles 1 and 2, this plateau accounted for more than 50% of the discharge capacity of each composition after 100 cycles. When compared to cycle 35 at the 4.8 V limit of the differential capacity plots in Figure 4.5 to Figure 4.9, the 3 V discharge peak almost doubles in magnitude for samples B₁ to B₄, with a small increase in sample B₅. The “layered peak” at 3.25 V remained constant or decreased marginally up to cycle 100. These changes during discharge were accompanied by increases in the spinel peak at 3.1 V and the layered peak at 3.2 V, and a decrease in the layered peak at 4 V during charge. Overall, these changes indicate that each material, with the exception of B₅, underwent dramatic layered to spinel phase transformations during cycling to high voltage. While spinel conversion causes voltage decay during discharge in many LRO materials, the extent of the conversion of the bump materials is unique among the Li-Mn-Ni-O compositions. Throughout the remainder of this thesis, this feature of the new spinel phase will frequently be referred to as the 3 V plateau and/or peak for simplicity.

Sample B₃ exhibits the greatest degree of spinel conversion, having the largest 3 V peak of each material. The voltage profile also has the lowest polarization and hysteresis observed, as well as the highest average discharge voltage, as shown in Figure 4.10. Unique to this composition is a small sloped capacity region near 4.7 V during charge and discharge. Broad dQ/dV peaks during charge and discharge also indicate an increase in capacity in this potential range. As discussed in Section 1.3.3, the HV spinel LiNi_{1/2}Mn_{3/2}O₄ exhibits Ni^{2+/4+} redox at this voltage, although dQ/dV plots typically show two distinct peaks for each redox couple (Ni^{2+/3+} and Ni^{3+/4+}) during charge and discharge [61, 62].

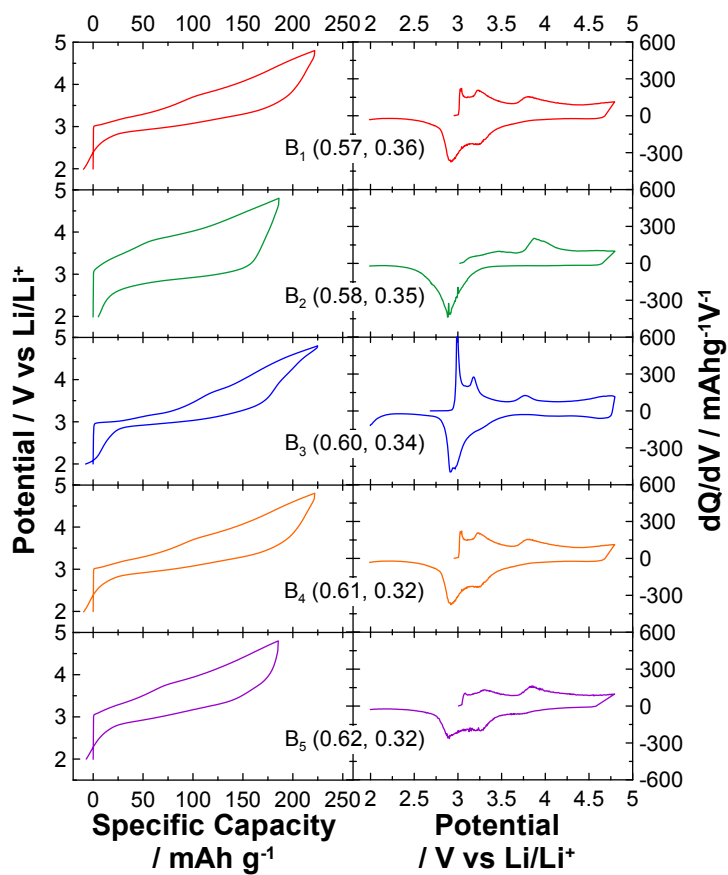


Figure 4.13. Potential versus specific capacity plots (left panel) and differential capacity plots (right panel) of cycle 100 for samples B₁ to B₅ cycled initially from 2.5 V to 4.8 V, then from 2.0 V to 4.8 V, as shown in Figure 4.12(c).

While the dQ/dV peaks of B₃ are very broad, their appearance at this potential suggests that they may originate from a HV spinel phase. Recent high resolution transmission electron microscopy and electrochemical studies have shown that the layered to spinel conversion in LROs involves the migration of Ni ions from the particle bulk to its surface [23]. It may be that the intermediate vacancy content of sample B₃ (within the bump series) allows Ni to move to the particle surface with extended cycling, resulting in a high Ni content spinel phase that exhibits redox near 4.7 V. Such migration may also result in a more Mn-rich spinel phase within the bulk exhibiting

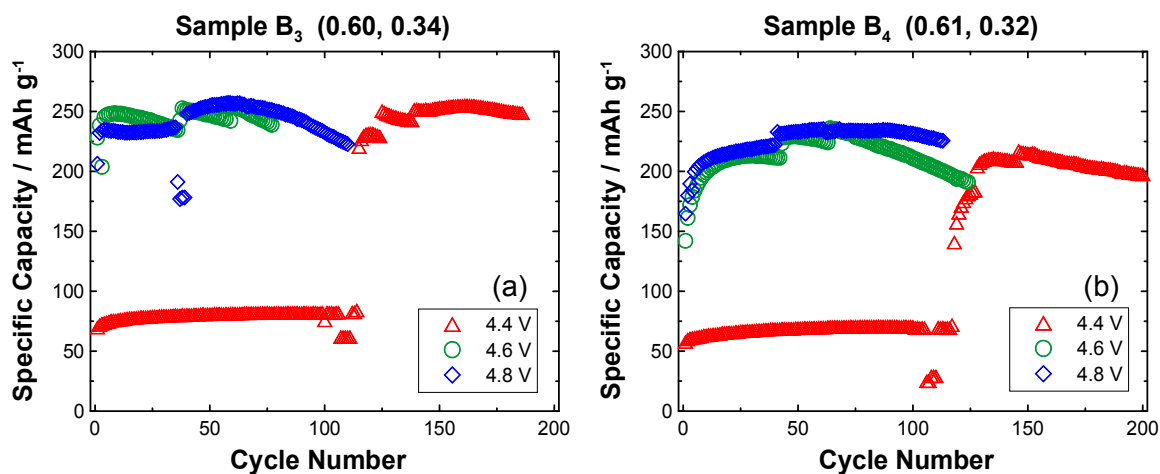


Figure 4.14. Specific capacity versus cycle number of samples B₃ and B₄ at each upper potential limit. Up to 100 cycles, each plot is the same as that shown in Figure 4.12 for the 4.4 V, 4.6 V, and 4.8 V limits of samples B₃ and B₄. After 100 cycles, the 4.4 V limit was increased to 4.6 V and then to 4.8 V, after which the lower potential limit was decreased to 2.0 V.

redox near 3 V on discharge, as observed during spinel conversion in LiMnO₂ [59]. Further study is required to determine the source of this capacity at high voltage.

Figure 4.14 shows plots of specific discharge capacity versus cycle number for samples B₃ and B₄ at each potential range studied. For cells cycled to the original 4.4 V limit (red triangles), stepping to the 4.6 V, 4.8 V, and lower 2.0 V limits in succession produces discharge capacities and cycling behaviour very similar to that of the cells originally cycled to those limits. Stepping from 4.4 V to 4.6 V in samples B₃ and B₄ results in the same initial capacities, maximum capacities, and capacity fade observed at the original 4.6 V limit of each sample. Stepping from 4.6 V to 4.8 V results in the same jump in capacity, amount of capacity, and capacity fade when compared to stepping from 4.6 V to 4.8 V. Finally, decreasing the lower potential limit from 2.5 V to 2.0 V results in similar capacity increases, maximum values, and fade behaviour of the original 4.8 V limit. Overall, the discharge capacities of each sample tend to

converge at the same values and exhibit the same trend in behaviour within each voltage window even after 100 cycles to 4.4 V. This indicates that these materials only undergo significant structural conversion at potentials above 4.4 V.

4.6 Discussion of Electrochemical Analysis

It is possible that the vacancy content of the bump materials facilitates greater TM migration during cycling, resulting in the formation of the spinel-like phase near 3 V. The high voltage plateau allows Mn^{4+} within the layered phase to become electrochemically active during discharge, resulting in Mn reduction at 3.25 V. The vacancy content of these compositions may facilitate greater TM migration from octahedral sites in the TM layer to those of the Li layer, imparting more spinel character to the structure. This spinel conversion may occur from the surface of the material to the bulk [23]. With extended cycling and conversion, Li which is removed from the layered phase during charge preferentially reinserts into 16c sites of the spinel phase during discharge rather than into the layered phase, possibly due to the presence of inactive domains of the original layered phase blocking Li-ion diffusion. As the inactive layered domains become electrochemically active and convert to spinel, the total discharge capacity of each composition would therefore increase as the spinel concentration increases.

The continual increase in capacity during the initial cycles to 4.6 V represents the incremental traverse of the high voltage plateau with repeated cycling. In LROs, traversing the HV plateau in increments over multiple cycles has been shown to increase the total attainable reversible capacity of a given material when compared to a single cycle. One approach involved a stepwise traverse based on voltage steps [63], while a

second approach used a stepwise traverse based on fractional capacity steps of the total HV plateau capacity [64]. The continual, partial traverse of the HV plateau of each bump composition at 4.6 V can therefore be viewed as a capacity-limited, stepwise traverse up to the voltage limit. For the bump compositions, cycling to 4.6 V in this manner results in capacities that are comparable to those at 4.8 V in which the capacity of the plateau is almost fully accessed during the first and second cycles, with less IRC and decrease in average discharge voltages. Therefore, cycling to 4.6 V does appear to benefit from less electrolyte oxidation at the higher potential while still exhibiting good electrochemical performance.

The spinel conversion is greater at 4.8 V than at 4.6 V. Moving to higher potential might allow even greater TM migration as the increased extraction of Li from the TM layer might introduce more diffusion pathways for TM movement into the Li layer. In Li-rich oxides, this process may lead to densification of the layer structure, increasing the IRC during discharge. It may be that within the Li-deficient bump composition, the reduced Li content facilitates less densification and more phase transformation due to TM migration, although additional studies are required to confirm this.

4.7 Summary of Electrochemical Characterization of Li-deficient Materials

Overall, further study is required to understand the combined effects of continual phase conversion and electrolyte oxidation on the cycling behaviour of the bump materials at each potential limit. It has been established here that the materials cycle reversibly at 4.4 V, and exhibit different capacity increases, maximum values, and capacity fade rates at both 4.6 V and 4.8 V. Based on its elemental, structural, physical,

and electrochemical characterization, sample B₃ appears to be the most promising material from a practical viewpoint. It has the largest reversible capacity and lowest polarization of any of the bump samples at every potential limit while maintaining a comparatively high average voltage on discharge. While conversion to spinel is significant, the magnitude of this conversion is similar to that seen in the other bump compositions. Thus, it appears that the combination of the moderate vacancy content (3.6%), small monoclinic distortion (no asymmetry of the (104) peak), and porous yet semi-spherical secondary particle characteristics combine to elevate the electrochemical capability of composition B₃ relative to the other bump samples. As such, this material was studied by high precision coulometry and compared with two Li-rich compositions in order to further access its electrochemical viability as a positive electrode material, as discussed in Chapter 6.

Chapter 5

Anomalous Capacity Growth in Slow Cooled Single-phase and Multi-phase Li-Mn-Ni-O Compositions

The establishment of the phase diagrams at 900°C in air represents an opportunity to explore previously neglected compositions in the Li-Mn-Ni-O system. The possibility exists that any number of compositions in the single-phase layered region in particular may have electrochemical properties which make them suitable for use as positive electrode materials. This chapter contains the structural and electrochemical characterization of a narrow range of samples in the slow cooled Ni:Mn 1:5 composition series near the single-phase layered boundary. It will be shown that all but one of these compositions underwent significant structural changes during cycling resulting in large, unanticipated increases in capacity relative to the original values. This increase in capacity will be referred to throughout this chapter as capacity “growth”, and the materials themselves will frequently be referred to as capacity growth materials (CGMs).

Figure 5.1 shows the slow cooled pseudo-ternary phase diagram at 900°C in air labelled with the various single- and multi-phase regions determined in Chapter 3. The inset highlights the five compositions, G₁ to G₅, which will be discussed throughout this chapter. The (Li, Mn) coordinates of each composition are shown in Table 5.1. As shown by the (Li, Mn) coordinates, these materials are effectively slow cooled counterparts of the bump materials in Chapter 5, albeit with slightly different Li contents

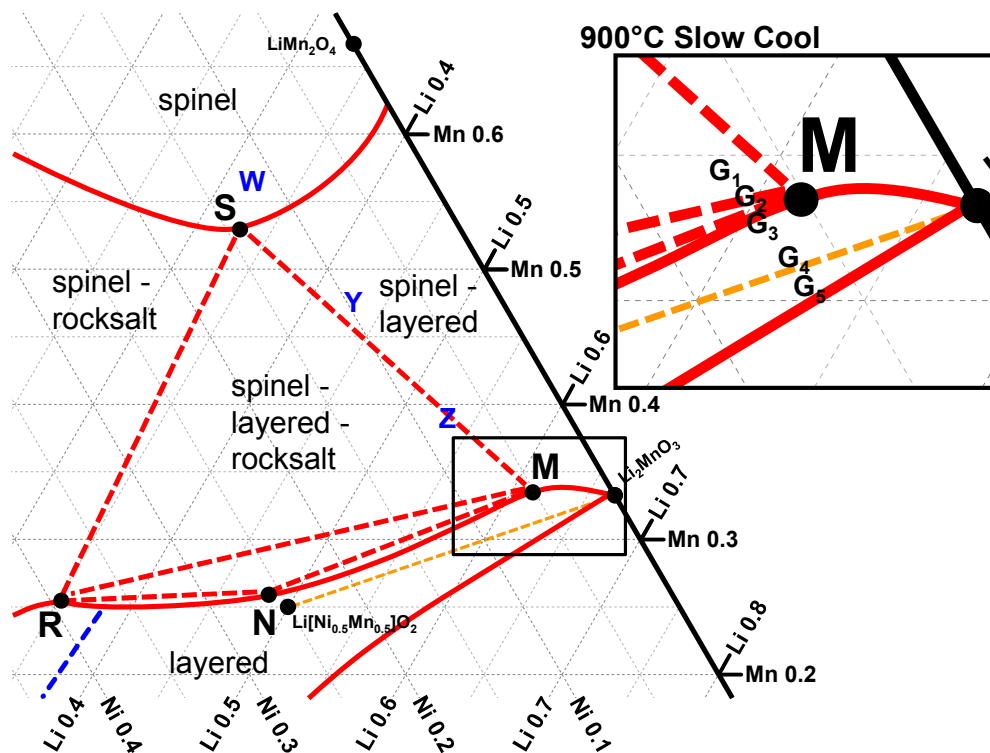


Figure 5.1. The pseudo-ternary phase diagram of the Li-Mn-Ni-O system at 900°C slow cooled highlighting the capacity “growth” compositions in the 1:5 composition series. The inset shows the single- and multi-phase regions containing samples G_1 to G_5 , the (Li, Mn) coordinates of which are shown in Table 5.1. The dashed orange line from $\text{Li}[\text{Ni}_{0.5}\text{Mn}_{0.5}]\text{O}_2$ to Li_2MnO_3 represents the stoichiometric Li-rich solid-solution series $\text{Li}[\text{Ni}_x\text{Li}_{(1/3-2x/3)}\text{Mn}_{(2/3-x/3)}]\text{O}_2$, and is shown for reference.

that extend past the nominal LRO line, as shown in Figure 5.1. Finally, data in this chapter are adapted and reprinted from reference [65] with the permission of the Electrochemical Society.

5.1 Experimental

The materials presented in this chapter were prepared according to the methods described in Section 2.1. For the solid-state synthesis process, a two-step heating pro-

cedure in air was used. The materials were first heated at 900°C for 3 hours, and then annealed at 750°C for 6 hours. Prior to the establishment of the Li-Mn-Ni-O phase diagrams, this annealing step was thought to help promote the formation of the layered-spinel composites [35, 36, 66]. The labelled slow cooled phase diagram at 900°C, shown in Figure 5.1, indicates that such layered-spinel composites do exist in the Li-Mn-Ni-O system, though not in the region of the diagram containing samples G₁ to G₅. Rather, the materials as synthesized and presented in this chapter exist as a narrow composition series which spans multiple phase regions. XRD measurements of the samples were made using the D5000 diffractometer, while SEM images were collected using a Hitachi S4700 field-emission scanning electron microscope.

For electrochemical characterization, half-cells of each composition were cycled in two separate sets, each using a different cycling protocol. Half-cells in the first set were cycled from 2.5 V to 4.9 V at 5 mA g⁻¹ for 1 cycle, then at 20 mA g⁻¹ for all subsequent cycles. Half-cells in the second set were initially cycled from 3.0 V to 4.9 V at a rate of 5 mA g⁻¹ for the first four cycles, followed by a repeating sequence of 20 cycles at 20 mA g⁻¹, then a 7-step discharge signature cycle from 320 mA g⁻¹ down to 5 mA g⁻¹. After running for an equivalent amount of cycling time, the lower potential limit of each half-cell in the second set was decreased to 2.0 V for all subsequent cycles. All cells in both sets were cycled at 30°C.

5.2 Materials Characterization

The elemental compositions of the samples as determined by ICP-OES are shown according to their (Li, Mn) coordinates in Table 5.1. Overall, the Li content within the

Table 5.1. Elemental compositions and lattice parameters of component phases of samples G₁ to G₅.

Sample ID	Sample (Li, Mn)	Layered		Rocksalt	Spinel
		a _{hex} / Å	c _{hex} / Å	a _{cubic} / Å	a _{cubic} / Å
G ₁	(0.59, 0.34)	2.8514(1)	14.284(1)	8.234(2)	8.1768(1)
G ₂	(0.60, 0.33)	2.8512(1)	14.280(1)	8.252(1)	8.1821(8)
G ₃	(0.61, 0.33)	2.8503(1)	14.277(7)	8.248(2)	-
G ₄	(0.62, 0.31)	2.8523(1)	14.258(1)	-	-
G ₅	(0.63, 0.31)	2.8541(1)	14.246(1)	-	-

compositions series was increased incrementally in order to determine its effect on crystallinity, particle morphology, and electrochemical performance.

Figure 5.2 shows the XRD patterns of the materials under study. The Miller indices of the single-phase cubic spinel (sample W) and single-phase hexagonal layered oxide (sample G₅) are labelled to clearly show the transition through the various phase regions shown in Figure 5.1. Peaks at positions corresponding to M-phase (44.6°) and S-phase (44.2° to 44.3°) end-members are clearly observed for samples containing those phases, as is a very broad peak at 43.625°. This is peak is believe to be primarily due to ordered rocksalt, possibly broadened on the right by the presence of N-phase forming in very low concentration due to non-equilibrium conditions experienced during slow cooling. The presence of superstructure peaks for all five samples in the 20.0° to 30.0° range in panel 2 indicates that the M-layered or layered phases within these compositions exhibit superstructure ordering. The intensity and sharpness of the ordering peaks are highest in samples G₁ and G₂, which also exhibit asymmetry in the (104) layered peak. This indicates that the layered phases in in these materials contain 3-D ordered superstructures. Peaks from both S- phase (clearly seen in panels 1 and 4)

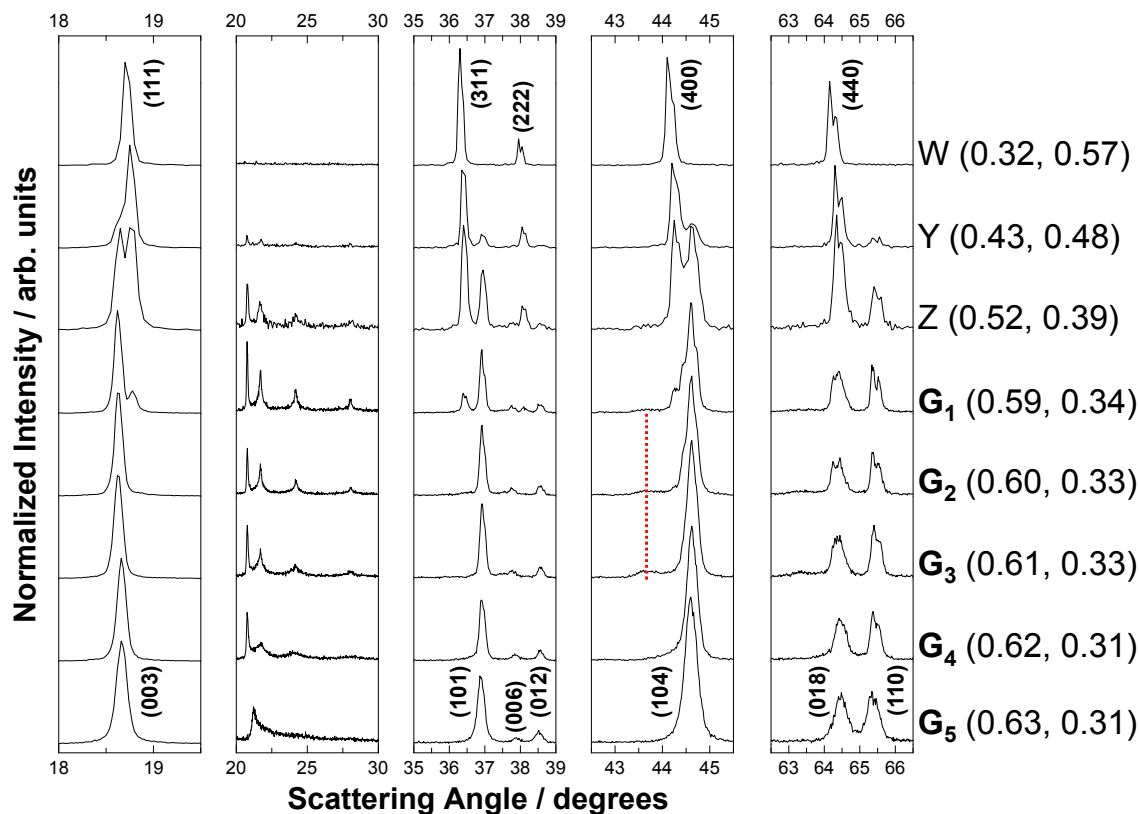


Figure 5.2. XRD patterns of samples G_1 to G_5 . Peaks of single-phase spinel (sample W) and single-phase layered (sample G_5) are labelled with Fd-3m and R-3m Miller indices, respectively. The ordered rocksalt phase is highlighted by the dashed red line.

and R-phase (broadened peak in panel 4) indicate that samples G_1 and G_2 are in the M-R-S triangle, located very close to the M-layered corner.

In sample G_3 the ordering peaks begin to broaden somewhat, especially the monoclinic (111) peak; the distortion of the (104) peak in panel 4 also begins to decrease. Coupled with the presence of the broadened rocksalt peak at about 43.63° , the location of sample G_3 appears to be in the region near the R-M line, the N-M line, the layered boundary, and the M end-member. It bears restating that the R-phase has poor electrochemical performance and is undesirable as a positive electrode material, but is effectively unavoidable in this region of the phase diagram at the compositions under

study. Indeed, the phase diagram is believed to become quite complex in the vicinity of sample G₃ due to the number of co-existence regions that surround it, such that further study is required to map this region thoroughly.

By comparison, sample G₄ and especially sample G₅ contain much broader ordering peaks and no distortion of the (104) peak, indicating that the layered phases in these compositions contain more 2-D ordering than 3-D ordering. In addition, these samples lay just above and below the nominal Li-rich oxide composition Li[Li_{0.250}Ni_{0.125}Mn_{0.625}]O₂. As no peaks from other phases were observed in their XRD patterns, samples G₄ and G₅ are confirmed as being single-phase Li-rich layered oxides. Overall, starting at the pure spinel (W) and continuing through the layered-spinel co-existence region (Y and Z) for reference, the narrow range 1:5 composition series starts in the three-phase M-R-S region (G₁ and G₂), moves through the region near the R-M tie-line, the N-M tie-line and the single-phase layered boundary (G₃), and finally ends in the single-phase layered region (G₄ and G₅).

The lattice constants of each phase present in samples G₁ to G₅ are shown in Table 5.1. The M-layered lattice constants of samples G₁ to G₃ are larger than expected for slow cooled samples, while the ordered rocksalt lattice constants are smaller than expected. It could be that the annealing step favours Li incorporation into the rocksalt phase at the expense of the layered phase. This would decrease the size of the rocksalt unit cell and increase that of the layered unit cell [16]. The spinel phase lattice constants of samples G₁ and G₂ are similar to the slow cooled values, while the layered lattice constants of samples G₄ and G₅ are in good agreement with the contour plots in Figure 3.12.

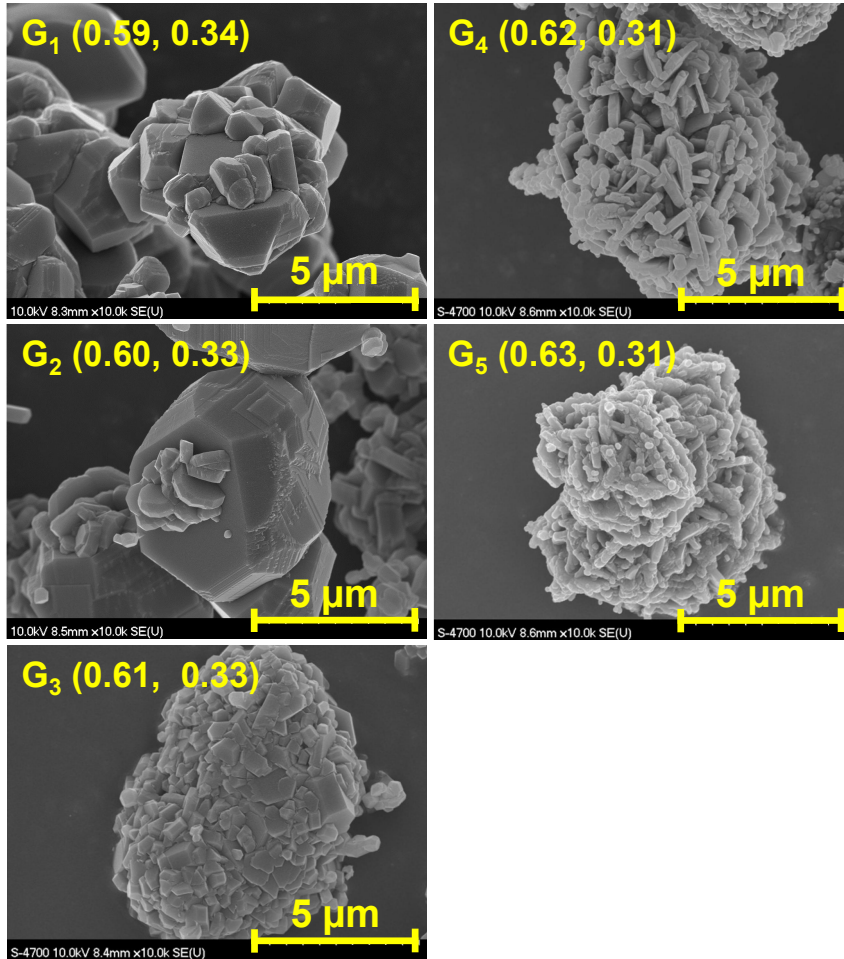


Figure 5.3. SEM images of secondary particles of samples G_1 to G_5 .

Figure 5.3 shows the SEM images of samples G_1 to G_5 . The Li content has a significant impact on the primary and secondary particle size, shape, and morphology of each sample. Sample G_1 shows intergrowth and nucleation of small primary particles into irregularly shaped secondary particles, while sample G_2 shows a co-existence of small plate-like crystallites as well as larger cubic-like particles which have 90° crystal facets. These distinct particle types support the XRD observation of co-existing hexagonal M-layered and cubic phases in these samples. The presence of large cubic-like particles is due to the spinel end-member, which has been shown to grow rapidly in

slow-cooled samples in this compositional region of the Li-Mn-Ni-O system [16, 28]. By contrast, the single-phase layered samples G₄ and G₅ show needle- and plate-shaped primary particles agglomerated into spherical, porous secondary particles which range in size from 1 to 10 μm . This particle morphology is typical of Li-Mn-Ni-O samples generated from hydroxide precursors which experience particle growth via metal ion coordination with ammonia during synthesis [38, 42, 67]. Finally, sample G₃ appears to have primary particles similar in shape to those of samples G₁ and G₂ agglomerated into a seemingly less porous, dense secondary particle similar in fashion to the pure layered samples G₄ and G₅. Overall, it is clear that the Li content of all five samples has a significant impact not only on the phases that form, but also on the size and shape of both the primary and secondary particles.

5.3 First Cycle Analysis and Observed Capacity Increase

Figure 5.4 shows the potential versus capacity curves of the first cycle for each of the highlighted capacity growth compositions. The impact of the different phase composition of each sample on the initial cycle is significant. Beginning with the two single-phase layered samples, G₄ and G₅ both exhibit two deintercalation regions during their first charge half-cycles: TM redox from open circuit voltage (OCV) to approximately 4.45 V, followed by a HV plateau up to 4.9 V. During discharge, a large IRC in excess of 30% was observed in both samples. As discussed in Section 1.3.3, these features are characteristic of the first cycle voltage curves of the Li-rich oxides and confirm the observations of these samples as such via XRD.

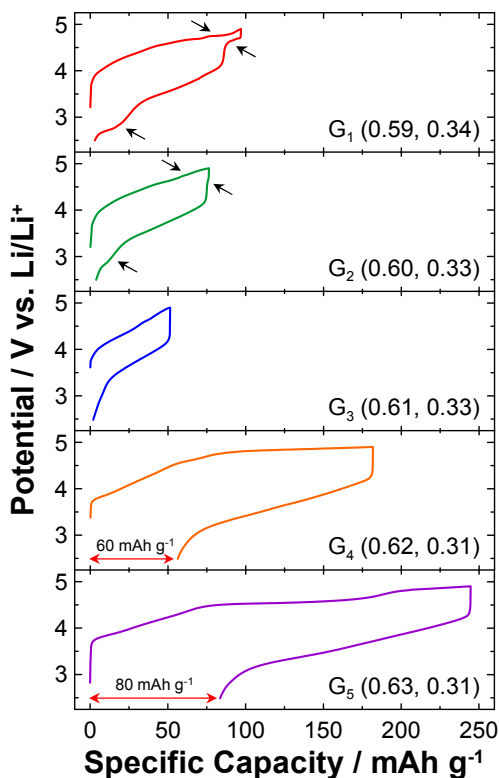


Figure 5.4. Potential versus specific capacity plots of the first cycle of half-cells for each growth composition from 2.5 V to 4.9 V at 5 mA g^{-1} and 30°C . Note the spinel features (black arrows) of the multi-phase materials (G_1 and G_2), the low capacity of the layered-rocksalt composite (G_3), and the large irreversible capacity (red arrows) of the single-phase layered materials (G_4 and G_5).

By comparison, the first cycles of the three remaining multi-phase samples were quite different from those of the layered samples. During charge, the layered phase components in samples G_1 to G_3 only underwent normal TM redox with little to no observable HV plateau up to 4.9 V. Both voltage curves of samples G_1 and G_2 show $\text{Ni}^{2+/4+}$ redox (highlighted by black arrows) due to a high-voltage spinel phase, with G_1 showing significantly more capacity. This is due to the higher amount of S-phase present in this sample, as confirmed by XRD in Figure 5.2. The S-phase in both samples appears to cycle reversibly during discharge at 4.7 V. In addition, a redox process at

2.75 V, likely due to Li insertion into the 16c octahedral site of the spinel [68, 69], is observed in both samples.

Table 5.2 shows a comparison of the theoretical capacities, 1st charge capacities, and IRC of each sample. The multi-phase materials have significantly less IRC (<5%) when compared to the single-phase layered materials (>30%), likely due to their lack of oxygen release during the first charge. However, the multi-phase samples have much smaller initial capacities compared to their layered counterparts. No sample came within appreciable range of its theoretical capacity after the first cycle, indicating that the majority of the potential capacity of these materials is initially inaccessible. Yet unexpectedly, the capacity of every sample except G₅ continually increased with each

Table 5.2. Cycling data from cycles 1 to 150 of samples G₁ to G₅. Note that the specific capacity and capacity percent increase of sample G₅ is based on 110 cycles only.

Sample ID	Specific Capacity / mAh g ⁻¹					
	Theor.*	Cycle 1 chrg	Cycle 2 dchrg	Cycle 150 dchrg	% IRC (cycle 1)	% increase (cycle 150)
G ₁	373	97	73	256	3.1	251
G ₂	394	76	46	185	5.0	302
G ₃	420	51	22	101	3.7	359
G ₄	425	182	96	227	30.9	136
G ₅	435	245	131	152	34.1	16

* calculated from ICP-OES results assuming full Li extraction per total mass of sample

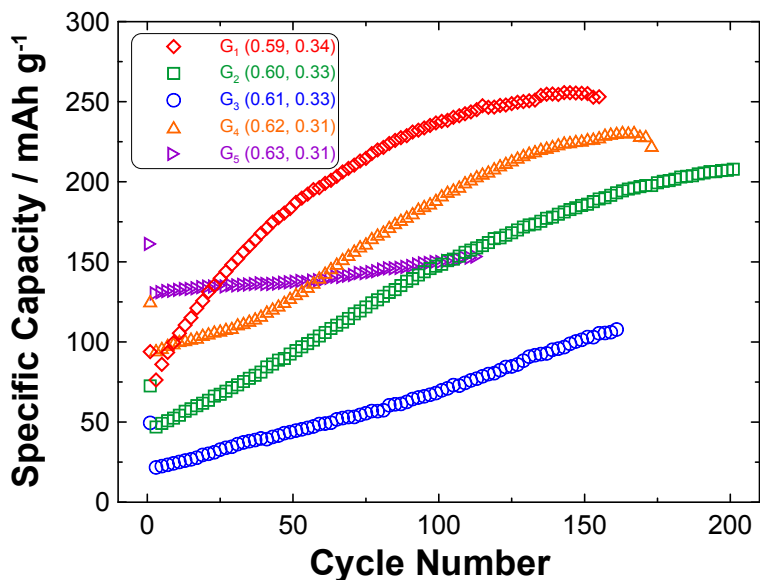


Figure 5.5. Specific discharge capacity versus cycle number for half-cells of compositions G_1 to G_5 cycled between 2.5 V to 4.9 V at 30 °C. A rate of 5 mA g⁻¹ was used for the first cycle, followed by 20 mA g⁻¹ for all subsequent cycles.

successive cycle in dramatic fashion. This is clearly seen in the specific discharge capacity plots in Figure 5.5. Remarkably, this apparent “growth” in capacity resulted in several compositions displaying capacities in excess of 300% of their initial values after 150 cycles, as shown by the initial and final capacity values and the increase percentage of every composition in Table 5.2.

With prolonged cycling, the growth process proceeded until the samples either approached or reached a maximum attainable capacity. This anomalous capacity “growth” phenomenon has rarely been reported in the literature, and increases of this magnitude have never before been observed in Li-Mn-Ni-O positive electrode materials. Several samples, namely G_1 and G_4 , eventually exhibit capacities in excess of 200 mAh g⁻¹. These findings warranted continued study of this composition series (and of other materials in this region of the Li-Mn-Ni-O phase diagram), whereas their initial

capacity values made them appear of little use from a practical viewpoint. Electrochemical analysis of the cycling of these materials over time has provided evidence of possible reasons as to why such significant capacity growth occurs.

5.4 Extended Cycling Electrochemical Characterization

Figure 5.6 shows differential capacity (dQ/dV) versus potential plots of each sample up to cycle 50 in 10-cycle increments. During the first charge, peaks in the range of 3.7 V to 4.4 V due to Ni redox in the layered phases were observed in all samples, with the single-phase layered samples yielding the largest capacities. With extended cycling, these peaks grew in magnitude during charge for all samples; the peaks for the layered phases remained fixed at 3.8 V, while those of the multi-phase samples shifted from 4.4 V to 3.85 V - 3.9 V after 50 cycles. Above 4.5 V, peaks due to the oxygen release process during the first charge were also observed in all samples to varying degrees. Sample G₅ produced the largest capacity due to oxygen release, with the remaining samples yielding less capacity by comparison. During the first discharge, the samples also showed redox peaks near 3.4 V to 3.5 V which can be attributed to the reduction of Mn⁴⁺ to Mn³⁺ within the layered phases [21, 40]. After multiple cycles, these peaks each separated into two peaks: one at 3.25 V and another at 3.0 V. Sample G₅ shows a larger peak at 3.25 V with cycling, while sample G₁ to G₅ have larger 3.0 V peaks.

Figure 5.6 also shows that the spinel phase of both three-phase M-R-S samples cycles reversibly at 4.7 V with no observed increase in capacity at this voltage after 50 cycles. Sample G₁ also shows a small peak near 2.75 V, present from the first cycle onward, which is likely associated with insertion of Li⁺ into an empty 16c octahedral

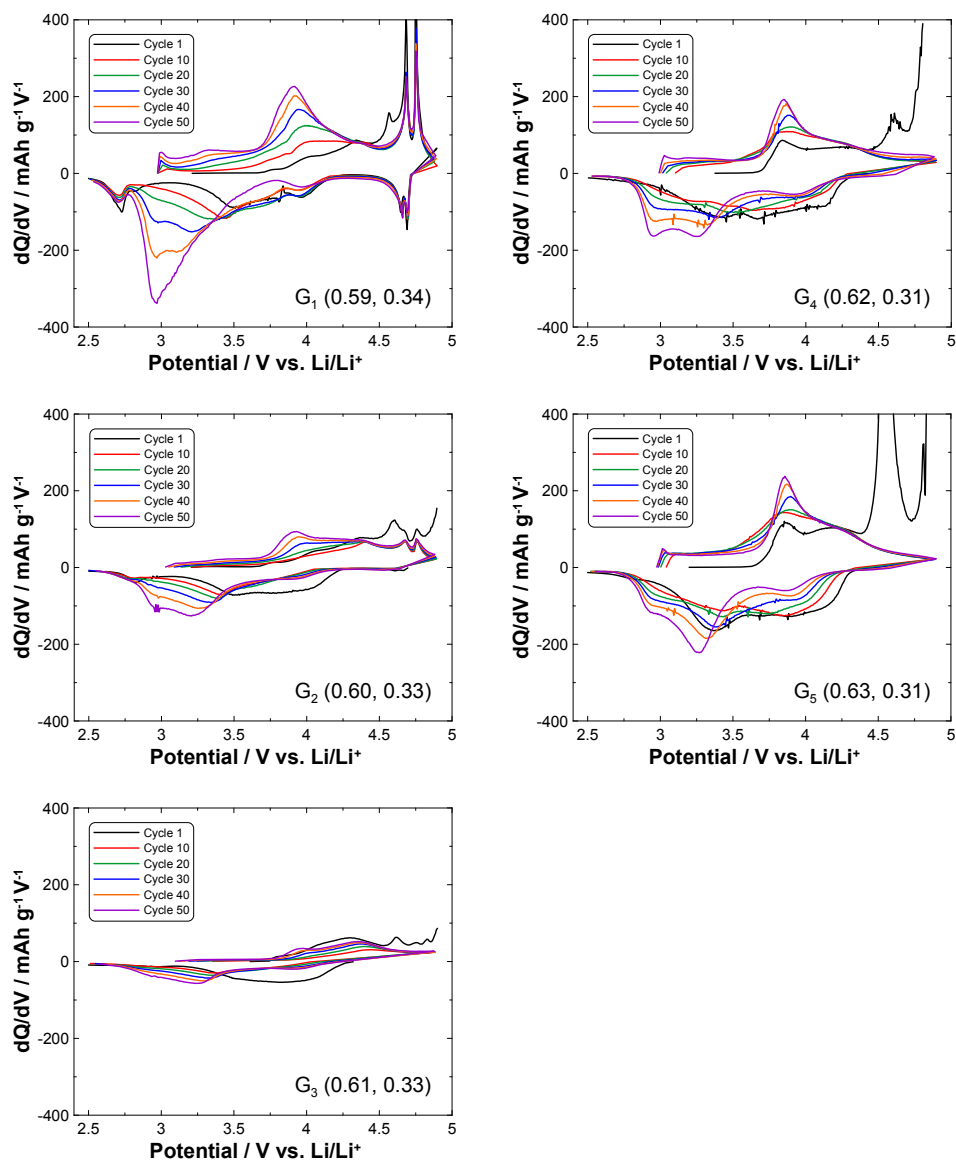


Figure 5.6. Differential specific capacity versus potential plots for half-cells of each growth composition from cycles 1 to 50 in 10 cycle increments. A rate of 5 mA g^{-1} was used for cycle 1, while subsequent cycles were run at 20 mA g^{-1} . All cells were cycled from 2.5 V to 4.9 V at 30°C .

site of the spinel phase [69]. There is no discernible contribution to capacity from the rocksalt phase from dQ/dV analysis. These results indicate that the presence of the two cubic phases neither impacts nor contributes to the observed increase in capacity with extended cycling. The possible presence of vacancies in the transition metal layer

of the layered phases in samples G_1 to G_4 may be related to the capacity growth with cycling, but further experiments are required to confirm this. Overall, the results show that the layered phases present in every sample were electrochemically active to some degree, regardless of the contribution to the total capacity of the material. Indeed, the layered phase also appears to be linked to the development of the 3.0 V peak during discharge, as the conversion is seen in varying degrees in every sample. Given that the samples which show conversion to the 3 V peak also exhibit an increase in capacity with cycling, the new 3 V peak and its associated phase or phases appears to be strongly linked to the growth process.

The changes in the dQ/dV plots with cycling shown in Figure 5.6 suggest that these materials undergo significant phase transformations when cycled. Figure 5.7 shows the effects of these transformations on the voltage profiles of the materials. Initially, the voltage curves of each composition were similar to or the same as the first cycle, with the pure layered materials showing no further oxygen loss and reversible cycling in the normal deintercalation region. With extended cycling over 150 cycles, the voltage curves of every sample except for G_5 changed significantly in the same fashion, although to different extents. During charge, extensive capacity growth was observed in two separate voltage ranges, from 3.0 V to 3.6 V and from 3.7 V to 4.4 V, as indicated by the continual elongation of the voltage curves in these regions with cycle number. The increase in capacity of the first range was moderate compared to the second range, which accounted for the majority of capacity growth during charge. During discharge, each voltage curve began to flatten out into a large plateau near 3.0 V which continued to elongate significantly with cycling. A sloped region also developed near 4.0 V with cycling, though with a small fraction of the capacity of the 3.0 V

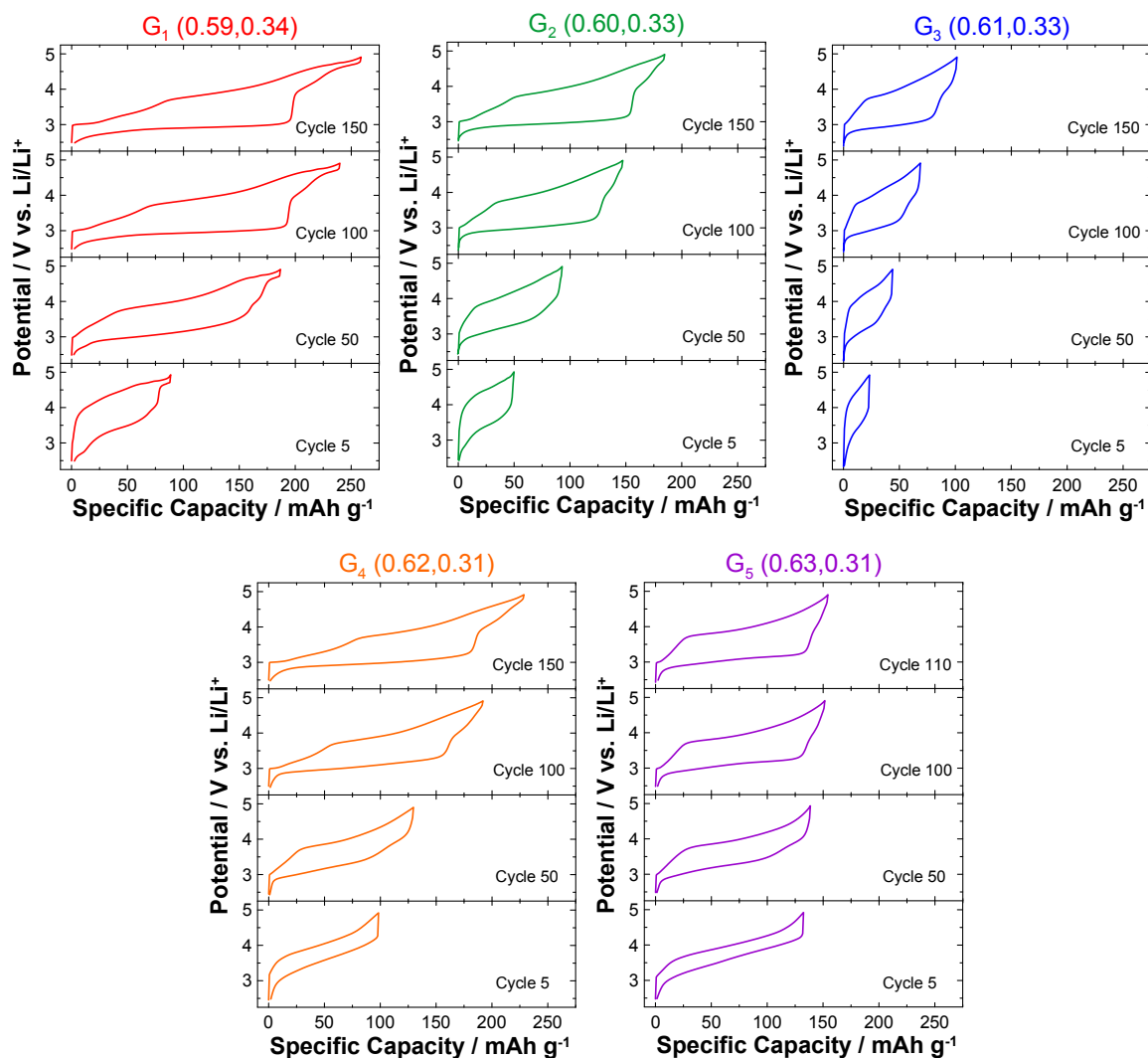


Figure 5.7. Specific capacity versus potential plots for half-cells of each growth composition after 5, 50, 100 and 150 cycles (110 cycles for sample G_5). All cycles were from 2.5 V to 4.9 V at 20 mA g^{-1} and 30°C.

plateau. The capacity in both regions continually increased with cycling, and overall, matched the capacity growth observed during charge, cycle after cycle.

Overall, the combination of the voltage curve features during charge and discharge of every composition resulted in “quasi-reversible” cycling, whereby the growth and total capacity of each charge half-cycle was matched in both growth and total capacity by the discharge half-cycle, with little to no IRC per cycle. This resulted in excep-

tionally large hysteresis in each voltage curve contributing to significant increases in polarization and a decrease in the average discharge voltage. This hysteresis, the most defining feature of which is the 3.0 V discharge plateau, further suggests that significant and irreversible phase transformations occurred during cycling. The possible role which these transformations play in the capacity growth phenomenon will be discussed later.

By comparison, sample G₅ only exhibited a 16% capacity increase after 150 cycles, which was an order of magnitude lower than the other samples (see Table 5.1). This is primarily because the initial capacity of this material was relatively large. However, while not exhibiting an appreciable increase in capacity, similarities in voltage curve features and behaviour with cycling between this single-phase layered LRO and the capacity growth compositions was observed. During charge, the capacity due to TM oxidation increased slightly from 3.0 V to 3.7 V up to 50 cycles. During discharge, a 3.0 V plateau also evolved, again producing hysteresis in the voltage curve and lowering the average discharge potential. As discussed in Section 4.3, LROs often exhibit voltage decay with cycling due to the structural rearrangement of the layered phase to spinel and “spinel-like” phases with cycling [57]. In particular, studies of the structural rearrangement of layered LiMnO₂ to spinel with cycling, including the phases which form and their electrochemical characteristics, thoroughly explain the spinel conversion process [59, 60]. A summary of this process is given below.

According to Armstrong et al. [59], when layered LiMnO₂ is cycled, Mn and Li ions migrate into tetrahedral sites in the Li layer prior to conversion to spinel, producing a phase which exhibits both layered and spinel character, coined a “splayed” phase. Differential capacity analysis showed that peaks at 3.75 V during charge and 3.9 V during discharge are due to the formation of this phase. As cycling continues, these

peaks (and hence the concentration of the splayed phase) reach a maximum, then begin to decrease as the splayed phase undergoes structural rearrangement to a spinel intermediate before converting to the final spinel phase. This conversion is seen in dQ/dV plots as a large peak at 4.0 V during charge which has no counterpart during discharge. Rather, this structural rearrangement during charge results in Li being inserted into the new spinel phase during discharge near 3.0 V, with a large associative peak in dQ/dV at this potential. Furthermore, as cycling continues, spinel Mn redox couples near 3.9 V and 4.1 V become evident with a simultaneous increase in and reversibility of the new phase at 3.0 V. With prolonged cycling, the phase transformation from layered to splayed to spinel continues until complete conversion to the new spinel phase is achieved. However, no appreciable increase in capacity with cycling was reported by Armstrong et al. [59] during the layered to spinel conversion process. Indeed, some apparent capacity increase was observed over the course of 50 cycles, but the trend did not continue, as the capacity began to fade continually with extended cycling. By contrast, the materials presented herein show gradual but steady increases in capacity coupled with the development and continual growth of a 3.0 V peak in dQ/dV with cycling. Figure 5.8 shows the differential capacity plots of each composition up to 150 cycles, highlighting the evolution of the 3.0 V peak on discharge and the extent to which it increases in magnitude with cycling.

To explore the relationship between capacity growth and lower cut-off potential, the materials were cycled to different lower potential limits. Figure 5.9 shows differential capacity plots of the materials cycled from 3.0 V to 4.9 V (left column) and then from 2.0 V to 4.9 V (right column). For the samples previously exhibiting capacity

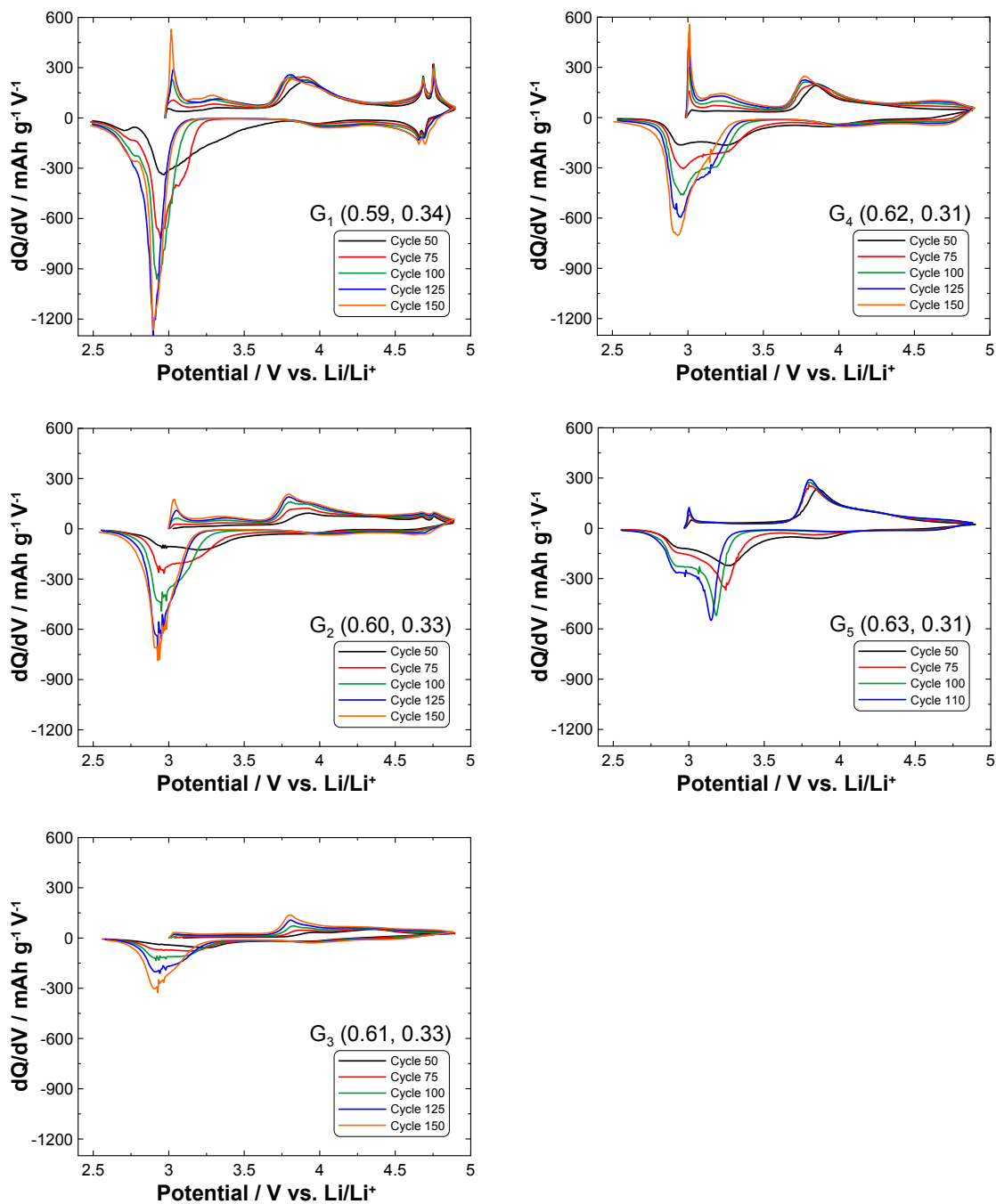


Figure 5.8. Differential specific capacity versus potential plots for half-cells of each growth composition from cycles 50 to 150 (110 for sample G_5) in 25 cycle increments. All cycles were from 2.5 V to 4.9 V at 20 mA g^{-1} and 30°C.

growth, small increases in peak magnitudes from 3.8 V to 4.4 V were again observed during charge. When cycling to only 3.0 V during discharge, slight increases in the 3.25 V peak occurred, but were significantly less pronounced when compared to the previous results. In the 3.0 V to 4.9 V range up to 50 cycles, minimal capacity growth was observed compared to the previous results, with the exception of slight capacity growth of sample G₁ due to partial conversion. Extensive conversion to the new spinel-like phase was suppressed by the 3.0 V lower potential limit, preventing significant increases in capacity with cycling from occurring.

Once this trend was confirmed, and after the cells were cycled for the same amount of time, the lower potential limit was decreased to 2.0 V. As shown in Figure 5.10, the initial results of this decrease were dramatic, as access to the extra voltage range resulted in a jump in the achievable capacity of each material due to the additional capacity between 2.0 V and 3.0 V. After the first full cycle from 2.0 V to 4.9 V, the materials contained the same peaks in dQ/dV as previously seen from 2.5 V to 4.9 V, with significant increases in magnitude compared to cycling to only 3.0 V. However, the most notable effect of decreasing the voltage was the rapid evolution of the 3.0 V peak with cycling (Figure 5.9, right panels) and the corresponding continual capacity increase with cycle number (Figure 5.10). The exception is sample G₅, which shows more conversion to the 3.25 V peak than the 3.0 V peak. The differences in peak evolution and capacity growth observed by simply changing the lower potential limit suggests that the creation of Mn³⁺ in these materials may be the driving force that leads to both the phase conversion and the capacity growth process.

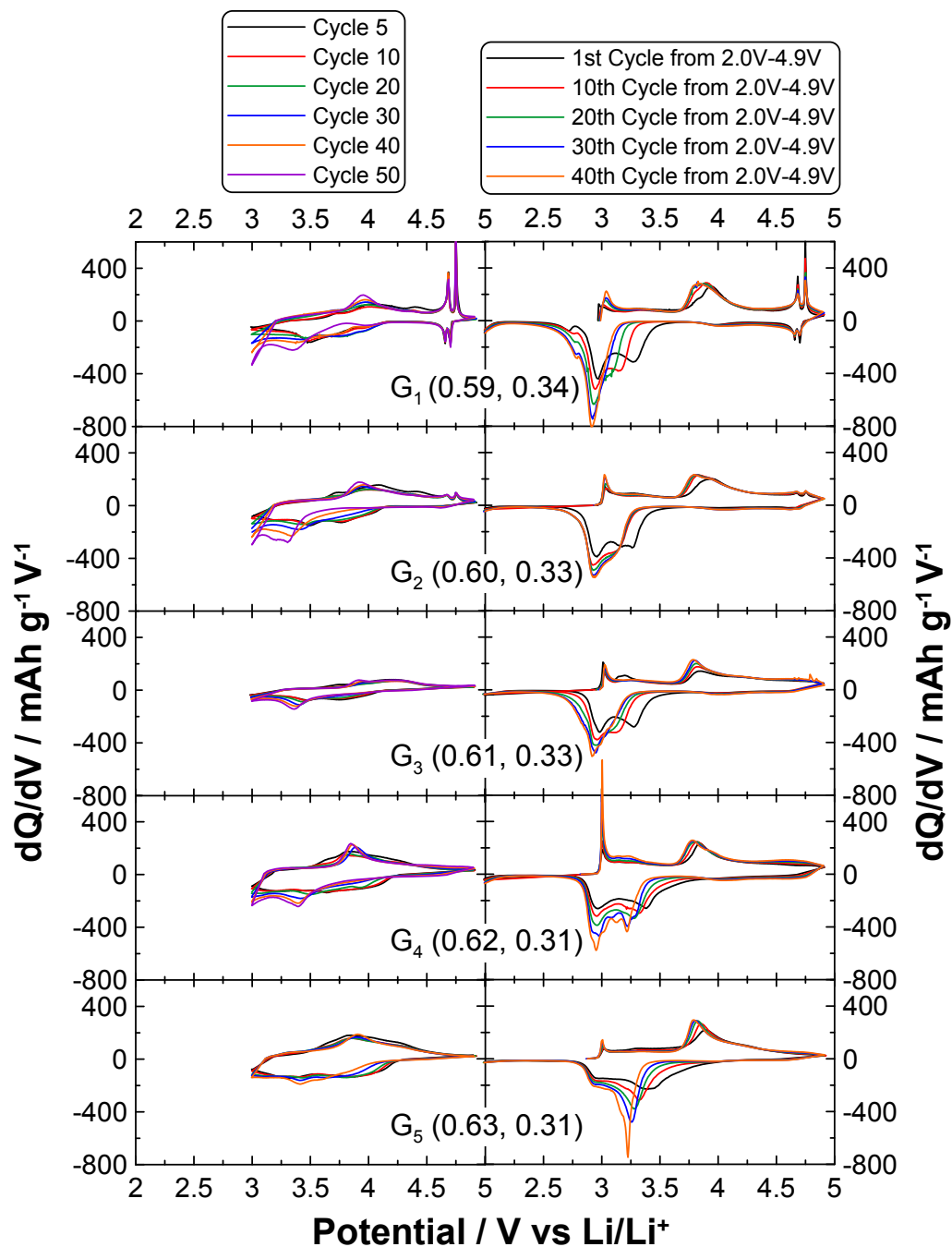


Figure 5.9. Differential specific capacity versus potential for half-cells of compositions G_1 to G_5 . The left column shows cycles from 3.0 V to 4.9 V up to cycle 50. The right column shows cycles from 2.0 V to 4.9 V after decreasing the lower potential limit from 3.0 V to 2.0 V. All cycles shown were run at 20 mA g^{-1} and 30°C.

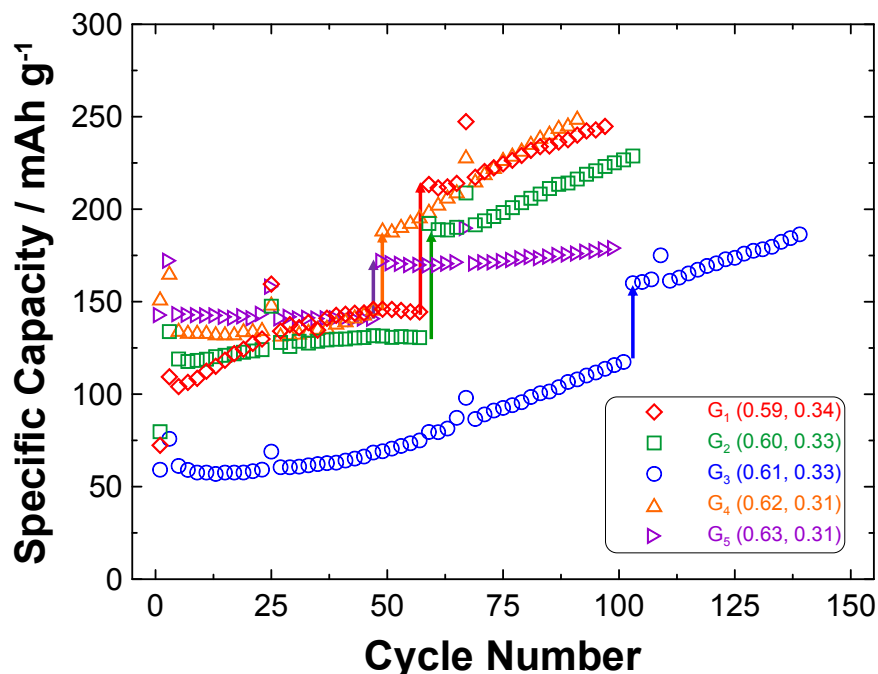


Figure 5.10. Specific discharge capacity versus cycle number for half-cells of compositions G₁ to G₅ cycled from 3.0 V to 4.9 V initially, then from 2.0 V to 4.9 V (see arrows). A rate of 5 mA g⁻¹ was used for the first four cycles, followed by a repeating sequence of 20 cycles at 20 mA g⁻¹, then a 7-step discharge signature cycle from 320 mA g⁻¹ down to 5 mA g⁻¹. All cells were cycled at 30°C. The lower voltage limit was decreased to 2.0 V only after the cells had cycled to 3.0 V for equal amounts of time.

5.5 Summary of Capacity Growth Materials

By varying the Li content of a narrow range series of slow cooled Ni:Mn 1:5 samples near the single-phase layered boundary, interesting Li-Mn-Ni-O compositions were successfully synthesized and characterized. The Li content was found to have a major impact on the phase composition, particle morphology, and electrochemical character of each sample. XRD measurements indicate that samples G₁ and G₂ are three-phase M-R-S, sample G₃ is two-phase layered-rocksalt, and samples G₄ and G₅ are single-phase layered LROs. SEM analysis revealed significant differences in primary and sec-

ondary particle size, shape, and morphology, depending on Li content and the phase(s) that formed.

During extended half-cell cycling to 4.9 V, most compositions underwent gradual yet significant crystal structure rearrangement as observed via differential capacity analysis. A phase transformation to a spinel phase exhibiting a 3.0 V redox process during discharge was observed, in a similar fashion to that of newly converted spinel phases in LiMnO_2 and of the “voltage decay” in cycled lithium-rich oxides. All but one composition (G_5) exhibited an anomalous, continual increase in capacity with prolonged cycling, with several compositions producing capacities in excess of 300% of their initial values over 150 cycles (samples G_2 and G_3). The magnitude of this apparent capacity “growth” was shown to be strongly dependent on the lower voltage limit during cycling, with significant growth occurring only when discharging below 3.0 V. While not well understood at present, the capacity growth phenomenon appears to be strongly associated with the phase transformation from the layered phase to the new spinel or “spinel-like” phase when discharging the material below 3.0 V. This may occur via a complex process during cycling in which the layered phase gradually extracts Li during repeated charges while partially converting to a “splayed” phase, in a similar fashion to layered LiMnO_2 . Whether by a slow surface-to-bulk transition and/or intrinsic kinetics, the layered phase apparently becomes more electrochemically active with cycling, indicated by the increasing magnitude of the Mn reduction peak at 3.25 V on discharge. Concurrently, the splayed phase converts to the new spinel, which inserts Li at 3.0 V. This gradual phase transformation with cycling results in progressively acute hysteresis in the voltage curves concurrent with notable decreases in the average charge and discharge voltages.

While it's been established here that capacity growth is tied to layered or spinel conversion, there are almost no reports of this phase transformation being accompanied by significant increases in capacity with cycling. However, recent studies by Lee et al. report apparent capacity growth with repeated cycling in the $x\text{Li}[\text{Li}_{0.2}\text{Mn}_{0.6}\text{Ni}_{0.17}\text{Co}_{0.03}]\text{O}_2 \cdot (1-x)\text{Li}[\text{Mn}_{1.5}\text{Ni}_{0.425}\text{Co}_{0.075}]\text{O}_4$ ($0 \leq x \leq 1$) system, comprised of Li-rich layered and spinel Li-Co-Mn-Ni-O composites [70]. This composition series is similar to the Li-Mn-Ni-O capacity growth materials in several respects. Both series have similar Ni:Mn ratios (1:3.5 compared to 1:5), contain lithium-rich layered and spinel transition metal oxide composites, and contain some compositions with an electrochemically undesired cubic phase. This cubic phase is described by the authors as an impurity; in the Li-Mn-Ni-O system, the cubic phase is the ordered rocksalt end-member which forms as part of the M-R-S co-existence region. The biggest difference between the two systems is the inclusion of a relatively small amount of Co, which is claimed to result in greater discharge capacities in LROs [71, 72]. Nonetheless, the similarities between the findings in the two systems are significant, such that further study of both may lead to the origin of the capacity growth phenomenon.

Chapter 6

Ultra High Precision Coulometry Measurements of Li-rich and Li-deficient Single-phase Layered Li-Mn-Ni-O Materials

The electrochemical analysis presented in this thesis so far has used upper potential limits of 4.4 V, 4.6 V, 4.8 V, and 4.9 V vs. Li/Li⁺. With the exception of 4.4 V, these potentials are considered to be in the high range for Li-ion battery positive electrode materials. At high potential (≥ 4.6 V vs Li/Li⁺), positive electrode materials are susceptible to electrolyte oxidation, transition metal dissolution, and electrode damage. The consequences of these reactions are electrolyte consumption, deterioration of the active material, and overall degradation in electrochemical performance. Thus, minimizing or removing these parasitic processes is essential for developing long-lived cells with high energy densities. The UHPC system [49, 50] developed at Dalhousie University yields accurate current, coulombic efficiency, and charge endpoint capacity measurements of both Li-ion full cells and half-cells [73]. These measurements provide information about parasitic reactions which occur between the active electrode material and the electrolyte during cycling. The UHPC system is therefore a useful tool for measuring and comparing the cycling stability of different positive electrode materials in half-cells. This chapter will focus on the elemental, structural, and UHPC cycling

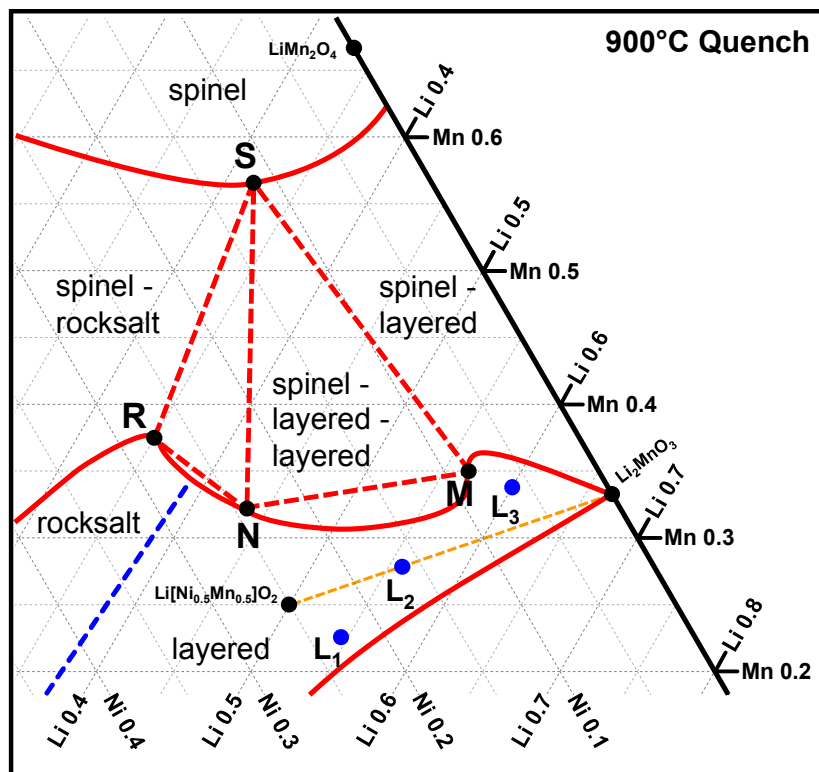


Figure 6.1. The pseudo-ternary phase diagram of the Li-Mn-Ni-O system at 900°C in air quenched showing layered samples L₁, L₂, and L₃ at (Li, Mn) coordinates of (0.55, 0.22), (0.56, 0.28), and (0.60, 0.34), respectively. The dashed orange line from Li[Ni_{0.5}Mn_{0.5}]O₂ to Li₂MnO₃ represents the stoichiometric lithium-rich solid-solution series $\text{Li}[\text{Ni}_x\text{Li}_{(1/3-2x/3)}\text{Mn}_{(2/3-x/3)}]\text{O}_2$, and is shown for reference.

analysis of three single-phase layered materials, labelled L₁ to L₃, as shown in Figure 6.1. Note that sample L₃ is the same material as sample B₃ in Chapter 4, but has been renamed in this chapter for clarity. Previously published HPC results for Li[Ni_{1/3}Mn_{1/3}Co_{1/3}]O₂ (NMC111) will be shown for comparison [49]. The (Li, Mn) coordinates, standard layered notations, and lattice constants of each sample are shown in Table 6.1. The CE, reversible discharge capacity, and charge endpoint capacity slip-page of samples L₁, L₂, L₃, and commercial NMC111 half-cells will be presented and

compared. Data in this chapter are adapted and reprinted from reference [74] with the permission of the Electrochemical Society.

6.1 Experimental

The samples presented in this chapter were prepared and analyzed according to the methods described in Chapter 2 with a few modifications, as samples L₁ and L₂ were synthesized by John Camardese. As such, the hydroxide precursors of samples L₁ and L₂ were prepared at a pH of 11.1 over 20 hours, while the precursor of sample L₃ was prepared at a pH of 10.3 over 10 hours. Each sample has a different Ni:Mn ratio, thereby requiring different pH values and reaction times in order to optimize conditions for ammonia coordination with the transition metals and subsequent particle growth during the reaction in the CSTR. For solid-state synthesis, samples L₁ and L₂ were reacted at 950°C in air for 12 hours, then slow cooled, as compositions in this region of the phase diagram are single-phase layered regardless of the cooling rate employed. By comparison, sample L₃ was reacted at 900°C in air, and then quenched between copper plates. Quenching was required for this sample in order to achieve a single-phase layered material, as its slow cooled counterpart is a multi-phase material (very close to sample G₃ in Chapter 5). The placement of samples L₁ and L₂ on the quenched phase diagram shown in Figure 6.1 is used for ease of comparison with sample L₃, which is located in the middle of the previously discussed bump region. Note that if plotted, samples L₁ and L₂ would appear at the same locations in the single-phase layered region of the slow cooled diagrams. XRD measurements of all compositions were performed on the D5000 diffractometer from 10.0° to 90.0° with a 0.05° step size and a 3 to 5 second dwell time.

The electrodes of samples L₁ and L₂ were prepared using 0.90/0.05/0.05 mass fractions of active material/carbon black/PVdF, respectively, while the electrode of sample L₃ used mass fractions of 0.86/0.07/0.07. Half-cells of all three samples were electrochemically characterized using the UHPC system. The cells were cycled individually from 2.5 V to upper potential limits of either 4.6 V or 4.8 V at a rate of 10 mA g⁻¹. Prior to cycling to the 4.6 V limit, sample L₁ and L₂ were initially charged up to 4.8 V for one half-cycle. All cells were cycled at 30°C in temperature-controlled boxes.

6.2 Materials Characterization

Table 6.1 shows the elemental compositions of samples L₁, L₂, and L₃ in (Li, Mn) notation as (0.55, 0.22), (0.56, 0.28), and (0.60, 0.34) according to ICP-OES analysis. Figure 6.2 shows the XRD patterns of each sample, all of which were indexed to the R-3m space group and fit as single-phase hexagonal layered oxides; the lattice constants from Rietveld refinement are shown in Table 6.1. Each pattern contains superstructure ordering peaks between 20.0° and 30.0°. In samples L₁ and L₂, the peaks are very weak and broad, indicating short-range 2-D ordering of Li, Mn, and Ni on the TM layer. These peaks represent the well-known superstructure in Li-rich oxides [10], confirming that both layered materials are Li-rich. The XRD pattern, lattice constants, and ICP-OES analysis of sample L₂ indicate it is very close to the Li[Li_{1/9}Ni_{1/3}Mn_{5/9}]O₂ composition, which is on the LRO solid solution line, while those of sample L₁ indicate that it is an approximate extra-lithiated analogue of the composition Li[Ni_{0.5}Mn_{0.5}]O₂, which is an end-member of the LRO series.

By comparison, sample L₃ is not a LRO, but rather a Li-deficient layered material containing metal site vacancies. As discussed previously, McCalla et al. [15] have re-

Table 6.1. Elemental composition, standard layered notation, and hexagonal lattice constants of samples L₁, L₂, and L₃.

Sample	(Li, Mn)	Layered Notation*	Lattice Parameters	
			a _{hex} (Å)	c _{hex} (Å)
L ₁	(0.55, 0.22)	Li[Li _{0.09} Ni _{0.46} Mn _{0.45}]O ₂	2.8810(2)	14.283(3)
L ₂	(0.56, 0.28)	Li[Li _{0.12} Ni _{0.32} Mn _{0.56}]O ₂	2.8732(1)	14.275(1)
L ₃	(0.60, 0.34)	Li[Li _{0.16} Ni _{0.12} Mn _{0.65} □ _{0.07}]O ₂	2.8564(1)	14.261(1)

* normalized to an oxygen stoichiometry of 2; assumes oxidation states of Ni²⁺ and Mn⁴⁺ for samples L₂ and L₃

cently shown that for samples near this bump region, decreasing the Li-content toward the upper boundary (i.e., making the materials become more Li-deficient) increases the number of metal site vacancies within the material. The XRD pattern of sample L₃ contains sharper and more intense superstructure peaks from 20.0° to 30.0°, indicating long-range 3-D ordering within the crystal structure. In addition, normalizing the elemental analysis results of sample L₃ to an oxygen stoichiometry of 2 and assuming average oxidation states of Ni²⁺ and Mn⁴⁺ yields a standard layered notation of Li[Li_{0.16}Ni_{0.12}Mn_{0.65}□_{0.07}]O₂, which indicates that the material contains approximately 3.6% metal site vacancies. By contrast, normalizing samples L₁ and L₂ in the same manner yields Li[Li_{0.09}Ni_{0.46}Mn_{0.45}]O₂ and Li[Li_{0.12}Ni_{0.32}Mn_{0.56}]O₂, respectively, which contain no metal site vacancies. None of these materials have been analyzed using UHPC before, providing an opportunity to characterize three similar yet distinct compositions in detail. Sample L₃ is of particular interest: its low Ni content makes it attractive commercially from a cost and toxicity perspective, while its composition, structure,

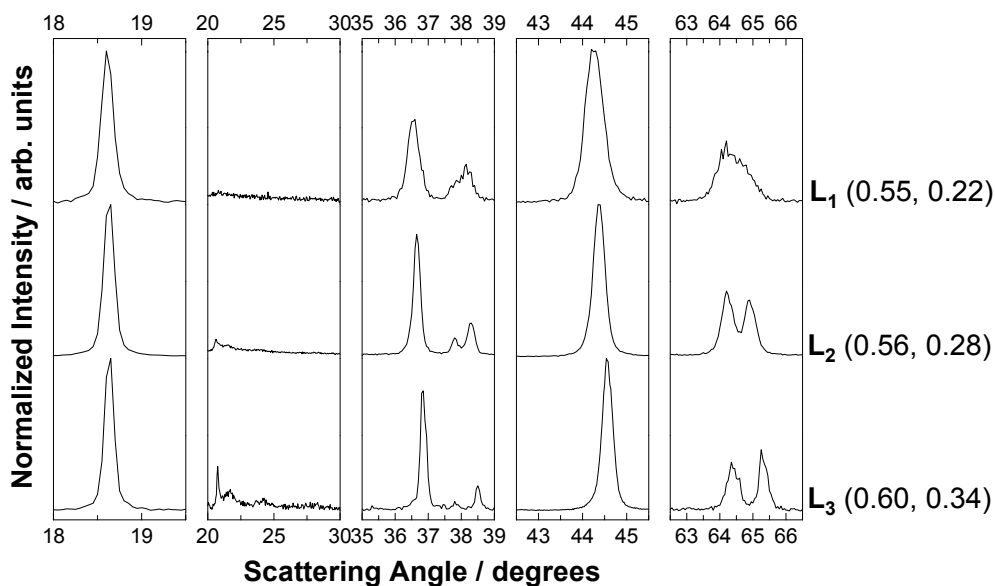


Figure 6.2. XRD patterns of samples L_1 , L_2 , and L_3 .

and vacancy content have the potential for unique electrochemical properties, as seen in Chapter 4.

6.3 Voltage Curves

Figure 6.3 shows the potential versus specific capacity plots for half-cells of each composition. These plots demonstrate charge endpoint capacity slippage, as electrolyte oxidation at high potential results in the charge endpoint capacity at the top of charge moving or “slipping” to the right relative to its previous value. For each curve, the first cycle after oxygen release is plotted in red, indicating where reversible cycling of the electrodes begins, while the last full cycle measured is plotted in blue. As shown, the potential-capacity curves for all three samples are different. The first half-cycle of sample L_1 to 4.8 V initially shows a large sloped region from 3.75 V to about 4.45 V due to $Ni^{2+/4+}$ oxidation. A small plateau above 4.45 V is seen before the potential limit is reached, indicating that little oxygen release takes place in this composition. How-

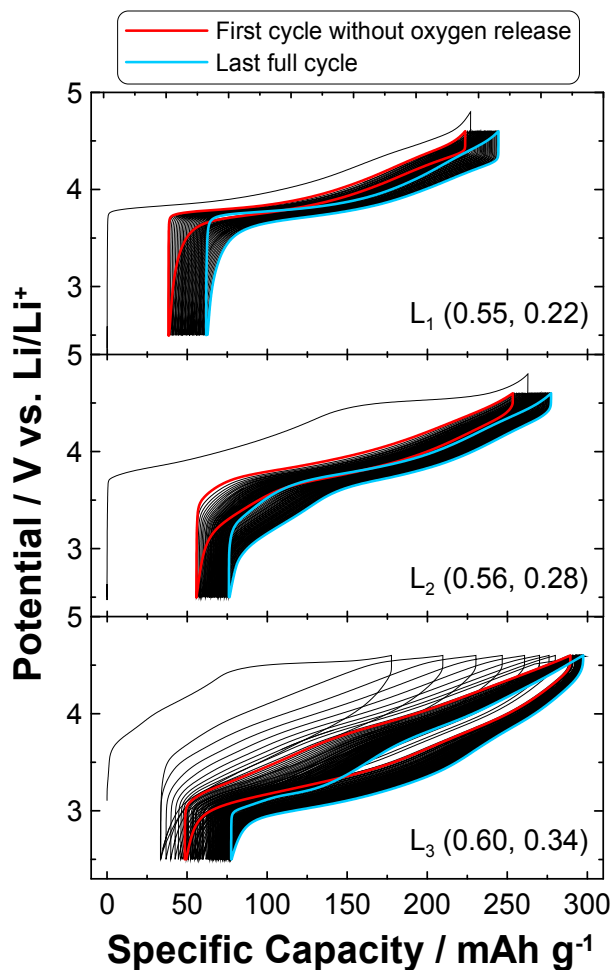


Figure 6.3. Potential versus specific capacity plots for half-cells of samples L_1 , L_2 , and L_3 from 2.5 V to 4.6 V collected using the UHPC. The first full cycles without oxygen release for samples L_1 , L_2 , and L_3 were cycles 2, 2, and 10, respectively, while the last full cycles to 4.6 V were cycles 29, 45, and 61, respectively.

ever, the first cycle IRC is 17.0%, indicating that some of the extracted Li was not reintercalated into the material during discharge. The first full cycle without oxygen release, cycle 2, has a specific capacity of 185 mAh g⁻¹, with a relatively flat voltage curve and minimal polarization.

The first half-cycle of sample L_2 also shows a sloped region from 3.75 V to 4.45 V, again due to TM oxidation. A large HV plateau is seen above 4.45 V, indicating a

greater amount of Li extraction with simultaneous release of $O_{2(g)}$ and reversible redox of O^{2-} within the crystalline lattice. The first cycle IRC is 21.2%, indicating that even more Li was not reversibly reinserted into the crystalline structure when compared with sample L_1 . The first full cycle without oxygen release, cycle 2, has a specific capacity of 198 mAh g^{-1} , with a steeper voltage curve and increased polarization from charge to discharge. Also observed near the end of discharge is a small sloped region associated with voltage decay due to Mn^{4+} reduction to Mn^{3+} in LROs [58].

The first half-cycle of sample L_3 is quite different than those of L_1 and L_2 , with a much smaller yet steeper sloped region from 3.75 V to 4.45 V due to transition metal oxidation. An oxygen release plateau, about the same length as that of sample L_2 , is observed from 4.45 V to the potential limit of 4.6 V. The IRC of the first cycle is 17.8%, approximately the same as sample L_1 . The presence of this plateau indicates that the Li-deficient sample L_3 cycles similarly to the Li-rich oxides. However, in contrast to both of the other samples, the second cycle of sample L_3 exhibited another plateau above 4.45 V, albeit smaller than that of cycle 1, after cycling through the sloped transition metal oxidation region. This indicates that the material did not fully traverse the oxygen release plateau during the first cycle, likely owing to that cycle's lower potential limit. A gradual traverse of the oxygen release plateau was observed in the next 7 cycles, accompanied by incremental increases in the IRC. The first full cycle without oxygen release, cycle 9, has a specific capacity of 246 mAh g^{-1} , with a steadily sloped voltage curve from about 3.0 V to 4.6 V. The polarization in the voltage curve is greater than that of either L_1 or L_2 . From about 3.25 V to 3.0 V during discharge, an elongated plateau-like region is observed, in the same fashion as that of the bump and growth materials. This plateau is thought to be due to conversion of the layered

phase to spinel and the insertion of Li into the new spinel phase during discharge, as established in Chapters 4 and 5.

The last full cycle of each composition is highlighted in blue in Figure 6.3. The differences in the shapes of the voltage curves indicate the difference in how the materials change with repeated cycling. The voltage curve of sample L_1 remains largely unchanged, maintaining its initial shape and polarization. This indicates little structural rearrangement taking place within the material as it reversibly intercalates and deintercalates Li^+ . The voltage curve of sample L_2 changes somewhat with cycling, showing an increase in the voltage decay near 3.25 V on discharge. This indicates that some structural rearrangement from layered to spinel has taken place, although not enough to significantly impact the polarization or capacity of the material. By contrast, the voltage curve of sample L_3 changes much more than that of either L_1 or L_2 . Decreases in the average charge and discharge voltages are observed, resulting in an increase in polarization and more hysteresis. In addition, the shape of the voltage curve changes, as the plateau between 3.25 V and 3.0 V during discharge increases in length due to further conversion of the layered phase to the new spinel phase. Interestingly, a plateau between 3.0 and 3.25 V is also observed during charge, suggesting reversible cycling behaviour in the new spinel phase. Overall, the changes in the voltage curves indicate how the electrode materials change structurally with cycling.

The most important feature of the voltage-capacity curves in Figure 6.3 is how they allow for differentiation between the amount of electrolyte oxidation occurring at the top of charge for each composition. The difference between the charge endpoint positions of the final cycle (blue) and those of the first cycles without oxygen release (red) indicate the relative amount of electrolyte oxidation that has taken place. Sample L_2 shows less electrolyte oxidation than sample L_1 when cycled repeatedly to 4.6 V,

while Sample L₃ shows far less electrolyte oxidation than samples L₁ and L₂, as the amount of charge endpoint capacity slippage is minimal by comparison. This observation makes sample L₃ unique among the three samples studied by UHPC, warranting further study to elucidate the extent to which electrolyte oxidation at high potential can be reduced and to determine the structural changes that the material undergoes while cycling.

6.4 The Effect of Potential Limit on Electrolyte Oxidation and Phase Conversion

Since the upper potential limit is known to have a direct impact on the amount of electrolyte oxidation which occurs, sample L₃ was repeatedly cycled to both 4.6 V and 4.8 V to observe the effect of potential limit. Figure 6.4 shows the potential versus capacity plots of half-cells of Li[Li_{0.16}Ni_{0.12}Mn_{0.65}□_{0.07}]O₂ (sample L₃) collected using the UHPC. As shown, the upper cutoff potential has a significant impact on the initial charge capacity, irreversible capacity, reversible cycling capacity, polarization, and most importantly, charge endpoint capacity slippage. During the first charge half-cycle, the cells exhibit deintercalation due to TM redox, followed by HV plateaus above 4.45 V at both the 4.6 V and 4.8 V limits. Cycling to 4.8 V resulted in complete oxygen release within 3 cycles, while cycling to 4.6 V resulted in an incremental traverse of the plateau over 9 cycles, as discussed above. The first cycle IRC at the 4.8 V limit is 17.8 %, approximately the same as that at 4.6 V. The first full cycle at 4.8 V without oxygen release (cycle 4) has a specific capacity of 247 mAh g⁻¹, which is almost identical to the capacity of the first full cycle to 4.6 V without oxygen loss (246 mAh g⁻¹). These similarities in first cycle IRC and first full cycle specific capacity indi-

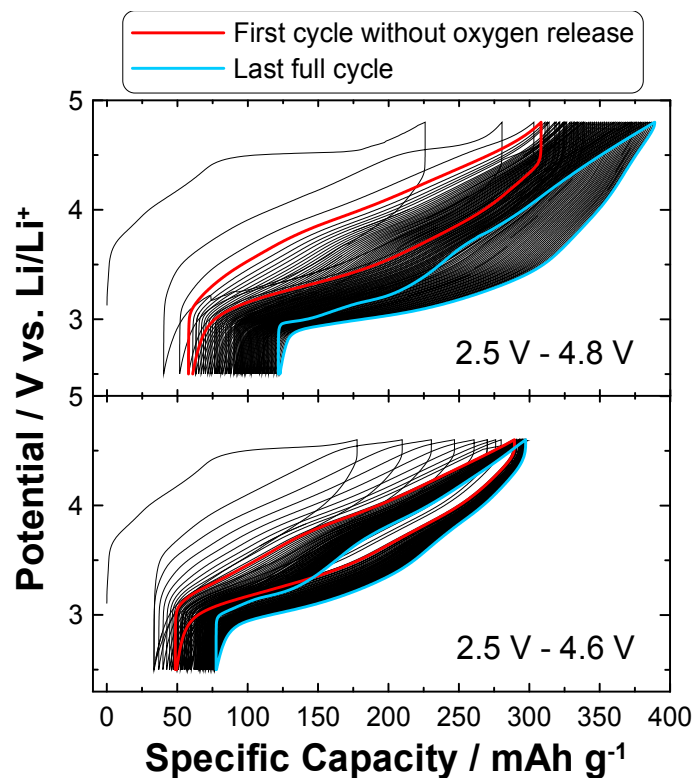


Figure 6.4. Potential versus specific capacity plots of sample L_3 from 2.5 V to 4.6 V and 2.5 V to 4.8 V collected using the UHPC. The first full cycles without oxygen release to 4.6 V and 4.8 V were cycles 4 and 10, respectively, while the last full cycles to 4.6 V and 4.8 V were cycles 61 and 69, respectively.

cate that the initially accessible capacity of the material is the same whether cycling to 4.6 V or 4.8 V.

When comparing the first reversible cycle (red) with the last full cycle (blue) of each potential limit, the shapes of the voltage curves change significantly. Cycling to 4.8 V results in gradual voltage decay during discharge, eventually yielding a long plateau near 3.0 V which was not seen initially. Again, this plateau is thought to be due to significant conversion of the layered phase to a spinel or spinel-like phase with cycling, and results in a large hysteresis in the voltage curve. By comparison, cycling to 4.6 V results in less conversion to spinel during cycling, as indicated by a compara-

tively small 3.0 V plateau on discharge. The 4.6 V potential limit also results in less voltage decay and polarization than the 4.8 V limit, producing less overall hysteresis in the voltage curve. Repeated cycling to 4.8 V significantly increases the amount of electrolyte oxidation while achieving a reversible capacity to 266 mAh g⁻¹ after 61 cycles. By comparison, cycling to only 4.6 V results in a relatively reversible capacity of 219 mAh g⁻¹ after 69 cycles, while significantly reducing the amount of electrolyte oxidation, indicating that cycling to high potential is not required to access the majority of the material's true capacity.

The most important effect of the 4.6 V and 4.8 V potential limits is the significant impact they have on the charge endpoint capacity slippage of each voltage curve. While the exact nature of electrolyte oxidation at high potential is complex, the accuracy of the current of the UHPC allows for the relative amount of electrolyte oxidation occurring to be tracked by the charge endpoint capacity slippage [73]. At the 4.8 V limit, significant charge endpoint capacity slippage was observed due to electrolyte oxidation. By comparison, cycling to 4.6 V resulted in much less charge endpoint capacity slippage, suggesting that virtually no electrolyte oxidation is occurring.

While sample L₃ shows minimal electrolyte oxidation at higher potentials, it does convert to spinel with extended cycling, as observed by the elongated plateau in the voltage curves near 3.0 V on discharge. Figure 6.5 shows the differential capacity curves of Li[Li_{0.16}Ni_{0.12}Mn_{0.65}□_{0.07}]O₂ cycled to 4.6 V and 4.8 V. Spinel conversion is clearly observed at both potential limits by the difference between the red and blue cycles. In both plots, the peaks due to layered redox from 3.5 V to 4.0 V during charge and to layered Mn^{4+/3+} redox at 3.25 V during discharge continually decrease in magnitude with cycling. Concurrently, peaks at 3.0 V and 3.25 V begin to emerge and increase in magnitude during charge, while a large peak at 3.0 V during discharge, cor-

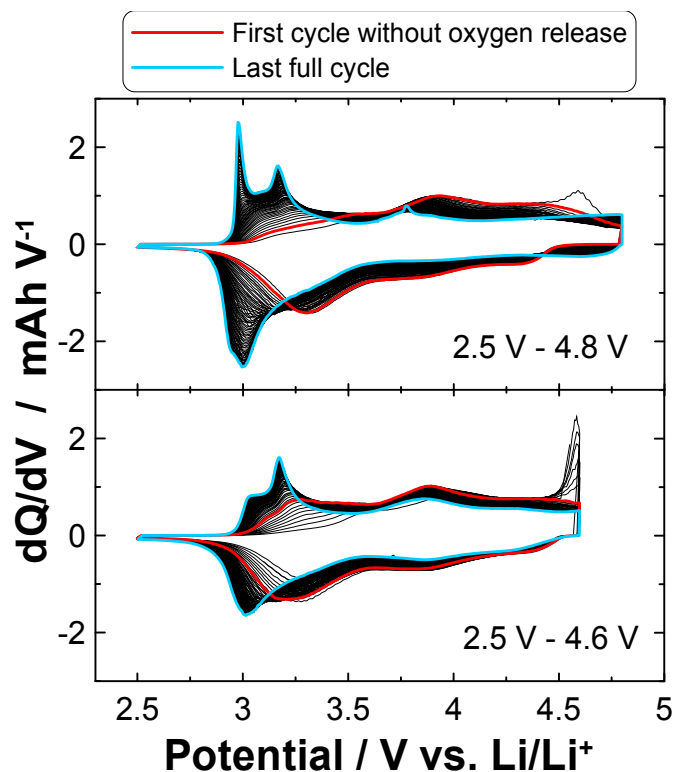


Figure 6.5. Differential capacity plots of sample L_3 from 2.5 V to 4.6 V and 2.5 V to 4.8 V collected using the UHPC. The last full cycles to 4.6 V and 4.8 V were cycle 61 and cycle 69, respectively. The first two cycles of each plot are omitted for clarity.

responding to the 3.0 V plateau in the voltage curves, emerges and begins to significantly increase in magnitude. These observations confirm the simultaneous decrease in capacity of the layered phase as it converts to spinel, which reversibly inserts Li during discharge. When comparing the two potential limits, it is clear that the layered to spinel phase conversion is greater at 4.8 V than at 4.6 V. The reasons for this are unknown at present, but may be due to the higher energy 4.8 V limit facilitating easier migration of Mn and Li ions into tetrahedral sites in the Li layer, thereby increasing the rate at which the layered phase converts to splayered before finally transforming into the new spinel phase.

6.5 Coulombic Efficiency and Charge Endpoint Capacity

Slippage Analysis

The high quality data obtained by UHPC measurements allows a thorough comparison of the coulombic efficiencies, specific discharge capacities, and normalized charge endpoint capacity slippage of the three layered samples to be made. Figure 6.6 shows each of these quantities plotted for samples L_1 to L_3 in the left column. In general, the coulombic efficiency is better when cycling to 4.6 V (green squares, orange diamonds) than when cycling to 4.8 V (blue triangles, purple circles) due to less electrolyte oxidation. Over 50 cycles, sample L_3 has the highest specific discharge capacity of all the materials analyzed at both potential limits. However, gradual conversion to spinel with cycling results in some capacity loss at the 4.6 V limit, while an apparent increase in capacity is observed at the 4.8 V limit after about 25 cycles. This observation is similar to that of the capacity growth materials discussed in Chapter 5, albeit with less dramatic capacity growth. Further study is required to determine the exact source of this capacity increase. By comparison, the $\text{Li}[\text{Li}_{0.09}\text{Ni}_{0.46}\text{Mn}_{0.45}]\text{O}_2$ (sample L_1) and $\text{Li}[\text{Li}_{0.12}\text{Ni}_{0.32}\text{Mn}_{0.56}]\text{O}_2$ (sample L_2) materials had poorer coulombic efficiencies, lower discharge capacities, and larger charge endpoint capacity slippages with successive cycles. The overall electrochemical behaviour of $\text{Li}[\text{Li}_{0.16}\text{Ni}_{0.12}\text{Mn}_{0.65}\square_{0.07}]\text{O}_2$ is striking in that it exhibits significantly lower charge endpoint capacity slippage and higher CE compared to samples L_1 and L_2 .

The apparent inertness of sample L_3 , especially at the 4.6 V limit, warranted further study by comparing it with a standard current generation material, namely NMC111. The second column in Figure 6.6 compares the results of sample L_3 with HPC results for $\text{Li}[\text{Ni}_{1/3}\text{Mn}_{1/3}\text{Co}_{1/3}]\text{O}_2$ collected at different upper potential limits.

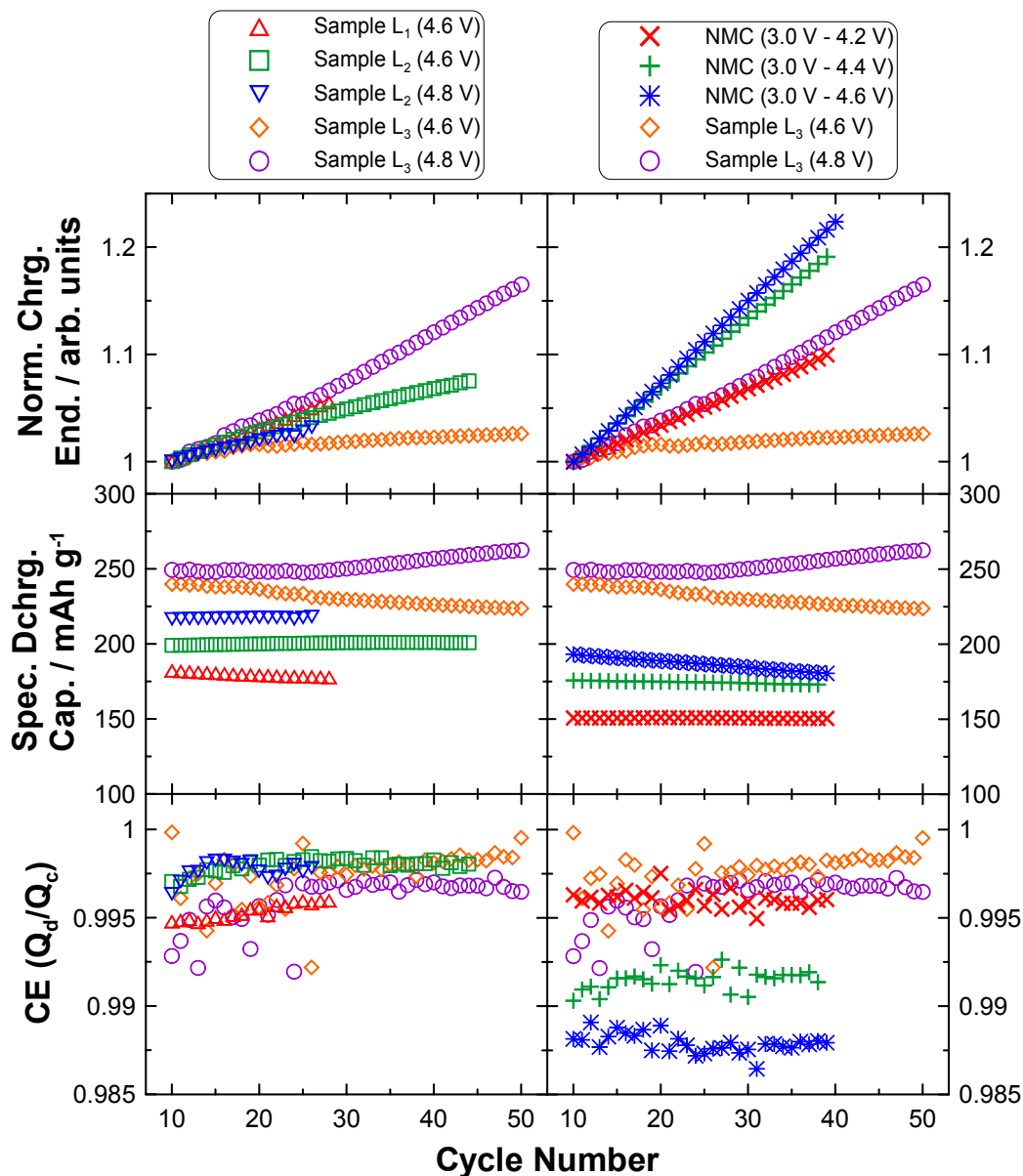


Figure 6.6. Coulombic efficiency, specific discharge capacity, and normalized charge endpoint versus cycle number. The left column compares samples L₁, L₂, and L₃, while the right column compares sample L₃ with Li[Ni_{1/3}Mn_{1/3}Co_{1/3}]O₂. The normalized charge endpoint of each composition was calculated individually by dividing the charge endpoint capacity of every cycle by the charge endpoint capacity of cycle 10.

In all three comparisons, sample L₃ outperforms NMC at almost every potential limit. The CE of sample L₃ at both 4.6 V and 4.8 V was comparable to or better than that of NMC at only 4.2 V, indicating that sample L₃ is very inert to electrolyte oxidation at high potential. At both the 4.4 V and 4.6 V limits, the charge endpoint slippage per cycle of NMC was much larger than that of sample L₃ at both 4.6 V and 4.8 V. These results indicate that sample L₃ can be cycled to higher potentials with greater achievable capacities than the current standard NMC111.

6.6 Discussion of the Inherent Cycling Stability of Li[Li_{0.16}Ni_{0.12}Mn_{0.65}□_{0.07}]O₂

For commercial applications requiring long-term cycling stability, including hybrid and fully electric vehicles, positive electrode materials require high specific capacities, high coulombic efficiencies, and low charge endpoint capacity slippages, all of which are exhibited by samples L₂ and L₃. Of the two materials, sample L₃ exhibits the highest CE and lowest charge endpoint capacity slippage at the 4.6 V limit, yielding the best long-term cycling results while maintaining a relatively high reversible discharge capacity over 50 cycles. The results presented for sample L₃ show that it is not necessary to cycle to 4.8 V to access the material's full capacity, and that limiting the potential to 4.6 V increases the cycling stability of the electrode by decreasing the amount of electrolyte oxidation that occurs. These desirable characteristics are inherent to the material itself, removing any immediate requirement of costly electrolyte additives to achieve the same cycling stability. Overall, Li[Li_{0.16}Ni_{0.12}Mn_{0.65}□_{0.07}]O₂ shows the smallest charge endpoint capacity slippage of any material charged repeatedly to 4.6 V vs. Li/Li⁺ in a simple carbonate-based electrolyte. This strongly suggests that

there is something “unique” about the surface of this material which limits electrolyte oxidation, although further study is required to identify how this occurs. While spinel conversion with cycling does result in a gradual decrease in the average discharge voltage, this may be an acceptable trade-off in order to achieve long-term electrode stability at high potentials such as 4.6 V.

In terms of practical applications, sample L₃ exhibits the properties required for a protective “shell” in a core-shell particle configuration [75, 76]. A high energy density material would be used as the core, surrounded by a 5.0 to 20.0 wt % shell of Li[Li_{0.16}Ni_{0.12}Mn_{0.65}□_{0.07}]O₂. The impact of spinel conversion in the shell on the average voltage would be minimal, as the shell itself would only compose a small fraction of the entire particle.

6.7 Summary of UHPC Analysis

The production of the Li-Mn-Ni-O phase diagrams introduces many opportunities for characterization of new positive electrode materials. In this chapter, three distinct single-phase layered compositions were characterized by elemental, structural, and electrochemical analysis. Sample L₁ was determined to be Li[Li_{0.09}Ni_{0.46}Mn_{0.45}]O₂, an extra-lithiated analogue of Li[Ni_{0.5}Mn_{0.5}]O₂, while sample L₂ was determined to be Li[Li_{0.12}Ni_{0.32}Mn_{0.56}]O₂, an essentially Ni-rich member of the LRO solid solution series. Sample L₃ was determined to be Li[Li_{0.16}Ni_{0.12}Mn_{0.65}□_{0.07}]O₂, a Li-deficient, Mn-rich material containing 3.6% metal site vacancies. As measured by ultra high precision coulometry, cycling half-cells of each composition to 4.6 V resulted in lower charge endpoint capacity slippages and higher coulombic efficiencies, while cycling to 4.8 V increased slippage due to electrolyte oxidation. Overall, Li[Li_{0.16}Ni_{0.12}Mn_{0.65}□_{0.07}]O₂ cycled

to 4.6 V had the lowest charge endpoint capacity slippage measured, which was even less than that of NMC111 at the much lower potential limit of 4.2 V. These results indicate the inherent stability of $\text{Li}[\text{Li}_{0.16}\text{Ni}_{0.12}\text{Mn}_{0.65}\square_{0.07}]\text{O}_2$ as a substrate to reduce electrolyte oxidation. In general, it is very likely that electrolyte oxidation reactions are catalytically promoted by the transition metals at the surfaces of the positive electrode materials [77]. It may be that $\text{Li}[\text{Li}_{0.16}\text{Ni}_{0.12}\text{Mn}_{0.65}\square_{0.07}]\text{O}_2$ has very poor characteristics as a catalyst for such reactions with carbonate-based electrolytes. While exhibiting voltage decay and capacity fade due to gradual spinel conversion, this material may be an ideal protective shell in a core-shell particle that does not rely on electrolyte additives to provide stability for long-term, high potential cycling. If electrolyte additives were used, the cycling stability of such core-shell particles could probably be even further improved.

Chapter 7

Conclusions and Future Work

7.1 Conclusions

This thesis has provided an in-depth study of the synthesis, structural analysis, and electrochemical characterization of numerous bulk-scale compositions in the Li-Mn-Ni-O system. Systematic analysis of the XRD patterns and lattice constant refinement have resulted in the production of pseudo-ternary phase diagrams of the positive electrode materials region for quenched and slow cooled Li-Mn-Ni-O samples prepared at 800°C and 900°C in air. These phase diagrams agree well with those produced by McCalla et al. using combinatorial methods [28], and indicate how initial composition, reaction temperature, and cooling rate affect the final phases that form in Li-Mn-Ni-O positive electrode materials. It is hoped that these diagrams will provide both academic and industrial researchers with a greater understanding of the Li-Mn-Ni-O system in the ongoing efforts to develop positive electrode materials with high energy densities. Using the phase diagrams to synthesize compositions which avoid the inclusion of electrochemically undesirable phases, such as the ordered rock-salt phase and the N-layered phase, highlight one practical application of these diagrams.

The phase diagrams also present opportunities for new research on many unstudied compositions, namely within the single-phase layered region and the two-phase lay-

red-spinel co-existence region. In particular, the compositions contained within the bump in the single-phase layered region have proven to be structurally, morphologically, and electrochemically unique. XRD analysis has confirmed that several of these materials have monoclinic crystal structures, with the remainder exhibiting hexagonal layered structures. Analysis by McCalla et al. [15] confirmed that these materials also contained varying amounts of metal sites vacancies. The SEM work in Chapter 4 revealed that vacancy-rich materials largely exhibit ellipsoidal primary particles with smooth surfaces and little porosity, while less vacancy-rich materials contain clustered, plate-like primary particles agglomerated into porous, semi-spherical secondary particles. These compositions exhibited specific capacities in the range of 179 mAh g⁻¹ to 237 mAh g⁻¹ after 35 cycles at 4.8 V.

Each bump composition exhibited normal transition metal redox and high voltage plateau cycling, producing IRC values that increased as the upper potential limit was raised. The potential limit also affected the reversible capacity exhibited by each composition, with higher limits yielding greater capacity values. Differential capacity analysis revealed that each composition underwent significant structural transformations during the first 100 cycles. These changes appear to involve gradual conversion of the layered phase into an electrochemically active spinel phase that inserts Li at low voltage during discharge, which both lowers the average discharge voltages and causes significant hysteresis in the voltage profiles. Among the materials studied, the compositions with intermediate vacancy contents near the middle of the bump region, particularly Li[Li_{0.16}Ni_{0.12}Mn_{0.65}□_{0.07}]O₂, had the highest discharge capacities and average discharge voltages.

Stark contrasts in structure, morphology, and electrochemical behaviour were observed in the slow cooled counterparts of the bump materials, highlighting the impact

of cooling rate on phase formation. XRD analysis determined their locations to be in the M-R-S triangle, near the M-R tie-line, or in the single-phase layered region of the slow cooled phase diagrams. Large cubic-shaped primary particles were observed for compositions containing spinel, while smaller primary particles agglomerated into dense, low porosity secondary particles were observed in the rocksalt-containing material. The layered compositions had plate-like agglomerated secondary particle sizes and shapes comparable to similarly located layered compositions in the quenched bump region.

While initially yielding capacities below 100 mAh g⁻¹, all but one of the slow cooled compositions began to show steady increases in capacity with increasing charge-discharge cycle number. Over 150 cycles, several compositions exhibited capacities in excess of 300% of their initial values. This anomalous capacity growth was accompanied by a large increase in the capacity near the 3.0 V region during discharge, which was again attributed to conversion of the layered phase to a spinel or spinel-like phase with prolonged cycling. As was the case for the quenched bump materials, acute voltage curve hysteresis was observed with extended cycling. Overall, the capacity growth phenomenon was attributed to the layered phase becoming more electrochemically active, coupled with extensive conversion to spinel during extended cycling at low rate.

The electrochemical studies of compositions within the 1:5 composition series of the quenched and slow cooled samples identified Li[Li_{0.16}Ni_{0.12}Mn_{0.65}□_{0.07}]O₂, near the middle of the quenched bump, as a promising material for use in positive electrodes. In comparison to other Li-rich compositions in the single-phase layered region, this composition was found to be a Li-deficient, Mn-rich, vacancy-containing layered structure. Ultra high precision coulometry studies indicated that at 4.6 V, this composition had coulombic efficiency and charge endpoint capacity slippage values that are better than

several layered materials such as $\text{Li}[\text{Li}_{1/9}\text{Ni}_{1/3}\text{Mn}_{5/9}]\text{O}_2$ at 4.6 V and $\text{Li}[\text{Ni}_{1/3}\text{Mn}_{1/3}\text{Co}_{1/3}]\text{O}_2$ at 4.2 V. These highly desirable electrochemical characteristics have been attributed to the material's ability to minimize the oxidation of the carbonate-based electrolyte at high potential. While still converting to spinel with extended cycling in the same manner as the other bump compositions studied, the Li-deficient material's inherent inertness might make it suitable for use as a thin protective shell in a core-shell particle configuration.

7.2 Future Work

The positive electrode materials region of the Li-Mn-Ni-O system discussed in this thesis provides an abundance of opportunities for future research of positive electrode materials. In terms of the phase diagrams, numerous opportunities exist for additional structural characterization studies, especially at the boundaries between the single- and multi-phase regions. For example, the locations of the upper and lower boundaries of the single-phase layered region in this thesis were determined by a limited range of samples within each composition series. However, more precise locations of the upper single-phase boundary, and the points at which the two-phase, crescent-shaped co-existence region bounded by the M-N tie-line begins, can certainly be refined. This may be particularly important for discovering new Li-deficient layered materials near the single-phase layered boundary while avoiding the electrochemically poor two-phase layered-layered composites found in the crescent-shaped co-existence region.

The boundary refinement process could involve synthesizing several new composition series with different Ni:Mn ratios along the single-phase boundary at regular intervals, e.g., Ni:Mn ratios of 1:2, 1:3, 1:4, and so on. Each series would contain a large

number of samples with Li contents that range from the M-N tie-line, where the compositions are two-phase layered-layered, down to the nominal LRO line, where the compositions are single-phase layered. Careful XRD analysis within this narrow range could then be used to precisely determine where the materials convert from two-phase to single-phase compositions, providing the exact location of the boundary. A similar study could also be conducted on the lower boundary of the single-phase spinel region.

Determining the exact locations of the four end-members in the manner outlined in Section 3.9 may also be part of future studies of the phase diagram. This may be especially relevant when synthesizing two-phase layered-spinel composites in the region parallel to the M-S tie-line in order to determine how the tie-lines in this region connect between the lower spinel boundary and the upper layered boundary near the bump. In addition, determining more precise locations of the rocksalt and N-layered phases may help avoid their inclusion in future materials.

In terms of electrochemical studies, the phase diagrams introduce new opportunities for future experiments using bulk-scale samples. The single-phase layered region could be mapped electrochemically as well as structurally, plotting useful quantities such as IRC, discharge capacity, average voltage, and CE at each Li-Mn-Ni-O composition studied. Studies of compositions in the two-phase layered-spinel region could lead to the development of composite materials containing variable amounts of HV spinel phases which might improve the rate capability of a high capacity layered component.

The materials in the bump and capacity growth series exhibit unique electrochemical behaviour, with the bump compositions being more suitable as positive electrode materials than the growth compositions after synthesis. In-situ XRD during the initial cycles of the bump materials could be used to determine how their vacancy contents

and/or particle morphologies impact the rapid capacity increase observed during their initial “stabilization” cycles, which contrast sharply with the comparatively poor initial performance of the growth materials. Ex-situ XRD measurements after extended cycling of materials in both series could help identify the new spinel and/or spinel-like phases which form, as well as the structure of the more active layered phases; similar studies on cycled LRO materials exhibiting voltage decay have been reported in the literature [78]. Given the development of the 3.0 V plateau in the voltage profiles of most of the quenched and slow cooled materials, a comparison of ex-situ XRD measurements may aid in determining whether the materials in this region convert to approximately the same phase or phases during cycling regardless of the initial cooling method used during synthesis.

Both the bump and the growth materials may benefit from a systematic study of the impact of rate, potential limit, and temperature on their electrochemical behaviour. Such studies could be used to optimize their performance for use in commercial applications. This could also help improve their rate capability, as the specific currents used to study the bump and growth materials were typically low to ensure thorough electrochemical characterization.

Finally, structural and electrochemical studies of the $\text{Li}[\text{Li}_{0.16}\text{Ni}_{0.12}\text{Mn}_{0.65}\square_{0.07}]\text{O}_2$ composition could be conducted in an effort to understand how it is able to minimize electrolyte oxidation at high potential. It could be that its particle morphology and vacancy content combine to limit catalytic activity at the electrode/electrolyte interface. It is also possible that structural rearrangement takes place at the particle surface during the traverse of the HV plateau resulting in a thin surface layer that minimizes electrolyte oxidation. Whatever the protective mechanism is determined to be, efforts are already underway by John Camardese and Jing Li of the Dahn research

group to harness its inherent stability in core-shell particle configurations. These particles will utilize a Ni-rich composition such as $\text{Li}[\text{Li}_{1/9}\text{Ni}_{1/3}\text{Mn}_{5/9}]\text{O}_2$ or $\text{Li}[\text{Ni}_{2/3}\text{Mn}_{1/3}]\text{O}_2$ as a high capacity, high voltage, and therefore high energy density core. An approximately 10 - 20 wt % shell of $\text{Li}[\text{Li}_{0.16}\text{Ni}_{0.12}\text{Mn}_{0.65}\square_{0.07}]\text{O}_2$ will be used both to minimize the amount of electrolyte oxidation at the high potentials required to access the full energy density of the total particle, and to protect the inner core from degradation during cycling. While the Li-deficient, Mn-rich shell will convert to spinel during cycling, its low weight percent and high reversible capacity are anticipated to have minimal impact on the discharge capacity and average voltage of the overall composition.

Overall, the $\text{Li}[\text{Li}_{0.16}\text{Ni}_{0.12}\text{Mn}_{0.65}\square_{0.07}]\text{O}_2$ composition exhibits the desired attributes of high capacity, high potential, and long-term cycling stability. Achieving cycling stability of positive electrodes at high voltage is often achieved by using complex and sometimes proprietary combinations of electrolyte additives. The performance of this Li-deficient composition, coupled with its comparatively low Ni and Li content, effectively make it an electrochemically active analogue of the mostly inactive Li_2MnO_3 . The low cost and toxicity of this composition are also highly desirable for industrial production and commercialization. As demonstrated by this and other materials in the bump region, it is possible that other undiscovered and possibly useful compositions still exist in the Li-Mn-Ni-O system. Thus, the phase diagrams can be used as practical guides to assist in the continued research and development of positive electrode materials in the Li-Mn-Ni-O system.

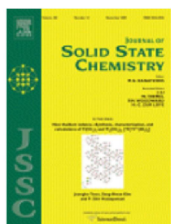
The work presented in this thesis on the Li-Mn-Ni-O system can be extended into other systems containing Li-ion battery positive electrode materials. For example, cobalt is frequently used in commercial positive electrode materials such as layered $\text{Li}[\text{Ni}_{1/3}\text{Mn}_{1/3}\text{Co}_{1/3}]\text{O}_2$ to increase operating voltage, capacity, and cycling stability [6].

Thus, the production of phase diagrams of the Li-Co-Mn-Ni-O system from bulk samples could provide researchers with yet another useful materials database. Combinatorial studies by McCalla et al. have produced pseudo-ternary phase diagrams of the Li-Co-Mn-O system [79]. The extension of both combinatorial and bulk-scale material phase diagram studies into the Li-Co-Mn-Ni-O system would be useful for discovering new electrode materials, as has been shown in this thesis for the Li-Mn-Ni-O system. In addition, examination of the particle morphology of compositions in single- and multi-phase regions could help determine optimal synthesis conditions for Li-Co-Mn-Ni-O bulk-scale materials that exhibit desirable electrochemical properties.

There are several oxide systems that have not received the same amount of research attention as the Li-Mn-Ni-O and Li-Co-Mn-Ni-O systems which could also benefit from the production of phase diagrams to help guide future research efforts. For example, recent studies by Lee et al. have shown that new cation-disordered oxide compositions in the Li-Cr-Mo-O system exhibit high specific capacities [80]. The production of phase diagrams of this system could help identify additional compositions within it that are suitable for use as positive electrode materials in Li-ion batteries.

Appendix

Copyright Permissions

[Home](#)[Account Info](#)[Help](#)

Title: High-resolution X-ray diffraction, DIFFaX, NMR and first principles study of disorder in the $\text{Li}_2\text{MnO}_3\text{-Li}[\text{Ni}_{1/2}\text{Mn}_{1/2}]\text{O}_2$ solid solution

Author: Julien Bréger, Meng Jiang, Nicolas Dupré, Ying S. Meng, Yang Shao-Horn, Gerbrand Ceder, Clare P. Grey

Publication: Journal of Solid State Chemistry

Publisher: Elsevier

Date: September 2005

Copyright © 2005, Elsevier

Logged in as:

Aaron Rowe

Account #:

3000766006

[LOGOUT](#)

Order Completed

Thank you very much for your order.

This is a License Agreement between Aaron Rowe ("You") and Elsevier ("Elsevier"). The license consists of your order details, the terms and conditions provided by Elsevier, and the [payment terms and conditions](#).

[Get the printable license.](#)

License Number	3352080119988
License date	Mar 18, 2014
Licensed content publisher	Elsevier
Licensed content publication	Journal of Solid State Chemistry
Licensed content title	High-resolution X-ray diffraction, DIFFaX, NMR and first principles study of disorder in the $\text{Li}_2\text{MnO}_3\text{-Li}[\text{Ni}_{1/2}\text{Mn}_{1/2}]\text{O}_2$ solid solution
Licensed content author	Julien Bréger, Meng Jiang, Nicolas Dupré, Ying S. Meng, Yang Shao-Horn, Gerbrand Ceder, Clare P. Grey
Licensed content date	September 2005
Licensed content volume number	178
Licensed content issue number	9
Number of pages	11
Type of Use	reuse in a thesis/dissertation
Portion	figures/tables/illustrations
Number of figures/tables /illustrations	1
Format	both print and electronic
Are you the author of this Elsevier article?	No
Will you be translating?	No
Title of your thesis/dissertation	Structural and Electrochemical Studies of Positive Electrode Materials in the Li-Mn-Ni-O System for Lithium-ion Batteries
Expected completion date	May 2014
Estimated size (number of pages)	200
Elsevier VAT number	GB 494 6272 12
Permissions price	0.00 USD
VAT/Local Sales Tax	0.00 USD / 0.00 GBP
Total	0.00 USD



Title: Structure of Li₂MnO₃ with different degrees of defects
Author: A. Boulineau, L. Croguennec, C. Delmas, F. Weill
Publication: Solid State Ionics
Publisher: Elsevier
Date: 29 January 2010
 Copyright © 2010, Elsevier

Logged in as:
 Aaron Rowe
 Account #:
 3000766006

[LOGOUT](#)

Order Completed

Thank you very much for your order.

This is a License Agreement between Aaron Rowe ("You") and Elsevier ("Elsevier"). The license consists of your order details, the terms and conditions provided by Elsevier, and the [payment terms and conditions](#).

[Get the printable license.](#)

License Number	3352080628749
License date	Mar 18, 2014
Licensed content publisher	Elsevier
Licensed content publication	Solid State Ionics
Licensed content title	Structure of Li ₂ MnO ₃ with different degrees of defects
Licensed content author	A. Boulineau, L. Croguennec, C. Delmas, F. Weill
Licensed content date	29 January 2010
Licensed content volume number	180
Licensed content issue number	40
Number of pages	8
Type of Use	reuse in a thesis/dissertation
Portion	figures/tables/illustrations
Number of figures/tables /illustrations	1
Format	both print and electronic
Are you the author of this Elsevier article?	No
Will you be translating?	No
Title of your thesis/dissertation	Structural and Electrochemical Studies of Positive Electrode Materials in the Li-Mn-Ni-O System for Lithium-ion Batteries
Expected completion date	May 2014
Estimated size (number of pages)	200
Elsevier VAT number	GB 494 6272 12
Permissions price	0.00 USD
VAT/Local Sales Tax	0.00 USD / 0.00 GBP
Total	0.00 USD

[ORDER MORE...](#)
[CLOSE WINDOW](#)

Copyright © 2014 [Copyright Clearance Center, Inc.](#) All Rights Reserved. [Privacy statement](#).
 Comments? We would like to hear from you. E-mail us at customercare@copyright.com



Title: The Role of Metal Site Vacancies in Promoting Li-Mn-Ni-O Layered Solid Solutions

Author: E. McCalla, A. W. Rowe, J. Camardese, and J. R. Dahn

Publication: Chemistry of Materials

Publisher: American Chemical Society

Date: Jul 1, 2013

Copyright © 2013, American Chemical Society

Logged in as:

Aaron Rowe

Account #:
3000766006

[LOGOUT](#)

PERMISSION/LICENSE IS GRANTED FOR YOUR ORDER AT NO CHARGE

This type of permission/license, instead of the standard Terms & Conditions, is sent to you because no fee is being charged for your order. Please note the following:

- Permission is granted for your request in both print and electronic formats, and translations.
- If figures and/or tables were requested, they may be adapted or used in part.
- Please print this page for your records and send a copy of it to your publisher/graduate school.
- Appropriate credit for the requested material should be given as follows: "Reprinted (adapted) with permission from (COMPLETE REFERENCE CITATION). Copyright (YEAR) American Chemical Society." Insert appropriate information in place of the capitalized words.
- One-time permission is granted only for the use specified in your request. No additional uses are granted (such as derivative works or other editions). For any other uses, please submit a new request.

[BACK](#)

[CLOSE WINDOW](#)



Title: Structural Study of the Li-Mn-Ni Oxide Pseudoternary System of Interest for Positive Electrodes of Li-Ion Batteries

Logged in as:

Aaron Rowe

Account #:

3000766006

Author: E. McCalla, A. W. Rowe, R. Shunmugasundaram, and J. R. Dahn

[LOGOUT](#)

Publication: Chemistry of Materials

Publisher: American Chemical Society

Date: Mar 1, 2013

Copyright © 2013, American Chemical Society

PERMISSION/LICENSE IS GRANTED FOR YOUR ORDER AT NO CHARGE

This type of permission/license, instead of the standard Terms & Conditions, is sent to you because no fee is being charged for your order. Please note the following:

- Permission is granted for your request in both print and electronic formats, and translations.
- If figures and/or tables were requested, they may be adapted or used in part.
- Please print this page for your records and send a copy of it to your publisher/graduate school.
- Appropriate credit for the requested material should be given as follows: "Reprinted (adapted) with permission from (COMPLETE REFERENCE CITATION). Copyright (YEAR) American Chemical Society." Insert appropriate information in place of the capitalized words.
- One-time permission is granted only for the use specified in your request. No additional uses are granted (such as derivative works or other editions). For any other uses, please submit a new request.

[BACK](#)

[CLOSE WINDOW](#)



Title: Mechanism of Electrochemical Activity in Li₂MnO₃
Author: Alastair D. Robertson and Peter G. Bruce*
Publication: Chemistry of Materials
Publisher: American Chemical Society
Date: May 1, 2003

Logged in as:
Aaron Rowe
Account #:
3000766006

[LOGOUT](#)

Copyright © 2003, American Chemical Society

PERMISSION/LICENSE IS GRANTED FOR YOUR ORDER AT NO CHARGE

This type of permission/license, instead of the standard Terms & Conditions, is sent to you because no fee is being charged for your order. Please note the following:

- Permission is granted for your request in both print and electronic formats, and translations.
- If figures and/or tables were requested, they may be adapted or used in part.
- Please print this page for your records and send a copy of it to your publisher/graduate school.
- Appropriate credit for the requested material should be given as follows: "Reprinted (adapted) with permission from (COMPLETE REFERENCE CITATION). Copyright (YEAR) American Chemical Society." Insert appropriate information in place of the capitalized words.
- One-time permission is granted only for the use specified in your request. No additional uses are granted (such as derivative works or other editions). For any other uses, please submit a new request.

If credit is given to another source for the material you requested, permission must be obtained from that source.

[BACK](#)[CLOSE WINDOW](#)

Request for Permission to Reproduce or Re-Publish ECS Material


Please fax this form to: The Electrochemical Society (ECS), Attn: Permissions Requests, 1.609.730.0629.
You may also e-mail your request to: copyright@electrochem.org. Include all the information as required on this form. Please allow 3-7 days for your request to be processed.

I am preparing a (choose one): paper chapter book thesis
entitled: Structural and Electrochemical Studies of Positive Electrode Materials in the Li-Mn-Ni-O System for Lithium-ion Batteries
to be published by: Dalhousie University
in an upcoming publication entitled: n/a

I request permission to use the following material in the publication noted above, and request nonexclusive rights for all subsequent editions and in all foreign language translations for distribution throughout the world.

Description of material to be used—Indicate what material you wish to use (figures, tables, text, etc.) and give the full bibliographic reference for the source publication. You may attach a separate list, organized by ECS title.

See attached list

Signature:  Date: March 20, 2014
Name: Aaron Rowe
Address: Dept. of Physics, Dalhousie University
6310 Coburg Road, Dunn Bldg, Room 218
Halifax, NS B3H 4R2 CANADA
Telephone: 902-494-2991 Fax: 902-494-5191
E-mail: aaron.rowe@dal.ca

Permission is granted to reproduce the above-referenced material. Please acknowledge the author(s) and publication title of the original material, and include the words: "Reproduced by permission of ECS — The Electrochemical Society."

4/4/14 Date  John Lewis, Associate Director of Publications

March 20, 2014

Subject: Use of figures/tables/data from items 1 to 3 listed below in the PhD Dissertation of Aaron Rowe at Dalhousie University (see signed request form)

List of copyright permission requests from The Electrochemical Society:

Item 1

Requested use: All figures and tables (first author of paper)

Publication: Journal of The Electrochemical Society

Issue Date: 2014

Volume Number: 161

Issue Number: 3

Pages: A308-A317

Title: "Positive Electrode Materials in the Li-Mn-Ni-O System Exhibiting Anomalous Capacity Growth during Extended Cycling"

Authors: A. W. Rowe and J. R. Dahn

Item 2

Requested use: All figures and tables (co-author of paper)

Publication: Journal of The Electrochemical Society

Issue Date: 2013

Volume Number: 160

Issue Number: 8

Pages: A1134-A1138

Title: "How Phase Transformations during Cooling Affect Li-Mn-Ni-O Positive Electrodes in Lithium Ion Batteries"

Authors: E. McCalla, A. W. Rowe, C. R. Brown, L. R. P. Hacquebard, and J. R. Dahn

Item 3

Requested use: Figure 27, page 113

Publication: Journal of The Electrochemical Society

Issue Date: 1996

Volume Number: 143

Issue Number: 1

Pages: 100-114

Title: "Synthesis and Characterization of $\text{Li}_{1+x}\text{Mn}_{2-x}\text{O}_4$ for Li-Ion Battery Applications"

Authors: Y. Gao and J. R. Dahn

References

- [1] T.B. Reddy, and D. Linden. *Linden's Handbook of Batteries*; McGraw-Hill: New York, 2011.
- [2] M. Winter, and R. J. Brodd. "What Are Batteries, Fuel Cells, and Supercapacitors?" *Chemical Reviews* **2004**, *104*, 4245–4270.
- [3] M. S. Whittingham. "Lithium Batteries and Cathode Materials." *Chemical Reviews* **2004**, *104*, 4271–4302.
- [4] A. Manthiram and T. Muraliganth. "Lithium Intercalation Cathode Materials for Lithium-Ion Batteries." In *Handbook of Battery Materials*; Wiley-VCH: Weinheim, Germany, 2011; pp. 341–375.
- [5] S.S. Zhang, "A Review on the Separators of Liquid Electrolyte Li-ion batteries." *Journal of Power Sources* **2007**, *164*, 351–364.
- [6] C. Daniel and J. O. Besenhard. *Handbook of Battery Materials*; 2nd Edition.; Wiley-VCH: Weinheim, Germany, 2011.
- [7] T. Ohzuku and R. J. Brodd. "An Overview of Positive-electrode Materials for Advanced Lithium-ion Batteries." *Journal of Power Sources* **2007**, *174*, 449–456.
- [8] Z. Lu, L. Y. Beaulieu, R. A. Donaberger, C. L. Thomas, and J. R. Dahn. "Synthesis, Structure, and Electrochemical Behavior of $\text{Li}[\text{Ni}_x\text{Li}_{(1/3-2x/3)}\text{Mn}_{(2/3-x/3)}]\text{O}_2$." *Journal of The Electrochemical Society* **2002**, *149*, A778–A791.
- [9] Z. Lu, Z. Chen, and J. R. Dahn. "Lack of Cation Clustering in $\text{Li}[\text{Ni}_x\text{Li}_{1/3-2x/3}\text{Mn}_{2/3-x/3}]\text{O}_2$ ($0 < x < 1/2$) and $\text{Li}[\text{Cr}_x\text{Li}_{(1-x)/3}\text{Mn}_{(2-2x)/3}]\text{O}_2$ ($0 < x < 1$)." *Chemistry of Materials* **2003**, *15*, 3214–3220.
- [10] K. A. Jarvis, Z. Deng, L. F. Allard, A. Manthiram, and P. J. Ferreira. "Atomic Structure of a Lithium-Rich Layered Oxide Material for Lithium-Ion Batteries: Evidence of a Solid Solution." *Chemistry of Materials* **2011**, *23*, 3614–3621.

- [11] J. Bréger, M. Jiang, N. Dupré, Y. S. Meng, Y. Shao-Horn, G. Ceder, and C. P. Grey. “High-resolution X-ray diffraction, DIFFaX, NMR and First Principles Study of Disorder in the $\text{Li}_2\text{MnO}_3\text{-Li}[\text{Ni}_{1/2}\text{Mn}_{1/2}]\text{O}_2$ Solid Solution.” *Journal of Solid State Chemistry* **2005**, *178*, 2575–2585.
- [12] A. Boulineau, L. Croguennec, C. Delmas, and F. Weill. “Reinvestigation of Li_2MnO_3 Structure: Electron Diffraction and High Resolution TEM.” *Chemistry of Materials* **2009**, *21*, 4216–4222.
- [13] A. Boulineau, L. Croguennec, C. Delmas, and F. Weill. “Structure of Li_2MnO_3 with Different Degrees of Defects.” *Solid State Ionics* **2010**, *180*, 1652–1659.
- [14] Z. Lu, D. D. MacNeil, and J. R. Dahn. “Layered Cathode Materials $\text{Li}[\text{Ni}_x\text{Li}_{(1/3-2x/3)}\text{Mn}_{(2/3-x/3)}]\text{O}_2$ for Lithium-Ion Batteries.” *Electrochemical and Solid-State Letters* **2001**, *4*, A191–A194.
- [15] E. McCalla, A. W. Rowe, J. Camardese, and J. R. Dahn. “The Role of Metal Site Vacancies in Promoting Li–Mn–Ni–O Layered Solid Solutions.” *Chemistry of Materials* **2013**, *25*, 2716–2721.
- [16] E. McCalla, and J. R. Dahn. “The Spinel and Cubic Rocksalt Solid-Solutions in the Li–Mn–Ni Oxide Pseudo-ternary System.” *Solid State Ionics* **2013**, *242*, 1–9.
- [17] S. R. Li, C. H. Chen, J. Camardese, and J. R. Dahn. “High Precision Coulometry Study of $\text{LiNi}_{0.5}\text{Mn}_{1.5}\text{O}_4/\text{Li}$ Coin Cells.” *Journal of The Electrochemical Society* **2013**, *160*, A1517–A1523.
- [18] S. R. Li, C. H. Chen, X. Xia, and J. R. Dahn. “The Impact of Electrolyte Oxidation Products in $\text{LiNi}_{0.5}\text{Mn}_{1.5}\text{O}_4/\text{Li}_4\text{Ti}_5\text{O}_{12}$ Cells.” *Journal of The Electrochemical Society* **2013**, *160*, A1524–A1528.
- [19] M. Sathiya, G. Rouse, K. Ramesha, C. P. Laisa, H. Vezin, M. T. Sougrati, M.-L. Doublet, D. Foix, D. Gonbeau, W. Walker, A. S. Prakash, M. Ben Hassine, L. Dupont, and J.-M. Tarascon. “Reversible Anionic Redox Chemistry in High-capacity Layered-oxide Electrodes.” *Nature Materials* **2013**, *12*, 827–835.

- [20] H. Koga, L. Croguennec, M. Ménétrier, K. Douhil, S. Belin, L. Bourgeois, E. Suard, F. Weill, and C. Delmas. “Reversible Oxygen Participation to the Redox Processes Revealed for $\text{Li}_{1.20}\text{Mn}_{0.54}\text{Co}_{0.13}\text{Ni}_{0.13}\text{O}_2$.” *Journal of The Electrochemical Society* **2013**, *160*, A786–A792.
- [21] Z. Lu and J. R. Dahn. “Understanding the Anomalous Capacity of $\text{Li}/\text{Li}[\text{Ni}_x\text{Li}_{(1/3-2x/3)}\text{Mn}_{(2/3-x/3)}]\text{O}_2$ Cells Using In Situ X-Ray Diffraction and Electrochemical Studies.” *Journal of The Electrochemical Society* **2002**, *149*, A815–A822.
- [22] A. R. Armstrong, M. Holzapfel, P. Novak, C. S. Johnson, S.-H. Kang, M. M. Thackeray, and P. G. Bruce. “Demonstrating Oxygen Loss and Associated Structural Reorganization in the Lithium Battery Cathode $\text{Li}[\text{Ni}_{0.2}\text{Li}_{0.2}\text{Mn}_{0.6}]\text{O}_2$.” *Journal of the American Chemical Society* **2006**, *128*, 8694–8698.
- [23] A. Boulineau, L. Simonin, J.-F. Colin, C. Bourbon, and S. Patoux. “First Evidence of Manganese–Nickel Segregation and Densification upon Cycling in Li-Rich Layered Oxides for Lithium Batteries.” *Nano Letters* **2013**, *13*, 3857–3863.
- [24] H. Koga, L. Croguennec, M. Ménétrier, P. Mannessiez, F. Weill, and C. Delmas. “Different Oxygen Redox Participation for Bulk and Surface: A Possible Global Explanation for the cycling mechanism of $\text{Li}_{1.20}\text{Mn}_{0.54}\text{Co}_{0.13}\text{Ni}_{0.13}\text{O}_2$.” *Journal of Power Sources* **2013**, *236*, 250–258.
- [25] A. D. Robertson and P. G. Bruce. “The Origin of Electrochemical Activity in Li_2MnO_3 .” *Chemical Communications* **2002**, 2790–2791.
- [26] A. D. Robertson and P. G. Bruce. “Mechanism of Electrochemical Activity in Li_2MnO_3 .” *Chemistry of Materials* **2003**, *15*, 1984–1992.
- [27] Huggins, R. *Advanced Batteries: Materials Science Aspects*; Springer: New York, 2008.
- [28] E. McCalla, A. W. Rowe, R. Shunmugasundaram, and J. R. Dahn. “Structural Study of the Li–Mn–Ni Oxide Pseudoternary System of Interest for Positive Electrodes of Li-Ion Batteries.” *Chemistry of Materials* **2013**, *25*, 989–999.

- [29] E. McCalla, A. W. Rowe, C. R. Brown, L. R. P. Hacquebard, and J. R. Dahn. "How Phase Transformations during Cooling Affect Li-Mn-Ni-O Positive Electrodes in Lithium Ion Batteries." *Journal of The Electrochemical Society* **2013**, *160*, A1134–A1138.
- [30] E. McCalla. "Structural and Electrochemical Studies of the Li-Mn-Ni-O and Li-Co-Mn-O Pseudo-ternary Systems", PhD Thesis, Dalhousie University, Halifax, NS, Canada, 2013.
- [31] J. Cabana, M. Casas-Cabanas, F. O. Omenya, N. A. Chernova, D. Zeng, M. S. Whittingham, and C. P. Grey. "Composition-Structure Relationships in the Li-Ion Battery Electrode Material $\text{LiNi}_{0.5}\text{Mn}_{1.5}\text{O}_4$." *Chemistry of Materials* **2012**, *24*, 2952–2964.
- [32] C. S. Johnson, J.-S. Kim, C. Lefief, N. Li, J. T. Vaughey, and M. M. Thackeray. "The Significance of the Li_2MnO_3 Component in 'Composite' $x\text{Li}_2\text{MnO}_3 \bullet (1-x)\text{LiMn}_{0.5}\text{Ni}_{0.5}\text{O}_2$ Electrodes." *Electrochemistry Communications* **2004**, *6*, 1085–1091.
- [33] M. M. Thackeray, S.-H. Kang, C. S. Johnson, J. T. Vaughey, R. Benedek, and S. A. Hackney. " Li_2MnO_3 -stabilized LiMO_2 ($M = \text{Mn, Ni, Co}$) Electrodes for Lithium-ion Batteries." *Journal of Materials Chemistry* **2007**, *17*, 3112–3125.
- [34] D. Kim, G. Sandi, J. R. Croy, K. G. Gallagher, S.-H. Kang, E. Lee, M. D. Slater, C. S. Johnson, and M. M. Thackeray. "Composite 'Layered-Layered-Spinel' Cathode Structures for Lithium-Ion Batteries." *Journal of The Electrochemical Society* **2013**, *160*, A31–A38.
- [35] H. Deng, I. Belharouak, Y.-K. Sun, and K. Amine. " $\text{Li}_x\text{Ni}_{0.25}\text{Mn}_{0.75}\text{O}_y$ ($0.5 \leq x \leq 2, 2 \leq y \leq 2.75$) Compounds for High-energy Lithium-ion Batteries." *Journal of Materials Chemistry* **2009**, *19*, 4510–4516.
- [36] H. Deng, I. Belharouak, R. E. Cook, H. Wu, Y.-K. Sun, and K. Amine. "Nanostructured Lithium Nickel Manganese Oxides for Lithium-Ion Batteries." *Journal of The Electrochemical Society* **2010**, *157*, A447–A452.
- [37] F. Zhou, X. Zhao, A. van Bommel, A. W. Rowe, and J. R. Dahn. "Coprecipitation Synthesis of $\text{Ni}_x\text{Mn}_{1-x}(\text{OH})_2$ Mixed Hydroxides." *Chemistry of Materials* **2010**, *22*, 1015–1021.

- [38] K.-S. Lee, S.-T. Myung, J.-S. Moon, and Y.-K. Sun. “Particle Size Effect of $\text{Li}[\text{Ni}_{0.5}\text{Mn}_{0.5}]\text{O}_2$ Prepared by Co-precipitation.” *Electrochimica Acta* **2008**, *53*, 6033–6037.
- [39] C. Deng, L. Liu, W. Zhou, K. Sun, and D. Sun. “Effect of Synthesis Condition on the Structure and Electrochemical Properties of $\text{Li}[\text{Ni}_{1/3}\text{Mn}_{1/3}\text{Co}_{1/3}]\text{O}_2$ Prepared by Hydroxide Co-precipitation Method.” *Electrochimica Acta* **2008**, *53*, 2441–2447.
- [40] A. Van Bommel and J. R. Dahn. “Kinetics Study of the High Potential Range of Lithium-Rich Transition-Metal Oxides for Lithium-Ion Batteries by Electrochemical Methods.” *Electrochemical and Solid-State Letters* **2010**, *13*, A62–A64.
- [41] Van Bommel, A. “Lithium-Rich Transition Metal Oxides as Positive Electrode Materials in Lithium-Ion Batteries”, PhD Thesis, Dalhousie University, Halifax, NS, Canada, 2010.
- [42] A. Van Bommel and J. R. Dahn. “Analysis of the Growth Mechanism of Coprecipitated Spherical and Dense Nickel, Manganese, and Cobalt-Containing Hydroxides in the Presence of Aqueous Ammonia.” *Chemistry of Materials* **2009**, *21*, 1500–1503.
- [43] D. A. Skoog, F. J. Holler, and T. A. Nieman. *Principles of Instrumental Analysis*; Saunders College Publishing: Philadelphia, 1998.
- [44] P. Atkins and J. de Paula. *Physical Chemistry*; W. H. Freeman: New York, 2010.
- [45] D. Munro. *Yorick (programming language)*; Lawrence Livermore National Laboratory: Livermore, California, 2010.
- [46] P. R. Bevington. *Data Reduction and Error Analysis for the Physical Sciences*; McGraw-Hill, 1969.
- [47] H. M. Rietveld. “A Profile Refinement Method for Nuclear and Magnetic Structures.” *Journal of Applied Crystallography* **1969**, *2*, 65–71.
- [48] B. A. Hunter. *Rietica - A Visual Rietveld Program*; Commission on Powder Diffraction; International Union of Crystallography, 1998.

- [49] T. M. Bond, J. C. Burns, D. A. Stevens, H. M. Dahn, and J. R. Dahn. “Improving Precision and Accuracy in Coulombic Efficiency Measurements of Li-Ion Batteries.” *Journal of The Electrochemical Society* **2013**, *160*, A521–A527.
- [50] A. J. Smith, J. C. Burns, S. Trussler, and J. R. Dahn. “Precision Measurements of the Coulombic Efficiency of Lithium-Ion Batteries and of Electrode Materials for Lithium-Ion Batteries.” *Journal of The Electrochemical Society* **2010**, *157*, A196–A202.
- [51] N. N. Sinha, J. C. Burns, R. J. Sanderson, and J. Dahn. “Comparative Studies of Hardware Corrosion at High Potentials in Coin-Type Cells with Non Aqueous Electrolytes.” *Journal of The Electrochemical Society* **2011**, *158*, A1400–A1403.
- [52] W. Li, J. N. Reimers, and J. R. Dahn. “Crystal Structure of $\text{Li}_x\text{Ni}_{2-x}\text{O}_2$ and a Lattice-Gas Model for the Order-Disorder Transition.” *Physical Review B* **1992**, *46*, 3236–3246.
- [53] F. N. Rhines. *Phase Diagrams in Metallurgy*; McGraw-Hill: New York, 1956.
- [54] Y. Shin and A. Manthiram. “Origin of the Capacity of Spinel $\text{LiMn}_{2-y}\text{Li}_y\text{O}_{4\pm\delta}$ ($0 \leq y \leq 0.15$) in the 5 V Region.” *Electrochemical and Solid-State Letters* **2003**, *6*, A249–A251.
- [55] J. Song, D. W. Shin, Y. Lu, C. D. Amos, A. Manthiram, and J. B. Goodenough. “Role of Oxygen Vacancies on the Performance of $\text{Li}[\text{Ni}_{0.5-x}\text{Mn}_{1.5+x}]\text{O}_4$ ($x = 0, 0.05, \text{ and } 0.08$) Spinel Cathodes for Lithium-Ion Batteries.” *Chemistry of Materials* **2012**, *24*, 3101–3109.
- [56] Q. Zhong, A. Bonakdarpour, M. Zhang, Y. Gao, and J. R. Dahn. “Synthesis and Electrochemistry of $\text{LiNi}_x\text{Mn}_{2-x}\text{O}_4$.” *Journal of The Electrochemical Society* **1997**, *144*, 205–213.
- [57] P. G. Bruce, A. R. Armstrong, and R. L. Gitzendanner. “New Intercalation Compounds for Lithium Batteries: Layered LiMnO_2 .” *Journal of Materials Chemistry* **1999**, *9*, 193–198.

- [58] J. R. Croy, D. Kim, M. Balasubramanian, K. Gallagher, S.-H. Kang, and M. M. Thackeray. “Countering the Voltage Decay in High Capacity $x\text{Li}_2\text{MnO}_3 \bullet (1-x)\text{LiMO}_2$ Electrodes (M=Mn, Ni, Co) for Li-ion Batteries.” *Journal of The Electrochemical Society* **2012**, *159*, A781–A790.
- [59] A. R. Armstrong, N. Dupre, A. J. Paterson, C. P. Grey, and P. G. Bruce. “Combined Neutron Diffraction, NMR, and Electrochemical Investigation of the Layered-to-Spinel Transformation in LiMnO_2 .” *Chemistry of Materials* **2004**, *16*, 3106–3118.
- [60] A. R. Armstrong, A. J. Paterson, N. Dupre, C. P. Grey, and P. G. Bruce. “Structural Evolution of Layered $\text{Li}_x\text{Mn}_y\text{O}_2$: Combined Neutron, NMR, and Electrochemical Study.” *Chemistry of Materials* **2007**, *19*, 1016–1023.
- [61] S. Patoux, L. Sannier, H. Lignier, Y. Reynier, C. Bourbon, S. Jouanneau, F. Le Cras, and S. Martinet. “High Voltage Nickel Manganese Spinel Oxides for Li-ion Batteries.” *Electrochimica Acta* **2008**, *53*, 4137–4145.
- [62] S. Patoux, L. Daniel, C. Bourbon, H. Lignier, C. Pagano, F. Le Cras, S. Jouanneau, and S. Martinet. “High Voltage Spinel Oxides for Li-ion Batteries: From the Material Research to the Application.” *Journal of Power Sources* **2009**, *189*, 344–352.
- [63] A. Ito, D. Li, Y. Ohsawa, and Y. Sato. “A New Approach to Improve the High-Voltage Cyclic Performance of Li-rich Layered Cathode Material by Electrochemical Pre-treatment.” *Journal of Power Sources* **2008**, *183*, 344–346.
- [64] A. Van Bommel, L. J. Krause, and J. R. Dahn. “Investigation of the Irreversible Capacity Loss in the Lithium-Rich Oxide $\text{Li}[\text{Li}_{1/5}\text{Ni}_{1/5}\text{Mn}_{3/5}]\text{O}_2$.” *Journal of The Electrochemical Society* **2011**, *158*, A731–A735.
- [65] A. W. Rowe and J. R. Dahn. “Positive Electrode Materials in the Li-Mn-Ni-O System Exhibiting Anomalous Capacity Growth during Extended Cycling.” *Journal of The Electrochemical Society* **2014**, *161*, A308–A317.
- [66] S.-H. Park, S.-H. Kang, C. S. Johnson, K. Amine, and M. M. Thackeray. “Lithium-Manganese-Nickel-Oxide Electrodes with Integrated Layered-Spinel Structures for Lithium batteries.” *Electrochemistry Communications* **2007**, *9*, 262–268.

- [67] M.-H. Lee, Y.-J. Kang, S.-T. Myung, and Y.-K. Sun. "Synthetic Optimization of $\text{Li}[\text{Ni}_{1/3}\text{Co}_{1/3}\text{Mn}_{1/3}]\text{O}_2$ via Co-precipitation." *Electrochimica Acta* **2004**, *50*, 939–948.
- [68] S.-H. Park, S.-W. Oh, C.-S. Yoon, S.-T. Myung, and Y.-K. Sun. "LiNi_{0.5}Mn_{1.5}O₄ Showing Reversible Phase Transition on 3 V Region." *Electrochemical and Solid-State Letters* **2005**, *8*, A163–A167.
- [69] S. H. Park, S.-W. Oh, S. H. Kang, I. Belharouak, K. Amine, and Y.-K. Sun. "Comparative Study of Different Crystallographic Structure of LiNi_{0.5}Mn_{1.5}O_{4- δ} Cathodes with Wide Operation Voltage (2.0–5.0 V)." *Electrochimica Acta* **2007**, *52*, 7226–7230.
- [70] E.-S. Lee, A. Huq, H.-Y. Chang, and A. Manthiram. "High-Voltage, High-Energy Layered-Spinel Composite Cathodes with Superior Cycle Life for Lithium-Ion Batteries." *Chemistry of Materials* **2012**, *24*, 600–612.
- [71] T. A. Arunkumar, Y. Wu, and A. Manthiram. "Factors Influencing the Irreversible Oxygen Loss and Reversible Capacity in Layered $\text{Li}[\text{Li}_{1/3}\text{Mn}_{2/3}]\text{O}_2 \bullet \text{Li}[\text{M}]\text{O}_2$ (M = $\text{Mn}_{0.5-y}\text{Ni}_{0.5-y}\text{Co}_{2y}$ and $\text{Ni}_{1-y}\text{Co}_y$) Solid Solutions." *Chemistry of Materials* **2007**, *19*, 3067–3073.
- [72] Z. Q. Deng and A. Manthiram. "Influence of Cationic Substitutions on the Oxygen Loss and Reversible Capacity of Lithium-Rich Layered Oxide Cathodes." *The Journal of Physical Chemistry C* **2011**, *115*, 7097–7103.
- [73] A. J. Smith, J. C. Burns, D. Xiong, and J. R. Dahn. "Interpreting High Precision Coulometry Results on Li-ion Cells." *Journal of The Electrochemical Society* **2011**, *158*, A1136–A1142.
- [74] A. W. Rowe, J. Camardese, E. McCalla, and J. R. Dahn, "High Precision Coulometry Studies of Single-phase Layered Compositions in the Li-Mn-Ni-O System." *Journal of The Electrochemical Society*, **2014**, *161*, A1189–A1193.
- [75] Y.-K. Sun, S.-T. Myung, B.-C. Park, J. Prakash, I. Belharouak, and K. Amine. "High-Energy Cathode Material for Long-life and Safe Lithium Batteries." *Nature Materials* **2009**, *8*, 320–324.

- [76] Y.-K. Sun, Z. Chen, H.-J. Noh, D.-J. Lee, H.-G. Jung, Y. Ren, S. Wang, C. S. Yoon, S.-T. Myung, and K. Amine. “Nanostructured High-Energy Cathode Materials for Advanced Lithium Batteries.” *Nature Materials* **2012**, *11*, 942–947.
- [77] N. P. W. Pieczonka, Z. Liu, P. Lu, K. L. Olson, J. Moote, B. R. Powell, and J.-H. Kim. “Understanding Transition-Metal Dissolution Behavior in $\text{LiNi}_{0.5}\text{Mn}_{1.5}\text{O}_4$ High-Voltage Spinel for Lithium Ion Batteries.” *The Journal of Physical Chemistry C* **2013**, *117*, 15947–15957.
- [78] J. R. Croy, K. G. Gallagher, M. Balasubramanian, Z. Chen, Y. Ren, D. Kim, S.-H. Kang, D. W. Dees, and M. M. Thackeray. “Examining Hysteresis in Composite $x\text{Li}_2\text{MnO}_3 \cdot (1-x)\text{LiMO}_2$ Cathode Structures.” *The Journal of Physical Chemistry C* **2013**, *117*, 6525–6536.
- [79] E. McCalla, C. M. Lowartz, C. R. Brown, and J. R. Dahn. “Formation of Layered–Layered Composites in the Li–Co–Mn Oxide Pseudoternary System during Slow Cooling.” *Chemistry of Materials* **2013**, *25*, 912–918.
- [80] J. Lee, A. Urban, X. Li, D. Su, G. Hautier, and G. Ceder. “Unlocking the Potential of Cation-Disordered Oxides for Rechargeable Lithium Batteries.” *Science* **2014**, *343*, 519–522.